HETEROGENEOUS RECOMBINATION OF NEUTRAL OXYGEN ATOMS ON THE SURFACES OF OXIDIZED MATERIALS

Domen Paul

Doctoral Dissertation
Jožef Stefan International Postgraduate School
Ljubljana, Slovenia

Supervisor: Prof. Dr. Miran Mozetič, Jožef Stefan Institute, Ljubljana, Slovenia
Co-Supervisor: Assoc. Prof. Dr. Rok Zaplotnik, Jožef Stefan Institute, Ljubljana, Slovenia

Evaluation Board:
Assist. Prof. Dr. Gregor Primc, Chair, Jožef Stefan Institute and Jožef Stefan International Postgraduate School, Ljubljana, Slovenia
Prof. Dr. Alenka Vesel, Member, Jožef Stefan Institute and Jožef Stefan International Postgraduate School, Ljubljana, Slovenia
Prof. RNDr. Petr Špatenka, Member, CSc., Faculty of Mechanical Engineering, Czech Technical University, Prague, Czech Republic

MEDNARODNA PODIPLOMSKA ŠOLA JOŽEFA STEFANA
JOŽEF STEFAN INTERNATIONAL POSTGRADUATE SCHOOL

Domen Paul

HETEROGENEOUS RECOMBINATION OF NEUTRAL OXYGEN ATOMS ON THE SURFACES OF OXIDIZED MATERIALS

Doctoral Dissertation

HETEROGENA REKOMBINACIJA NEVTRALNIH KISIKOVIH ATOMOV NA POVRŠINAH OKSIDIRANIH MATERIALOV

Doktorska disertacija

Supervisor: Prof. Dr. Miran Mozetič

Co-Supervisor: Assoc. Prof. Dr. Rok Zaplotnik

Ljubljana, Slovenia, November 2023

Acknowledgments

This dissertation and all the work concerning it was possible due to the financial support of the Slovenian Research and Innovation Agency (ARIS) on the following projects: P2-0082 and PR-09755.

More importantly, this dissertation would not have been possible without the help of my colleagues at the Department of Surface Engineering. First of all, I would like to thank my supervisor Miran Mozetič for all his help in writing articles and all his ideas that helped me solve many problems in the laboratory. Secondly, I would like to thank my co-supervisor Rok Zaplotnik, who taught me everything about working in the plasma laboratory and always provided guidance when I was unsure how to proceed with my studies. Special thanks go to Alenka Vesel for her help in my studies and her general concern for me during my time at the F4 department. This dissertation would also not be possible without Gregor Primc, who was always helpful with both my studies and other, more technical challenges. He also recorded all of the SEM images shown in this dissertation (and many more that are not). Another great contributor to this dissertation is Janez Trtnik, whom I would like to thank for all his assistance in the plasma laboratory and his excellent work as a technician, able to fix everything that I broke in the laboratory. I would also like to thank Jernej Ekar, who performed all the time-consuming measurements with AFM and ToF-SIMS and assisted with some of the articles. My thanks also go to Maja Šukarov for all the bureaucratic assistance and her nerves of steel. Of course, many other colleagues from my department, including Nina Recek, Dane Lojen, Mark Zver, Tatjana Filipič, Janez Kovač, Metka Benčina, Pia Starič, Ita Junkar, and Matic Resnik assisted me in various ways during my studies and truly made me feel like part of an excellent collective.

I would also like to thank two people who paved the way for my tenure at the IJS: my aunt Aleksandra Lobnik for introducing me to my supervisor Miran and Aleš Hančič, the director of the company TECOS, for employing me and giving me an opportunity to work with plasma.

Various other people also helped me on my way, especially my supporting family, including my wife Maruša, mother Petra, father Borut, and sister Lara. My thanks for sticking with me for so long. I hope that I can do the same for you one day.

Abstract

In this dissertation, we studied heterogeneous surface recombination of neutral oxygen atoms. We described plasma as a reliable source of neutral oxygen atoms and the behavior of neutral atoms in low-pressure plasma sustained by high-frequency discharges. Neutral atom density in the flowing afterglow and the recombination coefficient on several surfaces were measured. The recombination is explained via two mechanisms: Eley-Rideal and Langmuir-Hinshelwood. We pointed out the factors influencing the recombination coefficient, such as the temperature of the surface facilitating the recombination process, the morphology of said surface, and pressure in the experimental system. We deemed calorimetry a suitable measurement method for measuring both the neutral atom density and the recombination coefficient, with a detailed explanation of the workings of a standard catalytic probe, while a laser fiber-optics catalytic probe and its drawbacks are mentioned. Examples of practical applications utilizing neutral atoms were provided for context. Recombination coefficients of oxygen atoms on different materials, as revealed from the literature, were compared, and conclusions were drawn from correlating factors, such as the increase of the recombination coefficient with the increasing surface temperature. A few hypotheses were established: the viability of the Šorli-Ročak method to determine the absolute number density of neutral oxygen atoms, the variable nature of the recombination coefficient, and the increase of the recombination coefficient with increasing temperature and surface roughness, as well as decreasing pressure. The Šorli-Ročak method was explained in detail and used in a low-pressure microwave discharge to successfully determine the absolute neutral oxygen atom density with three different materials: nickel, cobalt, and iron, confirming the first hypothesis. In the same system, the recombination coefficient of oxidized nickel was determined. We discovered that the recombination coefficient is not constant but increases with increasing surface temperature and decreasing pressure, confirming three hypotheses. An empirical formula was devised to describe the temperature and pressure dependence of the recombination coefficient. We carried out similar experiments with a catalytic probe with an oxidized cobalt tip, with similar results as for nickel, re-confirming the hypotheses. We found oxidized cobalt to have a stable recombination coefficient at elevated temperatures. The validity of the Šorli-Ročak method was again confirmed with the study of the penetration depth of oxygen atoms inside metallic tubes, with nickel, cobalt, and copper proven to be efficient recombinators. Carbon nanomaterials were examined as possible candidates for efficient recombination due to their high surface-to-mass ratio. We explained the synthesis of various carbon nanomaterials, and the importance of a carbon atom source was shown. The materials were examined using various measurement techniques. Lastly, the much higher recombination coefficient of carbon nanomaterial-covered oxidized cobalt samples was determined, confirming the last hypothesis.

Povzetek

Glavna tema te disertacije je heterogena površinska rekombinacija nevtralnih kisikovih atomov. Plazmo smo opisali kot zanesljiv vir nevtralnih kisikovih atomov in opisali tudi obnašanje le-teh v nizkotlačnih plazemskih razelektritvah. Definirali smo dve ključni količini: gostoto nevtralnih atomov in rekombinacijski koeficient. Rekombinacijo smo pojasnili preko Eley-Rideal in Langmuir-Hinshelwood mehanizma. Na rekombinacijski koeficient vplivajo različni faktorji, med njimi temperatura in morfologija površine ter tlak v okolici. Za metodo merjenja gostote nevtralnih atomov in rekombinacijskega koeficienta smo izbrali kalorimetrijo, kjer smo podrobneje opisali delovanje katalitične sonde. Omenili smo tudi lasersko katalitično sondo in njene pomanjkljivosti. Opisanih je nekaj praktičnih primerov uporabe nevtralnih atomov. Med seboj smo primerjali rekombinacijske koeficiente kisikovih atomov na različnih materialih iz literature, na podlagi česar smo ugotovili, da se rekombinacijski koeficient v večini primerov viša z višanjem temperature površine. Podali smo naslednje hipoteze: Šorli-Ročak metoda je ustrezna za določanje absolutne gostote nevtralnih atomov. Rekombinacijski koeficient se spreminja, in sicer se viša z višanjem temperature in površinsko hrapavostjo ter niža s tlakom v okolici. Opisali smo Šorli-Ročak metodo in jo uporabili za določanje absolutne gostote nevtralnih kisikovih atomov v nizkotlačni mikrovalovni plazmi s pomočjo treh različnih materialov: nikelj, kobalt in železo. Ustreznost rezultatov je potrdila prvo hipotezo. V istem sistemu smo določili rekombinacijski koeficient oksidiranega niklja, ki ni konstanten, kar potrdi še eno hipotezo. Ugotovili smo, da se rekombinacijski koeficient viša z višanjem temperature in niža z višanjem tlaka, kar potrdi še dve hipotezi. Z empirično formulo smo opisali odvisnost rekombinacijskega koeficienta od temperature in tlaka. Enak eksperiment smo ponovili še za oksidiran kobalt, ki se obnaša podobno kot oksidiran nikelj, kar je še enkrat potrdilo naše hipoteze. Izjema je bila stabilnost rekombinacijskega koeficienta oksidiranega kobalta pri višjih temperaturah. Ustreznost Šorli-Ročak metode smo še enkrat potrdili z eksperimentom, kjer smo gledali vdorno globino nevtralnih kisikovih atomov znotraj kovinskih cevk. Uporabili smo cevke iz niklja, kobalta in bakra; njihova majhna vdorna globina je še enkrat potrdila ustreznost Šorli-Ročak metode. Opisali smo še ogljikove nanomateriale, ki so potencialno odlični rekombinatorji zaradi njihovega visokega razmerja med površino in maso, kar se odraža tudi v visoki hrapavosti površine. Sintetizirali smo nekaj različnih ogljikovih nanomaterialov, kar nam je pokazalo pomembnost izbire materiala za vir ogljikovih atomov, ki so gradniki ogljikovih nanomaterialov. Ogljikove nanomateriale smo preučili s pomočjo različnih merilnih tehnik. Nazadnje smo določili še rekombinacijski koeficient ogljikovih nanomaterialov, nanešenih na oksidiranem kobaltu. Zelo visoka vrednost rekombinacijskega koeficienta je potrdila še zadnjo hipotezo.

Contents

List of Figures **xiii**

List of Tables **xv**

1 Introduction **1**
- 1.1 Plasma 2
- 1.2 Atom species generation by plasma 12
- 1.3 A review of recombination coefficients of neutral oxygen atoms for various materials 64
- 1.4 Hypothesis 115

2 Recombination of oxygen atoms on oxidized surfaces **117**
- 2.1 Recombination of oxygen atoms on the surface of oxidized polycrystalline nickel – temperature and pressure dependences 118
- 2.2 Loss of oxygen atoms on well-oxidized cobalt by heterogeneous surface recombination 134
- 2.3 The penetration depth of atomic radicals in tubes with catalytic surface properties 148

3 Recombination of atoms on nanostructured materials **167**
- 3.1 Comparison of plasma decomposition of carbon nanomaterials using various polymer materials as a carbon atom source 168
- 3.2 Recombination coefficient of carbon nanomaterials deposited on a cobalt sample 183

4 Conclusions **191**

References **193**

Bibliography **201**
    - 4.1.1.1 1.01 Original scientific article 201
    - 4.1.1.2 1.02 Review article 202
    - 4.1.1.3 1.12 Published scientific conference contribution abstract 202
    - 4.1.1.4 1.16 Independent scientific component part or a chapter in a monograph 203
  - 4.1.2 MONOGRAPHS AND OTHER COMPLETED WORKS 203
    - 4.1.2.1 2.09 Master's thesis 203
    - 4.1.2.2 2.11 Undergraduate thesis 203

Biography **205**

List of Figures

Figure 1. Schematic of a simple vacuum system above and the approximation of the pressure gradient along the vacuum system below. 3
Figure 2. A simplified graph of potential energy (Wp) versus the distance (d) from the surface of a material for a neutral atom and a two-atom molecule. The difference between the atom and molecule potential energies (ΔWp) far away from the surface of the material is equal to half the dissociation energy of the molecule [14]. 4
Figure 3. A simple schematic of the Eley-Rideal mechanism: a) atoms from the gaseous state approach a surface; b) they are adsorbed to the surface because another atom approaches the same position on the surface; c) the approaching atom recombines with the already adsorbed atom; d) the resulting molecule leaves the surface..................................6
Figure 4. A simple schematic of the Langmuir-Hinshelwood mechanism: a) atoms from the gaseous state approach a surface; b) they are adsorbed to the surface, and migrate along with it; c) two migrating atoms reach one another and recombine; d) the resulting molecule leaves the surface. 6
Figure 5. Possible elastic collisions of gaseous atoms with a: a) smooth and b) rough surface. 7
Figure 6. A simple schematic of a standard catalytic probe connected to a voltmeter with thermocouple wires encased in a glass housing. 8
Figure 7. Measurements of probe tip temperature (T) versus time with a standard catalytic probe. The moment the plasma is switched off the temperature starts falling rapidly. The probe tip was made of cobalt and submerged in oxygen gas with a radiofrequency discharge. Listed above are the powers of the generator and the pressures inside the plasma system. Under specific conditions (green line), a plasma can spontaneously switch from a low-power mode (red line) to a high-power mode (blue line). 10
Figure 8. Measurement performed with a laser fiber-optics catalytic probe with the probe tip made of cobalt and submerged in oxygen plasma sustained by an RF discharge at the given pressure. The graph shows the neutral oxygen atom density (nO) over time (t). We were changing the input power of the radiofrequency generator in steps shown on the graph. 11
Figure 9. Schematic of a metallic tube positioned at a similarly sized orifice downstream of a plasma discharge so that all the neutral atoms have to pass through the metallic tube. 118
Figure 10. Schematic of the experimental setup using the low-pressure microwave plasma system. 118
Figure 11. The root-mean-square surface roughness (Sq) of nickel samples oxidized at different temperatures (T) in oxygen plasma. 119
Figure 12. A simple schematic of carbon nanowalls (blue) on a substrate (yellow) from the (a) top-down view and (b) from the side-view...168
Figure 13. A simple schematic of the experimental setup used for the synthesis of carbon nanomaterials on the cobalt tip of a catalytic probe. 184

Figure 14. The temperature (T) of the cobalt tip of the catalytic probe versus time (t) during a typical 30-second deposition (blue section) of carbon nanomaterials using propane gas as a carbon atom source.. 185
Figure 15. SEM images of the surface of the cobalt sample where carbon nanomaterials were grown. The first row shows a larger part of the surface, the second row is a close-up of finer details, and the third row shows the thickness of the carbon nanomaterial layer. Pictures were taken for deposition times of 30 s (first column: a, e, and i), 60 s (second column: b, f, and j), 120 s (third column: c, g, and k), and 300 s (last column: d, h, and l). 186
Figure 16. Recombination coefficient (γ) of oxidized cobalt with different thicknesses of the deposited carbon nanomaterial layer versus temperature (T) of the oxidized cobalt sample at 42 Pa. 187
Figure 17. Recombination coefficient (γ) of oxidized cobalt with different thicknesses of the deposited carbon nanomaterial layer versus temperature (T) of the oxidized cobalt sample at 79 Pa. 187
Figure 18. Recombination coefficient (γ) of oxidized cobalt with different thicknesses of the deposited carbon nanomaterial layer versus temperature (T) of the oxidized cobalt sample at 117 Pa.188
Figure 19. Recombination coefficient (γ) of oxidized cobalt with different thicknesses of the deposited carbon nanomaterial layer versus temperature (T) of the oxidized cobalt sample at 156 Pa.188
Figure 20. Recombination coefficient (γ) of oxidized cobalt with different thicknesses of the deposited carbon nanomaterial layer versus temperature (T) of the oxidized cobalt sample at 214 Pa.189

List of Tables

Table 1. The average thickness of carbon nanomaterial layers (d) for four different times of deposition (td), with a statistical error of ±10%..185

Chapter 1

Introduction

Any kind of outside interaction with the material, be it of electromagnetic, mechanical, or chemical nature, often starts at the surface of that material, regardless of the penetration depth of the interaction. In light of that, the surface of a given material and its properties have always been a highly important topic of research throughout history. From the hardest metals to the softest linen fabrics, their surface has always been of great interest to the prying eyes of a researcher.

While surfaces can be studied with non-invasive methods, such as photon or electron-based microscopy and spectroscopy, a large insight into the properties of the surface of a material can also be gleaned with more invasive methods, which can completely change the surface properties of a material. Such methods usually involve high-energy photons, ions, and sometimes even neutral particles, such as molecules, radicals, and atoms [1].

One such method is plasma treatment where we submerge a material into plasma which interacts with the material's surface. But first of all, what is plasma? Plasma is the so-called fourth state of matter. It is in a gas phase, has a larger number of meta-stable particles (radicals, ions, free electrons, neutral atoms), and is not in thermal equilibrium, which means different particles have different thermal energies. Therefore, defining the temperature of the plasma is a little bit more complicated. Usually, plasma temperatures are given for specific particles, for example, electron temperature, ion temperature, neutral gas kinetic temperature, etc. [1], [2].

A plasma sustained by a gaseous discharge is a reliable source of charged and neutral reactive particles, chief among them being neutral atoms. For our work, we will be focusing on them and limiting ourselves to low-pressure plasma systems filled exclusively with oxygen (and traces of impurities). We will look closely at the effects neutral atoms have when the surface of a given material is exposed to them, and what their different uses are in surface treatment of materials. One example is controlled surface oxidation, widely used in different applications [3], [4], [5], [6], [7], [8], [9].

The recombination of oxygen atoms into an oxygen molecule requires the oxygen atoms to be much closer to each other than is the typical interatomic distance in a solid material [10], [11]. This means that at least one oxygen atom must be mobile on the surface of a solid to initiate recombination, which will be explained by two known mechanisms of heterogeneous surface recombination.

In the first chapter, we will examine plasma as a steady source of neutral oxygen atoms. We will define the neutral atom density and the recombination coefficient and examine the mechanisms behind heterogeneous surface recombination. We will examine what factors influence the recombination coefficient and describe calorimetry as a viable measurement method. We will detail different discharges and other measurement methods that could help us determine the recombination coefficient. Afterwards, we will outline a few hypotheses.

In the second chapter, we will describe the Šorli-Ročak method and use it to determine the absolute neutral oxygen atom density. This will be used to determine the recombination coefficients of oxidized nickel and cobalt. Lastly, we will confirm the validity of the Šorli-Ročak method by studying the penetration depth of oxygen atoms inside metallic tubes.

In the third chapter, we will focus on carbon nanomaterials. We will examine a method of synthesis of such nanomaterials on metallic substrates using plasma-enhanced chemical vapor deposition (PECVD). After examining the surface properties of carbon nanomaterials, we will deposit them on the tip of a catalytic probe to determine the recombination coefficient of carbon nanomaterials.

In the final chapter, we will summarize the conclusions of the dissertation and explain the experimental results.

1.1 Plasma

Plasma particles, such as partially ionized, dissociated, and excited radicals, which range from atoms and diatomic molecules to larger fragments of original molecules, can be used to modify the surface properties of materials [2], [12]. Depending on the type of a plasma particle and the surface properties of a material, there can be a difference in reactivity between the particle and the surface. This difference is partially a result of certain surface properties and partially a result of the reactivity of the particles interacting with the surface, which in turn is dependent on the potential energy of the particles. Let us assume that a molecule in its ground state has a potential energy $W_p = 0$. If such a molecule were to dissociate into atoms, its potential energy, defined as dissociation energy, would be the same as the binding energy of the parent molecule [1], [2]. In our case, the dissociation energy W_D for a two-atom oxygen molecule is $W_D = 5.16\ \mathrm{eV}$ [13].

Atoms formed inside gaseous plasma move freely and collide with one another. A direct two-body collision between two atoms cannot result in recombination (the formation of the parent molecule) since both atoms adhere to the law of conservation of both energy and momentum [2], [14]. The potential energy before the collision thus cannot transform into the kinetic energy of the formed molecule. Generally, recombination requires a three-body collision [14]. In special cases, there is also radiative association where simultaneously with the association occurs the formation of a photon [15].

We shall focus on three-body collisions. In gaseous plasma, the possibility of three-body collisions rises with density, which in turn rises with pressure. In general, the pressure (p) of gas can be calculated as:

$$p = n\,k\,T \tag{1.1}$$

where n is the number density of gaseous particles, $k = 1.38 \cdot 10^{-2}\ \frac{\mathrm{kg\,m^2}}{\mathrm{K\,s^2}}$ is the Boltzmann constant, and T is the kinetic temperature of the gas [1], [2], [14]. The frequency (ν), at which three-body collisions can occur in a rigid sphere model, is determined as:

$$\nu = \sigma^{5/2} n^2 \langle v \rangle \tag{1.2}$$

where σ is the collisional cross-section and $\langle v \rangle = \sqrt{\frac{8\,k\,T}{\pi\,m}}$ is the average value of the speed of particles with a certain mass (m). As evident from equations (1.1) and (1.2), the frequency of three-body collisions inside gaseous plasma is pressure-dependent, making the lifetime of a neutral atom range from a few hours at low pressures to microseconds at atmospheric pressure [14]. Therefore, we shall assume that, at low pressures, three-body collisions in gaseous plasma are negligible. Of course, a neutral atom does not necessarily recombine in every three-body collision, and the limits of a practical plasma system mean the neutral atom will eventually hit a boundary of the system and recombine there.

Let us look at a simple vacuum chamber shown in Figure 1 where gas is introduced on one side and pumped out on the other. Gas drifts from the inlet to the pump with the drift velocity (v_d), defined as:

$$v_d = S/A' \tag{1.3}$$

where S is the effective pumping speed at which the gas is being pumped out of the system, and A' is the cross-section of the vacuum chamber [14], [16]. Typical effective pumping speeds are expressed in dm^3/s [14]. The pressure gradient inside the wide tube, as seen in Figure 1, is minimal, allowing for an approximation of uniform pressure inside the wide tube. If such a system were host to a plasma, the radicals would be pumped out of the system at a considerably faster rate than they would recombine in three-body collisions.

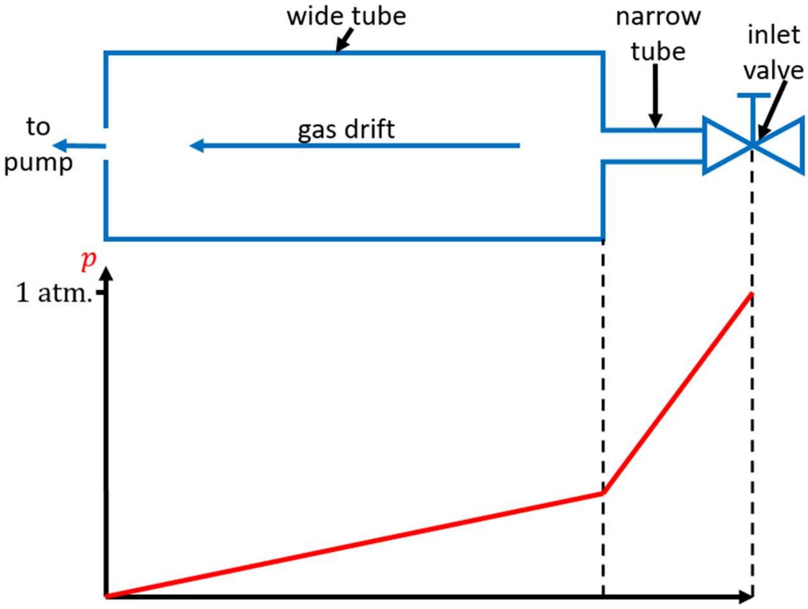

Figure 1: Schematic of a simple vacuum system above and the approximation of the pressure gradient along the vacuum system below.

Let us focus on the surface of the plasma system where the flux of particles, in our case atoms (j_{atoms}), onto a surface is defined as:

$$j_{atoms} = \frac{1}{4} n \langle v \rangle \ . \tag{1.4}$$

While stable molecules in their ground state may not be very reactive, the same cannot be said about radicals, among them neutral atoms, which are more chemically reactive. Such particles feel an attractive force on the surface and stay on it for certain time periods which depend on the surface properties of the material. In general, surfaces become saturated with a single layer of atoms, with the surface saturation time depending on the flux of atoms onto the surface and, consequently, the density of atoms [14]. Adsorbed particles may migrate, dissociate, recombine, or, in some cases, desorb from the surface. If the residence time of an atom on the surface of a material is long enough, the atom may interact with another atom, satisfying the conditions of a three-body collision. However, not every three-body collision results in recombination. The probability (and at the same time the fraction of recombined molecules) is described with the recombination coefficient (γ), which is defined as:

$$\gamma = \frac{j_{atoms}}{2j_{molecules}} \tag{1.5}$$

where $j_{molecules}$ is the flux of molecules from the surface [14], [17]. There are a couple of necessary conditions for recombination to take place: the density of atoms adsorbed on the surface must be high enough, and the adsorbed atoms must be trapped in a potential well of the surface [18]. Once that atom recombines with an incident atom, the resulting molecule has a much lower energy barrier to overcome to escape the surface, as shown schematically in Figure 2. The difference in potential energy is transferred to the internal energy of the solid, which means that a recombination process warms up the surface of the material.

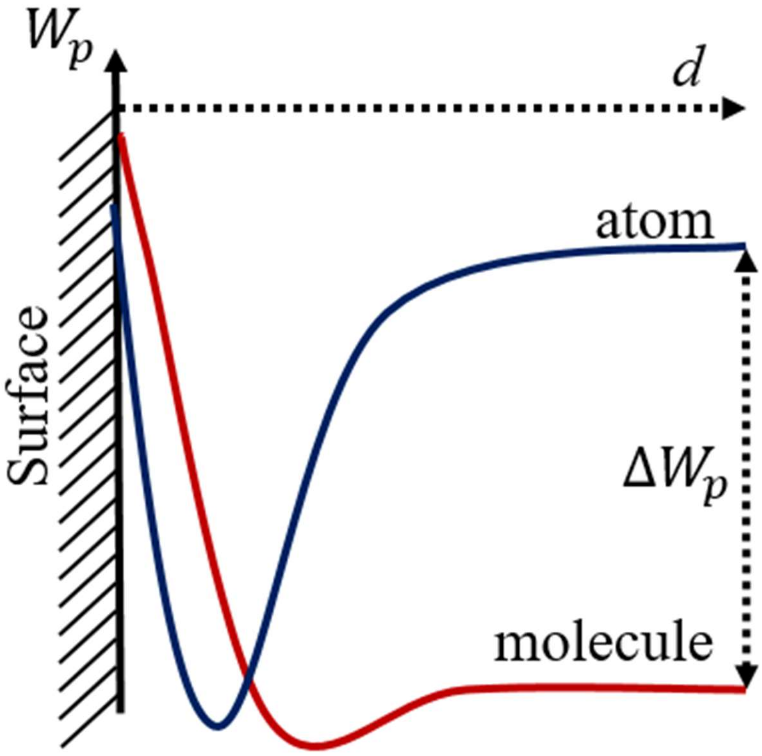

Figure 2: A simplified graph of potential energy (W_p) versus the distance (d) from the surface of a material for a neutral atom and a two-atom molecule. The difference between the atom and molecule potential energies (ΔW_p) far away from the surface of the material is equal to half the dissociation energy of the molecule [14].

A substantial fraction of the potential energy of the atoms is transferred to the internal energy of the solid material, thus heating it. The power (P_h) of such heating is:

$$P_h = \frac{1}{2} j_{atoms} W_D A \gamma \tag{1.6}$$

where W_D is the dissociation energy of the molecule and A is the geometrical surface area of the material that is exposed to the flux of atoms [14], [17]. If we insert equation (1.4) into equation (1.6), we get the following relation:

$$P_h = \frac{1}{8} W_D n \langle v \rangle A \gamma \,. \tag{1.7}$$

The same solid also releases energy via gray body radiation according to Stefan – Boltzmann law. Let us assume our solid material has a spherical shape and is suspended on a thin wire inside a vacuum system, approximating a levitating sphere with negligible absorption of gray body radiation from its surroundings (when the system temperature is much lower than the temperature of the material). The power of gray body radiation (P') of that material is:

$$P' = (1 - a) A \sigma_S T_S^4 \tag{1.8}$$

where a is the albedo of the material, $\sigma_S = 5.67 \bullet 10^{-8}\ W/m^2K^4$ is the Stefan-Boltzmann constant, and T_S is the temperature of the solid material. After exposing a solid material to such a system for a while, it reaches its equilibrium temperature (T_e) once the heating power (equation (1.7)) and the cooling power (equation (1.8)) are equal:

$$T_e = \sqrt[4]{\frac{W_D n \langle v \rangle \gamma}{8(1 - a)\sigma_S}} \,. \tag{1.9}$$

For an atom density of $n \geq 10^{21}\mathrm{m}^{-3}$, which is fairly common for low-pressure plasma sustained by electrodeless discharges [19], [20], a material with a sufficiently high recombination coefficient ($\gamma \geq 0.1$) may reach temperatures well over 1000 K [14], [21]. Materials with such a high recombination coefficient are considered catalytic for surface recombination. There are two underpinning mechanisms explaining surface recombination, and the first we will examine is the Eley-Rideal mechanism [21], [22].

One of the proposed models for neutral atom recombination on a surface, the Eley-Rideal mechanism describes the interaction between two neutral atoms: one already adsorbed to the surface and another arriving at the same position on the surface from the gas phase (Figure 3). A strong interaction between these two atoms leads to their association with the parent molecule, which leaves the surface very quickly [21], [22], [23].

The recombined molecules on the surface are not necessarily in thermal equilibrium with the surface. Thus, they can retain a substantial fraction of the potential energy as internal energy after desorption. This fraction can be as high as roughly half the dissociation energy of the molecule [22]. The resulting molecule leaving the surface is therefore often in an excited rotational or vibrational state. However, there is another mechanism for the recombination of neutral atoms atop the surface of a material.

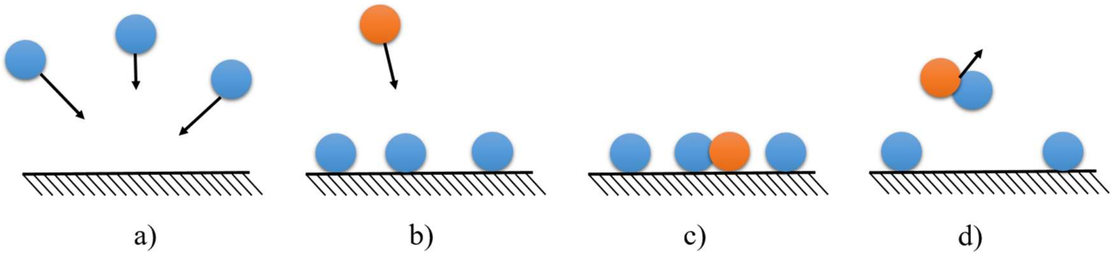

Figure 3: A simple schematic of the Eley-Rideal mechanism: a) atoms from the gaseous state approach a surface; b) they are adsorbed to the surface because another atom approaches the same position on the surface; c) the approaching atom recombines with the already adsorbed atom; d) the resulting molecule leaves the surface.

Another prominent model for surface recombination is the Langmuir-Hinshelwood mechanism, which describes the interaction of two atoms that are already adsorbed to the surface of the material [21]. Those two atoms diffuse on the surface and recombine once they are in each other's vicinity (Figure 4). Both atoms lose most of their potential energy upon adsorption. Therefore, the resulting recombined molecule does not have substantial potential energy [14], [17].

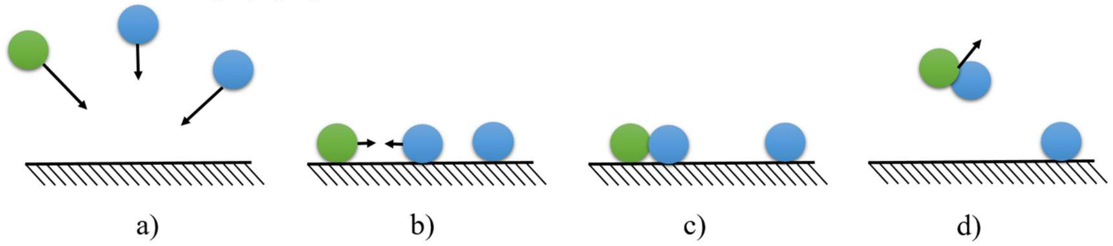

Figure 4: A simple schematic of the Langmuir-Hinshelwood mechanism: a) atoms from the gaseous state approach a surface; b) they are adsorbed to the surface, and migrate along with it; c) two migrating atoms reach one another and recombine; d) the resulting molecule leaves the surface.

The predominant mechanism is tied to the conditions of the system, such as the binding energy of atoms to the surface, the surface mobility of atoms, and the temperature of the solid material. The recombination coefficient also changes with the changing of the mechanism. However, many different factors influence the recombination coefficient of a material. While recombination coefficients for different types of plasma particles have been measured (for example, surface ion neutralization is almost 100%), our sole focus will be the recombination of neutral atoms [24], [25], [26], [27].

While the exact nature of the recombination coefficient has not been entirely determined or described in theory, we can rely on experimental results to study its behavior. First, let us examine what the recombination coefficient of a certain material tells us. Each type of material has a different recombination coefficient for a different gas. If the recombination coefficient is low (below 0.01), which is the case for borosilicate glass and oxygen atoms, then most of the oxygen atoms will not recombine on the glass surface [28], [29], [30]. Such materials are considered inert because the density of available binding sites for adsorption of gaseous atoms is low [14]. For example, the lack of interaction between borosilicate glass and oxygen makes the glass an almost perfect material for building a plasma system. On the other hand, a material with a high recombination coefficient ($\gamma \geq 0.1$) can be used inside a plasma system for different purposes. For example, nickel and nickel oxide are both used as materials for a catalytic probe that can measure the density of atoms in plasma [14], [15], [31], [22]. Because the material heats up from frequent recombinations on its surface, the temperature of the material can be directly correlated to the density of neutral atoms inside the plasma.

Materials with a high recombination coefficient are called catalytic materials since they act as catalyzers for heterogeneous surface recombinations. Catalytic materials have numerous binding sites for atoms. However, only sites for weakly bonded gaseous atoms increase the recombination rate since strongly bonded gaseous atoms have great difficulty interacting with other particles [14]. Only a few materials, most of them of high purity or perfect nature, such as monocrystals, have well-documented availabilities of binding sites and potential good shapes for gaseous atoms, resulting in well-defined recombination coefficients [32], [33]. In most other cases, the recombination coefficient is determined experimentally.

The difference between the recombination coefficient of a catalytic and an inert material can be in several orders of magnitude, which even further emphasizes the difference between such materials. Submerged in the same reactor under the same conditions, a catalytic material reaches a considerably higher temperature than an inert material. However, the recombination coefficient of material can change, depending on many factors. The first factor we will examine is the temperature.

Here, we must consider both the temperature of the gaseous particles and the surface temperature of the material. In a typical plasma system, the gaseous particles and the surface are not in thermal equilibrium. On one hand, the temperature of the gaseous particles directly correlates with their mobility, making the collision with another particle more likely [1]. In our case, an adsorbed gaseous atom on the surface of the material with greater mobility is more likely to encounter another gaseous atom and have enough energy to result in recombination [14]. On the other hand, a particle with greater mobility (and more energy) is more likely to leave the surface of a material on its own, circumventing the recombination process altogether.

Similar two-fold effects can be observed for the surface temperature of a material [34]. In general, at higher temperatures of the surface, the recombination coefficient increases, only dropping off at extremely high temperatures. This varies for inert and catalytic materials. The more interesting behavior happens at lower temperatures (it differs depending on the material and usually ranges in a couple of hundred Kelvins) [34], [35].

Temperature plays a significant role in the value of the recombination coefficient but it is not the only factor. The type of gas and surface, as well as their properties, greatly influence the recombination coefficient. One such factor is the surface morphology of a material.

Let us take a look at the material with an almost perfectly smooth surface (Figure 5a). If a gaseous atom were to collide with such a surface, there would be two possible outcomes since not every collision of an atom with a surface results in adsorption [1], [14]. The atom would either stick to the surface or bounce off it. Now let us look at material with a much rougher surface (Figure 5b). If a gaseous atom approaches such a surface and reflects off it, it can collide with it again, and another opportunity for adsorption arises. In essence, the same type of material (the same chemical composition and the same temperature) can have very different recombination coefficients depending on its surface roughness.

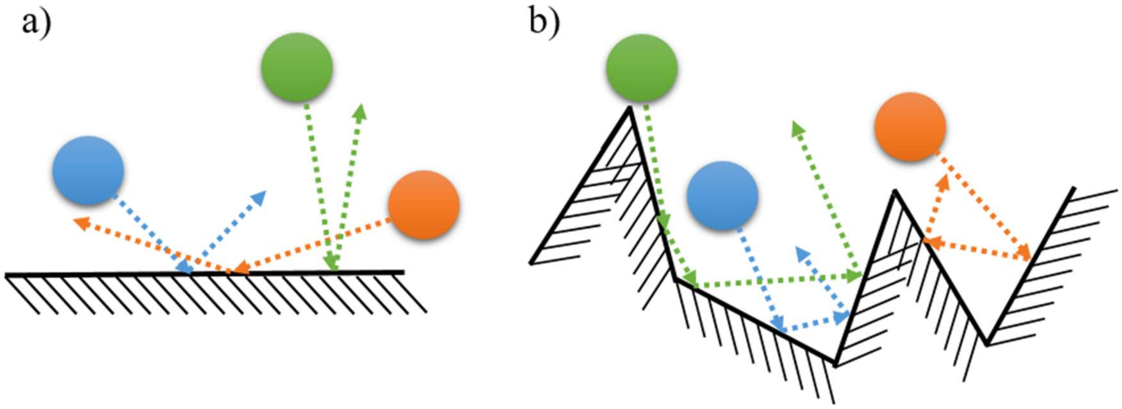

Figure 5: Possible elastic collisions of gaseous atoms with a: a) smooth and b) rough surface.

Another way to look at the surface roughness is that it increases the effective surface area of the material, facilitating more possible collision sites for gaseous atoms [36]. A good example of surface roughness impacting the recombination coefficient is the comparison between smooth carbon and some of the nanomaterials made out of it [14], [31], [36]. The finer the nanostructure of carbon, the rougher the surface, which means a larger effective surface area.

Another important factor affecting the recombination coefficient of a surface with a gaseous atom is surface chemistry. The most obvious is the chemical composition of the material since different combinations of elements make completely different materials. However, chemical modifications to the surface of the material also play a large role in changing the recombination coefficient. One such modification is the oxidation of the surface layer of metals.

Most metallic materials quickly adsorb organic impurities and form a native layer of oxide (thickness of about 1 nm), both of them being rather strongly bonded to the surface. The oxidation occurs by itself in atmospheric conditions but it can also be induced in plasma. Some metallic materials exhibit a significant increase in their recombination coefficient if they are first treated in oxygen plasma [37]. Not only does this form a thin oxide layer on the surface of the metal but it also removes most organic surface impurities. This process is called plasma activation.

While plasma systems are built from inert materials with low recombination coefficients, materials with high recombination coefficients are sought after for entirely different applications. Plasma particles interact heavily with a catalytic material, which can not only heat up the surface of the material but also modify it. There are many plasma applications for surface modifications, such as functionalization, etching, ashing, cleaning, and material deposition [14]. Among the main reactants for most of these processes are neutral atoms. Because of their importance in these processes, we need a measurement method for their detection. This brings us to catalytic probes.

A catalytic probe uses the heating from neutral atom recombination on the surface of a catalytic material to measure the number density of neutral atoms around it. An ideal probe would be an infinitely small piece of catalytic material that levitates inside the gaseous plasma. A close approximation of that ideal is a small and thin piece of catalytic material that acts as the tip of the probe connected to a thermocouple made of very thin wires (Figure 6). The thermocouple converts the temperature of the probe tip into voltage, which we can easily measure [14], [38]. A probe using this setup is a standard catalytic probe.

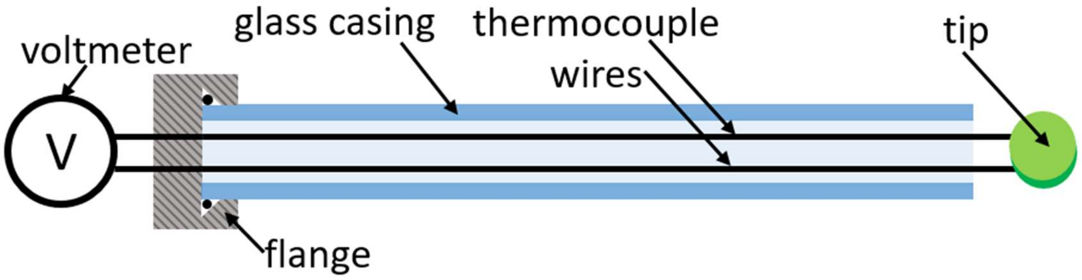

Figure 6: A simple schematic of a standard catalytic probe connected to a voltmeter with thermocouple wires encased in a glass housing.

While measuring temperature is straightforward, measuring the number density of neutral atoms in plasma is a bit more complicated. When the probe tip is immersed in the gaseous plasma, it heats up due to the recombination of neutral atoms on the surface of the tip (equation (1.7)).

At the same time, the probe tip is cooled by the thermal conductance of the nearby gas, the thermal conductance of the wires, and via radiation described by the Stefan –

Boltzmann law. While cooling via thermal conductance increases linearly with temperature (T) difference, the same cannot be said about gray body radiation which is proportional to T^4. To avoid any complications, we summarize the cooling of the probe tip as:

$$P_C = m\,c_p\frac{dT}{dt} \tag{1.10}$$

where m is the mass of the probe tip, c_p is the specific heat capacity of the probe tip material, and dT/dt is the absolute value of the first derivative of probe tip temperature over time upon turning off the discharge [38]. As the probe tip gradually heats up while exposed to the plasma, the cooling mechanisms increase in power with the rising temperature until a thermal equilibrium is reached. At that temperature, the heating power of plasma is equal to the cooling power of all the mechanisms. If we turn off the plasma while the probe tip is in thermal equilibrium, the probe tip stops heating up, leaving only the cooling mechanisms to bring it back to ambient temperature. At the moment of switching off the plasma, the cooling power is the same as the heating power of the plasma during the plasma discharge. Therefore, we can combine equations (1.7) and (1.10) to calculate the number density of neutral atoms with respect to the cooling rate (dT/dt) at the moment we switch off the discharge:

$$n = \frac{8\,m\,c_p}{v\,W_D\,\gamma\,A}\frac{dT}{dt}\,. \tag{1.11}$$

Since we can directly measure the temperature of the probe tip in real-time, we can determine the number density of neutral atoms inside plasma from the measurement (Figure 7). We do this by calculating the absolute value of the time derivative at the point of switching off plasma from the measurements while everything else in equation (1.11) is a known parameter (apart from the recombination coefficient, which can be found in literature or determined with a separate measurement). The results of such measurements can correlate known parameters (input power of the generator, pressure, position, etc.), also known as discharge parameters, with plasma parameters, such as neutral atom density.

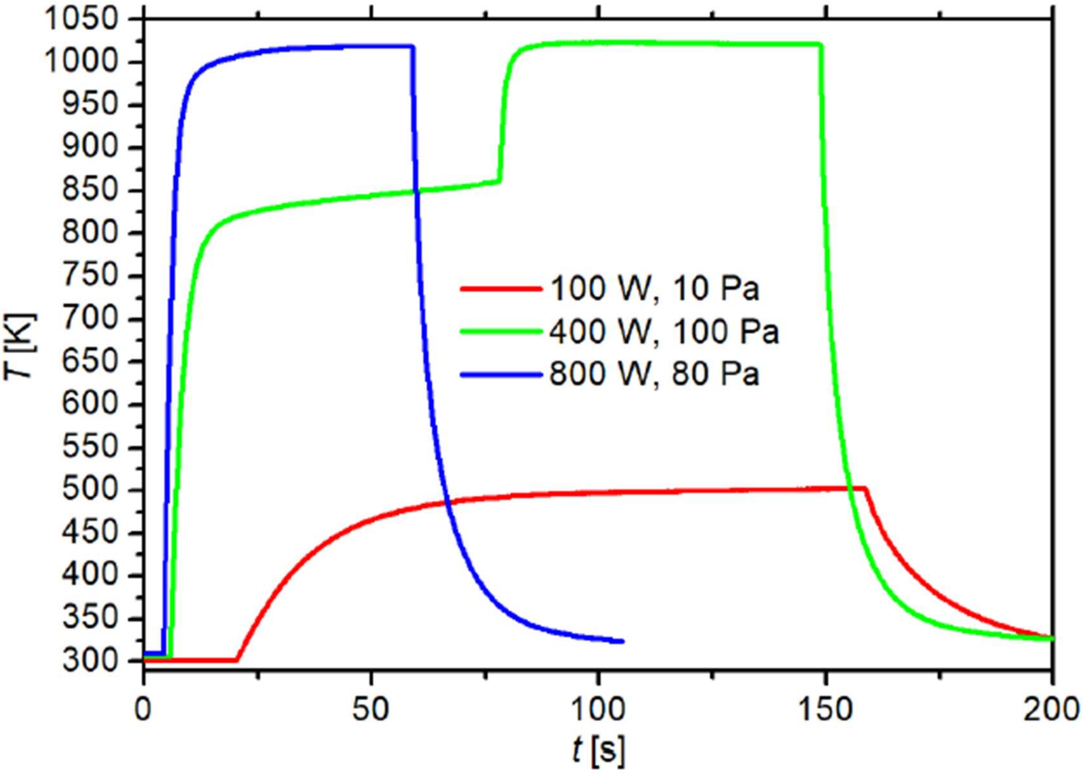

Figure 7: Measurements of probe tip temperature (T) versus time with a standard catalytic probe. The moment the plasma is switched off the temperature starts falling rapidly. The probe tip was made of cobalt and submerged in oxygen gas with a radiofrequency discharge. Listed above are the powers of the generator and the pressures inside the plasma system. Under specific conditions (green line), a plasma can spontaneously switch from a low-power mode (red line) to a high-power mode (blue line).

Over time, the surface of the probe tip deteriorates. Because of high thermal straining, the surface composition and structure of the probe tip change. Therefore, the lifetime of a probe tip is limited. Luckily enough, it is cheap and easy to replace. While measurements with a standard catalytic probe are reliable, they are time-consuming and do not give us real-time information on neutral atom density in a plasma. We can only determine that after obtaining the full measurement. A more sophisticated alternative to a standard catalytic probe is the laser fiber-optics catalytic probe which can give us real-time information on the neutral atom density inside a plasma discharge [39].

A laser fiber-optics catalytic probe works on the same principles as the standard catalytic probe with a few modifications. The probe tip is again a small and thin catalytic material that is now instead of wiring connected to an optic fiber [39], [40]. Laser radiation is guided along with that fiber to the probe tip and the same fiber is used to receive the radiation from the probe tip. The tip heats up to the equilibrium temperature that is adjustable with the power of the laser. The higher the laser power, the higher the equilibrium temperature. Once the probe is exposed to the plasma, it is heated up by heterogeneous surface recombination (equation (1.7)) but the probe is set up in a way that the probe tip temperature does not change. Once we receive data that the probe is heating up above the prior equilibrium temperature, the laser power (P_{laser}) automatically decreases to bring the probe tip temperature back down to the same temperature. This allows for continuous measurements during which we can change certain discharge parameters, such as the input power of the radiofrequency generator [39], [40].

During a typical measurement, the temperature of the probe remains roughly the same. Thus, the absolute value of the temperature derivative (equation (1.10)) is equal to zero. Before we turn on the plasma at the temperature equilibrium, the sums of powers of cooling mechanisms are equal to the power of the laser:

$$P_{laser} = P_{conductance} + P_{radiation} \tag{1.12}$$

where $P_{conductance}$ is the power of cooling via conductance and $P_{radiation}$ the power of cooling via radiation. After turning on the plasma, the same equilibrium is maintained, and the power of the laser is lowered (ΔP) by the same amount of power as the power of plasma heating (equation (1.7)) up the probe:

$$P_h + P_{laser} - \Delta P = P_{conductance} + P_{radiation} \, . \tag{1.13}$$

Combining equations (1.7), (1.12), and (2.5) gives us the relation between the number density of neutral atoms and the drop in laser power:

$$n = \frac{8\,\Delta P}{v\,W_D\,A} \, . \tag{1.14}$$

Since we constantly monitor laser power, we in turn also determine the number density of neutral atoms in real-time, as long as the temperature of the surrounding gas stays roughly the same (Figure 8).

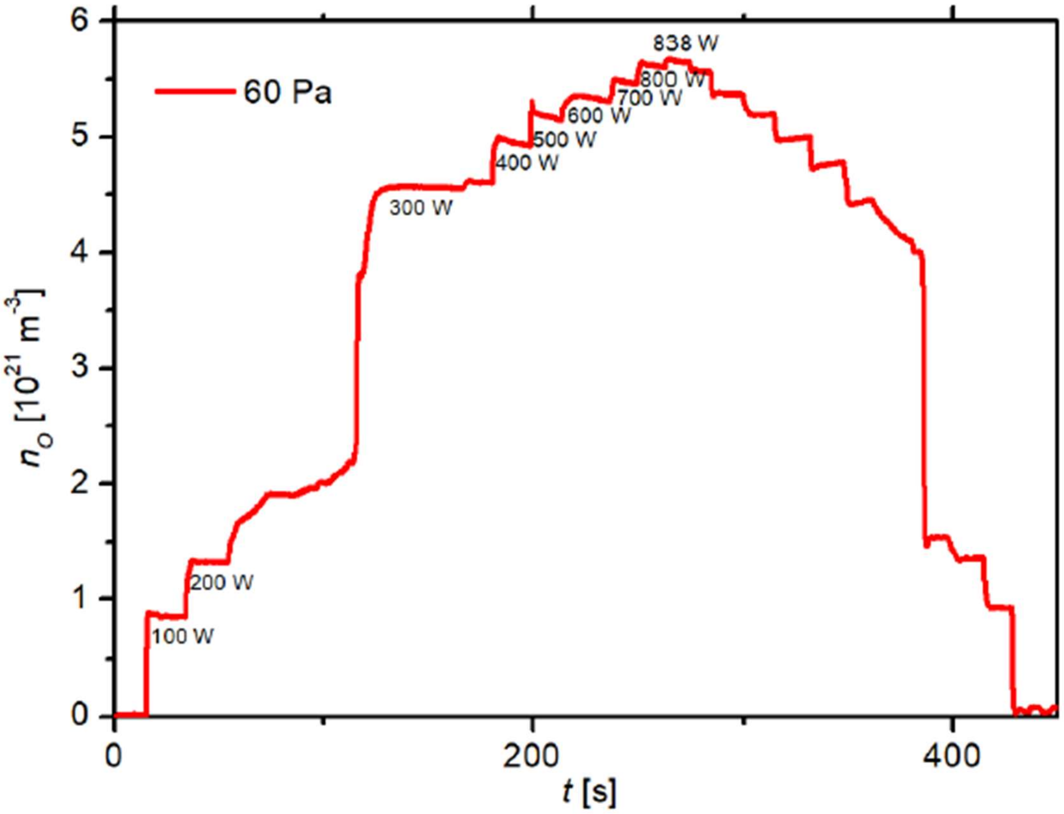

Figure 8: Measurement performed with a laser fiber-optics catalytic probe with the probe tip made of cobalt and submerged in oxygen plasma sustained by an RF discharge at the given pressure. The graph shows the neutral oxygen atom density (n_O) over time (t). We changed the input power of the radiofrequency generator in the steps shown on the graph.

A laser fiber-optics catalytic probe is especially well suited for continuously measuring neutral atom density at different probe positions inside a vacuum system [39]. Not only is the laser fiber-optics catalytic probe a much quicker method for measuring neutral atom density in a plasma discharge but it is also more reliable. Since the temperature of the probe tip remains the same during the entire measurement, the recombination coefficient for neutral atoms on the surface of the probe tip stays the same throughout the measuring process. However, the complexity of the system along with the use of a laser and an optic fiber makes this method more expensive and harder to replace if it breaks down. The optic fiber also presents a weakness for the system because of its fragility. Thus, the use cases for a laser fiber-optics catalytic probe are limited when compared to a regular catalytic probe.

1.2 Atom Species Generation by Plasma

As we have already established, gaseous plasma contains not only gaseous molecules but also ions, free electrons, and molecular fragments, such as radicals and neutral atoms. The higher reactivity of neutral atoms when compared to molecules was already demonstrated in Figure 2. Since neutral atoms can interact with a sample exposed to plasma in several ways, many different surface treatment applications using neutral atoms have been devised: deposition [41], etching [42], [43], implantation [44], surface modification [45], [46], [47], surface functionalization [48], activation [49], sterilization [50], cleaning [51], [52], ashing [53], degreasing [54], and so on.

In the proceeding book chapter [14], the various mechanisms behind the dissociation and recombination of neutral atoms are described. Due to the conservation of momentum and energy, two-body collisions between neutral atoms cannot result in them recombining into a molecule. At least a three-body collision is, therefore, necessary to achieve recombination. Therefore, an important parameter to consider is the frequency of three-body collisions between neutral atoms and with it the lifetime of neutral atoms. However, not every three-body collision results in a successful recombination.

A general description of vacuum systems is provided, with special attention given to gas drift velocity along the vacuum system which can inform the design of the vacuum chamber. Gas drift velocity describes the drift of gas from a point with higher pressure (the gas inlet) to a point with lower pressure (the pump). Gas drift velocity in vacuum systems can reach 100 $\mathrm{m/s^3}$ or more [55]. The maximal theoretical limit is the speed of sound (about 340 m/s).

Emphasis is placed on the heterogeneous recombination of neutral atoms on solid surfaces. Both recombination mechanisms (Eley-Rideal and Langmuir-Hinshelwood) are described in detail, and the importance of the recombination coefficient is demonstrated with the example of the temperature of a small particle levitating in plasma. A distinction is made between catalytic ($\gamma \geq 0.1$), semi-catalytic ($0.1 \geq \gamma \geq 0.01$), and inert ($0.01 \geq \gamma$) materials for three different gases: oxygen, nitrogen, and hydrogen. All of the listed gases are commonly used both in research and in industry.

Factors affecting the recombination coefficient are studied. The effect of surface roughness on the recombination coefficient is demonstrated with the example of graphite samples: a smooth sample turns out to be a much worse recombinator than a rough sample. The highest recombination coefficients were measured on materials with nanostructured surfaces, such as carbon nanowalls. Along with surface roughness, the surface temperature of a solid is an important factor for heterogeneous surface recombination. Generally, surfaces with higher temperatures are better at recombining neutral atoms. Lastly, surface activation is mentioned as another factor influencing the recombination coefficient. For example, when immersed in hydrogen plasma, the surface of a sample will eventually be reduced by any oxides, which will change the recombination coefficient of the sample.

A couple of high-frequency plasma sources are described, starting with a capacitively coupled radio-frequency discharge, followed by variations of an inductively coupled radio-frequency discharge, with the focus placed on the latter. The results shown in the book chapter were produced when working with a low-pressure inductive coupled radiofrequency discharge. Oxygen, nitrogen, and hydrogen plasmas were characterized using optical emission spectroscopy and a standard catalytic probe, with a distinction made between the lower-power E-mode and higher-power H-mode of plasma. The former has a larger volume but a lower density of neutral atoms while the latter has a much smaller volume with significantly higher neutral atom density.

The book chapter signifies the importance of plasma characterization while hinting at the complex mechanisms behind heterogeneous surface recombination and the varying factors that influence it, such as surface topography, chemistry, temperature, etc.

Atomic species generation by plasmas

1.1. Introduction

Plasmas of molecular gases like oxygen, nitrogen, hydrogen, ammonia, sulphur dioxide, hydrogen sulphide, water vapour, hydro-carbons, fluorinated, nitrated and oxidized hydrocarbons, carbon dioxide etc. are widely used for tailoring surface properties of solid materials. The molecules are partially ionised, dissociated and/or excited upon plasma conditions. Plasma created in a molecular gas is therefore rich in molecular fragments which interact between each-other and with solid materials facing plasma. The molecular fragments are often called "radicals" and may be atoms, di-atomic molecules or larger fragments of original molecules. The major difference between the original molecules and their fragments is in chemical reactivity. The original molecules are rather stable and they will usually not interact with solid materials at low temperature. The fragments are chemically unstable and tend to interact with any object placed into gaseous plasma including themselves. An illustrative example is methane (CH_4). The original molecule CH_4 is regarded inert at room temperature. Upon colliding with a solid material the molecule will just bounce off from the surface. Under plasma conditions, however, the CH_4 molecule is dissociated to fragments including CH_3, CH_2, CH, C and H. The radicals will interact with any object placed into gaseous plasma. The interaction of carbon atoms with a solid material causes condensation of carbon on the surface of a solid material. A carbon atom arriving to a solid material will stick to the surface with a very high probability, almost 100%. The sticking coefficient depends on the temperature of the solid material but is regarded very high even for the highest temperatures available for solid materials before they melt or sublimate. The sticking coefficient for CH_x radicals decreases with increasing content of hydrogen: it is still very high for CH and marginal for CH_4 [1].

The interaction of radicals between each-other often leads to formation of molecules in gaseous plasma. Such an effect is shown schematically and in a rather simplified manner in Figure 1.1. The molecules formed at the interaction of gaseous radicals may or may not be stable. Oxygen, for example, forms a stable two- or three-atoms molecule: O_2 and O_3 (ozone). Carbon, on the other side, forms clusters of almost arbitrary number of atoms. The association of the atoms in the gas phase as shown schematically in Figure 1.1 is governed by the natural rules, in particular, conservation of an energy and momentum. By definition, a molecule in the ground state will have the potential energy 0. When the molecule dissociates to atoms, the potential energy of atoms is equal to the binding energy of the parent molecule. Dissociation energies of simple molecules are shown in Table 1.1. The dissociation energy is of the order of few eV. This energy should be preserved upon association of the atoms to a molecule. The excessive energy before association could be transferred either into the internal energy of the formed molecule or to its kinetic energy. If all potential energy of atoms before the collision is transferred to the internal energy of the formed molecule, the molecule would dissociate immediately because the internal energy of the formed molecule would be equal to the dissociation energy.

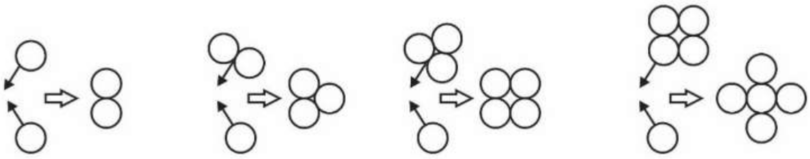

Figure 1.1. Schematic of a cluster formation in gaseous plasma.

Table 1.1. Dissociation energies of selected molecules [2].

Molecule	Dissociation energy
O_2	5.16 eV
N_2	9.8 eV
H_2	4.52 eV

The conservation of momentum, on the other hand, forbids the transformation of the potential energy before the collision to the kinetic energy of the formed molecule. The simple reactions shown in Figure 1.2 are therefore forbidden because of the requirement of the conservation of energy and momentum. The consequence of this simple explanation is perfect stability of radicals such as neutral atoms under vacuum conditions. A possible way for conserving energy and momentum in simple association reactions illustrated in Figure 1.2 is the radiative association. In this case, the association occurs simultaneous with the formation of a light quantum (a photon) which holds the available energy and momentum. Such collisions are unlikely to occur in examples shown in Figure 1.2, but may be predominant in plasma created in gas mixtures. A good example is association of an O and N atom, which results in a highly excited NO molecule that de-excites readily by a radiation in the UV range of the spectrum [3].

$$\left.\begin{array}{l} \mathrm{O}+\mathrm{O}\rightarrow \mathrm{O}_2 \\ \mathrm{N}+\mathrm{N}\rightarrow \mathrm{N}_2 \\ \mathrm{H}+\mathrm{H}\rightarrow \mathrm{H}_2 \end{array}\right\} \begin{array}{l}\text{this reactions}\\ \text{are forbiden}\end{array}$$

Figure 1.2. Some forbidden association reactions between atoms in the gas phase.

$$\begin{array}{l} \mathrm{O}+\mathrm{O}+\mathrm{O}_2\rightarrow \mathrm{O}_2+\mathrm{O}_2 \\ \mathrm{N}+\mathrm{N}+\mathrm{N}_2\rightarrow \mathrm{N}_2+\mathrm{N}_2 \\ \mathrm{H}+\mathrm{H}+\mathrm{H}_2\rightarrow \mathrm{H}_2+\mathrm{H}_2 \end{array}$$

Figure 1.3. Some allowed reactions in the gas phase.

If the density of gaseous particles is high enough there is a certain possibility that three particles will appear in a small volume where the distance between the particles is small enough that they are capable of interacting. Such a condition will lead to a three-body collision. Some simple thee-body collisions are shown in Figure 1.3.

The probability for a three-body collision obviously depends on the density of gaseous particles, which in turn depends on the pressure:

$$p = nkT, \qquad (1)$$

where p is the gas pressure, n is the density of particles, k is Boltzmann constant (k = 1.38064852 × 10^{-23} m^2 kg s^{-2} K^{-1}) and T is the gas temperature expressed in Kelvin (K). The probability for three-body collisions is often expressed in the terms of the collision frequency (ν), which was found to be roughly

$$\upsilon = \sigma^{5/2} n^2 \langle v \rangle , \qquad (2)$$

where σ is the collisional cross-section, n is the density of particles and $\langle v \rangle$ is the average speed of the random (thermal) motion of the particles, i.e.:

$$\langle v \rangle = \sqrt{\frac{8kT}{\pi m}} . \qquad (3)$$

Here, k is Botlzmann constant, T is the gas temperature, and m is the mass of a particle. The relation shown in Eq. (2) is a rough estimation obtained by rounding some constants and taking into account a rigid-sphere model. In plasma created in a simple molecular gas, the collision frequency for three-body collisions is roughly 10^7 s^{-1} (ten million collisions per second only) at an atmospheric pressure and room temperature. The relation in Eq. (2) exhibits that the three-body collision depends on the square of the pressure as long as the temperature is almost constant. The rough estimates for the three-body collision frequency at various pressures and room temperature are indicated in Table 1.2.

Table 1.2. The rough estimates of the three-body collision frequency at different pressures.

Pressure / Pa	Pressure / mbar	Pressure / torr	Pressure / bar	3-body collision frequency / s^{-1}	Atom life time
0.1	10^{-3}	7.5×10^{-4}	10^{-6}	10^{-5}	30 hours
0.3	3×10^{-3}	2.3×10^{-3}	3×10^{-6}	10^{-4}	3 hours
1	10^{-2}	7.5×10^{-3}	10^{-5}	10^{-3}	20 min
3	3×10^{-2}	2.3×10^{-2}	3×10^{-5}	10^{-2}	2 min
10	10^{-1}	7.5×10^{-2}	10^{-4}	10^{-1}	10 s
30	3×10^{-1}	2.3×10^{-1}	3×10^{-4}	1	1 s
100	1	7.5×10^{-1}	10^{-3}	10^{1}	0.1 s
300	3	2.3	3×10^{-3}	10^{2}	10 ms
1000	10	7.5	10^{-2}	10^{3}	1 ms
3000	30	2.3×10^{1}	3×10^{-2}	10^{4}	0.1 ms
10.000	10^{2}	7.5×10^{1}	10^{-1}	10^{5}	10 µs
30.000	3×10^{2}	2.3×10^{2}	3×10^{-1}	10^{6}	1 µs
100.000	10^{3}	7.5×10^{2}	1	10^{7}	0.1 µs

A three-body collision, however, does not assure for the association of two atoms to the parent molecule. If all atoms that have suffered a three-body collision actually associate to parent molecules as shown in Figure 1.3, the life-time of the atoms would be inversely proportional to the collision frequency. The life time in this rough (not fully justified) approximation is added to Table 1.2. just for a rough guidance.

The neutral atoms may or may not associate to parent molecules according to the three-body collisions presented in Figure 1.3. If the probability for such homogeneous reactions at the three-body collisions would be close to 1 then the life-time of an atom would be as shown in Table 1.2. The observed life-times are somewhat larger; therefore, the values presented in Table 1.2 are just to get an impression regarding the order of magnitude. The life times at pressures below few Pa are really large and have never been reported for laboratory experiments because other effects leading to the loss of radicals prevail.

If the pressure is low, the loss of atoms by the three-body collision is marginal. Vacuum systems suitable for sustenance of non-equilibrium gas of high atom density are usually pumped continuously. The reaction chambers are often cylindrical. They are pumped on one side, whereas on another side, molecular gas is introduced via a needle valve or a flow-controller. Schematic of the simplest experimental chamber is shown in Figure 1.4. The gas flows from the right to the left because of the pressure gradient. The pressure at the valve inlet is often atmospheric. The pressure drops along the narrow tube between the valve and the vacuum chamber. If the diameter of the narrow tube is much smaller than the vacuum chamber and the pumping speed of the vacuum pump is much larger than the conductance of the narrow tube, the major pressure drop is between the valve and the exhaust of the narrow tube to the vacuum chamber as shown in Figure 1.4. The gas drift velocity along the narrow tube and at the exhaust is close to the maximal possible value, which is equal to the sound velocity in gas. The sound velocity in air at room temperature is approximately 343 m/s. The gas expanding into the vacuum chamber forms a jet as shown in Figure 1.4. Far away from the narrow tube, the gas drift assumes the normal radial velocity distribution – the drift velocity is the largest at the axis of the tube and the lowest at the edges because of the finite viscosity of the gas. The average drift velocity of the gas in the tube depends on the effective pumping speed as

$$v_{\mathrm{d}} = S/A, \qquad (4)$$

where v_{d} is the gas drift velocity as indicated in Figure 1.4, S is the effective pumping speed and A is the cross section of the vacuum chamber. In many practical cases, the conductivity of the vacuum chamber for gas flow is much larger than the pumping speed of the vacuum pump, therefore one can take into account the pump's pumping speed as S in Equation (4) and calculates the drift velocity along the vacuum tube. This approximation is often justified at an elevated pressure, because the conductivity of vacuum elements increases with increasing pressure. If the condition is fulfilled, the pressure gradient along the vacuum tube will be marginal.

Figure 1.5 represents typical values for the gas drifting through a vacuum chamber. The chamber is assumed cylindrical, thus the cross section A (Equation 4) is $\pi d^2/4$, where d is the tube diameter. The gas in the vacuum tube spends some time, which is often referred as the residence time. In a good approximation, the residence time of gas in a simple vacuum chamber as in Figure 1.4 is L/v_{d}, where L is the length of the vacuum tube. Typical residence times for a vacuum tube of a length L = 1 m are plotted in Figure 1.6 versus the tube diameter for selected pumping speeds of the vacuum pump.

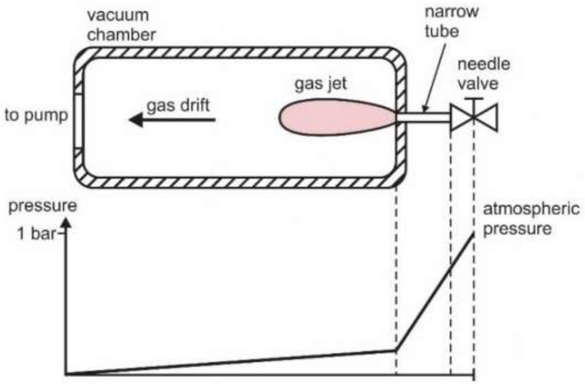

Figure 1.4. Schematic of a simple experimental configuration.

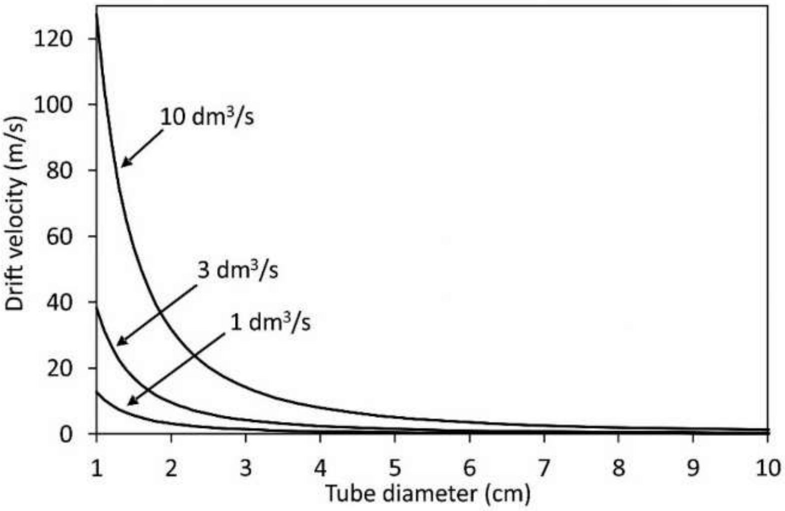

Figure 1.5. The rough estimation of the gas drift velocity versus the vacuum tube diameter for pumping speeds of 1, 3 and 10 dm^3/s.

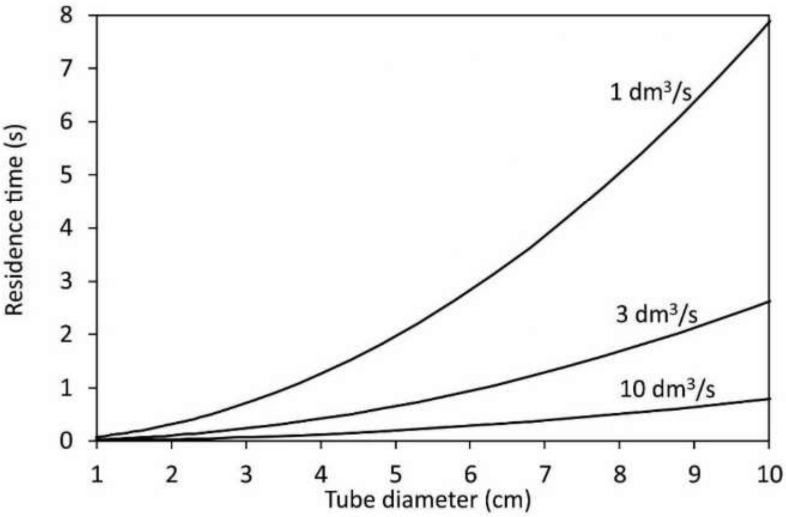

Figure 1.6. Typical residence times for a vacuum tube of a length L = 1 m versus the tube diameter for selected pumping speeds of the vacuum pump.

The values in Figure 1.6 give a rough estimation of the gas residence time, i.e. the time gas spends inside the vacuum chamber shown schematically in Figure 1.4 before it is pumped away. Although they were obtained using rough assumptions, they represent valuable estimates. For typical systems, the residence time is between 1 ms and 1 s. The gaseous radicals that are formed in such a vacuum chamber upon plasma conditions are therefore pumped away much faster than lost by a three-body collision in the gas phase (see rightmost column in Table 1.2) Any discussion about the loss of atoms in the gas phase at the pressures below, say, 10 Pa is therefore unnecessary.

The atoms may recombine to parent molecules also on surfaces. The flux of atoms onto a surface is

$$j_{atoms} = \frac{1}{4} n \langle v \rangle . \qquad (5)$$

In the rigid sphere approximation, the atoms are just reflected from the solid surface thus the kinetic energy is conserved and only the normal component of the velocity inverses. The atoms, however, are chemically reactive, thus they tend to interact with the solid material and the rigid sphere approximation is usually not justified. Because the atoms feel an attractive force, they will stay on the surface for a certain time which depends on the surface properties. The residence time is often large enough that another atom from the gas phase arrives to the binding side. The atom arriving from the gas phase interacts strongly with an atom already adsorbed on the surface and association to the parent molecule occurs. The molecule formed on the surface by association of two atoms leaves the surface almost immediately. The association depends on the surface density of atoms and strength of the binding sites on the surface. The probability of surface association is usually expressed in the terms of the recombination coefficient *γ,* which is defined as a ratio between the flux of atoms to the surface and flux of molecules (which have been formed by surface association of atoms) from the surface. For two-atom molecules the recombination coefficient is:

$$\gamma = \frac{j_{atoms}}{2 j_{molecules}} . \qquad (6)$$

The mechanism explained above is usually called "Eley – Rideal" model [4]. The necessary condition for association of atoms into parent molecules is a good density of atoms adsorbed on the solid surface. Adsorbed atoms are trapped in the potential well on the surface of a solid material. The potential energy of an atom trapped in the potential well is much lower than the potential energy of an atom in the gas phase as shown in a simplified manner in Figure 1.7. In reality, the potential is three-dimensional and of a complex structure. Some authors reported binding sites of different binding energies (different depths of the surface potential wells), thus the illustration in Figure 1.7 should be understood just as a very rough picture useful for understanding the basic concepts of heterogeneous surface recombination.

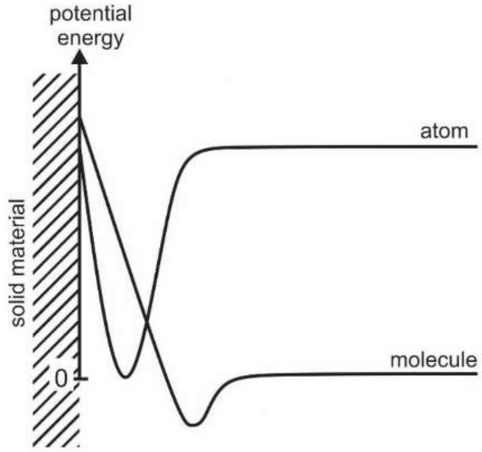

Figure 1.7. Schematic simplified one-dimensional potential curve for atoms and molecules next to the surface of a solid material.

The difference in the potential energies between atoms and the newly formed molecule is transferred to the internal energy of the solid material. The solid material therefore warms up upon exposure to neutral atoms from the gas phase. The molecule formed on the surface according to Eley – Rideal model may or may not be in thermal equilibrium with the solid material. The potential energy of the atoms in the gas phase is equal to the dissociation energy of the molecule. After desorption, the molecule may keep a substantial part (roughly up to about half of the dissociation energy) of the potential energy in the form of its internal energy [5]. The molecule may therefore desorb from the surface in a highly excited vibrational state. Although some research has been performed on the distribution of such molecules over excited states, the phenomenon is still far from being well-understood. Schematic of the Eley – Rideal model is presented in Figure 1.8.

Another possibility is that two adsorbed atoms interact on the surface of the solid material and leave the surface in the form of a molecule. This mechanism is called Langmuir-Hinshelwood and is schematically presented in Figure 1.9 [4]. In this case, the atoms have already lost their potential energies upon adsorption, therefore the molecule cannot leave the surface with a substantial internal energy.

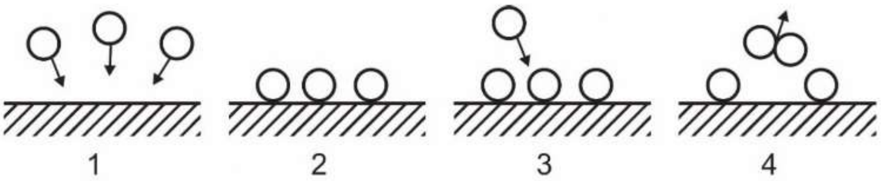

Figure 1.8. Schematic of the Eley – Rideal recombination. 1 – atoms move randomly in the gas phase, 2 – atoms adsorb on the surface, 3 – an atom from the gas phase interacts with an adsorbed atom, 4 – a molecule desorbs from the surface.

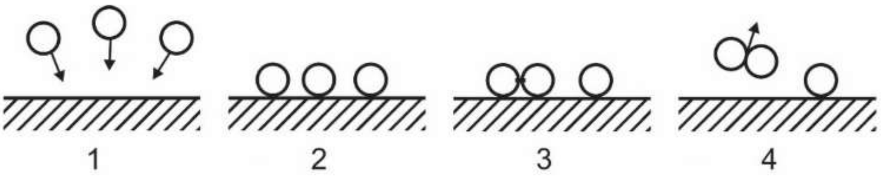

Figure 1.9. Schematic of the Langmuir-Hinshelwood recombination. 1 – atoms move randomly in the gas phase, 2 – atoms adsorb on the surface, 3 – two adsorbed atoms interact on the surface, 4 – a molecule desorbs from the surface.

The predominant mechanism depends on various factors from the binding energy to the surface mobility of atoms and temperature of the solid material. Experimentally it is difficult to distinguish between these two mechanisms. In any case, a substantial fraction (usually much more than half) of atoms' potential energy is transferred to the internal energy of a solid material.

The surface recombination causes heating of the solid material exposed to radicals. The heating rate obviously depends on the flux of radicals onto the surface, the dissociation energy of the molecule formed on the surface by association of radicals, and probability for association which is expressed in the terms of the recombination coefficient as in Equation (6). For the case of association of atoms to two-atom molecules, the heating power is

$$P = j_{atoms} \cdot ½W_d \cdot A' \cdot \gamma \, . \qquad (7)$$

Here, A' is the surface of the solid material exposed to a flux of atoms j_{atoms}. In the case a three-atom molecule is formed, the factor ½ should be replaced with ⅓. Combining the Equations (5) and (7) gives the heating power

$$P = \tfrac{1}{8} W_d \cdot n \cdot \langle v \rangle \cdot A' \cdot \gamma \,. \tag{8}$$

Suppose there is a small particle of a simple shape levitating in an atmosphere rich in atoms. The particle is heated at the rate as in Equation (8) and radiates according to Stefan-Boltzmann law:

$$P' = (1-a) \cdot A' \cdot \sigma_S \cdot T^4 \,, \tag{9}$$

where a is albedo, σ_s is the Stefan-Boltzmann constant and T is a temperature of the levitating particle. The temperature of the small particle assumes a much higher value than the gas temperature. Taking into account the relations (8) and (9) and neglecting some effects, the temperature of the levitating particle is

$$T = \sqrt[4]{\frac{W_D \cdot n \cdot \langle v \rangle \cdot \gamma}{8(1-a) \cdot \sigma_S}} \,. \tag{10}$$

The temperature of a levitating particle versus the atom density in its surrounding is shown in Figure 1.10 for the dissociation energy of 5 eV, albedo 0 and different recombination coefficients γ. In Figure 1.11 the temperature is shown for the same parameters except that the albedo was taken 0.9. Here, it should be stressed that several approximations were assumed to simplify the calculations. In real cases, the particle is not only cooled by radiation but also by other effects including heat transfer because of the thermal conductivity of gas and convection. The approximation is justified only for high differences between gas and particle temperatures. That's why in Figures 1.10 and 1.11 the curves at lower temperatures are presented with dashed lines.

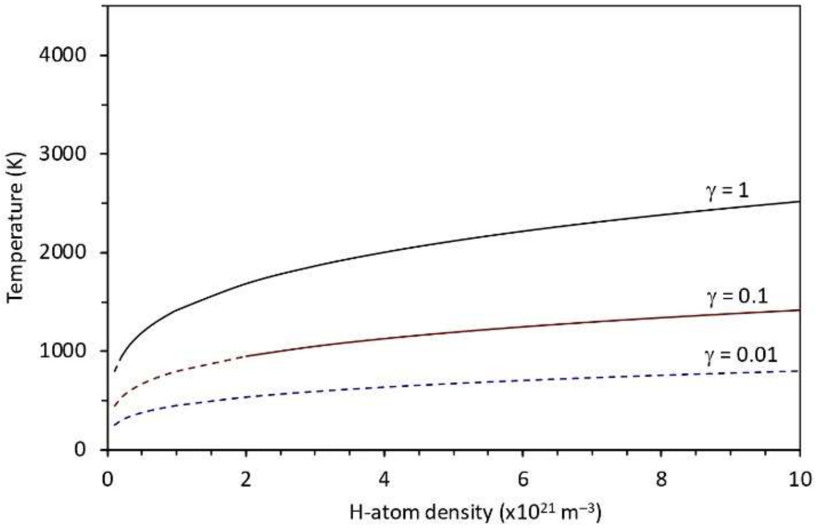

Figure 1.10. The temperature of a small particle levitating in gas rich in atoms versus the atom density for a = 0.

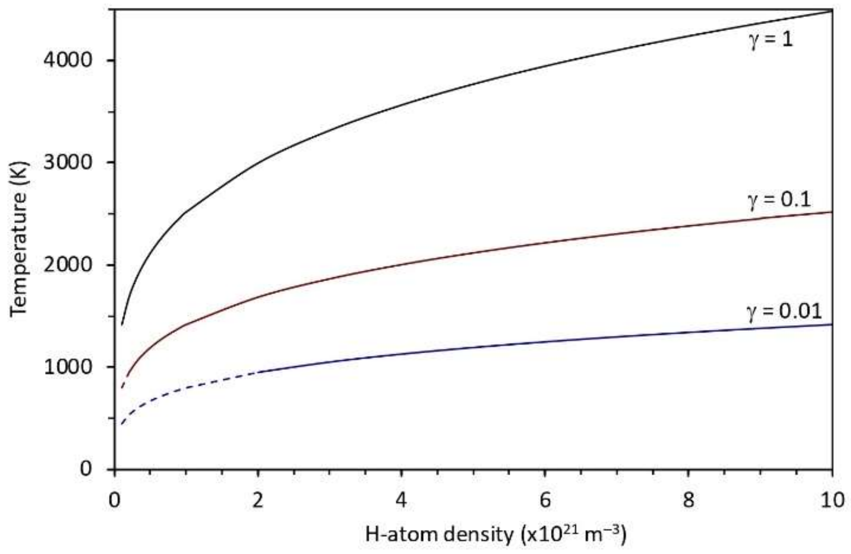

Figure 1.11. The temperature of a small particle levitating in gas rich in atoms versus the atom density for a = 0.9.

Simple approximations are useful for a rough estimation of the temperature of a small particle. If a particle is large, gradients in the atom density next to the surface occur because of the loss of atoms on the surface. From this point of view, the results summarized in Figures 1.10 and 1.11 should be used only as the upper values. The approximation is valid for particles up to the dimension of, say, a millimetre. For larger particles, the temperature is lower but still substantially higher than the ambient temperature. The approximation is valid also for a small object immersed into the gas rich in atoms and connected to a thin wire of a low thermal conductivity.

Sometimes, it is also useful to estimate the temperature of small particles sitting on the surface of a larger object providing the thermal connection between such particles and the object is poor, for example, metallic dust on the surface of poor thermal conductors such as glass or polymer. In the case the small particles sit on the surface, the flux of radicals in Equations (7-10) should be divided with a factor of two because the particles are exposed to atoms from one side only.

The heating of a solid material therefore depends on the recombination coefficient γ which has been defined in Equation (6). The recombination coefficient depends on the composition and structure of the surface of the solid material [6, 7]. From this perspective, different groups of materials have been identified.

One group contains materials whose surface has a very limited density of available binding sites for adsorption of gaseous atoms. These materials are often called inert. Contrary, there are materials of numerous binding sites that are quickly occupied by relatively weakly bonded atoms. Such materials are often called “catalytic” because they serve as catalysers for heterogeneous surface recombination. Within these two extremes, there are materials of numerous binding sites where atoms bond strongly, and materials of moderate density of binding sites capable for binding atoms relatively weakly. The exact picture of available binding sites and shape of the potential wells is available only for few materials of a perfect structure, such as mono crystals and is still a subject of scientific investigation. In practice, however, the materials do not have perfect properties; therefore, the recombination coefficients have been determined experimentally. For a rough guidance, the materials falling into each category according to available scientific literature and practical experiences of the authors of this text are summarized in Table 1.3.

Table 1.3. Smooth clean materials of different recombination coefficients at room temperature for oxygen, nitrogen and hydrogen atoms.

Recombination coefficient	oxygen	nitrogen	hydrogen
Over 0.1	iron nickel [9] cobalt [10] copper [10] silver	iron [8] nickel cobalt tungsten	iron nickel stainless steel copper aluminium gold manganese platinum titanium
Between 0.01 and 0.1	graphite [11] stainless steel niobium [10] tungsten titanium tungsten	aluminium copper stainless steel	graphite Al_2O_3 tungsten cobalt
Below 0.01	Pyrex quartz Teflon [12] Al_2O_3 PET [12] PS [12]	Pyrex quartz Teflon molybdenum	Pyrex quartz Teflon [12] PET [12] PS [12]

It should be stressed that the values given in Table 1.3 are just recommended values for materials of a high purity with the native layer of oxide (if applicable) and almost free from other surface impurities. The values are for smooth materials and valid for the range of temperatures not deviating much from room temperature.

While the surfaces of many polymers cleaned by routine techniques are almost free from adsorbed impurities, most metals are quickly covered with a very thin film of impurities in a short time after the cleaning. Many metals form a native layer of oxide whose thickness is often around a nanometre. Furthermore, they tend to adsorb organic impurities which are always presented in air at minute quantities. Both films are rather strongly bonded to the surface of a metallic object and cannot be removed at room temperature even upon prolonged exposure to an ultrahigh vacuum. It is common to detect carbon on metallic samples by surface sensitive methods under ultrahigh vacuum conditions such as Auger electron spectroscopy, X-ray photoelectron spectroscopy and secondary ion or neutral mass spectrometry. The surface impurities often have a strong influence on the recombination coefficient; therefore, a small object placed inside an atom-rich atmosphere does not heat up to elevated temperatures according to Figures 1.10 and 1.11. The thin film of organic impurities is quickly removed upon exposure to oxygen or nitrogen atoms, but may remain on the surface even after prolonged exposure to hydrogen atoms.

The native oxide film does not influence the coefficient for surface recombination of oxygen atoms because the oxide is formed anyway as a result of chemical interaction of O atoms with metallic surfaces, but it influences the coefficient for hydrogen recombination. H-atoms often do not bind much on the surface of an oxidized metal, definitely much weaker than on pure metals. The values in Table 1.3 are for pure metals. Once a metal with a layer of surface impurities is exposed to H atoms, chemical interaction occurs and the H atoms may eventually etch the layer of organic impurities and reduce the native oxide film. Figure 1.12 illustrates this effect. It shows dependence of the temperature of small nickel and gold discs versus the fluence of H atoms. For low fluences, the temperatures of both samples remain close to room temperature which indicates very small recombination coefficient for these materials covered with surface impurities. After receiving a certain fluence, the temperature starts rising and eventually assumes a steady value typical for catalytic materials. The density of H atoms in the vicinity of the samples was 2×10^{21} m^{-3} at experiments shown in Figure 1.12. The behaviour as shown in Figure 1.12 is often called "catalyst activation" and it is explained by the removal of surface impurities. Gold does not form a significant oxide film; therefore, it is activated much faster than nickel. Many metals can be activated by this way, providing the binding energy of oxygen in the film is not too high and the thickness of the oxide film is up to few nm only. Thick oxide films cannot be removed at low temperature in a reasonable time and strongly bonded oxides cannot be removed at all by exposure to atomic hydrogen, except at very high temperatures [13-15]. A classic example is aluminium – even the native oxide film will not be reduced upon treatment with H atoms unless the temperature is very high. Titanium, on the other hand, serves as a good catalyser for heterogeneous surface recombination of hydrogen atoms, providing it is not covered with a compact and thick oxide film [16].

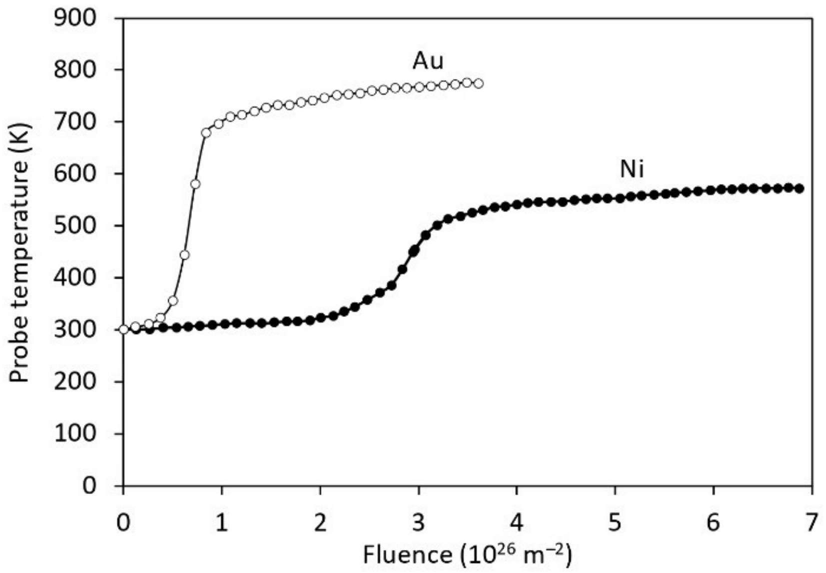

Figure 1.12. The temperature of nickel and gold discs upon exposure to atomic hydrogen versus the fluence.

The recombination coefficient also depends on the surface morphology [7]. If the surface is almost perfectly smooth, a substantial fraction of atoms is simply reflected upon a collision with the solid material. In contrast, rough materials exhibit higher recombination coefficients than their smooth counterparts. The effect is illustrated in Figure 1.13. In this illustration, an atom is regarded a rigid sphere. As mentioned earlier, the atoms in this (often not justified) approximation do not feel any attractive force on the surface, therefore their kinetic energy is preserved and only the normal component of their velocity inverses. Two cases are considered: in the left-side illustration of Figure 1.13 an atom enters a gap on the surface of a solid material at a large angle. Once it suffers an elastic collision, it is reflected to another side of the gap and experiences several collisions before escaping from the gap. The right illustration in Figure 1.13 shows a rare case where an atom is directed almost perpendicular to the surface. If this happens, the atom suffers only one surface collision. The number of collisions in the rigid sphere approximation obviously depends on the aspect ratio of the gap: if the depth of the gap is much larger than its lateral dimension, the collisions are numerous. The simple drawings are valid for the case when the mean free path is much longer than the gap lateral dimension. Otherwise, an atom also experiences gas phase collisions with other gaseous particles. The collision-less gaps are common in practical cases of rough materials because the mean free path is roughly 1 cm at the pressure of 1 Pa.

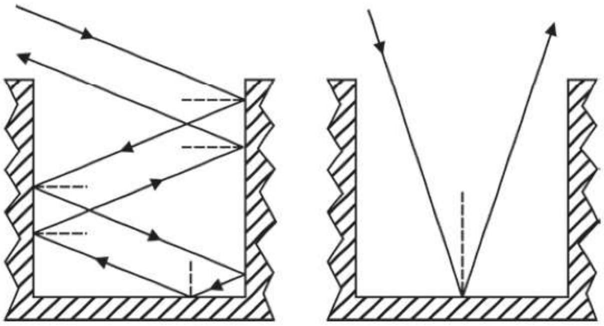

Figure 1.13. Schematic of atom collisions within gaps on the rough surface in the rigid sphere approximation.

The rigid sphere approximation has limited validity. In practice, there is a certain probability that an atom will stick to the surface at each collision. The probability is actually the recombination coefficient for a smooth material as defined in Equation (6). The real recombination coefficient for a rough material is obviously the value for a smooth material multiplied with the number of collisions in the gap. If there are numerous collisions, the recombination coefficient will be large even for materials whose smooth surfaces exhibit a moderate recombination coefficient. In fact, in the approximation of gaps with infinite aspect ratio separated by infinitely narrow walls, the recombination coefficient for all materials will approach 1. Such materials do not exist, of course, but close approximations are available.

The influence of the surface roughness on the recombination probability for oxygen atoms for the case of a graphite is shown in Table 1.4 [11]. As received graphite wash polished with the abrasive paper with a different grit. One sample of graphite was made smooth and the other one rough. The surface roughness as measured by profilometer is shown in Table 1.4 (Figure 1.14). A smooth graphite exhibits a moderate recombination coefficient and the measured value for oxygen atoms is 0.04. This means that 96% collisions obey the rigid sphere approximation and only 4% results in adsorption of an atom onto the smooth surface. If the surface is made rough, the atoms suffering an elastic collision are not reflected perpendicularly but most of them experience several collisions before leaving the surface. Because the probability of adsorption at each collision is 0.04 (i.e. the value measured for a smooth surface), the recombination coefficient as determined for a rough sample is much larger, i.e. $\gamma = 0.09$ for the roughest surface in Table 1.4 [11].

Table 1.4. Dependence of the recombination probability for oxygen atoms on surface roughness of graphite samples

Sample	Roughness (nm)	Recombination probability
Smooth polished graphite	4.5×10^2	0.04
Rough polished graphite	1.8×10^3	0.06
As-received graphite	3.2×10^3	0.09

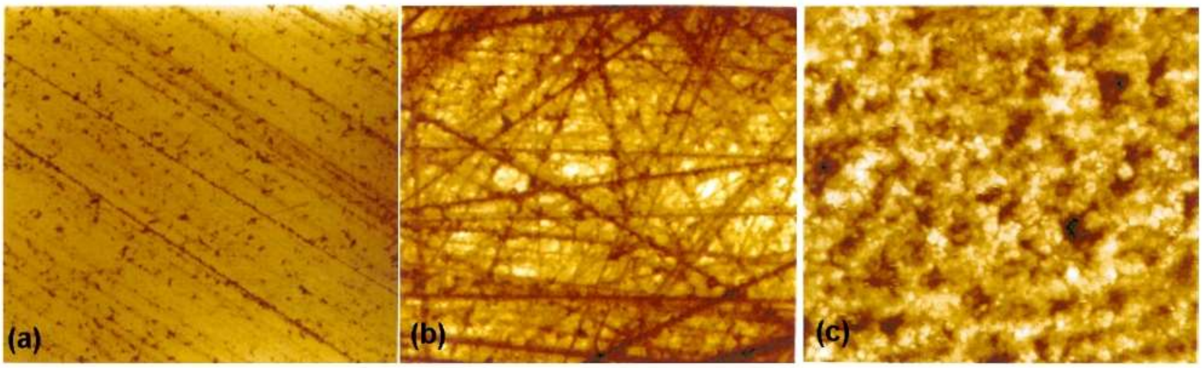

Figure 1.14. Profiles of the surface (1.1 × 1.1 mm) of graphite samples with different surface morphology and roughness as measured by a profilometer: (a) smooth, (b) rough and (c) as-received.

Carbon material of deep and dense gaps separated with thin walls is called carbon nanowalls. The nanowalls are often deposited by PECVD process. Organic precursor is dissociated upon plasma conditions and the radicals condensate on the surface. In the limited range of plasma parameters, dense nanowalls of vertically oriented multilayer graphene sheets are formed as shown in Figure 1.15. Most atoms from the gas phase will be trapped in the gaps between nanowalls and will suffer numerous collisions before escaping. The effect is illustrated in Figure 1.15. The measure value of the recombination coefficient for this material is approximately $\gamma = 0.6$ [17].

Even larger recombination coefficients are measured for materials with a very high porosity. Figure 1.16 shows a SEM image of a nickel foam. The recombination coefficient for oxygen atoms on a smooth nickel foil is 0.27 [9]. In the case of the foam, the atoms are trapped in the open volume within the foam as shown schematically in the illustration of Figure 1.16. Very few atoms are reflected on the walls on the surface of the foam because of a high porosity. Most atoms enter the foam and suffer numerous collisions and very few leave the material. Practically all atoms adsorb on the walls inside the foam and only molecules are capable of escaping. That is a reason why the recombination coefficient for the nickel foam is practically 1.

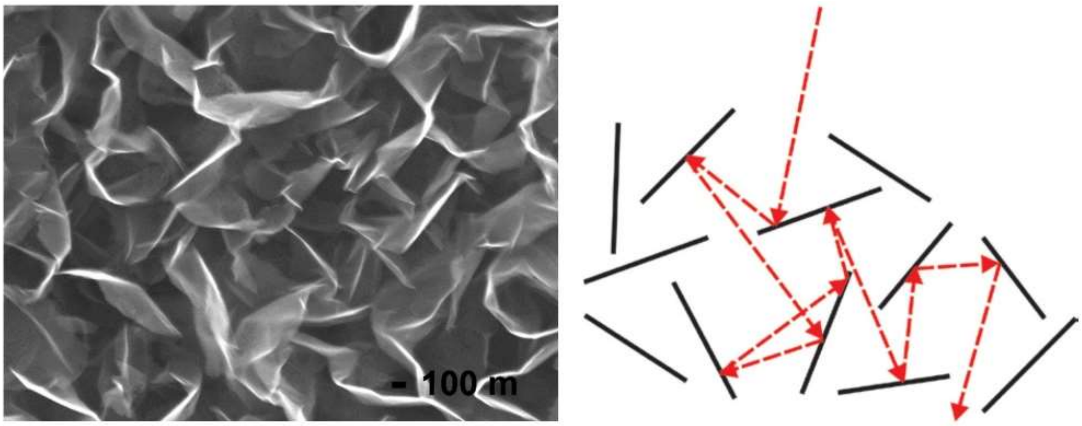

Figure 1.15. SEM image of vertically oriented carbon nanowalls (left) and illustration of an atom collisions (right).

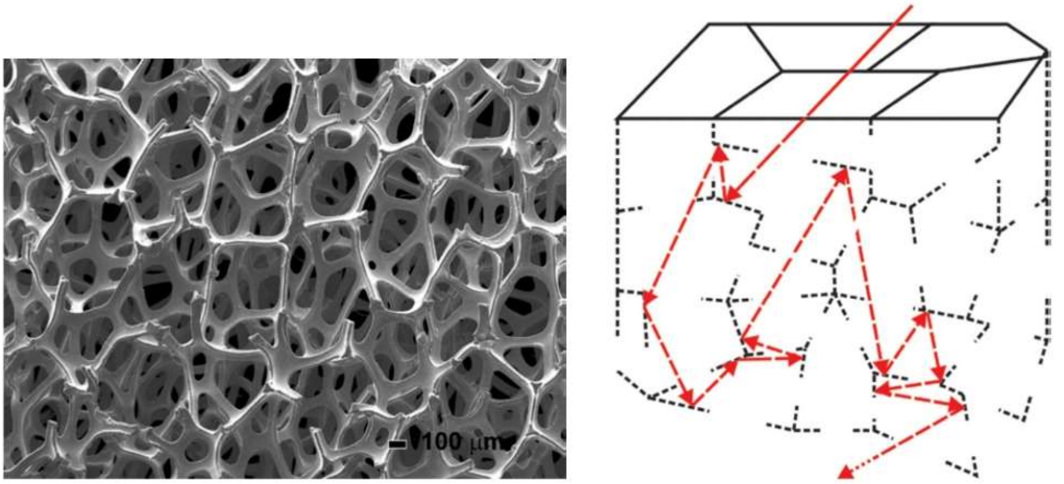

Figure 1.16. SEM image of a nickel foam (left) and schematic of collisions in the rigid sphere approximation (right).

The recombination coefficients summarized in Table 1.3 were measured at room temperature. Very few experiments have been performed at lower temperatures because of the lack of a practical interest. The materials facing plasma, however, are often heated to high temperatures either deliberately or just because of the exothermic surface reactions such as charged-particles neutralization, bombardment with positively charged ions and, of course, heterogeneous surface recombination of radicals to stable molecules. In some plasmas, the heating of surfaces by absorption of light quanta is not negligible, too. Any investigation of the loss of atoms on surfaces of plasma-facing materials should therefore include thermal effects. Not much work has been done on temperature dependence of the recombination coefficient for catalytic materials, except for some high temperature ceramics[18-24]. Figure 1.7 demonstrates that atoms trapped in the potential well cannot leave the surface without associating to a molecule; therefore, the recombination coefficient cannot decrease with increasing temperature. In fact, the recombination coefficient was found increasing with increasing temperature [18-24]. In some cases, the recombination coefficient increases monotonously with increasing temperature. Figure 1.17 demonstrates this effect. Such a monotonous increase could be explained by a higher mobility of atoms adsorbed on the surface. The higher mobility should favour more intensive recombination following the Langmuir – Hinshelwood model. In some other cases, however, the recombination coefficient was reported almost constant over a broad range of temperatures indicating the predominant Eley – Rideal model. Interesting results have been found for some alloys. Figure 1.18 shows the temperature of a small Inconel disc immersed into H-rich atmosphere. The disc was previously activated well to avoid the effect shown in Figure 1.12. One observes three knees in the curve. The first one at the time of approximately 10 s after turning on the H-atom source indicates that the material has assumed the constant temperature because the heating and cooling rates have equalized. The temperature, however does not stabilize completely but keeps increasing slowly for the next 100 s. Such an increase is easily attributed to increasing gas kinetic temperature, but could be also attributed to a slow increase of the recombination coefficient in the range of temperatures between approximately 450 and 550 K. The second knee is observed at approximately 175 s. Thereafter, the Inconel temperature increases quickly until the third knee is observed at the temperature of approximately 1000 K. Such an effect can only be explained by an almost instant increase of the recombination coefficient at the temperature of approximately 550 K. After the third knee the temperature stabilizes to an almost perfectly constant value of approximately 1000 K, which is explained by equalization of the heating and cooling rates according to equation (10). The curve presented in Figure 1.18 is perfectly reversible. This material therefore exhibits two distinct recombination coefficient: a moderately low one at temperatures below approximately 450 K and a high one above approximately 550 K. No scientific explanation for such an unexpected result is available. The effect illustrated in Figure 1.18 only demonstrates that heterogeneous surface recombination of atoms to stable molecules is still far from being well understood, therefore a user of non-equilibrium gases rich in atoms has to take the values presented in Table 1.3 with some caution.

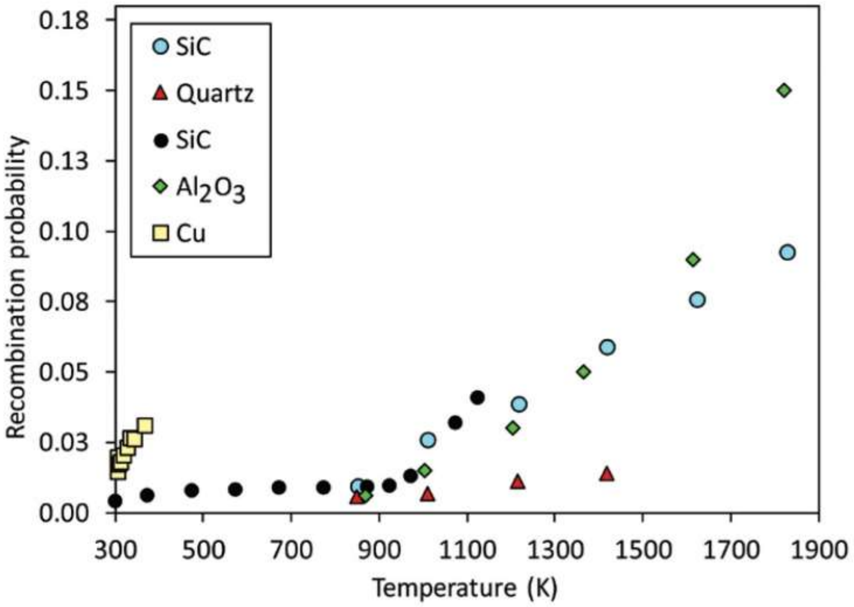

Figure 1.17. The temperature dependence of the recombination coefficient for oxygen atoms on some materials: SiC [18, 20], quartz [18], Al_2O_3 [24] and Cu [23].

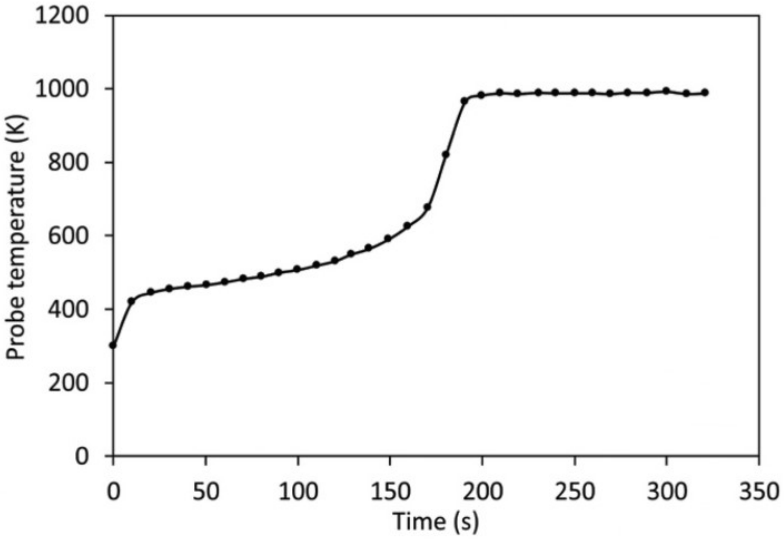

Figure 1.18. The temperature of a small Inconel disc immersed into H-rich atmosphere of constant density of H-atoms of 2×10^{21} m^{-3}.

1.2. Plasma sources of neutral atoms

The considerations explained in the previous chapter are useful and should be taken into account at any attempt to construct an efficient source of radicals, in particular neutral atoms. Although there are several mechanisms that enable dissociation of molecules into parent atoms, only a couple have been used widely: (i) dissociation on a hot surface, and (ii) dissociation upon plasma conditions. This textbook refers to the second one. Dissociation occurs in the gas phase at very high gas temperatures, but such a hot source of atoms is not suitable for treatment of solid materials except materials that remain stable at high temperatures. Technologically more important is dissociation at a low gas temperature in non-equilibrium states of gases such as gaseous plasma sustained at a low power density. Here, it should be stressed that the term “gas temperature” is not defined in highly non-equilibrium gases. Many authors adopted the expression “neutral gas kinetic temperature” or just “gas kinetic temperature” which indicates the temperature arising from random motion of gaseous particles. The expressions “electron temperature” and “ion temperature” indicate the temperature arising from the random motion of electrons and ions, respectively. Few authors adopted the expressions “dissociation temperature” or “ionization temperature” which actually indicate the dissociation and ionization fractions, respectively. Most authors rather indicate the densities of neutral radicals and charged particles.

Following the considerations explained in chapter 1.1. enables construction of efficient radical sources. The most straight-forward method for dissociation of molecules is by electron impacts. Gaseous plasma is rich in electrons and their temperature is much higher than the neutral gas kinetic temperature. If an electron is energetic enough (i.e. that its energy is higher than the dissociation threshold), an inelastic collision with a molecule may cause dissociation. The probability for such an event is really small at the threshold and increases with increasing electron energy, peaking at roughly approximately 100 eV. Such high-energy electrons are really scarce in common plasmas, therefore the probability for direct dissociation of a molecule from the ground state is low. The dissociation energies of many molecules are rather large at the values between approximately 5 and 10 eV, but many molecules have metastable states that help increase the dissociation efficiency. For example, oxygen molecules have two metastable states at the excitation energies of roughly 1 and 2 eV. The dissociation energy for oxygen molecule is 5.16 eV, thus the intermediate excitation to those metastable states effectively lowers the required electron energy, what is useful, especially because the electron energy distribution function is usually almost exponential in the high-energy tail.

The dissociation fraction of molecules in gaseous plasma definitely increases with increasing discharge power but so does the energy consumption; therefore, increasing the power is not the best way for assuring a high dissociation fraction. More important is minimizing the loss rate which is either in the gas phase by three-body collisions following equation (2) or on surfaces by heterogeneous recombination. The efficiency for the surface loss of atoms depends on the recombination coefficient – see Table 1.3. There should be a maximum density of atoms in gaseous plasma at an optimal pressure. At pressures below the optimum, the atom density should decrease because of surface effects, whereas at pressures above it should decrease because of the loss of atoms in the gas phase. Figure 1.19 illustrates the effects. The pressure at which the optimum occurs, depends on the discharge power density: at larger powers the optimum is shifted to larger pressures.

Figure 1.19 clearly demonstrates that high pressure discharges are inefficient sources of atoms. In fact, the specific power needed to sustain a large density of atoms at atmospheric pressure is just huge as compared to low-pressure counterparts. For example, a simple atmospheric-pressure discharge operates in a volume of the order of 1 cm^3 at the power of the order of 10 W giving the power density of 10 W cm^{-3} = 10^7 W m^{-3} and gives the atom density of the order of 10^{21} m^{-3}. The same atom density in low pressure chambers is obtained at power densities of 10^3 – 10^4 W m^{-3}. The power used for sustaining gaseous plasma is used for different reactions, but practically all power is finally transferred to heat because a thermodynamically non-equilibrium system approaches equilibrium conditions spontaneously soon after the discharge power has been turned off. The atmospheric-pressure atom sources are thus energetically inefficient.

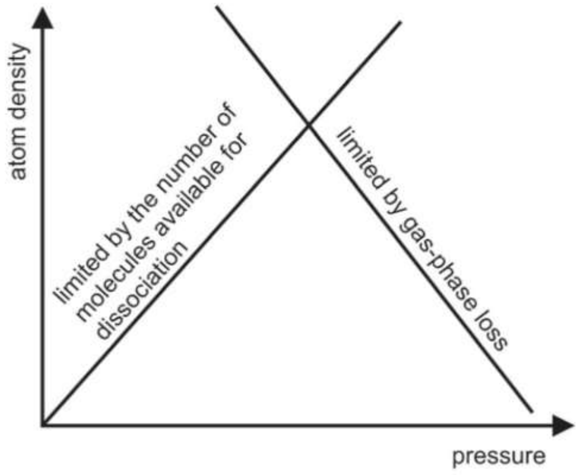

Figure 1.19. Schematic of the O-atom density versus pressure.

Low-pressure sources of radicals employ different gaseous discharges. High-power discharges are often avoided because they cause increased neutral gas kinetic temperature and are therefore useful only for treatment of materials that can stand high thermal loads. Low-power discharges are divided into DC or low-frequency AC, and high-frequency discharges such as radio-frequency (RF) and microwave (MW) discharges. DC and low-frequency discharges are rarely used as radical sources because they employ two electrodes inserted into the plasma chamber. An electrode is made from an electrically conductive material such as metals or graphite. These materials exhibit rather high catalytic activity for surface recombination of atoms (see Table 1.3), therefore they are often avoided when constructing radical sources.

High-frequency sources are common. Gaseous plasma is either sustained by low-frequency RF discharges (frequency of the order of 10 kHz), high-frequency RF (roughly from 1 to 100 MHz) or MW discharges (of the order of GHz). Particularly popular are industrial frequencies of 13.56 MHz for RF discharge and 2.45 GHz for MW discharge and their harmonics.

Low-frequency RF discharges usually employ an electrode immersed into the grounded housing and powered with a generator. Schematic of such a setup is shown in Figure 1.20. The metallic chamber as well as the electrode definitely represent a sink for radicals because of heterogeneous surface recombination. One solution of this problem is a dielectric coating of the metallic components facing plasma. The coating is preferably made from a material of a low recombination coefficient, for example a thin layer of the quartz glass. The layer should be thin enough to assure for a reasonable impedance. The impedances involved in the configuration presented in Figure 1.20 are shown schematically and in a simplified manner in Figure 1.21. The total impedance is the sum of capacitive and resistive components. The capacitance occurs across both the glass film and the sheath between the glass surface and plasma. The capacitive component of impedance is inversely proportional to the frequency and capacity of the plane-parallel capacitor:

$$Z_C = \frac{1}{\omega \cdot C} = \frac{1}{\omega \cdot \left(\varepsilon \cdot \varepsilon_0 \cdot A'' / x \right)} . \tag{11}$$

Here, ω is the frequency of the power supply, ε is a relative permittivity, ε_0 is the vacuum permittivity, A'' is the area of a capacitor and x is the thickness of either thin dielectric film or the sheath. The capacitive component of the impedance is thus inversely proportional to the electrode area. To minimize it, one should apply the electrode as large as possible. Obviously, if one wants almost all discharge power to be dissipated on the powered electrode, the electrode should be small. In the case of radical sources, small electrodes should be avoided to minimize the power lost for heating of the electrode. The capacitive component of the impedance is proportional to the thickness of the dielectric layer; therefore, the glass film should be made as thin as possible.

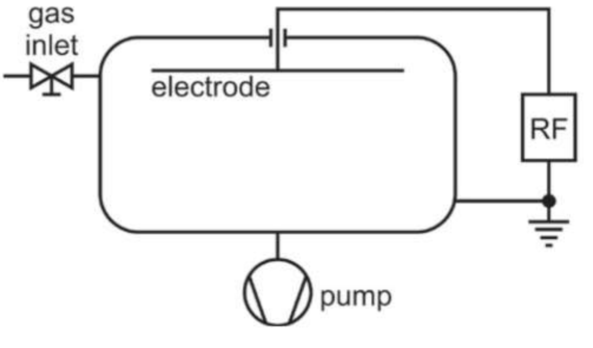

Figure 1.20. Schematic of the capacitive coupled RF discharge with an electrode immersed into the plasma reactor.

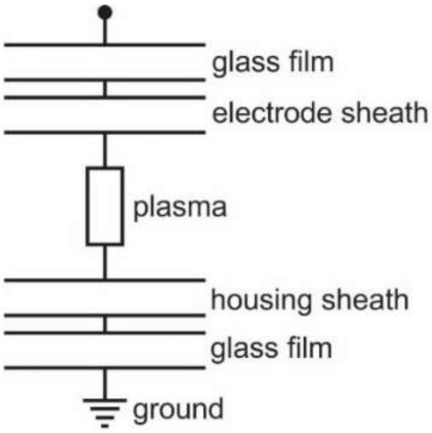

Figure 1.21. Simplified electric circuit for the configuration presented in Figure 1.20.

There is a substantial impedance across the plasma sheath next to the electrode. The sheath thickness depends on the Debye length which in turn depends on the electron density and temperature as

$$\lambda_D = \sqrt{\frac{\varepsilon_0 k_B T_e}{e_0^2 n_e}}, \qquad (12)$$

where ε_0 is vacuum permittivity ($\varepsilon_0 = 8.85 \times 10^{-12}$ F/m), e_0 is the elementary charge, T_e is the electron temperature and n_e is the electron density.

The fact that the capacitive component of the sheath cannot be neglected is because of a poor electrical conductivity of the sheath as compared to plasma. In gaseous plasma, the current is carried by electrons which have an excellent mobility because of their low mass. In the sheath, the density of electrons is much lower than in plasma because of a self-biasing effect (the electrode is highly negative against plasma), therefore the current carriers in the sheath are positively charged ions of a limited mobility.

Same effects as for the powered electrode occur also on the grounded housing, but the surface (A'') is usually larger, therefore the impedance of capacitors in the bottom of Figure 1.21 is smaller than in the top capacitors. The capacitive component of the impedance is easily supressed by increasing the frequency of the RF generator as demonstrated from equation (11). Still, low-frequency RF discharges are popular as sources of specific radicals because of the low cost of low-frequency RF generators and because of a highly effective transfer of generator's power to gaseous plasma – no complex matching network is needed.

Low-frequency RF discharges are particularly useful as sources of radicals containing several atoms. They are widely used as sources of radicalized monomers. A monomer is introduced through a gas inlet as shown schematically in Figure 1.20. It radicalizes upon plasma conditions and the radicals stick to the surface of any material immersed into plasma reactor. Low specific power (often around 1 kW m^{-3}) is applied to enable only partial radicalization of the monomer what in turn enables preservation of the monomer original composition and structure. The process is often called "plasma polymerization" and is used nowadays on the industrial level.

Such low-power discharges are useful for partial radicalization of molecules containing numerous atoms, but are impractical for the efficient dissociation of molecules to the smallest fragments - atoms. The high dissociation fraction is obtained at somehow larger power densities and larger frequencies. Particularly popular sources of neutral atoms are electrodeless high-frequency RF discharges. Schematic of a simple setup widely used on experimental level is presented in Figure 1.22. A dielectric tube is made from a material of a low recombination coefficient. Considering Table 1.3, the choice of materials includes some glasses, ceramics, and polymers. Because the polymers often interact chemically with plasma radicals, they are usually avoided. The most frequently used materials for the discharge tube are borosilicate and quartz glasses. Some types of borosilicate glass can be sealed with some metals (kovar alloy is particularly useful) to make perfectly hermetically tight joins free from gaskets. An alternative to sealing of the flanges to the glass tube is the application of gaskets made from elastomers. Borosilicate glass is practical because it is easily blown to an arbitrary shape and exhibits a low recombination coefficient for many atoms including oxygen and nitrogen. For hydrogen, however, it should be avoided because the recombination coefficient is moderate and increases with increasing glass temperature. One advantage of borosilicate glass is effective absorption of UV radiation, especially hard UV radiation. If radiation penetrates the glass, it represents a health risk. Not only it is harmful for eyes, but hard UV radiation also causes formation of ozone in the laboratory. From this point of view, borosilicate glass exhibits a definite advantage over some other types of glass such as quartz.

Quartz glass is also popular for discharge chambers in the configuration presented in Figure 1.22. It is a particularly useful material for construction of sources of hydrogen atoms because the recombination coefficient is rather low. A user of quartz, however, should beware of its transparency for UV radiation. Namely, hydrogen plasma is a source of continuum radiation in the range of UV wavelengths arising from transition of the triplet H_2 molecules from highly excited states to the dissociative state. The photon energy is high enough to dissociate oxygen molecules which results in appearance of ozone in the laboratory.

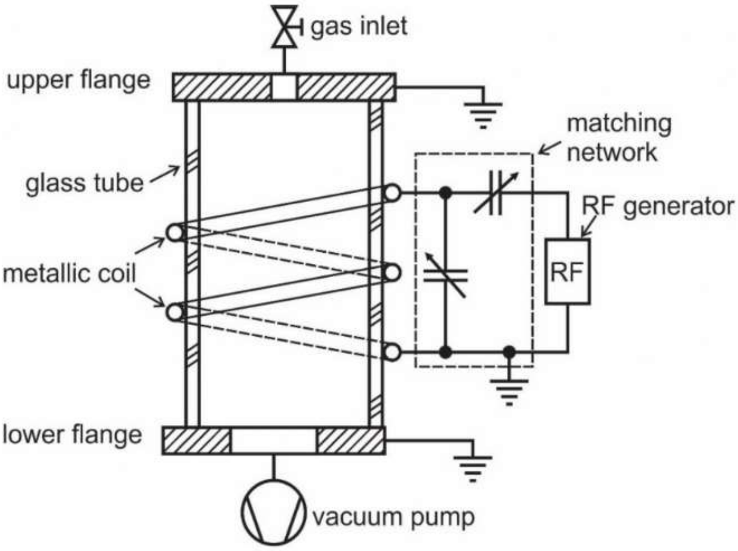

Figure 1.22. Schematic of the electrodeless RF discharge powered with an inductor.

The coupling of RF power to plasma in Figure 1.22 is through a coil. The coil is connected to an RF generator operating at high frequencies, often 13.56 or 27.12 MHz, via a matching network. The network may consist of variable capacitors and/or coils, but typically a couple of capacitors is used as shown in Figure 1.22. One capacitor is connected in series and the other in parallel. The matching network is essential because the plasma impedance depends on the plasma density; therefore, the electrical circuit should be matched for each discharge condition. If not, the generator would be mismatched and the majority of the available power would be just reflected.

At a low discharge power used in configuration presented schematically in Figure 1.22, the basic concept of the electrical circuit applies, but with an important modification to include the influence of both flanges. Such a modified circuit is presented in Figure 1.23, still in a simplified manner.

The circuit presented schematically in a simplified manner in Figure 1.23 shows an important difference in the capacitances next to the coil and flanges. Next to the coil, two capacitances occur in series: one is attributed to the capacitance of the sheath between the bulk plasma and the inner surface of the glass tube, and the other capacitance is attributed to the capacitance of the glass wall. The capacitive component of the impedance is inversely proportional to the capacitance of a capacitor as in equation (11). The thickness of the glass tube is usually larger than the sheath thickness because of practical reasons – the glass tube should withstand the force as a result of the pressure difference, which is approximately 1 bar. Next to the flanges, there is only the capacitance owing to the sheath, because plasma is in a direct contact with the metallic flange. The absence of the impedances because of the absence of the glass wall next to the flanges has an important consequence: The impedance of the circuit from the powered part of the coil and the grounded flanges is lower than the impedance of the circuit from the powered part of the coil to the grounded part of the coil despite the rather large distance between the coil and the flange. As a result, a uniform plasma expands throughout the glass tube. It should be stressed again that the considerations presented in this paragraph are valid only for the case of a low power where the density of charged particles in gaseous plasma is low. In scientific literature, such a configuration is often called "inductively coupled plasma in E-mode". "E" indicates that the electrons gain energy in the electric field next to the sheath rather than in an induced electric field which appears because of an oscillating magnetic field inside the coil.

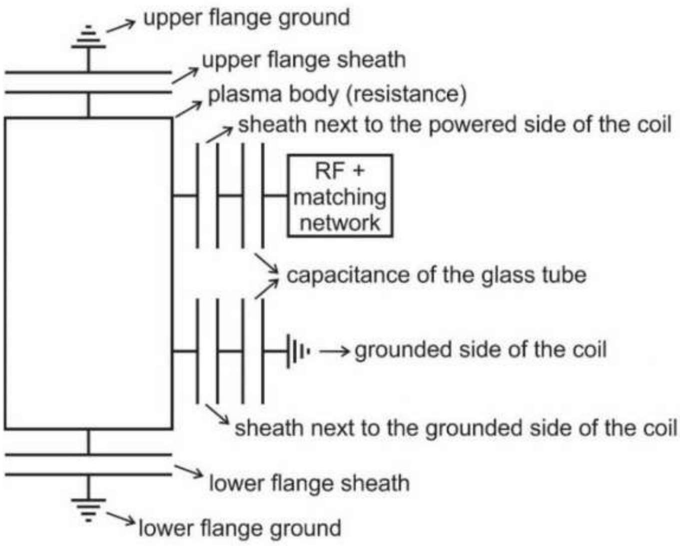

Figure 1.23. Schematic of the simplified electrical circuit for the experimental setup presented in Figure 1.22 when a discharge power is low (plasma in the E-mode, capacitive coupling).

In the case of a high available power, the circuit presented in Figure 1.23 is not valid. At a high power, the electron density is high enough that plasma can be presented as a highly conductive medium. In such a case, the circuit shown in Figure 1.23 should be replaced with a completely different one to include the inductance of gaseous plasma, which becomes important and eventually predominant when the electron density is large. A suitable circuit for such a case is presented in Figure 1.24 in a very simplified manner. The coil connected to the RF generator via the matching network (see Figure 1.22) represents the primary coil of a transformer. The secondary coil is plasma, which is coupled with the primary coil by the mutual inductance which occurs when the current in one inductor induces a voltage in another nearby inductor. Gaseous plasma is, of course, inside the primary coil. Such a picture is justified for a high density of charged particles. Plasma has also its resistivity (Ohmic impedance) which is represented by a resistor connected in parallel with plasma's inductance. Highly conductive plasma following the scheme in Figure 1.24 is often called "inductively coupled plasma in H-mode". "H" indicates that the electrons gain energy in the induced electric field inside the coil which is a result of an oscillating magnetic field.

The simplified picture presented in Figure 1.24 neglects the capacitive components of the circuit impedance because of the presence of the glass tube which is usually not justified, therefore it should be regarded only as a rough approximation. Still, it is useful to understand the huge difference in the mechanisms of the inductive RF plasma powering in E and H modes. It is also worth mentioning than the impedance, which is a result of the capacitance of the sheath between plasma and a surface, is neglected because the electron density is large, therefore the Debye length (equation (12)) is small and so is the impedance.

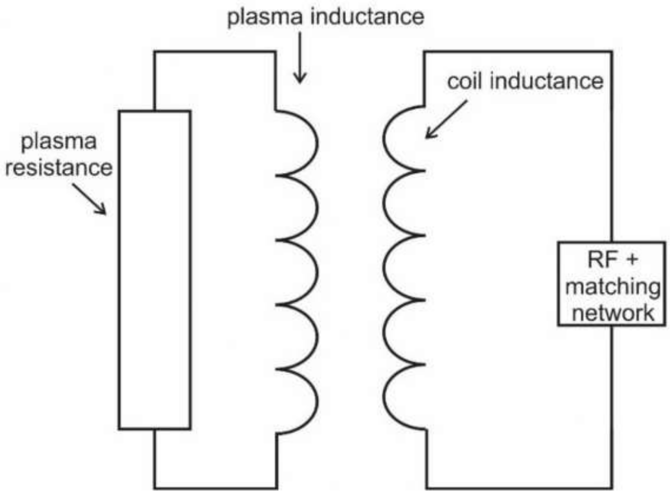

Figure 1.24. Schematic of the simplified electrical circuit for the experimental setup presented in Figure 1.22 when discharge power is high (plasma in the H-mode, inductive coupling).

Plasma can be sustained in the H-mode only when the power density is large enough to assure for a high electron density. The high power is attributed to high voltages on the coil. Such high voltages cause intensive radiation (the coil acts as an antenna) what represents a health hazard. Furthermore, the high voltages may damage the capacitor in the matching network and also cause increased capacitive coupling to nearby grounded metallic components. For large plasma reactors, the voltages may be too high, therefore alternative couplings are recommended. One possibility is an application of several coils connected in parallel to decrease the voltage and enable expansion of the coil length. This solution is schematically presented in Figure 1.25. In this case, the distance between coils should be large enough to prevent predominant electric current between neighbouring coils. Otherwise, the configuration in Figure 1.25 can be represented as a large cylinder placed onto the glass tube. In practice, the coils should be few cm apart each other.

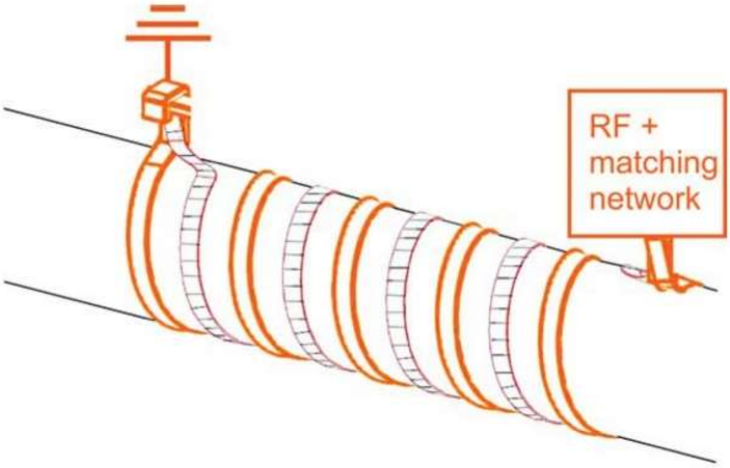

Figure 1.25. Schematic of two coils connected in parallel suitable for an industrial-size inductively-coupled RF plasma in the H-mode.

Yet another coupling suitable for sustaining plasma in long cylindrical discharge tubes is presented in Figure 1.26. This configuration benefits from the quadrupole coupling. There are four rods placed symmetrically along the glass tube. Two opposite rods are powered and the other two are grounded. The coupling can be either in the E-mode (predominant capacitive coupling as schematically shown in Figure 1.21) or in the H-mode (predominant inductive coupling as schematically shown in Figure 1.24). Obviously, the capacitive coupling will be established at a low power of the RF generator and inductive at a large power. An important parameter is also a diameter of the discharge tube. The coupling presented in Figure 1.26 is effective in the H-mode at a rather low diameter, say up to approximately 10 or 20 cm. In the configuration presented in Figure 1.26 the rods connected to the RF generator represent almost perfect antennas, therefore the EM radiation is never negligible. If such a configuration is adopted, the plasma reactor should be encaged into a metallic shield. Obviously, the distance between the rods and the shield should be large (over 10 cm) to minimize the capacitive ground of the powered rods to the metallic shield.

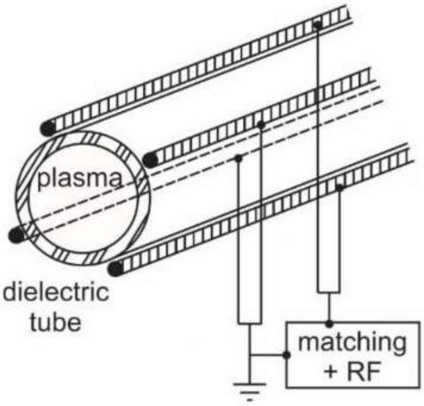

Figure 1.26. Schematic of the coupling using a quadrupole coupling.

The configurations presented in Figures 1.25 and 1.26 are useful for powering long and rather narrow plasma reactors. In many practical examples, however, reactors of a large diameter are preferred. In such cases, a different coupling between the RF generator and gaseous plasma should be applied. Three possible configurations are shown in Figures 1.27, 1.28 and 1.29.

Figure 1.27 shows a coupling suitable for sustenance of gaseous plasma in a low-pressure reactor using a spiral. The spiral is placed onto a dielectric plate and connected to the RF generator via a matching network at the centre of the system as shown in Figure 1.27. The other side of the spiral may or may not be grounded with an electrical conductor. If it is not grounded deliberately, the electrical circuit is closed via the capacitive coupling with the metallic chamber or through gaseous plasma, or the spiral just represents an antenna. Such a configuration is useful for powering plasma in reactors of a large diameter, but one should consider the limitations arising from the simple fact that a long conductor also represents a high inductive impedance. Too long spirals will represent such a high impedance that the voltage across the spiral would be detrimental for the capacitor inside the matching network. Furthermore, the dielectrics are often fragile so if the diameter of the dielectric plate is too large, the pressure difference would cause an extremely large force and the dielectric would break. Here, it is worth mentioning that the pressure difference of 1 bar is 10 N/cm^2. If the area of the dielectric plate is 1 m^2, the force because of the pressure difference would be equivalent to the weight of a 10-ton mass. The configuration presented in Figure 1.27 is therefore suitable for powering plasma in medium size reactors only. In cases, where the dielectric plate dimension exceeds approximately a square meter, it should be straightened mechanically and the spiral should be replaced with several parallel coupled spirals using the same philosophy as presented schematically in Figure 1.25.

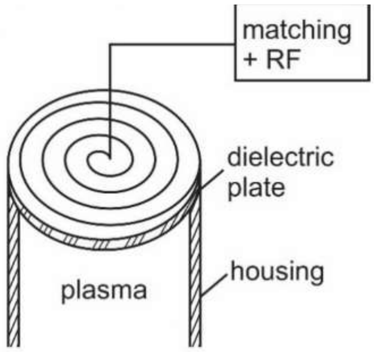

Figure 1.27. Schematic of the coupling using a spiral.

Another solution to reasonably uniform plasma in chambers of a wide diameter and a rather short length is presented in Figure 1.28. In this case, the upper plate is metallic so one benefits from the toughness of metals. The plate can be further reinforced by ribs (not shown in Figure 1.28). Plasma is sustained in several inductively coupled discharges which are connected in parallel and powered with one powerful RF generator. Each discharge operates in a glass tube. For the sake of clarity only two such discharges are shown in Figure 1.28, but in practice several individual discharges may be used. The impedances of particular discharges vary; therefore, it is not trivial to distribute available power evenly to all discharge tubes. An important characteristic of gaseous plasma is that its electrical conductance increases with increasing plasma density; therefore, if a particular discharge creates plasma of a higher electron density than others, its impedance will decrease causing more current flowing through the denser plasma what further decreases its impedance, and so on. Eventually, the current will flow through one discharge only. Fortunately, the impedance does not decrease with increasing plasma density infinitely because other effects suppress it. The most important one is the skin effect: if plasma density becomes very large, the electromagnetic field does not penetrate deep into the conductive medium, therefore the impedance increases with further increasing of the plasma density. As a result, the configuration shown in Figure 1.28 remains suitable for powering plasma in the entire reactor. At a low power of the RF generator, plasma is ignited in one discharge tube. As the power is increased, plasma appears also in another discharge tube, and eventually, at the large RF power, plasma is sustained in all discharge tubes. Such an effect is actually achievable, providing the impedances of the connecting lines are adjusted properly. In practice, it is difficult to match all impedances involved in the electric circuit containing numerous discharges; therefore, the uniform density of gaseous plasma in a reactor presented in Figure 1.28 remains a technological challenge.

A method to supress the abovementioned effect is presented schematically in Figure 1.29. Here, the individual inductively coupled discharges are connected with dense plasma which, according to the previous text, has a rather low impedance at a high electron density. Although the technological problem of equilibration of the total impedances of separate discharges still persist, it is less severe than in the configuration presented in Figure 1.28. The configuration of Figure 1.29 usually contains numerous separate inductively coupled discharges thus making reasonably uniform plasma in the entire reactor. A drawback of the configuration in Figure 1.29 is appearance of dense gaseous plasma in the entire glass tube outside the main chamber, therefore the energy efficiency of such a configuration is rather inadequate.

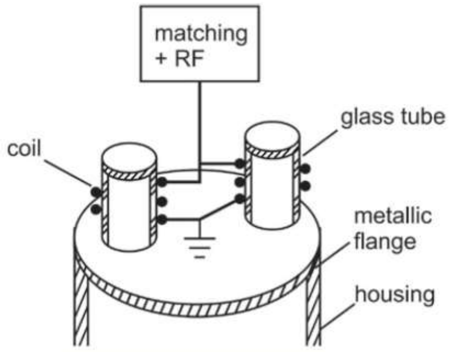

Figure 1.28. Schematic of the coupling using multiple (two) inductively coupled discharges.

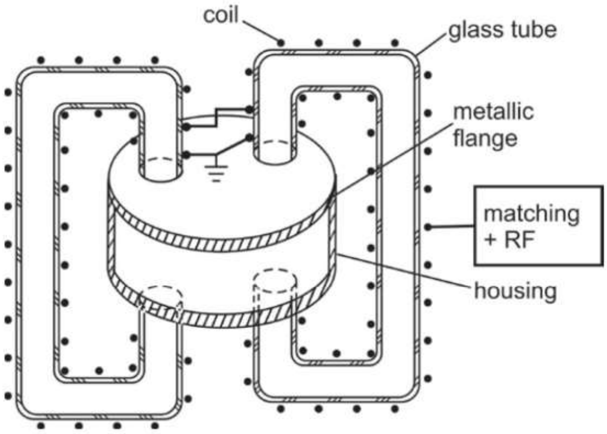

Figure 1.29. Schematic of the coupling using multiple inductively coupled discharges suitable for narrow reactors.

All configurations of the inductive RF coupling as described above employ an antenna or inductor placed outside the vacuum chamber. The reason is trivial: if a coil is placed inside the reactor, the electrical circuit would be closed through the element of least impedance, i.e. dense gaseous plasma. As a result, the powered side of the coil would be subjected to an intensive heat load and an arcing would occur. This effect, however, can be supressed rather effectively using very low-impedance antennas immersed into the plasma reactor. Figure 1.30 represents schematic of the plasma reactor employing numerous low-impedance antennas. Each antenna is actually a U-shaped conductor, which is fully covered with a thin glass or ceramic film for dielectric isolation from the plasma. A typical impedance of a single antenna is of the order of 10 Ω only. The antennas are connected in parallel to the RF generator as shown schematically in Figure 1.30. Such a configuration allows for an efficient high-density plasma production and a low-potentials between the powered sides of antennas and the grounded housing. The problems of adjusting impedances of connecting elements still persists, but careful matching allows for a rather uniform plasma in the entire volume. The configuration of Figure 1.30 is scalable to very large plasma reactors providing the generator is capable of delivering very large electrical currents.

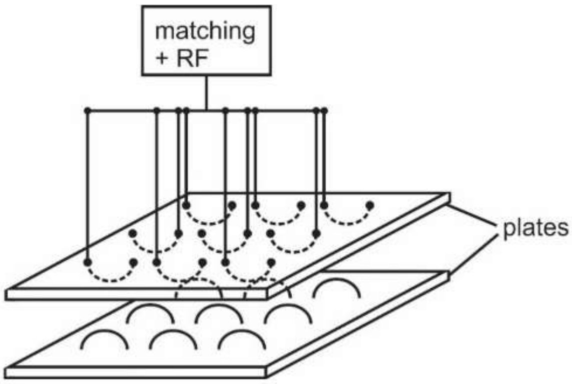

Figure 1.30. Schematics of a plasma reactor with numerous low-impedances antennas immersed inside the vacuum chamber.

Inductively coupled plasma powered with high-frequency RF generators is probably to most common source of neutral atoms. Another option is application of microwave discharges which are particularly suitable for sustenance of gaseous plasma in a small volume. When the frequency of the electromagnetic field is in the range of GHz, the skin effect cannot be neglected. The penetration depth of electromagnetic field in a conductive medium decreases as the square root of the electrical conductivity, therefore heating of plasma electrons is limited to a thin plasma layer next to the surface. Most popular atom sources are plasmas created in glass tubes of a diameter of approximately 1 cm. The dissociation efficiency is large but plasma is never really cold in such discharges.

1.3. Production of O, H and N atoms in inductively coupled RF discharge

This chapter describes a practical example about production of neutral atoms in gaseous plasma sustained by an inductively coupled radiofrequency discharge. As explained in the previous chapters the electrodeless configuration of the high-frequency RF discharge is particularly suitable for efficient dissociation of oxygen, nitrogen of hydrogen molecules into parent atoms. The reason for high efficacy is twofold: 1 – the RF power is efficiently absorbed by electrons in gaseous plasma, and 2 – the loss of atoms by heterogeneous surface recombination is minimal.

In the example elaborated here, the RF power is transferred to gaseous plasma either by the predominant capacitive coupling (schematic of the equivalent electrical circuit is shown in Figure 1.23.) or by almost pure inductive coupling (as shown schematically in Figure 1.24.). The RF generator operates at the most frequently used industrial frequency of 13.56 MHz up to the nominal power of 1000 W. There are two power meters on the RF generator: one measuring the forward power and the other indicating the reflected power. If the reflected power is larger than 200 W, the generator shuts down automatically to prevent any damage. The predominant capacitive coupling will be called “E-mode”, whereas the expression “H-mode” will be assigned for predominant inductive coupling. The matching network in the example shown in this chapter was optimized for the coupling in the H-mode thus enabling also high discharge powers and thus high density of electrons.

The experimental system will be described to details thus enabling a reader to replicate the results. Schematic of the experimental system is shown in Figure 1.31. The discharge chamber is a tube of a length of 80 cm and outer and inner diameters of 40 and 36 mm, respectively. The tube is made from borosilicate glass of a recombination coefficient approximately 10^{-3} for either O or N atoms, whereas the recombination coefficient for H atoms is closer to 10^{-2} at room temperature. The coefficient for H atoms increases with increasing glass temperature [25]. The glass tube is connected to standard KF flanges using elastomer gaskets. The RF coil is mounted asymmetrically onto the discharge tube. This was done intentionally to facilitate different couplings to the flanges. The coil of 6 turns is made from a copper tube of outer and inner diameters of 3 and 1.5 mm, respectively, and is connected to an RF generator Cesar supplied by Advanced Energy. The coil is cooled with water, whereas the segment of the discharge tube with intensive plasma is forced-air cooled. Such cooling prevents heating of the outer walls of the discharge tube over approximately 50 °C even for large discharge powers. Gases are introduced into the discharge tube through a Aera FC-7700 mass flow controller (MFC). An absolute vacuum gauge MKS baratron 722A absolute pressure transducer is used for measuring the pressure inside the discharge tube, which is pumped by Edwards Two-stage rotary pump of a nominal pumping speed of 80 m^3/h. A valve IEVT KV-R-32 supplied by Vacutech enables separation of the pump from the discharge tube without turning it off. There is also a flow restrictor above the vacuum pump which enables adjustment of the effective pumping speed. Between the pump and the discharge chamber there is a recombinator supplied by Vacutech to catalyse atoms to parent molecules to prevent any chemical interaction of atoms with the oil in the vacuum pump. The atom densities are measured with movable catalytic probes supplied by Plasmadis (Ljubljana, Slovenia). The probe tip is moved along the discharge tube from the coil towards the flange next to the pump as shown in Figure 1.31. The probe tip is never inside the coil where intensive plasma appeared in the H-mode. The probe would melt immediately, if placed in powerful plasma inside the coil according to the considerations presented in Figures 1.10 or 1.11. The recombination coefficients for the catalytic tips are 0.12, 0.066 and 0.50 for O, H and N atoms, respectively. An optical spectrometer is connected to a movable optical fibre for measuring characteristic spectra in the range between approximately 200 and 1100 nm. The vacuum system is often vented to an ambient atmosphere and never baked, therefore water is adsorbed on the inner surfaces.

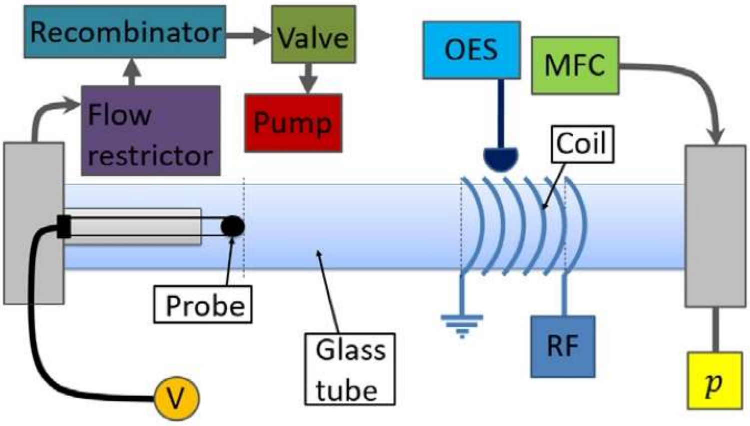

Figure 1.31. Schematic of the experimental system.

1.3.1 Oxygen atoms

Oxygen of commercial purity 99.9% was introduced into the experimental system presented schematically in Figure 1.32. A photo of the discharge tube at the discharge power of 100 W and the pressure of 20 Pa is shown in Figure 1.33. The photo reveals three distinguished regimes: 1 – plasma of a rather intensive radiation which is limited to the coil volume, 2 – less luminous plasma between the coil and the grounded right-hand flange, and 3 – very weak plasma in the volume between the coil and the left-hand flange. The RF power is effectively transferred into gaseous plasma in regime 1. This is due to the capacitive coupling between the coil and the gaseous plasma inside the coil. The electrons are accelerated in the sheath next to the coil between the glass tube and the plasma inside the coil. Once the fast electrons enter plasma, they are quickly thermalized at elastic collisions with plasma electrons. Such a constant supply of energetic electrons (the voltage across the sheath is hundreds of Volts) from the sheath to the plasma inside the coil makes the electron temperature rather high in regime 1. The glowing plasma, however, does not terminate at the end of the coil but expands 10 cm away towards the right-hand side grounded flange. The reason for such expansion is the capacitive coupling between the coil and the flange. The reason for appearance of a rather uniform plasma in the regime 2 is simple: the capacitive component of an impedance across the glass wall next to the grounded part of the coil is larger than the resistance of plasma of a length of approximately 10 cm. As explained in the chapter 1.2., the electrons have large mobility, therefore the impedance of plasma itself (without sheaths) is easily approximated by a pure resistive impedance, which is usually much lower than other impedances involved in the electrical circuit. In fact, plasma of the regime 2 does not terminate at the grounded flange but rather expands into the entire metallic tube (not shown in Figure 1.33). This is called “hollow electrode effect”. The reason for such an expansion is the fact that the resistance of plasma is smaller than the capacitive component of the sheath impedance: it is favourable to have a large “capacitor” (i.e. the surface of the sheath next to the grounded flange) and somehow larger resistance in series than vice a versa.

The same considerations apply for the left-hand flange, except that the length between the coil and this flange is larger. Because a larger length results in a larger resistance of the capacitive coupling of the asymmetric configuration as adopted in this work, plasma is much more intensive to the right-hand side of the discharge tube than to the left-hand side. If the configuration was symmetric, the regime 2 would have been observed also in the left-hand side of the discharge tube providing the pressure is low enough to allow for a rather high mobility of electrons. At higher pressures, a capacitive discharge is established on one side only. From these considerations, one can deduce that plasma would be limited to the regime 1 only if the capacitive impedance across the glass wall next to the coil is lower than the resistance of the plasma in regimes 1 and 2, i.e. if the distance between the coil and any grounded flange and/or the pressure is large.

Figure 1.34 shows an image of oxygen plasma at a high power of 500 W and the pressure of 20 Pa when it is in the H-mode. The plasma luminosity in the volume inside the coil is much larger than in the case of the E-mode which is presented in Figure 1.33. The very luminous plasma indicates large electron density, therefore the coupling as shown in Figure 1.24 prevails. The coupling is thus almost entirely inductive in Figure 1.34. The voltage is somehow smaller in the H-mode and the current larger, however they do not differ dramatically between the E- and H-mode [26]. The main difference is in the phase shift between the voltage and current. The dissipated RF power is a product of voltage, current and phase shift, i.e.

$$P_{\mathrm{plasma}} = U\,I\cos(\varphi). \qquad ()$$

In the E-mode, the $\cos(\varphi)$ is small, whereas in the H-mode it is large. Plasma between the coil and flanges is not observed in Figure 1.34 due to the large luminosity inside the coil, but it may occur because of the capacitive coupling between the coil and the flanges. The impedance of the capacitive coupling is large compared to the inductive impedance, therefore any effects due to the capacitive coupling are marginal when plasma is in the H-mode.

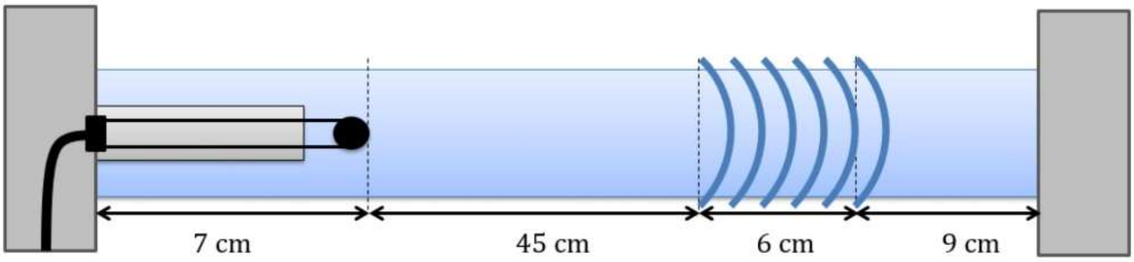

Figure 1.32. Details about the configuration of the discharge tube for measuring the density of O atoms.

Figure 1.33. A photo of the discharge tube when oxygen plasma is in the E-mode.

Figure 1.34. A photo of the discharge tube when oxygen plasma is in the H-mode.

The optical spectra from plasma sustained in the E- and H-mode are shown in Figure 1.35. The spectra in both modes are similar – the most intensive radiation arises from transitions in the red part of spectra at 777 nm and near infrared at 845 nm. The predominant line at 777 nm gives oxygen plasma its typical red colour. The intensity of radiation in the H-mode is roughly three orders of magnitude larger than in the E-mode. The differences in intensities are explained by differences in the electron density and thus predominant coupling. Another spectral features observed in the lower spectrum of Figure 1.35 are attributed to radiative transition of ionized oxygen molecules [27]. Although the height of the atomic line at 777 nm is much higher than the spectral features arising from molecular transitions in the broad range around 600 nm, the oxygen plasma in the E-mode inside the coil does not assume red colour but rather white. The reason for this impression is the fact that the molecular transitions are much broader than atomic, therefore the integral radiations around 600 nm and at 777 nm are comparable. The spectrum acquired from plasma in the H-mode is free from the molecular transitions. Such a spectrum indicates very high dissociation fraction of oxygen in the H-mode.

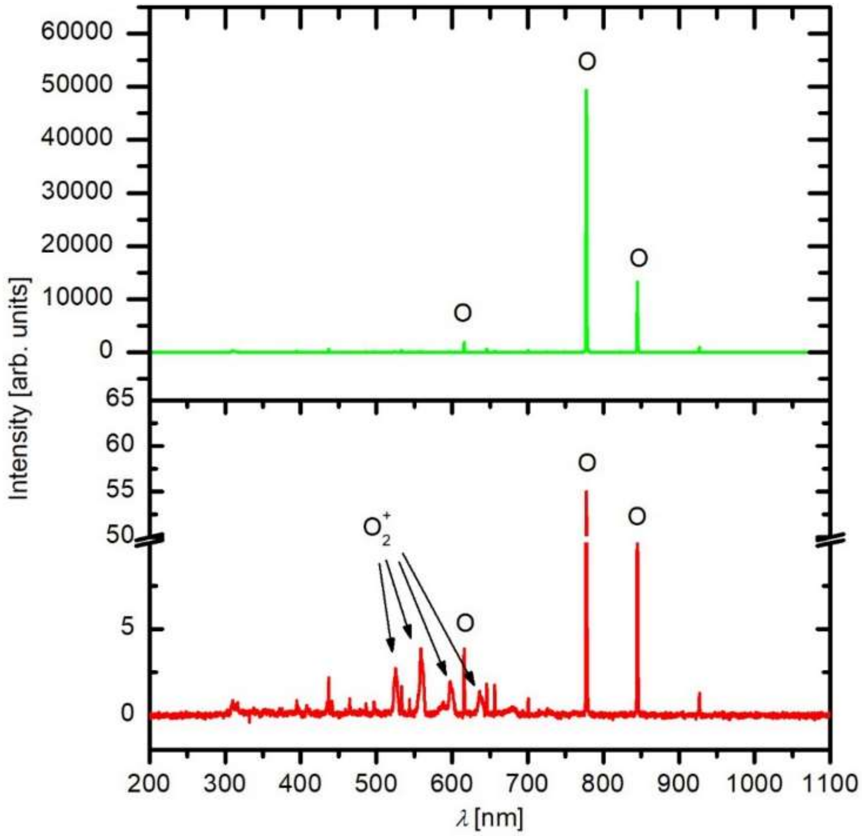

Figure 1.35. The spectra of oxygen plasma in the E-mode (lower curve) and the H-mode (upper curve).

The density of oxygen atoms in the discharge tube shown in Figure 1.32 obviously depends on the following parameters: the position inside the tube, the flow of gas through the tube, the pressure and the power. The number of measurements for complete characterization is therefore too large, therefore only representative results are presented in the following text. The power indicated in all figures is the forward power as indicated by the power meter attached to the RF generator unless stated otherwise. It should be stressed again that the forward power is never equal to the power absorbed by gaseous plasma. The forward power is always larger and the real power absorbed by plasma can be only a fraction of the forward power, depending on the coupling efficiency.

The probe was fixed at the position indicated in Figure 1.32 and the O-atom density was measured at various pressures and discharge powers. Figure 1.36 represents the O-atom density at the position 7 cm away from the left-hand flange of Figure 1.32. The measurements were performed as follows: The values of the oxygen pressure and forward RF power were pre-selected. The smallest pressure was set and the forward power, supplied by the RF generator, was varied while the density of O-atoms was measured. Then, the pressure was changed and the measurements were repeated at the same forward RF powers. The procedure was repeated until the entire range of pressures was characterized.

Figure 1.36 reveals increase of the O-atom density with increasing power. The effect is explained by more power absorbed in plasma at increasing forward power. The density, however, does not increase monotonously with increasing power, but there is an instant increase which occurs at a certain forward power. The instant increase of the O-atom density is explained by transformation of the discharge coupling from the E- to H-mode. As long as the discharge is in the E-mode, the density is up to approximately 1x10^{21} m^{-3}. The density in the E-mode depends on the forward power only for pressures up to approximately 30 Pa and remains fairly constant (rather independent from pressure) thereafter. Obviously, the density of O-atoms in the E-mode cannot be very large because of poor transfer of available power for heating plasma in the E-mode. When the discharge is in the H-mode, the O-atom density increases monotonously with increasing power. This effect is explained by the fact that a variable fraction of the forward RF power is actually absorbed by plasma. In the E-mode, the fraction of a power absorbed by plasma using the setup as in Figure 1.32 is rather small, therefore any increase of the forward power does not reflect in the increase of the absorbed power and thus on the density of atoms. This effect is often overlooked in scientific literature.

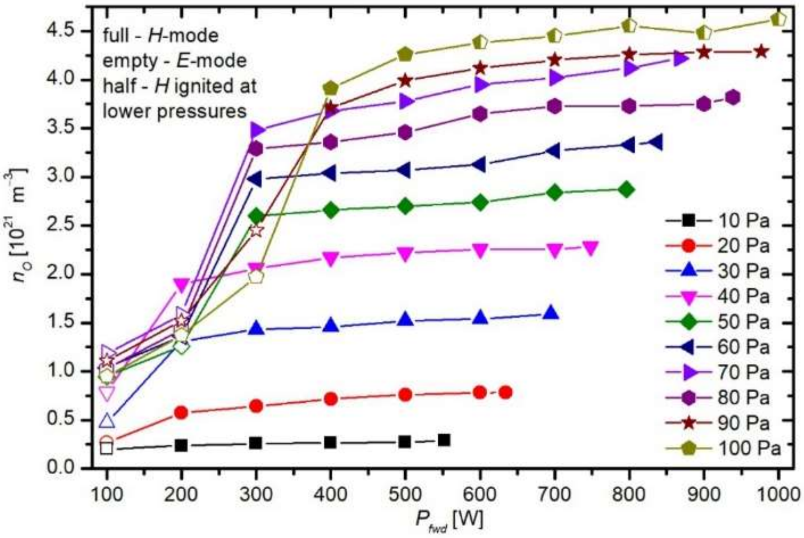

Figure 1.36. The O-atom density versus the forward power of the FR generator at different pressures inside the discharge chamber at the probe position of 45 cm left from the coil. The setup as in Figure 1.32.

The experimental system is equipped with a meter of reflected power. Because the accuracy of measuring the reflected power is not the best, it may be more appropriate to present the O-atom density versus the difference between the forward and reflected powers. Such a graph is shown in Figure 1.37. In this figure, the curves are monotonous, therefore such a presentation of measurements is more appropriate. It appears rarely in scientific literature, though.

The difference between the forward and reflected powers is a better parameter than the forward power itself, however, it still cannot be equalized with the power absorbed by plasma. Such measurements have rarely been reported because they are not trivial. An interesting feature is observed in Figure 1.37: The measured points are not equidistant, but there is a gap between the E- and H-mode. For example, the O-atom density at the pressure of 100 Pa was determined for powers up to approximately 100 W and above 400 W. In between, it was impossible to sustain gaseous plasma using configuration in Figure 1.31. The powers up to 100 W are attributed to a discharge in the E-mode, and above 200 W to the H-mode. Between the modes, there is a power gap which is sometimes called “forbidden zone”. This effect occurs due to different discharge couplings. As the forward power is increasing in the E-mode, the reflected power increases too, therefore, the increase of the powers difference is not linear with increasing forward power. The physical explanation of the forbidden zone is as follows: As the power on the coil increases in the E-mode, the voltage increases, too. Once a certain power is reached, the voltage in the E-mode is equal to the maximal voltage of the power supply. Although an attempt is made to increase the power to reach the power that was set, the forward power cannot be increased any more in the E-mode because the maximal available generator voltage has been reached.

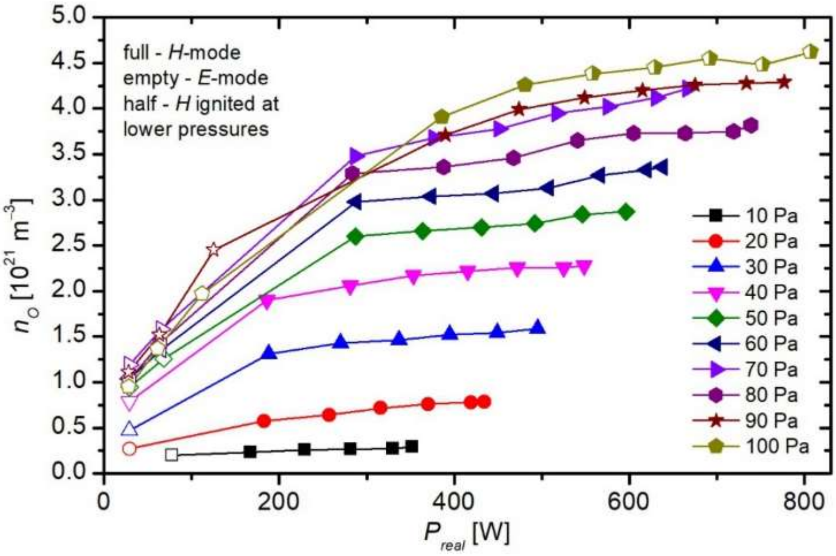

Figure 1.37. The O-atom density versus the difference between the forward and reflected powers at different pressures inside the discharge chamber at the probe position of 45 cm left from the coil. The setup as in Figure 1.32.

The situation is completely different in the H-mode. The coupling is predominantly inductive as shown schematically in Figure 1.24. For inductive coupling, somehow lower voltage is necessary to sustain gaseous plasma, therefore the maximal available voltage of the power supply is not reached. The necessary condition for plasma in the H-mode is a large conductivity, i.e. large density of electrons. A high density of electrons cannot be obtained at a low discharge power. In the case, when the pressure is 100 Pa, the plasma in the H-mode is only sustained at powers over approximately 400 W. This is a simple but useful explanation of the forbidden zone of powers as revealed from Figure 1.37.

Another lawfulness is evident from Figure 1.37: the power gap (the difference between the minimal power achievable in the H-mode and the maximal power achievable in the E-mode) increases with increasing pressure. At 10 Pa it is roughly 40 W (Figure 1.38), at 20 Pa it is already approximately 60 W, whereas at 100 Pa it is as much as 250 W. The width of the power gap (forbidden zone) increases monotonously with increasing pressure. Figure 1.38 represents this effect. Here, it should be stressed that the curve in Figure 1.38 is valid for the system shown to details in this chapter only. If the configuration is different, the width of the power gap is different.

Figure 1.38 also reveals an important rule: plasma can be sustained in the H-mode at elevated pressures only if the RF generator is powerful enough and if the matching network allows for the efficient transfer of the available generator power into gaseous plasma. As the pressure decreases, the power gap decreases as well. In fact, the transition between the E- and H-mode is not abrupt at pressures below approximately 1 Pa for configuration presented in this chapter. The effect is explained by decreasing the frequency of electron collisions and thus increasing the mean free path of electrons with decreasing pressure. As a consequence, the electrons have higher mobility at low pressures and thus ability to sustain dense plasma at a relatively low power at low pressures.

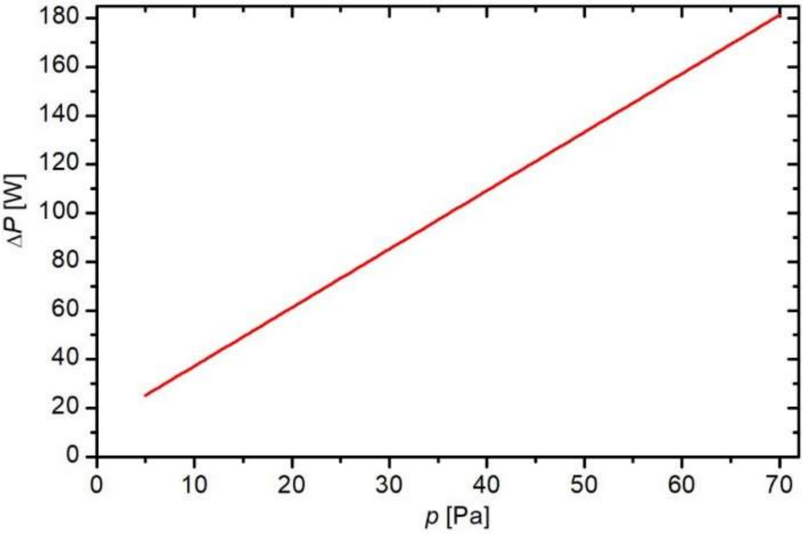

Figure 1.38. The width of the power gap between the E- and H-mode (forbidden zone) versus the oxygen pressure in the discharge tube of the configuration shown in Figure 1.32.

Usually, it is useful to present the density of O atoms versus the pressure with the power as a parameter as in Figure 1.39. One can observe an interesting effect: all curves (except the lowest) in Figure 1.39 follow the general curve and deviate at a certain pressure which depends on the pre-set generator power. This observation is useful when one designs the discharge configuration. Obviously, a large generator power is unnecessary at a low pressure. The effect has been already explained but it is useful to recall it: as long as plasma is in the H-mode, the electron density is very high in plasma within the coil. As a consequence, the molecules are highly dissociated already at a moderate power, therefore, any increase of the discharge power does not result in dissociation but rather in the other effects such as increased electron density and more energy dissipated for other phenomena than dissociation. The deviation of the atom density from the general curve presented in Figure 1.39 obviously occurs when the discharge mode is transformed from the H- to E-mode. Here, it is useful to mention that if the power is increased while the plasma is already ignited, the transition from the E- to H-mode does not appear at the same forward power as from the H- to E-mode if the power is decreased, therefore a hysteresis is observed. The hysteresis is due to the fact that a power needed for ignition of the H-mode is larger than a power needed for sustaining the H-mode at a given pressure. As the pressure increases, the ignition power increases too, therefore at an elevated pressure the available generator power is not sufficient to ignite the H-mode but enough to sustain it. A practical consequence of this effect is that one can first ignite the H-mode at a rather low pressure at a given generator power and then increase the pressure to sustain the H-mode at an elevated pressure. This praxis was adopted in some measurements shown in Figure 1.39.

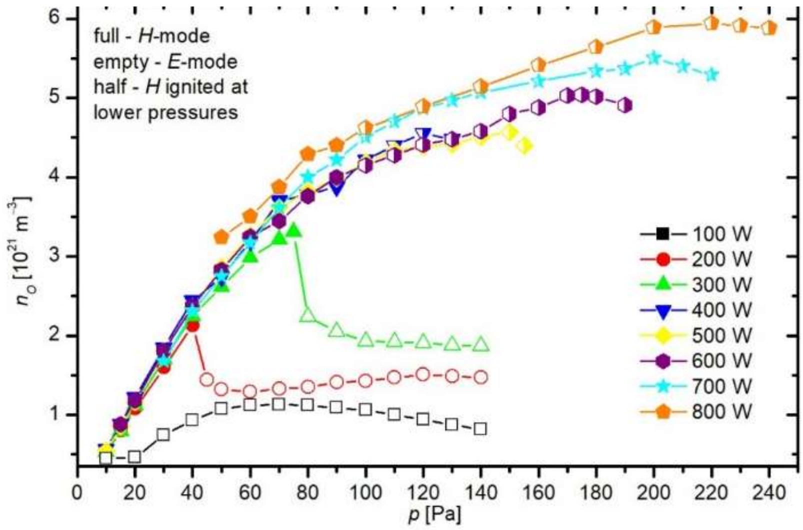

Figure 1.39. The O-atom density at the probe position of 45 cm away from the RF coil towards the left-hand flange of Figure 1.32. The parameter is the forward power.

A useful parameter is also the dissociation fraction which is defined as the ratio between the atom density and twice the density of molecules in the discharge chamber before igniting the discharge. The dissociation fraction for experimental conditions adopted for measuring the O-atom densities as in Figure 1.39 is shown in Figure 1.40. The dissociation fraction depends largely on the discharge mode: in the E-mode it is several times lower than in the H-mode. The difference is explained by more efficient dissociation of molecules when the discharge is in the H-mode. As already stated, the electron density in the H-mode is much larger than in the E-mode. Similar behaviour of the oxygen dissociation fraction is observed as for the case of O-atom density: there is a general curve in the H-mode. As long as plasma is in the H-mode, the dissociation fraction does not depend much on the discharge power because the dissociation is efficient enough already at moderate powers as long as the pressure is not too high.

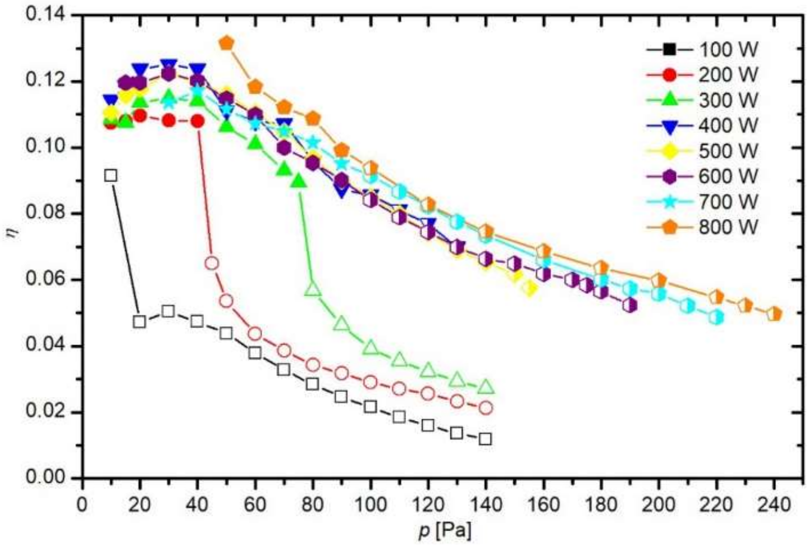

Figure 1.40. The dissociation fraction of oxygen molecules at the position 45 cm away from the RF coil towards the left-hand flange of Figure 1.32. The parameter is the forward power.

The density of oxygen atoms at a given position in the discharge tube does not depend only on the pressure and power, but also on the time the gas spends on the way from the intensive plasma within the coil to the position of the probe. Figure 1.41 reveals this effect. The curves reveal monotonous increase of the O-atom density with an increasing flow rate. This observation indicates that the residence time of the gas flowing through the intensive plasma inside the coil does not affect the density of atoms downstream. If the residence time was too short to ensure for appropriate dissociation of oxygen molecules, the curves would have decreased with increasing flow at large flows. Theoretically, there should be a maximum in the curves presented in Figure 1.41: when the flow is zero, the O atom density should be very low due to poor migration (by diffusion) of atoms from plasma inside the coil (where they are formed by an electron-impact dissociation of parent molecules) to the position of the probe. When the flow is infinitely large, the residence time should approach zero, also resulting in a poor atom density at the probe position because the electrons would miss numerous molecules. In practice, however, the flow is limited due to limited gas drift (the theoretically maximum drift velocity is equal to the sound velocity as explained in chapter 1) and due to a finite pumping speed. The latter limitation prevails at experimental conditions adopted in this study. The fact that no extreme is observed in curves of Figure 1.41 therefore clearly indicates that the residence time of the gas in plasma inside the coil does not influence the O atom density in the experimental system adopted in this work.

The monotonous increase of the O atom density with increasing gas flow in Figure 1.41 also indicates that the dissociation of oxygen molecules by plasma electrons in region 3 of Figure 1.33 is not efficient enough to replace the loss of atoms on the way from the coil to the probe position. If it was sufficient, the curves in Figure 1.41 would have been constants. The region 3 in Figure 1.33 indicates a rather poor capacitive coupling between the coil and the left-hand grounded flange – see figures 1.33 and 1.34. Obviously, the production of atoms in such a weak discharge is insufficient for a reasonable atom density. The loss of atoms at this pressure (50 Pa) is almost exclusively by heterogeneous surface recombination. To minimize this loss, the gas flow should be rather large. Although the recombination coefficient for oxygen atoms on the surface of borosilicate glass is low at about 10^{-3}, the loss of atoms is not negligible.

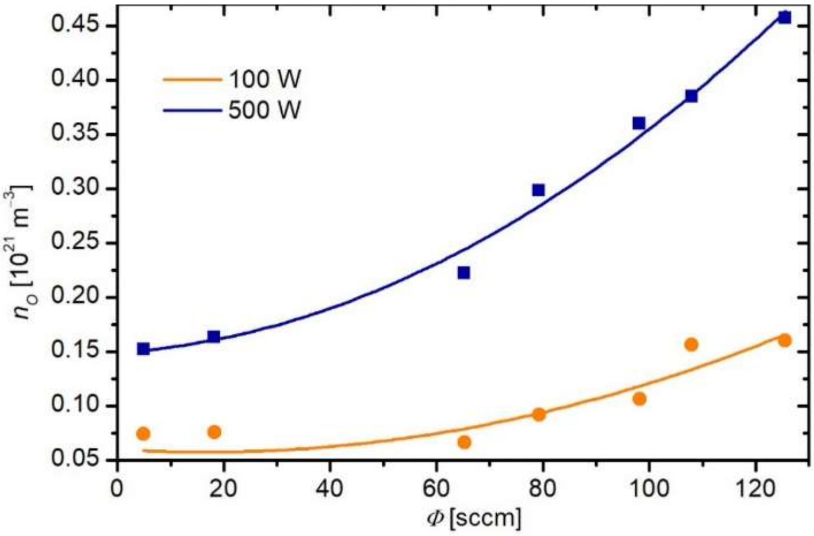

Figure 1.41. The density of O atoms at the position 45 cm away from the RF coil towards the left-hand flange of Figure 1.32 versus the flow of the gas through the discharge tube at the pressure of 50 Pa when plasma is in the E- (lower curve) and H-mode (upper curve).

The effect of decreasing atom density due to surface recombination to parent molecules can be monitored using a movable probe. Figure 1.42 reveals the dissociation fraction versus the probe position and fixed other parameters, i.e. the gas pressure either 20 or 50 Pa and the forward power either 100 or 500 W. The dissociation fraction slowly decreases with increasing distance from the coil which is explained by a weak surface recombination because of the small recombination coefficient. The curves are linear except close to the coil when plasma is in the H-mode (at 500 W). The deviation close to the coil is explained by the fact that the intensive plasma causes a very high dissociation fraction in plasma, therefore the O-atom density in plasma within the coil is much larger than at any probe position adopted in this experiment. The dissociation fraction as shown in Figure 1.42 is moderate – only 20% at the closest position to the coil what suggest a discrepancy with the claim that the oxygen molecules are almost fully dissociated in a dense plasma inside the coil. The virtual discrepancy is explained by thermal effects: although the discharge tube is forced-air cooled, the inner surface of the glass tube warms up when the plasma is in the H-mode. As a consequence, the O-atoms are lost more efficiently close to the coil because the recombination coefficient increases with temperature. At the distance of 15 cm from the coil, the discharge tube is cold (at room temperature) irrespective from the discharge power, therefore the atom density slowly decreases with increasing distance from the coil in this part of the tube.

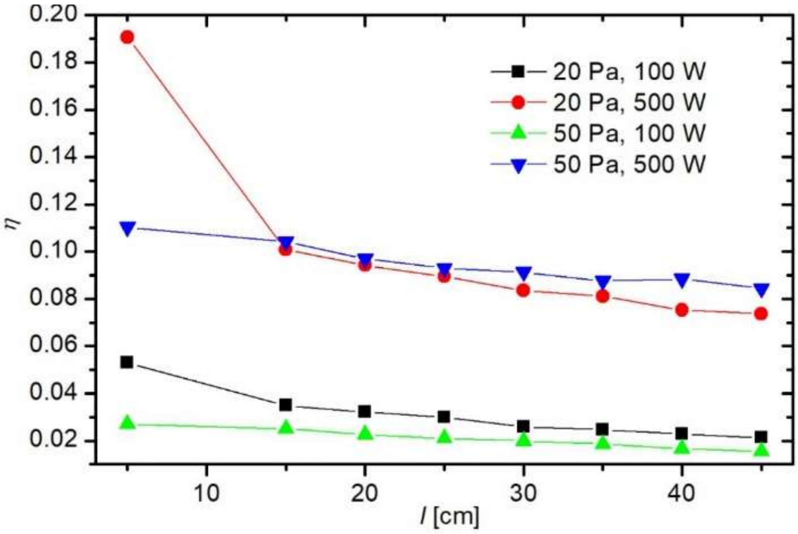

Figure 1.42. The oxygen dissociation fraction versus the distance from the coil at a fixed flow and two different pressures and forward powers.

1.3.2 Hydrogen atoms

The dissociation energy of hydrogen molecules is somehow lower than oxygen, therefore one would expect somehow larger dissociation fractions at the same discharge condition. Such a simple consideration, however, is not justified for experimental setup adopted in this research. As mentioned earlier, the recombination coefficient for hydrogen atoms on the surface of borosilicate glass is larger than for oxygen and the coefficient increases significantly with increasing temperature. These effects influence the density of H-atoms in the experimental system shown in Figure 1.31. The configuration of Figure 1.32 which proved very useful for oxygen, failed for the case of hydrogen. A reason for this is the fact that at the probe position of 45 cm away from the coil, the atom density was close to the detection limit of the probe when the discharge was in the E-mode. The system was thus slightly modified to enable comprehensive characterization of the RF source of H-atoms. The details of the discharge tube adopted for experiments with hydrogen are shown in Figure 1.43.

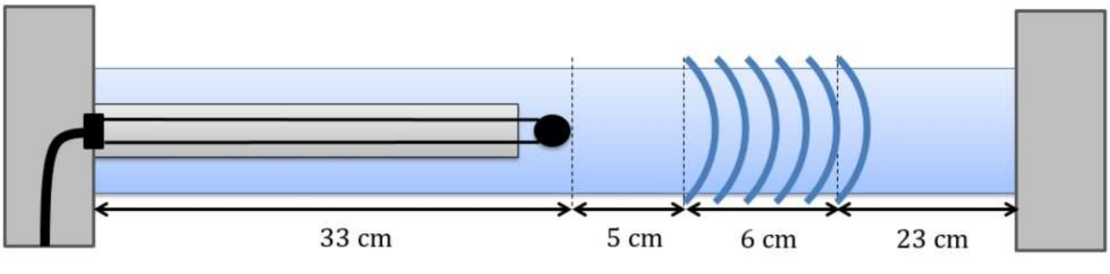

Figure 1.43. Details about the configuration of the discharge tube for measuring the density of H atoms.

A photo of hydrogen plasma in the E-mode is shown in Figure 1.44. Luminous plasma expands throughout the discharge tube and is somehow more luminous inside the coil. Almost equal plasma luminosity in the tube both left and right from the coil indicates a rather equal capacitive coupling between the coil and the grounded flanges. The difference between hydrogen and oxygen plasma is explained by different positions of the coil. In the case of oxygen (Figure 1.33), the coil was placed highly asymmetric, whereas in the case of hydrogen (Figure 1.43), an almost symmetric geometry was chosen. The somehow more luminous plasma inside the coil is explained by somehow larger electron temperature due to the constant supply of high-energetic electrons from the sheath between plasma and the glass tube backed by the powered coil as explained to details for the case of oxygen plasma.

Figure 1.45 shows a photo of hydrogen plasma in the H-mode. Luminous plasma is now concentrated in the volume inside the coil and only very weak plasma expands over the rest of the discharge tube. The reasons are the same as explained for oxygen plasma. The interface between the luminous plasma within the coil and dim plasma elsewhere is rather sharp. In the volume of luminous plasma, the coupling is the same as shown schematically in Figure 1.24. The dense plasma expands few cm outside the coil where the density of electrons is still high enough to assure for the effective inductive coupling.

Figure 1.44. A photo of the discharge tube when hydrogen plasma is in the E-mode, i.e. at 20 *Pa and 150 W forward power.*

Figure 1.45. A photo of the discharge tube when hydrogen plasma is in the H-mode, i.e. at 20 *Pa and 500 W forward power.*

The spectra of hydrogen plasma in the E-mode (photo in Figure 1.44) and H-mode (Figure 1.45) are shown in Figure 1.46. In both modes the atomic transitions indicated by sharp lines prevail. The atomic lines indicate transitions from a higher to the first excited state. The transitions to the ground state (although more intensive than to the first excited states) are not observed because they appear in the far UV range of spectra not detectable by the optical spectrometer. Instead, one can observe other features when plasma is in the E-mode (lower curve in Figure 1.46): there are bands peaking at approximately 600 nm which correspond to neutral molecule transitions (Fulcher band). There is also a broad continuum in the near UV range of the spectrum. The continuum arises from relaxation of triplet molecules from the excitation level at about 12 eV to a lower state that dissociates immediately. Because the lower state is not bonded (molecules in this state dissociate immediately), the radiation from this triplet state causes a continuum. The continuum observed in the lower curve of Figure 1.46

terminates at the wavelength of approximately 300 nm because of the fact that the borosilicate glass is not transparent for the radiation of shorter wavelengths. The spectrum of hydrogen plasma in the H-mode (upper curve in Figure 1.46) reveals only atomic transitions. This observation indicates that the dissociation fraction of hydrogen molecules when plasma is in the H-mode is very high, same as for oxygen plasma.

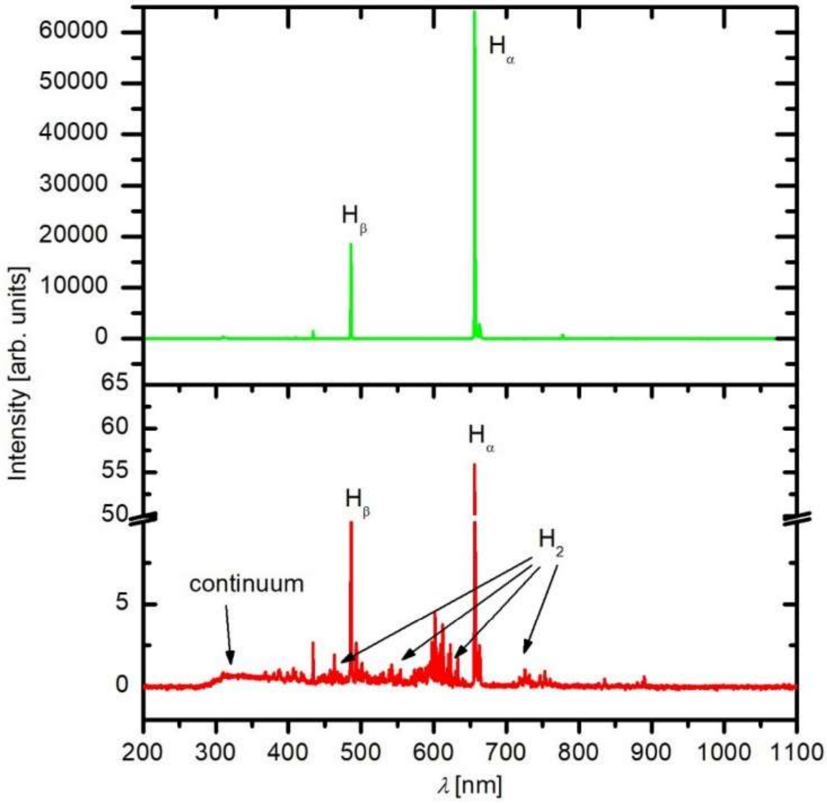

Figure 1.46. The spectra of hydrogen plasma in the E-mode (lower curve) and the H-mode (upper curve).

The density of H-atoms in the configuration presented in Figure 1.43 was measured with the catalytic probe whose tip was placed 5 cm from the coil in the direction of the gas flow (see Figure 1.43). The measurements were performed using the same procedure as for oxygen. The H-atom density versus the forward power of the RF generator is plotted in Figure 1.47. As in the case of oxygen, there is an abrupt increase of the H-atom density at a certain power which depends on the pressure. At the pressure of 15 Pa the abrupt increase of the H-atom density appears at the forward power of approximately 250 W, whereas at 50 Pa it appears at approximately 400 W. As already stressed, the forward power is not an indicator of the power absorbed in plasma. To this end, it is better to present the H-atom density versus the difference between the forward and reflected powers as shown in Figure 1.48. The curves are now rather monotonous: the H-atom density increases fairly linearly with increasing power up to the highest available powers. This effect is somehow different than for the case of oxygen where some sort of saturation was observed at elevated powers (see Figure 1.37). The discrepancy is explained by different distances between the luminous plasma inside the coil and the probe position – the probe was closer in the case of hydrogen plasma. As shown in Figure 1.42 the H-atom density increases rapidly with decreasing distance close to the coil.

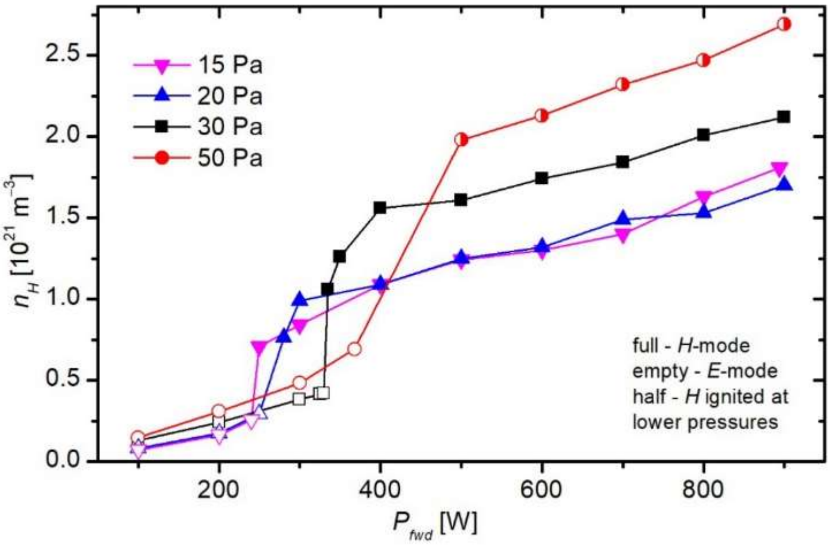

Figure 1.47. The H-atom density versus the forward power of the FR generator at different pressures inside the discharge chamber at the probe position 5 cm left from the coil. The setup as in Figure 1.43.

As for oxygen (Figures 1.37 and 1.38) a forbidden zone of powers in observed also for hydrogen as shown in Figure 1.48. The range of forbidden powers increases with increasing pressure. The reason was already explained for the case of oxygen: insufficient voltage of the power supply when the discharge is in the predominant capacitive mode. The width of the power gap (the forbidden zone), i.e. the difference between the minimal power for sustaining plasma in the H-mode and the maximum power achievable for sustaining plasma in the E-mode, is similar to the width observed in oxygen plasma (Figure 1.38). The width for the case of hydrogen plasma at experimental conditions adopted in this work is shown in Figure 1.49.

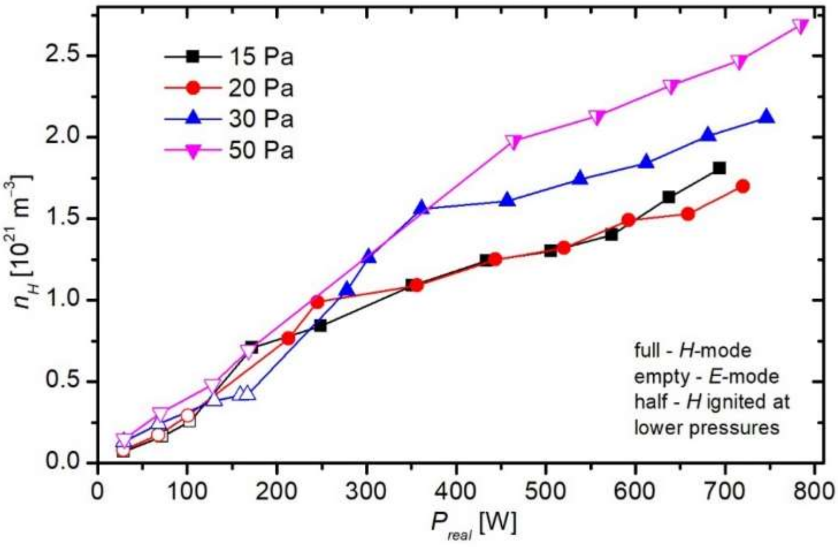

Figure 1.48. The H-atom density versus the difference between forward and reflected powers at different pressures inside the discharge chamber at the probe position 5 cm left from the coil. The setup as in Figure 1.43.

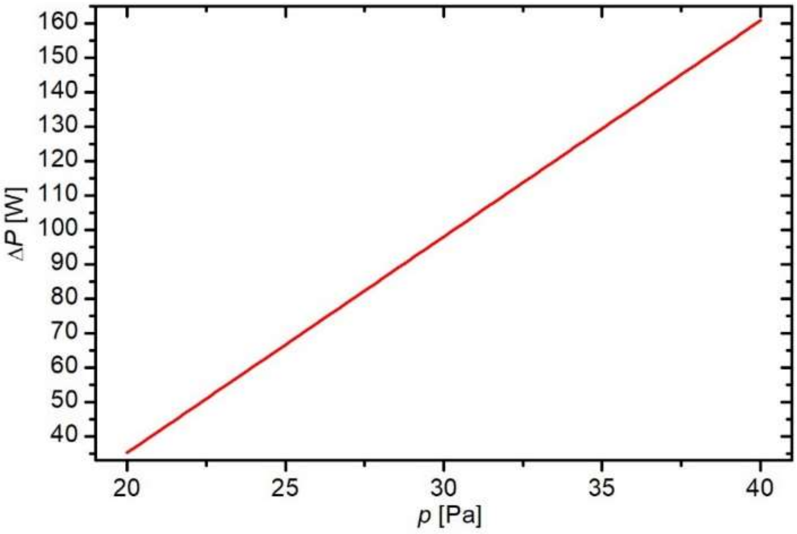

Figure 1.49. The width of the power gap between the E- and H-mode (forbidden zone) versus the hydrogen pressure in the discharge tube of the configuration shown in Figure 1.43.

The density of hydrogen atoms at the position 5 cm from the coil (see Figure 1.43) versus the pressure is shown in Figure 1.50. The forward power is the parameter. The H-atom density was measured at the pre-set forward powers of 100, 500 and 700 W. When the forward power was 100 W the discharge was in the E-mode for the entire range of pressures, whereas for 500 and 700 W it was in the H-mode. Hydrogen plasma in the H-mode does not ignite at our experimental conditions in the H-mode at pressures above 35 Pa, therefore it was ignited at a lower pressure and sustained at an elevated pressure. As mentioned earlier, this procedure was adopted to benefit from the fact that the power needed to sustain plasma in the H-mode is lower than the power needed to ignite plasma in the H-mode.

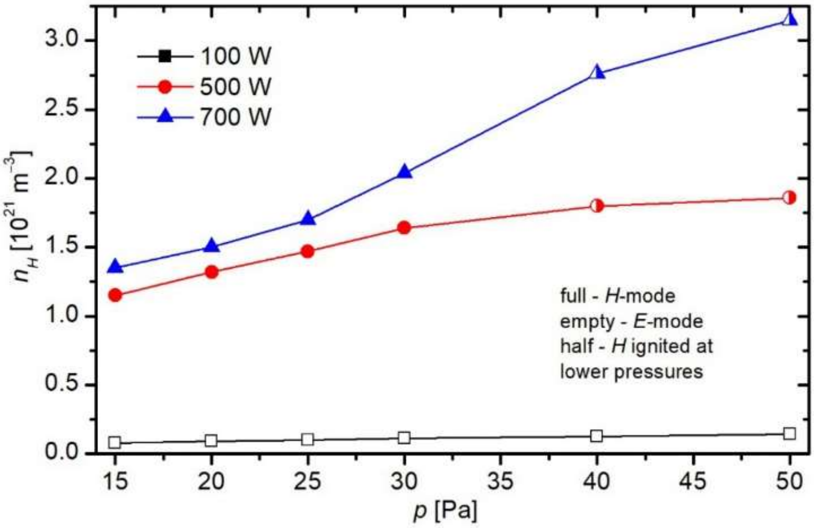

Figure 1.50. The H-atom density at the position of 5 cm away from the coil of Figure 1.43. The parameter is the forward power.

Figure 1.50 reveals that the H-atom density is similar to the O-atom density (Figure 1.39) as long as hydrogen plasma is in the H-mode. In the E-mode, however, it is much lower. The lowest curve in Figure 1.50 indicates the H-atom density of around 10^{20} m^{-3} what is much lower than for oxygen. The dissociation energies are comparable (5.16 eV for oxygen and 4.52 eV for hydrogen molecule [2]), therefore one would expect also comparable atom densities. The reason for poor dissociation of hydrogen molecules 5 cm away from the coil is explained by more efficient surface recombination of H atoms. The borosilicate glass exhibits a moderate value of the recombination coefficient for H atoms (see table 1.3 earlier in this chapter) which reflects in a poor dissociation fraction of hydrogen molecules (below 1%) when plasma is in the E-mode. Such a weak discharge is therefore a useful source of O-atoms, but for H-atoms one should use H-mode plasma to create large densities of H-atoms in a borosilicate discharge tube powered with an RF generator.

There is no “general curve” for hydrogen plasma in the H-mode in Figure 1.50 as observed for oxygen plasma (Figure 1.39) but the H-atom density is much higher at 700 W than at 500 W. Obviously, a rather large power even in the H-mode is necessary to achieve good dissociation of hydrogen molecules 5 cm away from the discharge tube. This effect can be attributed to the fact that luminous hydrogen plasma in the H-mode (Figure 1.45) stretches outside the coil and the expansion increases with increasing discharge power.

The results presented in Figures 1.47 – 1.50 were obtained at fully open flow restrictor. As the flow is decreased at a constant pressure in the discharge tube, the H-atom density at the probe position 5 cm away from the coil decreases rapidly due to more extensive surface recombination and eventually reaches the detection limit of the probe; therefore, it is pointless to present results for hydrogen as are shown for oxygen in Figure 1.41. More interesting are results obtained with a movable probe shown in Figure 1.51. The probe was moved from the distance 2.5 cm away from the coil to 35 cm where the atom density reached the detection limit of the probe. A huge difference between the E- and H-mode are observed in Figure 1.51 at close distances, but already 15 cm away the dissociation fractions are comparable. The dissociation fraction 2.5 cm away from the coil is more than 20% indicating that inside the coil it should approach 100% which is sound with the upper curve of Figure 1.46. When plasma is in the H-mode, the hydrogen molecules are dissociated efficiently, but the dissociation fraction quickly decreases downstream from the luminous plasma. The reason for this undesired effect is extensive surface recombination of H atoms on the borosilicate glass. Unlike for the case of oxygen (Figure 1.42) where fairly linear decrease of atoms was observed along the discharge tube towards the pump, the decrease is extensive for the case of hydrogen. The lower curve in Figure 1.51 might give an impression of a linear dependence, but it is not. To make it clear, the behaviour of hydrogen dissociation fraction versus the distance from the coil is plotted separately in Figure 1.52. In this figure, one can observe qualitatively the same behaviour as the upper curve in Figure 1.51 which is easily explained by the same recombination efficacy except that the initial H-atom density in the H- and E-modes are different. An important observation concerning hydrogen plasma is therefore quick decay of the H-atom density away from the plasma because of the extensive recombination of H atoms on the surface of the borosilicate glass.

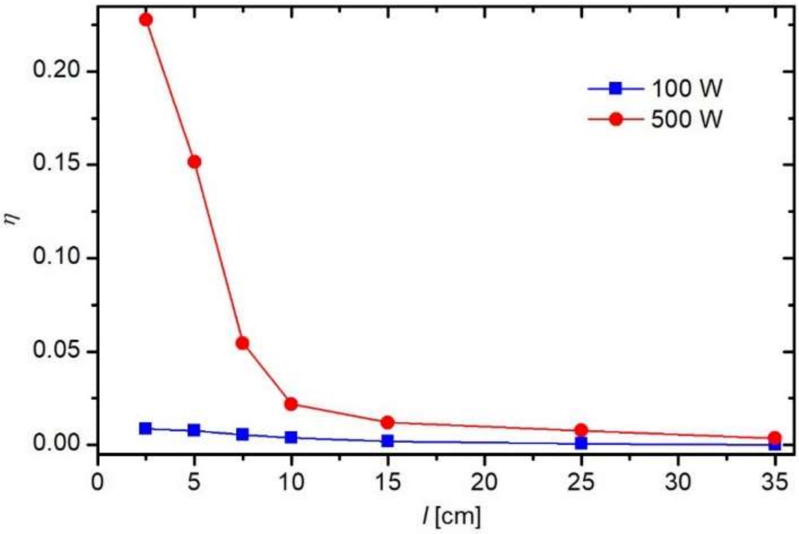

Figure 1.51. The hydrogen dissociation fraction versus the distance from the coil at the pressure of 30 Pa and forward powers 100 (plasma in the E-mode) and 500 W (H-mode).

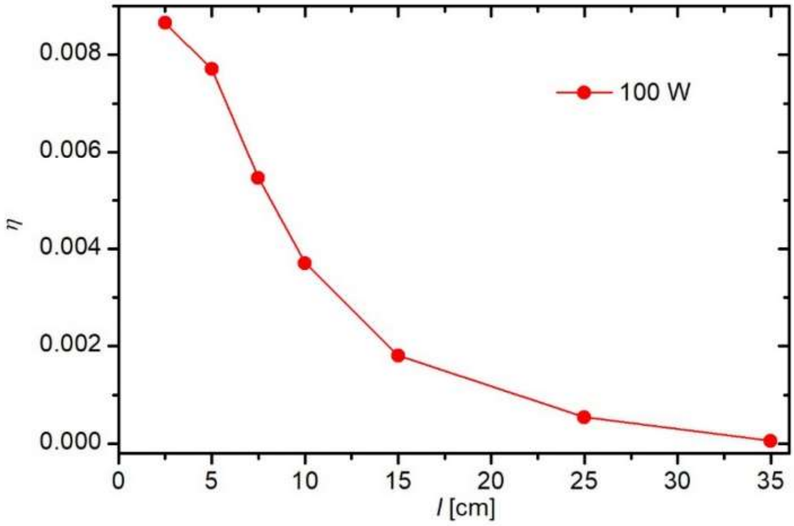

Figure 1.52. The hydrogen dissociation fraction versus the distance from the coil at the forward power of 100 W and the pressure of 30 Pa when plasma is in the E-mode.

1.3.3 Nitrogen atoms

Like O_2 and H_2, nitrogen molecule consists of two atoms, but there are huge differences between these simple molecules. The dissociation energy of N_2 molecules is large at about 9.8 eV, therefore one will immediately conclude that sustaining plasma of a high dissociation fraction is a difficult task. However, nitrogen molecules are easily excited to high-energy vibrational levels which are not quenched at superelastic collisions with other species like H-atoms, therefore the rotational temperature of N_2

molecules is usually measured in thousands of K. There are several metastable states of N_2 molecules that accumulate the potential energy obtained upon plasma conditions.

The density of nitrogen atoms was measured in the experimental system presented in Figure 1.31. The RF coil was placed almost symmetrically into the discharge tube as shown in Figure 1.53. A photo of the discharge tube when plasma is in the E-mode is shown in Figure 1.54. Rather luminous plasma expands from the coil towards the grounded flanges indicating a good capacitive coupling as shown schematically in Figure 1.23. The plasma luminosity decays gradually from the coil towards the flanges what is explained by a gradual decrease of the energy stored in plasma particles (not only electrons) in the region inside the coil.

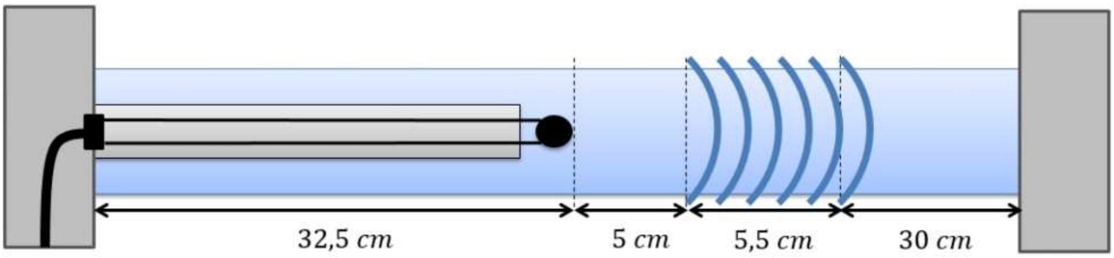

Figure 1.53. Details about the configuration of the discharge tube for measuring the density of N atoms.

A photo of nitrogen plasma in the H-mode is shown in Figure 1.55. Luminous plasma is now concentrated within the coil indicating prevalence of the inductive coupling as shown schematically in Figure 1.24. Much weaker plasma expands also to the grounded flanges because of the weak capacitive coupling. The effect was already explained before for oxygen and hydrogen plasma.

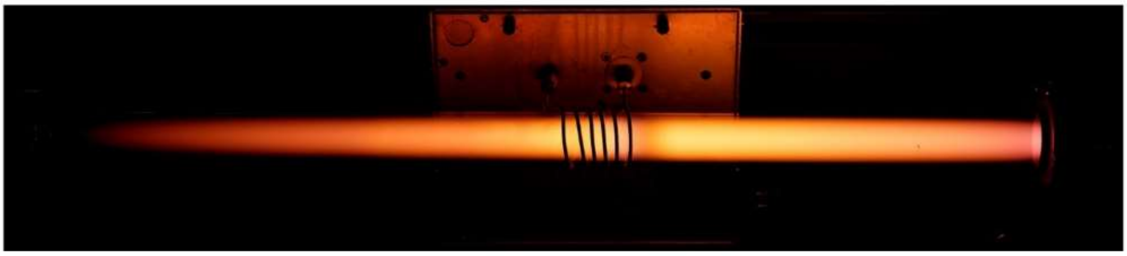

Figure 1.54. A photo of the discharge tube when nitrogen plasma is in the E-mode, i.e. at 40 Pa *and* 200 W *forward power.*

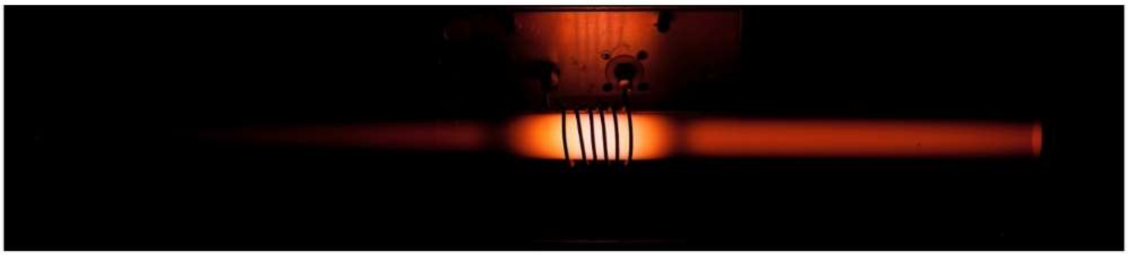

Figure 1.55. A photo of the discharge tube when nitrogen plasma is in the H-mode, i.e. at 40 Pa *and* 500 W *forward power.*

The optical spectra for both the E- and H-mode nitrogen plasma are shown in Figure 1.56. The lower spectrum was acquired in the E-mode, whereas the upper one in the H-mode. The spectra are completely different from those acquired for oxygen and hydrogen plasma: the radiation arising from atoms in nitrogen plasma is negligible to that arising from neutral nitrogen molecules. The spectra shown in Figure 1.56 therefore qualitatively indicate a rather low dissociation fraction of nitrogen molecules, even when the discharge is in the H-mode where the absorbed power is large. The main reason for such a rather poor dissociation is a large dissociation energy and not the extensive surface recombination what will become apparent from measurements presented below.

The nitrogen spectra are rich in molecular transitions of neutral molecules. There are numerous vibrational bands which are broadened by rotational bands indicating that the rotational temperature is elevated, too, not only the vibrational one. In fact, nitrogen plasma at elevated discharge powers is never really cold but it is still highly non-equilibrium.

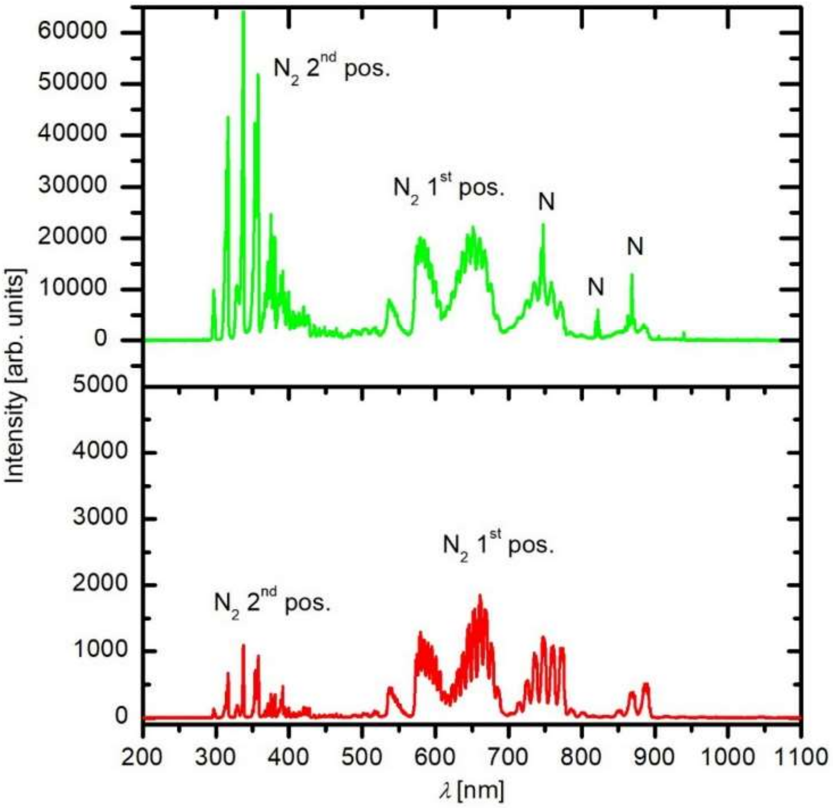

Figure 1.56. The spectra of nitrogen plasma in the E-mode (lower curve) and the H-mode (upper curve).

The density of N atoms was measured with a catalytic probe whose tip was placed 5 cm away from the RF coil in the direction of the gas flow as shown in Figure 1.53. The pressure of nitrogen was set to a desired value and the measurements were performed using the same routine as explained for oxygen or hydrogen. The results are plotted in Figure 1.57. As for other gases, the same results are plotted versus the difference between the forward and reflected powers in Figure 1.58. An important difference as compared to oxygen and hydrogen is the order of magnitude in diagrams of Figures 1.57

and 1.58. For oxygen and hydrogen, it was 10^{21} m^{-3}, whereas for nitrogen it is 10^{20} m^{-3}. The difference is explained by the very high dissociation energy of nitrogen molecule as compared to oxygen or hydrogen. Despite the high vibrational population as well as the presence of molecules excited to metastable states of a high excitation energy (over 6 eV), the dissociation fraction remains low – up to approximately 1% at the position 5 cm from the coil. The forbidden zone (Figure 1.59) is rather similar to that of oxygen (Figure 1.38) and hydrogen (Figure 1.49). Obviously, the forbidden zone is not affected much by the presence of atoms – it is rather correlated with impedances that are in turn correlated with charged particles in gaseous plasma. The N-atom density versus the pressure in the discharge chamber with forward power as the parameter is shown in Figure 1.60.

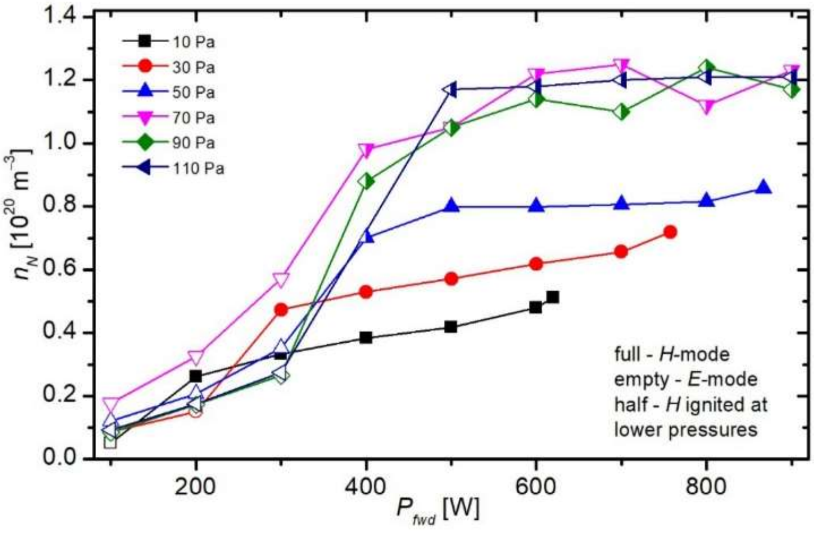

Figure 1.57. The N-atom density versus the forward power of the RF generator at different pressures inside the discharge chamber at the probe position 5 cm left from the coil. The setup as in Figure 1.53.

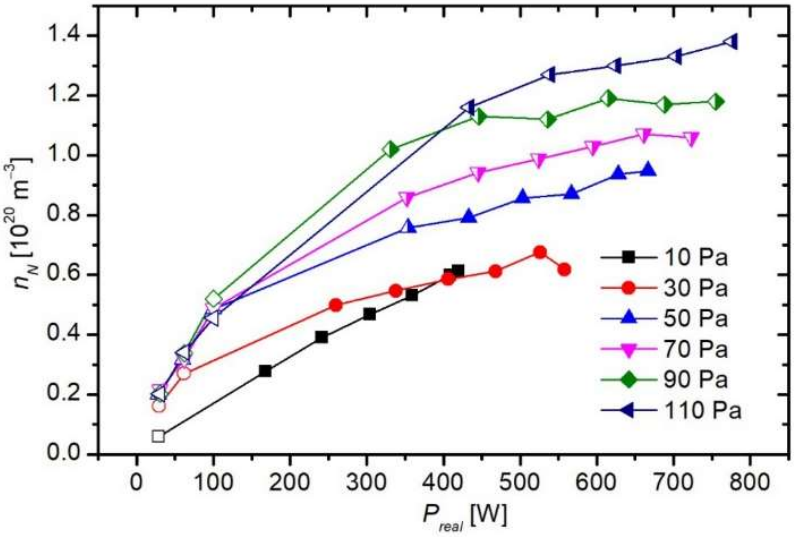

Figure 1.58. The N-atom density versus the difference between the forward and reflected powers at different pressures inside the discharge chamber at the probe position of 5 cm left from the coil. The setup as in Figure 1.53.

The N-atom density was also determined with a movable probe and the results are presented in Figure 1.61. The N-atom density is decreasing slowly with increasing distance from the coil indicating qualitatively similar behaviour as was observed for oxygen (Figure 1.42). Such a slow decrease reveals a reasonably low loss of N-atoms on the way from the powerful plasma inside the coil towards the flange in the direction of the gas flow. As for oxygen, the loss of nitrogen atoms is attributed predominantly to heterogeneous recombination on the surface of the borosilicate glass. The recombination coefficient for N atoms is thus similar to that of O atoms and definitely much smaller than for H atoms, for which a rapid decay of the H-atoms was observed (Figures 1.51 and 1.52). Somehow larger values of the nitrogen dissociation fraction very close to the coil when plasma is in the H-mode is explained with the same arguments as for oxygen plasma: deviations because of thermal effects. Such deviations are not observed as long as nitrogen plasma is in the E-mode when the glass tube remains close to the room temperature.

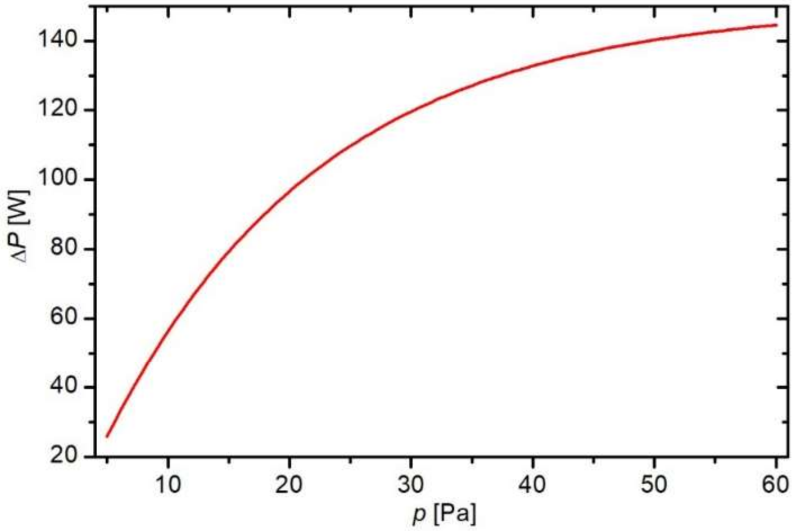

Figure 1.59. The width of the power gap between the E- and H-mode (forbidden zone) versus the nitrogen pressure in the discharge tube of the configuration shown in Figure 1.53.

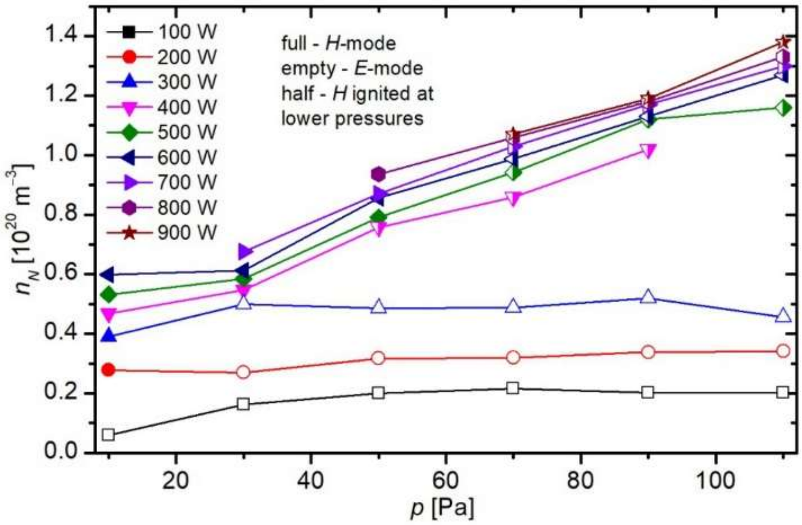

Figure 1.60. The N-atom density at the position of 5 cm left from the coil as shown in Figure 1.53. The parameter is the forward power.

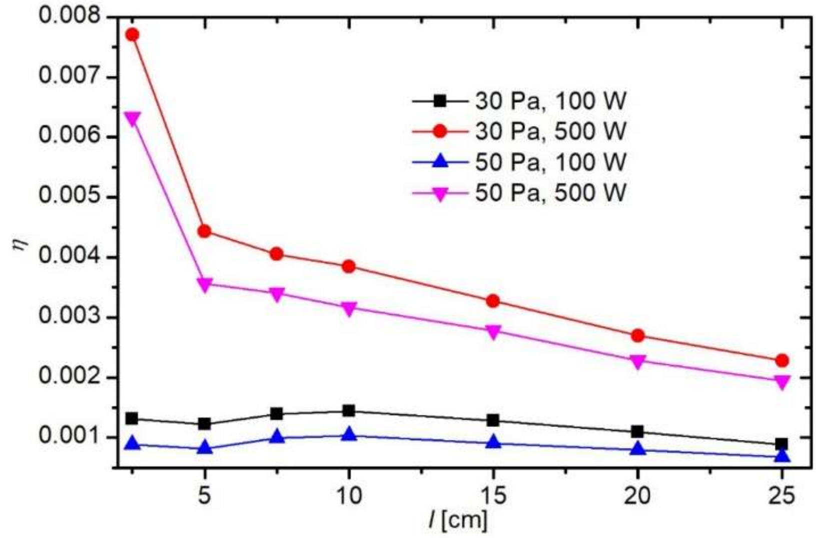

Figure 1.61. The nitrogen dissociation fraction versus the distance from the coil at the pressures of 30 and 50 Pa and forward powers 100 (plasma in the E-mode) and 500 W (H-mode).

1.4 Conclusions

Two-atom molecules such as oxygen, hydrogen and nitrogen are effectively dissociated to parent atoms in gaseous plasma sustained by electrodeless radiofrequency discharges in a dielectric tube. Although a coil connected to the RF generator via a matching network is applied, the predominant coupling of plasma with the RF field is not always inductive. At low power absorbed by gaseous plasma, the predominant coupling is rather capacitive. As the power increases, the transformation from capacitive to inductive coupling occurs instantly and so thus the increase of the atom density. The atom density in a discharge tube in the predominantly inductively coupled power is always larger than in the capacitively coupled power because of a higher electron density in such plasma. The density of atoms away from the inductive discharge decreases with increasing distance, despite the fact, that at least a weak capacitive coupling persists. The decrease is attributed to heterogeneous recombination of atoms to parent molecules on the surface of the borosilicate glass. The recombination efficiency is rather low for O and N atoms and extensive for H atoms. The dissociation fraction inside the intensive plasma in the H-mode is close to 100% for oxygen and hydrogen in the range of pressures up to several 10 Pa, whereas for nitrogen it is below 10%. Gas flow along the borosilicate glass tube affects the density of atoms away from the main discharge. As a general rule, a higher flow will result in better transfer of atoms from the source (i.e. powerful plasma) towards the remote parts of the discharge tube. The effect is particularly severe for hydrogen where the decay length could be of the order of cm. The atom density of the order of 10^{21} m^{-3} is achievable already in the E-mode (predominant capacitive coupling) for oxygen, whereas for nitrogen and hydrogen high atom densities are achievable only in the H-mode (inductive coupling).

References

[1] K. Tichmann, U. von Toussaint, W. Jacob, Determination of the sticking coefficient of energetic hydrocarbon molecules by molecular dynamics, J. Nucl. Mater., 420 (2012) 291-296.

[2] B. deB. Darwent, Bond dissociation energies in simple molecules, U.S. National Bureau of Standards, USA, Washington, 1970.

[3] P. Vašina, V. Kudrle, A. Tálský, P. Botoš, M. Mrázková, M. Meško, Simultaneous measurement of N and O densities in plasma afterglow by means of NO titration, Plasma Sources Sci. Technol., 13 (2004) 668-674.

[4] M. Cacciatore, M. Rutigliano, Dynamics of plasma–surface processes: E–R and L–H atom recombination reactions, Plasma Sources Sci. Technol., 18 (2009) 023002.

[5] S. Markelj, I. Čadež, Production of vibrationally excited hydrogen molecules by atom recombination on Cu and W materials, J. Chem. Phys., 134 (2011) 124707.

[6] A. Vesel, Heterogeneous surface recombination of neutral nitrogen atoms, Mater. Tehnol., 46 (2012) 7-12.

[7] A. Drenik, A. Vesel, A. Kreter, M. Mozetic, Recombination of hydrogen atoms on fine-grain graphite, Appl. Surf. Sci., 257 (2011) 5820-5825.

[8] M. Mozetic, U. Cvelbar, A. Vesel, A. Ricard, D. Babic, I. Poberaj, A diagnostic method for real-time measurements of the density of nitrogen atoms in the postglow of an Ar-N_2 discharge using a catalytic probe, J. Appl. Phys., 97 (2005).

[9] I. Sorli, R. Rocak, Determination of atomic oxygen density with a nickel catalytic probe, J. Vac. Sci. Technol. A, 18 (2000) 338-342.

[10] U. Cvelbar, M. Mozetic, A. Ricard, Characterization of oxygen plasma with a fiber optic catalytic probe and determination of recombination coefficients, IEEE Trans. Plasma Sci., 33 (2005) 834-837.

[11] A. Drenik, The probability of heterogeneous recombination of hydrogen and oxygen atoms on the surfaces of fusion-relevant materials, in, Jozef Stefan International Postgraduate School, Ljubljana, Slovenia, 2009.

[12] R. Zaplotnik, A. Vesel, M. Mozetic, Atomic oxygen and hydrogen loss coefficient on functionalized polyethylene terephthalate, polystyrene, and polytetrafluoroethylene polymers, Plasma Process. Polym., 15 (2018) e1800021.

[13] A. Vesel, M. Mozetic, M. Balat-Pichelin, Reduction of a thin chromium oxide film on Inconel surface upon treatment with hydrogen plasma, Appl. Surf. Sci., 387 (2016) 1140-1146.

[14] A. Vesel, M. Mozetic, M. Balat-Pichelin, Sequential oxidation and reduction of tungsten/tungsten oxide, Thin Solid Films, 591 (2015) 174-181.

[15] M. Mozetic, A. Vesel, J. Kovac, R. Zaplotnik, M. Modic, M. Balat-Pichelin, Formation and reduction of thin oxide films on a stainless steel surface upon subsequent treatments with oxygen and hydrogen plasma, Thin Solid Films, 591 (2015) 186-193.

[16] B.J. Wood, H. Wise, Kinetics of hydrogen atom recombination on surfaces, J. Phys. Chem., 65 (1961) 1976–1983.

[17] M. Mozetic, A. Vesel, S.D. Stoica, S. Vizireanu, G. Dinescu, R. Zaplotnik, Oxygen atom loss coefficient of carbon nanowalls, Appl. Surf. Sci., 333 (2015) 207-213.

[18] M. Balat-Pichelin, J.M. Badie, R. Berjoan, P. Boubert, Recombination coefficient of atomic oxygen on ceramic materials under earth re-entry conditions by optical emission spectroscopy, Chem. Phys., 291 (2003) 181-194.

[19] M. Balat-Pichelin, D. Hernandez, G. Olalde, B. Rivoire, J.F. Robert, Concentrated solar energy as a diagnostic tool to study materials under extreme conditions, J. Sol. Energy Eng., 124 (2002) 215-222.

[20] P. Cauquot, S. Cavadias, J. Amouroux, Heat transfer from oxygen atoms recombination on silicon carbide. Chemical evolution of the material surface, High Temp. Mater. Process., 4 (2000) 365-378.

[21] T. Marshall, Surface recombination of nitrogen atoms upon quartz, J. Chem. Phys., 37 (1962) 2501-2502.

[22] Y.C. Kim, M. Boudart, Recombination of oxygen, nitrogen, and hydrogen atoms on silica: kinetics and mechanism, Langmuir, 7 (1991) 2999-3005.

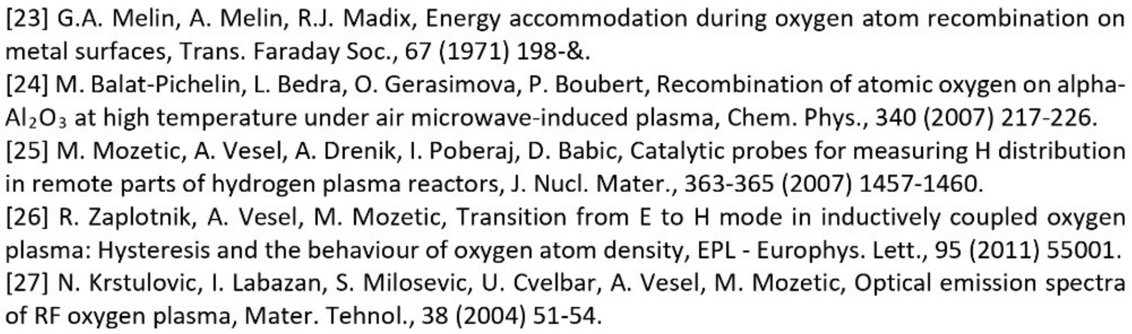

[23] G.A. Melin, A. Melin, R.J. Madix, Energy accommodation during oxygen atom recombination on metal surfaces, Trans. Faraday Soc., 67 (1971) 198-&.
[24] M. Balat-Pichelin, L. Bedra, O. Gerasimova, P. Boubert, Recombination of atomic oxygen on alpha-Al_2O_3 at high temperature under air microwave-induced plasma, Chem. Phys., 340 (2007) 217-226.
[25] M. Mozetic, A. Vesel, A. Drenik, I. Poberaj, D. Babic, Catalytic probes for measuring H distribution in remote parts of hydrogen plasma reactors, J. Nucl. Mater., 363-365 (2007) 1457-1460.
[26] R. Zaplotnik, A. Vesel, M. Mozetic, Transition from E to H mode in inductively coupled oxygen plasma: Hysteresis and the behaviour of oxygen atom density, EPL - Europhys. Lett., 95 (2011) 55001.
[27] N. Krstulovic, I. Labazan, S. Milosevic, U. Cvelbar, A. Vesel, M. Mozetic, Optical emission spectra of RF oxygen plasma, Mater. Tehnol., 38 (2004) 51-54.

1.3 A review of Recombination Coefficients of Neutral Oxygen Atoms for Various Materials

With the proceeding article [56], we limit our scope to oxygen plasma, commonly used in several different applications. For these applications to be successful, we need to understand plasma processes. Understanding the recombination coefficient – especially how it behaves under different experimental conditions – is paramount to any plasma application. However, firstly we need ways to ignite a gaseous discharge. While discharges can occur at different pressure ranges, we limit ourselves to low-pressure discharges where the lifetime of oxygen atoms is longer, as explained in subsection 1.2.

In the proceeding article, brief descriptions are given of various low-pressure discharges, starting with the simplest: direct current (DC) discharges where plasma is ignited by applying sufficient voltage to two electrodes. Such discharges are simpler when compared to other discharges. DC discharges do achieve lower atom densities and are less efficient at ionization than other discharges. This is followed by radio frequency (RF) discharges where the electric field alternates with a high frequency (13.56 MHz is commonly used). There are two types of RF discharges: capacitively coupled plasma (CCP) and inductively coupled plasma (ICP). CCP discharges reliably sustain plasma and are scalable which is why they are commonly used in industrial applications. They achieve lower atom densities than ICP discharges which are very efficient at ionizing gas but the induction can interfere with certain measuring methods. Pulsed RF discharges are mentioned separately for their ability to hinder the plasma heating of the experimental system but the short pulse duration requires sufficiently quick measuring methods to characterize it successfully. Another form of high-frequency discharges is microwave (MW) discharges which can achieve very high atom densities but limit the design of the plasma system, since the dimensions need to adhere to the MW wavelength (around 1 cm). Afterward, two discharges that are more exotic are described: atomic beams and shock tubes. The atomic beam is produced by heating a sample (usually tungsten) to a very high temperature (above 3000 K) and exposing it to molecular oxygen which dissociates into atoms upon impact with the sample. The experimental setup is somewhat simpler when compared to other types of discharges but produces lower atom densities. Lastly, shock tubes are used to reproduce blast waves by generating a shockwave in a special tube with a diaphragm. This allows the study of high-energy and high-pressure discharges but has a limited range of experimental conditions.

Afterward, measurement methods for the determination of the recombination coefficient are described, starting with calorimetry which relies on the heat exchange between a plasma and a detector. Calorimetry is a relatively simple technique, cheap, and reliable. It is, however, a slower method and slightly invasive. On the other hand, optical emission spectroscopy (such as actinometry) is a quicker and non-intrusive method. It is more expensive and limited to the glow region of the plasma, and the interpretation of the data is not always straightforward. Similarly, laser-induced fluorescence (LIF) is another quick and non-intrusive method with even better spatial and temporal resolution held back by the complicated interpretation of data and being quite expensive. In contrast to the more complicated methods is NO titration where gaseous NO is added to the experimental system, and the chemiluminescence of its products with oxygen atoms is observed. NO titration is quick but introduces a foreign gas into the experimental system, which alters the plasma conditions and can poison the experimental system. Another simpler method is the Wrede-Harteck gauge since it only requires a separate chamber and a couple of pressure gauges. Regrettably, the Wrede-Harteck gauge can only operate in the afterglow region of plasma and usually requires a complementary method to corroborate the results. Lastly, two less common methods are described: mass spectrometry and paramagnetic resonance, both being non-intrusive methods for the determination of the recombination coefficient. Both methods are rather complicated and require complementary methods to interpret the results.

Later in the article, the recombination coefficient of different materials is compared, and a few conclusions can be drawn from the cited literature. Most authors agree on which materials are more catalytic for oxygen (have a higher recombination coefficient) and which are more inert (have a lower recombination coefficient). However, studies on the same materials using different measurement methods report different values of the recombination coefficient. While the choice of measurement method has no systematic impact on the recombination coefficient, it seems that most authors agree that higher values of the recombination coefficient were measured in the glow region of plasma as opposed to the afterglow region. This is explained by ion bombardment in the glow region of plasma since ions impacting the surface of a material create new bonding sites for the neutral atoms. In general, the presence of other species in the gas phase seems to affect the recombination coefficient as does the purity of the materials themselves – adsorbed gaseous species, such as metallic oxides alter the recombination coefficient of a material.

Most authors also agree that materials with a higher surface roughness exhibit larger catalytic properties for oxygen atoms, resulting in a higher recombination coefficient. It is evident that the temperature of the material also affects the recombination coefficient, with materials at higher temperatures exhibiting better catalytic properties for oxygen atoms. Not all authors reported this behavior of the recombination coefficient but most agree that the dependence of the recombination coefficient on the surface temperature takes the form of the Arrhenius plot. Another factor affecting the recombination coefficient is the pressure inside the experimental system. Not much agreement was found between different authors. However, some results do point to an inverse proportionality between the pressure inside the experimental system and the recombination coefficient, opening an avenue for further study. Such reviews of the published literature, although not as common [57], are important in understanding heterogeneous surface recombination.

materials MDPI

Review

A Review of Recombination Coefficients of Neutral Oxygen Atoms for Various Materials

Domen Paul [1,2], Miran Mozetic [1], Rok Zaplotnik [1], Gregor Primc [1], Denis Đonlagić [3] and Alenka Vesel [1,*]

[1] Jozef Stefan Institute, Jamova cesta 39, 1000 Ljubljana, Slovenia
[2] Jozef Stefan International Postgraduate School, Jamova cesta 39, 1000 Ljubljana, Slovenia
[3] Faculty of Electrical Engineering and Computer Science, University of Maribor, Koroska cesta 46, 2000 Maribor, Slovenia
* Correspondence: alenka.vesel@guest.arnes.si

Abstract: Relevant data on heterogeneous surface recombination of neutral oxygen atoms available in the scientific literature are reviewed and discussed for various materials. The coefficients are determined by placing the samples either in non-equilibrium oxygen plasma or its afterglow. The experimental methods used to determine the coefficients are examined and categorized into calorimetry, actinometry, NO titration, laser-induced fluorescence, and various other methods and their combinations. Some numerical models for recombination coefficient determination are also examined. Correlations are drawn between the experimental parameters and the reported coefficients. Different materials are examined and categorized according to reported recombination coefficients into catalytic, semi-catalytic, and inert materials. Measurements from the literature of the recombination coefficients for some materials are compiled and compared, along with the possible system pressure and material surface temperature dependence of the materials' recombination coefficient. A large scattering of results reported by different authors is discussed, and possible explanations are provided.

Keywords: heterogeneous surface recombination; recombination coefficient; surface catalicity; catalytic efficiency; atom loss coefficient; oxygen; neutral atoms; plasma

check for updates

Citation: Paul, D.; Mozetic, M.; Zaplotnik, R.; Primc, G.; Donlagić, D.; Vesel, A. A Review of Recombination Coefficients of Neutral Oxygen Atoms for Various Materials. *Materials* **2023**, *16*, 1774. https://doi.org/10.3390/ma16051774

Academic Editors: Carles Corbella Roca and Norbert Robert Radek

Received: 9 January 2023
Revised: 13 February 2023
Accepted: 16 February 2023
Published: 21 February 2023

1. Introduction

For several decades, oxygen plasma has seen widespread use in various industrial applications, ranging from advances in the food industry [1–3] to uses in the bustling semiconductor industry [4–6], novel approaches in medicine [7–9], and various other applications [10]. The use of plasma is even more prevalent in many fields of research, from nuclear fusion [11,12], studies on cell growth [13], and various advances in surface science [14], such as surface modification [15,16], surface functionalization [17], sterilization [18], etc.

Such widespread use of plasma demands research into the characterization of the plasma itself. Many researchers have characterized different properties of different plasmas sustained by various discharges, from neutral atom density [19], ion density [20], electron density [21], and energies of plasma particles [22], to the plasma emission spectra in the optical [23], infrared [24], and ultraviolet ranges [25]. Such studies are very important in understanding plasma discharges, but the interactions of plasma with different materials must not be overlooked to devise any applications from such studies.

Interactions of plasma with the surface of a material are a complex topic, with many different plasma particles interacting with the surface in different ways. On the one hand, plasma discharges emit radiation in a broad range from infrared (IR) to vacuum ultraviolet (VUV), which can strongly interact with certain surfaces and has been studied in ref. [26]. The plasma particles, such as positive and negative ions, free electrons, excited neutral molecules, and radicals, can also interact with the surface. High-energy ions can have the most drastic effects on a surface, from etching [27] to ion implantation [28,29], while free electrons have hardly any effects on a surface and are more commonly utilized in different measurement methods [30]. Setting aside charged particles, we will focus on the neutral particles. Among those are rotationally or vibrationally excited molecules [31] and, more important for this paper, molecular radicals. Since oxygen plasmas are most often used, our attention will be focused on the interactions of oxygen plasmas with surfaces, in particular, on the interaction of neutral oxygen atoms. To be specific, the major reactants in many oxygen plasmas suitable for tailoring the surface properties of solid materials are, in many cases, neutral oxygen atoms in the ground state [32].

Neutral oxygen atoms are mainly created in the plasma discharge, where parent oxygen molecules are dissociated at a collision with an energetic electron. In some cases, neutral atoms can also be created from molecules dissociating on the material surface via heterogeneous surface atomization [33]. Our interest is in the reverse process, the heterogeneous surface recombination of neutral oxygen atoms.

There are two widely accepted mechanisms describing neutral atom recombination. The first is the Langmuir–Hinshelwood mechanism [33], which describes the recombination of two neutral oxygen adatoms ($\mathrm{O}(s)$) after they adsorb to the surface. Once they diffuse on the surface (S):

$$S + \mathrm{O}(s) + \mathrm{O}(s) \rightarrow \mathrm{O}_2 + S. \tag{1}$$

We obtain the resulting oxygen molecule (O_2), which can leave the surface through desorption [33]. Such molecules are in thermal equilibrium with the surface, and their energy depends on the temperature of the surface. The second mechanism is the Eley–Rideal mechanism [33], which describes an adatom at the surface recombining with an incident atom from the gas ($\mathrm{O}(g)$):

$$S + \mathrm{O}(s) + \mathrm{O}(g) \rightarrow \mathrm{O}_2 + S. \tag{2}$$

The resulting molecule is not necessarily in thermal equilibrium with the surface due to the molecule receiving energy from the incident atom [33].

Regardless of the mechanism of neutral atom recombination, we can define the recombination coefficient (γ) of a certain surface as the ratio between the flux of incident neutral atoms (j_{atoms}) and the number of recombined molecules leaving the surface in a unit of time ($j_{molecules}$):

$$\gamma = \frac{2\, j_{molecules}}{j_{atoms}}, \tag{3}$$

with factor 2 to counterbalance the fact that two atoms create a single molecule. Since not every atom which reaches the surface recombines with another atom into a molecule, and on the opposite side, there is always an (even infinitesimally) small fraction of atoms that do recombine at the surface, the recombination coefficient has values between 0 and 1.

Often, the term «recombination coefficient» is used interchangeably with the terms catalytic efficiency, surface catalicity, and sometimes with the term atom loss coefficient. The latter also takes into account any other losses of neutral atoms at the surface, including physisorption, chemisorption, implantation, etc. [33]. While it is perfectly valid to consider such processes, we will be forgoing that. The first reason is that surface recombination is usually the prevalent process in plasma–surface interactions [33,34]. The second reason is that we are dealing with oxygen plasma, where most samples have had their surface already exposed to oxygen prior to any measurements. Thus, an oxide layer already appeared prior to exposure to oxygen plasma, minimizing any atom losses due to oxidation-related processes. Therefore, all further mentioning of recombination coefficients will not distinguish between actual surface recombination and combined surface atom losses.

This paper will examine scientific articles by different authors and their methods for determining the recombination coefficients of oxygen atoms on surfaces of various solid materials. Firstly, we will briefly go through various plasma systems and gaseous discharges, as well as the choice of parameters for said discharges, focusing mainly on the total pressure of gas in the experimental system and the surface temperature of the examined materials. We will also compare the resulting recombination coefficients achieved in similar experimental setups and explain any discrepancies. Along with direct current (DC), radiofrequency (RF), and microwave (MW) discharges, some theoretical models for determining the recombination coefficient will be examined.

Secondly, we will describe different measurement techniques for determining the recombination coefficient, such as the widely used actinometry, two-photon absorption laser-induced fluorescence (TALIF), calorimetry, etc. We will categorize the techniques for easier comparison of determined recombination coefficients.

Lastly, we will compare the recombination coefficients of different materials and divide the materials into three groups: catalytic, semi-catalytic, and inert materials, depending on the materials' recombination coefficient.

The motivation for such a review article is to provide readers easier access to somewhat comprehensive literature on recombination coefficients of neutral oxygen atoms on the surfaces of different materials, which is important information that needs to be known either when designing experiments or when interpreting and discussing results. Additionally, since recombination coefficients may depend on system pressure and surface temperature, we pay special attention to reported pressures and temperatures and their effects on the recombination coefficient. Less comprehensive lists have been compiled in other review articles, namely for neutral nitrogen atoms [35], modeling nitrogen–oxygen hybrid systems [36], general atom recombinations on surfaces [37], recombination coefficients determined via the spinning wall method [38], a study of atom recombinations on high-temperature materials [39], and a study of the pressure dependency of the recombination coefficient in a shock tube system [40].

2. Low-Pressure Discharges as Sources of Oxygen Atoms

The type of gaseous discharge used for ignition and sustaining gaseous plasma can alter the interaction of plasma with a surface due to varying densities and energies of plasma particles. Therefore, different low-pressure discharges will be presented in this section, starting with the more common and ending with more exotic and less frequently used discharges, as well as theoretical models. Non-equilibrium gaseous plasma can also be sustained at atmospheric pressure, but the loss of atoms at elevated pressures is predominantly in the gas phase at three-body collisions, so atmospheric pressure plasmas are not feasible for studying the surface recombination phenomenon.

2.1. DC Discharges

The simplest discharge is a DC discharge, schematically shown in Figure 1. A DC plasma discharge can be created by applying a sufficient voltage of several hundred volts to a volume of a gas at low pressure (e.g., below 7000 Pa). As a primary electron is released from the cathode and accelerated by the applied electric field, it can ionize atoms in the volume of gas, which also produces electrons, which, in turn, become accelerated [41]. Thus, a sustainable plasma discharge is created.

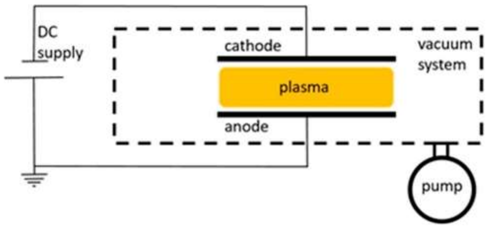

Figure 1. Schematic of a typical DC plasma system.

In the proceeding articles, different types of DC discharges have been used, from regular DC glow discharges used by Lopaev et al. [42,43] to the pulsed DC discharges used by Cartry et al. [44,45] and to variations of an arc discharge used in NASA's arc jet facilities [46]. The DC glow discharges operate in the normal glow mode with lower applied voltages. In such a mode, the surface area of the cathode, covered in luminous plasma, is proportional to the current [41]. In a pulsed DC discharge, the same glow discharge is continuously switched on and off. With the correct timing of these pulses, the neutral atoms remain in the system in between the pulses, while other species (ions, free electrons) are mostly eliminated [47]. This provides plasma with a higher concentration of neutral atoms with respect to the time-averaged concentrations of charged particles compared to regular DC glow discharges. As for arc jet discharges, they are a more exotic approach to a DC discharge, where the high discharge current creates an unstable discharge with arcs forming between electrodes [41].

2.2. RF Discharges

RF discharges are the most prevalent both in academic studies and in industry. During the process of collecting data for this article, around two-thirds of all data found was produced in an RF discharge system. Unlike DC discharges, the current (and the electric field) alternates in an RF discharge. The frequencies of such discharges are usually set at 13.56 MHz. The RF voltage generates an electric field that oscillates, thus accelerating electrons. Like in the DC discharge, this results in electrons with sufficient energy triggering ionizations. Among some of the advantages of using an RF discharge over a DC discharge is a more efficient ionization, resulting in a plasma with a denser plasma particle population [48].

Three different RF discharges can be distinguished: capacitively coupled plasma (CCP), inductively coupled plasma (ICP), and pulsed RF discharge [34]. In CCP discharge, the plasma is capacitively coupled to an RF generator. A sheath is formed between the electrodes and bulk plasma, and it oscillates with the same frequency, albeit not in phase with the electrodes [41]. Unlike its widespread use in various industries, the use of CCP discharges was rare in the reviewed literature concerning recombination coefficient determination. Some combined use with ICP discharges was reported by Mozetič et al. [49] and Gomez et al. [50], but the exclusive use of CCP discharges seems to be limited to Tsutsumi et al. [51], Tserepi et al. [52], Shibata et al. [53], and Rakhimova et al. [54].

The amount of experimental results using CCP discharges is overshadowed by the use of ICP discharges, which represent around half of all results presented in this paper. The ICP discharge is created by inductive coupling between an RF transmitter and the ionized gas in the system. The transmitter can be a simple antenna or a coil around the plasma reactor, as shown in the example in Figure 2. The electrons receive their energy via the oscillating electromagnetic field. The advantage of an ICP discharge over a CCP discharge is the ability to achieve higher plasma densities [41]. ICP discharges were used in experiments determining catalytic coefficients in seminal works by Melin and Madix [55], Graves and Linnett [56], Dickens and Sutcliffe [57], and Linnet and Marsden [58]. ICP discharges remain popular to this day, seeing use in works by Mozetič et al. [59], Wickramanayaka et al. [60], Stafford et al. [61], and many others.

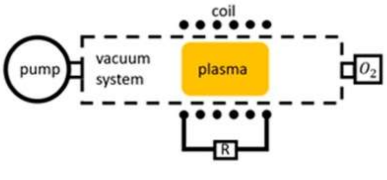

Figure 2. Schematic of a typical inductively coupled radiofrequency plasma discharge.

RF discharges may also operate in the pulsed mode. Here, RF power is applied in pulses that may vary in length and frequency. One of the compelling reasons to choose a pulsed RF discharge over a static one is to avoid heating the plasma system with bulk plasma, which can negatively impact the measurements. Authors such as Matsushita et al. [62], Myerson [63,64], and Guyon et al. [65,66] have successfully used a pulsed RF discharge to determine the recombination coefficient of various materials.

2.3. MW Discharges

Similarly to RF discharges, MW discharges are ignited and sustained by high-frequency oscillating electromagnetic fields. A standard MW frequency most commonly used in MW discharges is 2.45 GHz, which provides wavelengths comparable to experimental-size plasma reactor dimensions [67]. Because of such high frequencies, practically all the energy is transferred to electrons, triggering ionizations [68]. The same is true for other high-frequency discharges (namely RF). Generally, MW discharges produce high densities of radicals, such as neutral oxygen atoms, compared to other types of discharges. There are different types of MW discharges based on the source of microwaves, such as cyclotron or magnetron (Figure 3).

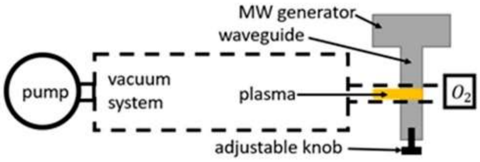

Figure 3. Schematic of a magnetron MW plasma system.

Most authors experimenting with MW discharge systems did not specify the type of discharge used. A few exceptions include Booth and Sadeghi [69], who used a cyclotron to determine the recombination coefficient of stainless steel. A magnetron was used by Greaves and Linnett [70] in their study of oxygen atom recombination on quartz, as well as by Kaufman when studying quartz [71] and Pyrex [72].

Along with the source of microwaves, discharge requires something connecting the source with the reactor. Waveguides and MW cavities are most commonly used. The MW cavity, which acts as a special resonance chamber to strengthen the electromagnetic field, was used by Hacker et al. [73] in their studies of platinum and quartz as well as by Brake et al. [74,75] in their study of recombination on quartz glass. Zaplotnik et al. [76] reported using a type of MW cavity called a surfatron when studying the recombination coefficients of different polymers. Cartry et al. [77] also reported using a surfatron in their studies of quartz glass. A plasmatron, which is another type of MW cavity, was used by Kolesnikov [78] when studying quartz glass. The use of a waveguide was reported by Balat-Pichelin et al. [79–84] in providing a great set of data for a variety of materials. While the rest of the authors did not provide the full details of their method, their studies of recombination coefficients for various materials are nevertheless of great importance. We will examine two additional sources of atoms useful for studying heterogeneous surface recombination.

2.4. Other Discharges

In addition to the most common discharges presented above, other setups were also used to investigate recombination coefficients, such as the atomic beam used by Sjolander [85]. In this work, a heated tungsten ribbon (at approximately 3000 K) is exposed to molecular oxygen, which dissociates into atoms. Due to high surface temperature, desorption of atomic oxygen is possible, which is then drifted towards a metal sample (Figure 4).

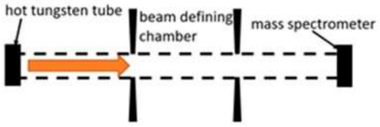

Figure 4. Schematic of the atomic beam plasma system, which was exclusively used in conjunction with mass spectrometry in the referenced works.

Another type of discharge is the shock tube, used by Yang et al. [40], Park [86], and Goulard [87]. This type of discharge is used to replicate blast waves, which occur during violent explosions. In essence, a shockwave is generated on one side of the tube by the driver gas at a higher pressure, which, upon coming into contact with and rupturing a membrane, pushes the lower-pressure driven gas to the other side of the said membrane (Figure 5). Due to the high energy of the shockwave, plasma may be formed.

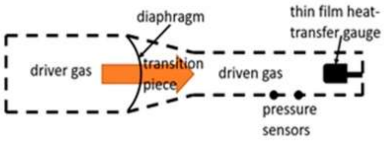

Figure 5. Schematic of a typical shock tube plasma system.

2.5. Models

Some researchers used simulations instead of experiments to determine the recombination coefficient (γ) of different materials. While their models vary in both approach and scope, some common denominators may be taken from their research. What is most interesting is that for a given material, the proposed surface temperature dependence of the recombination coefficient seems to take the form of:

$$\gamma\ (T_s) = Ae^{-B/T_s}, \tag{4}$$

where A and B are parameters which are usually determined experimentally [36,37,55,57,88,89]. Of course, this is a simplification, as the measured plots of γ are usually more complex and can not be solved analytically. Nevertheless, Equation (4) provides us an interesting and testable formula. Pressure dependence of γ is less clear, with some researchers proposing a formula similar to Equation (4):

$$(p) = Ce^{D/p}, \tag{5}$$

where C and D are again experimentally determined parameters [88,90]. The models used by various researchers will be explained in the last section of the next chapter.

To summarize, a reader must be aware that the use of different discharges presented in this chapter and different methods for the determination of recombination coefficients, which will be presented in the next chapter, may have a strong influence on the reported values. In Figure 6, we show a comparison of average values of γ for oxygen recombination on various materials determined in different plasma systems [37–40,42–47,50–66,69–130]. We can observe that, in general, larger values were reported in RF plasmas (especially ICP), which are incidentally also the most commonly used plasma systems. In Table 1, we provide a brief overview of the advantages and disadvantages of various types of plasma discharges.

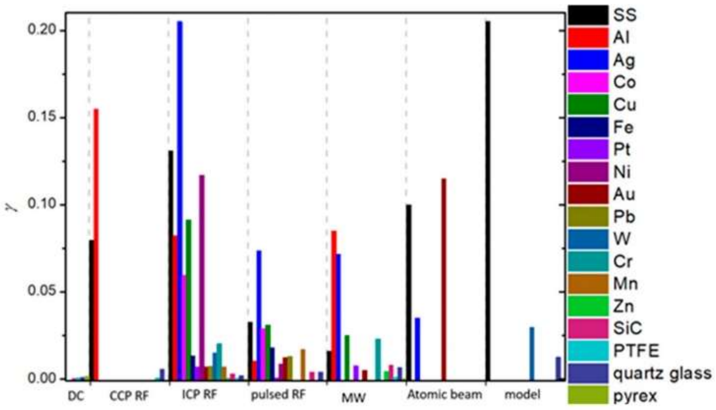

Figure 6. Comparison of average values of γ determined using different experimental and theoretical approaches.

Table 1. Advantages and disadvantages of various types of gaseous discharges.

Plasma Source	Advantages	Disadvantages
DC	Simpler setup, lower applied voltages required	Lower atom densities, less efficient ionization
CCP RF	Reliable in sustaining plasma, scalable (widely used in industry)	Lower atom densities
ICP RF	Efficient ionization, high atom density	Induction can interfere with certain measuring methods
Pulsed RF	Less heating of plasma system	Requires quick measuring methods
MW	Efficient ionization, high atom density	Design of plasma reactor must adhere to MW wavelength
Atomic beam	Simpler setup	Source requires high temperatures, comparably lower atom densities
Shock tube	Enables study of high-energy, high-pressure discharges	Limited range of experimental conditions

3. Methods for γ Determination

Different methods for the determination of recombination coefficients were used by various researchers and will be presented below. These methods can be divided into several categories: calorimetry, emission spectroscopy, actinometry, NO titration, induced fluorescence, Wrede–Harteck gauges, and other experimental methods and modeling. Some of these methods were also used in conjunction with other methods.

The samples used for measuring the surface recombination coefficients were either placed into the oxygen (or oxygen-containing) plasma or in the afterglow. In the case a sample is facing plasma, its surface will charge negatively against the plasma because the mobility of plasma electrons is much larger than the mobility of ions. The negative surface potential will form a sheath between the negatively biased sample and the plasma. The sheath voltage will assure for equal flows of negatively and positively charged particles and, thus, stable conditions. Obviously, the voltage depends on the electron temperature in gaseous plasma. The positively charged ions entering the sheath are accelerated toward the sample and bombard the surface. The ions thus supply kinetic energy, which is shared with the surface atoms upon impinging. The kinetic energy in most plasmas reviewed above will be roughly 10 eV in the case of collision-less sheaths and below this value in cases where the sheath thickness is not much smaller than the mean free path. The energy supplied to surface atoms by surface bombardment with positively charged ions may influence the recombination coefficient.

3.1. Calorimetry

One of the most often used methods is calorimetry which is based on measurements of heat exchange. These measurements can be performed by catalytic probes (thermocouple, fiber optic), other methods utilizing thermal resistivity (thin film resistance thermometers, thin film heat-transfer gauges), pyrometry, and other calorimetric detectors. In all cases, an O-atom-sensitive material is introduced into the plasma reactor, and the change in temperature due to the surface recombination of O-atoms is measured. In Figure 7, we show an example of using a catalytic probe for the determination of the recombination coefficient because of heat dissipation on the surface of the probe during the recombination of O atoms.

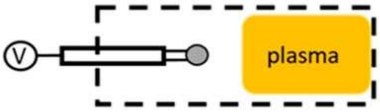

Figure 7. Schematic of a typical calorimetric probe for measuring the O-atom density via the heat dissipated on the surface of the probe, which enables the determination of the recombination coefficient.

In a study by Mozetič and Zalar [59], a thermocouple probe was used to measure neutral atom density and later replaced by a thermocouple probe attached to the investigated material, which was stainless steel. Comparison of measured data between the two probes helped determine the recombination coefficient of stainless steel as 0.07 in the regime of 10–100 Pa and 400–700 K. In a similar study by Mozetič and Cvelbar [92], recombination coefficients of several metals were determined using a thermocouple probe. In addition, discharge was monitored with a Langmuir probe for electron energy and density detection and an optical spectrometer. The latter was used in NO titration to confirm the readings of the catalytic probes. Another study with a similar experimental procedure was performed for a niobium surface by Mozetič et al. [91], with the result $\gamma = 0.09$, constant for pressures between 100 and 400 Pa and temperatures between 420 and 620 K. Yet, another study by Mozetič et al. [49] brought results for carbon nanowalls, a carbon-based nanomaterial best described as shredded ribbons of graphene growing perpendicular to a surface. This exotic material exhibited an especially high recombination coefficient with $\gamma = 0.59$ at 50 Pa and 300 K.

In a paper by Zaplotnik et al. [76], recombination coefficients for polyethylene terephthalate (PET), polystyrene (PS), and polytetrafluoroethylene (PTFE) were determined with the help of two catalytic probes. One probe had a catalytic tip, while the other had a tip made of the studied polymer, and the responses of both probes were compared in order to determine the recombination coefficient. A similar twin catalytic probe approach was used by Cvelbar et al. [93] to determine the recombination coefficient of various metals, with a minor difference in the catalytic probes, because the heat dissipated on a surface due to recombination of O-atoms was monitored through an optical fiber instead of a thermocouple. The measured densities of neutral atoms were confirmed with NO titration, while the energy and density of electrons were measured with a Langmuir probe.

A method used often in conjunction with calorimetry is the side-arm method [57,94–96,103,104]. In such a method, atoms are created in the discharge chamber and then let through a small orifice to a tube-shaped side-arm chamber. The gas diffuses along the length of the tube, with atom losses occurring at the walls of the side-arm. In a study by Drenik et al. [94], such a side-arm method was used, with the walls of the side-arm covered in amorphous carbon. The decrease in neutral atom density along the arm was measured with a fiber optic catalytic probe, and both hydrogen and oxygen recombination was determined. Another work by Drenik et al. [95] used the same approach for the oxygen atoms on aluminum surfaces, both clean and with a layer of deposited carbon. In Drenik's thesis [96], this same approach was used to determine γ for graphite and different deposits of amorphous carbon. The measured γ of amorphous carbon deposits was not very high (at around 0.001), but was more than 10 times higher for polished graphite at 0.05. However, this is still nowhere near the reported $\gamma = 0.59$ of nanostructured carbon reported by Mozetič et al. [49]. Comparing γ of different forms of carbon hints at the impact surface morphology can have on surface recombination.

Linnett and Marsden [58] also used a catalytic probe to measure the drop in neutral atom density inside a side-arm with deposits of various salts and oxides. They found that the γ of the studied materials increased drastically with an increase in surface temperature, with some materials exhibiting a rise in several orders of magnitude. For example, the γ of KCl rose from 0.00008 to 0.01 in the temperature range from 300 to 700 K. Very similar behavior was noticed for LiCl, but not for oxides such as PbO, MoO_3, quartz, and Pyrex, where an increase in γ in respect to surface temperature was not as drastic.

The same method, albeit modified, was used by Greaves and Linnett [56] when measuring γ for several groups of materials: metals, non-metals, oxides, and halides. It was found that metals exhibited the highest γ, with Ag and Cu showing the highest γ at $\gamma_{Ag} = 0.24$ and $\gamma_{Cu} = 0.17$. This study also confirmed the formation of an oxide layer on metals during exposure to oxygen, which eventually stabilizes the recombination process. In a paper by Goulard [87], the results of Linnett and Marsden [58] were compared to a theoretical model for surface recombination and to results obtained in a shock tube, where the neutral O-atom density was measured with a thin copper film heat-transfer gauge. The $\gamma_{Cu} = 0.4$ reported is somewhat high, which might be due to a different type of discharge used.

Elias et al. [97] determined the recombination coefficient of Pyrex ($\gamma_{pyrex} = 0.000077$) with a movable detector, which consisted of a platinum wire coated in a catalytic material. An electrical current was applied through the platinum wire, which kept the detector at a constant temperature, measured by its resistance. Upon recombination of atoms on the surface of the detector, the current was lowered so that the resistance (and temperature) of the detector remained the same. The energy dissipated due to surface recombination was calculated from the drop of the electrical current needed to sustain a constant temperature.

Another use of catalytic probes in the side-arm was reported by Dickens and Sutcliffe [57], who measured γ for various metal oxides and quartz. In their findings, they noticed discontinuity in the temperature dependence of γ for several materials, as well as a general trend, where γ was highest for *p*-type oxides, lower for *n*-type oxides, and lowest for insulating oxides. They also found that for certain oxide films, conductivity rose with exposure to atomic oxygen. However, not all oxides exhibited such behavior.

Hartunian et al. [98] also used a catalytic probe having a fast response time (less than 1 µs). This allowed instantaneous measurements of changes in surface temperature. The probe had a thin platinum resistance thermometer in the shape of a sphere or cylinder at the tip, which was coated in a layer of silicon oxide, a dielectric. This dielectric layer was, in turn, coated with a catalytic film. γ for quartz, Pyrex, silver oxide, nickel oxide, aluminum oxide, and spinel ($MgAl_2O_3$) was measured in this setup at room temperature, and pressures ranging from 7 to 15 Pa were noted. Spinel and silver oxides were proved to be the most efficient catalytic materials.

A very similar approach was used by Myerson for measuring the γ of gold, platinum, palladium, and TiO_2 [64] and for measuring the γ of copper, iron, nickel, aluminium, gold, and silver [63]. Measurements were carried out in the pressure range from 400 to 1300 Pa, with the surface temperature of materials kept around room temperature. While most noble metals were not found to be good catalysts for oxygen recombination, silver was again the material with the highest γ.

Another use of calorimetry was presented by May and Linnett [99] in conjunction with Wrede–Harteck gauges and the effusion method, where gaseous plasma is effused through a small orifice into another chamber, with a detector placed immediately behind said orifice. Through surface recombination, atoms heat up the detector, and the change in temperature is detected via thermal resistivity. Again, silver proved to be the most catalytic material, followed by copper and then by chromium and gold. However, those measurements were carried out in a limited range of surface temperatures (300–400 K) and at pressures of around 2 Pa.

Measurements of reaction-cured glass (RCG), an exotic material used as a coating for spacecraft reentering the planetary atmosphere, were performed by Scott [100]. Samples of RCG were attached to water-cooled holders equipped with platinum thermocouples. A referential nickel thermocouple probe was installed to measure the neutral atom density in the vicinity. It was shown that with higher surface temperatures (around 1500 K), the γ of RCG increased by a factor of 3 compared to room temperature (from 0.008 to 0.023).

Another use of a moving platinum thermocouple probe to measure the neutral atom density of gas diffusing along a tube was employed by Kim and Boudart [101] when determining γ for oxygen, hydrogen, and nitrogen atoms on quartz glass. The quartz walls were kept at the desired temperature by being submerged in a constant temperature bath. Therefore, a wide range of temperatures of quartz was achievable, from 200 to 1200 K. The γ of quartz glass increased at higher temperatures for all three gases.

Gordiets et al. [102] used thermocouple probes in combination with electrostatic probes and NO actinometry to measure the γ of Pyrex for oxygen, nitrogen, and their mixtures. While NO actinometry was used to measure neutral atom density and electrostatic probes to measure electron density, the γ of Pyrex was determined by the heat transferred from plasma to the walls. An interesting observation was reported: γ for both oxygen and nitrogen changed when the two gases were mixed and increased with an increasing percentage of oxygen in the gas mixture.

The popularity of using a catalytic probe in a side-arm as a method of determining γ is again demonstrated by Stewart [103,104]. In his work, he studied thermal protection materials (Pyrex, SiC, and other, more exotic silica-based materials, as well as carbon-based coatings) as candidates for spacecraft shielding during planetary reentry. Stewart also employed a heavy-duty electric furnace to heat the materials to very high temperatures, essentially reaching the upper limit of the materials (in some cases, approximately 2000 K). Interestingly, most of those materials exhibited an increase in γ with temperature up to a certain point. At higher temperatures, γ seemed to decrease with increasing temperatures. Additionally, noteworthy is the use of laser-induced fluorescence to corroborate the values of neutral oxygen atom density.

Bykova et al. [105] used a continuous-flow stationary calorimeter while testing the γ of different heat-shield candidate materials at high temperatures. Coated molybdenum, quartz glass, and Pyrex were attached to thermocouple probes, and the temperature response of the probes was measured in oxygen plasma. With the help of a mathematical model, γ was determined. Quartz glass catalyticity was increased with temperature, while Pyrex exhibited a decline in catalyticity with surface temperature. Molybdenum was not studied beyond room temperature, where $\gamma_{Mo} = 0.0048$.

Another comprehensive study of γ for various metals (copper, silver, cobalt, zinc, nickel, gold, and steel) was reported by Cauquot et al. [106]. In this study, samples of metals were placed in stainless-steel heater cartridges and kept at room temperature and a pressure of 300 Pa. The temperature was measured with a platinum resistance temperature detector probe, and the neutral atom density was measured by NO titration. Copper and silver were again determined to be the materials with the highest γ for the recombination of oxygen atoms.

In an experiment by Šorli and Ročak [107], γ was determined for nickel with the help of two catalytic probes, the first having a disk-shaped nickel tip, and the second having a tube-shaped nickel catalyst. The tube was placed next to a narrow glass tube so that all (or at least the vast majority of) the atoms passing through it recombined. Afterward, the tube was removed, and the neutral atom density was measured with the second probe. Comparing the response of both probes yielded a constant $\gamma_{Ni} = 0.27$ of nickel for a range of temperatures from 500 to 1100 K and the pressure ranging from 10 to 100 Pa. Along with that, the γ for Pyrex was determined as $\gamma_{pyrex} = 0.00019$ at room temperatures and in the same pressure range as before.

Zheludkevich et al. [108] studied the oxidation of silver and silver oxide and determined for both that $\gamma_{Ag} = \gamma_{Ag_2O} = 0.1$ at extremely low pressures (about 10^{-7}Pa) and in the temperature range 373–673 K. This was determined by measuring the time dependence of electrical resistance of silver filaments. Experiments were reproduced three times without major discrepancies. Researchers noted that at temperatures higher than 673 K, the oxide layer became unstable, yielding unreliable results.

Kolodziej and Stewart employed both thin film calorimeters and thermal capacitance (slug) calorimeters to measure heat fluxes in their system. The walls of the experimental system were made of Pyrex, and their temperature was also measured by IR pyrometry. All the acquired data were used in conjunction with a mathematical model to determine γ. They found that for Pyrex, the increase in γ for oxygen can be of a whole order of magnitude and five times less for nitrogen when working at temperatures above 1000 K and pressures between 800 and 3000 Pa.

Another use of both theoretical and experimental results was presented by Kolesnikov [78]. He used water-cooled stationary heat flux probes to study the experimental parameters of oxygen and nitrogen recombinations on quartz glass. He later used a tethered particle motion (TPM) model to determine $\gamma_{quartz} = 0.003$ at 10^4 Pa and 300 K. The TPM model was used to calculate the movements of physisorbed atoms on the surface of the quartz glass, as surface mobility of adatoms seems to play a key role in the heterogenous surface recombination of neutral atoms.

Herdrich et al. [109] determined the γ of oxygen atoms for a ceramic material known as PM1000. The material is made of carbon, nickel, chromium, iron, aluminium, titanium, and yttrium oxide and is considered a thermal protection material for spacecraft during planetary reentry. The material was put inside pure oxygen plasma with a heat flux sensor at the stagnation point (the point of the material which takes the brunt of the flowing gas). This sensor produces an electric signal proportional to the applied heat flux to the sensor's surface. The temperature of the material was also monitored with an optical pyrometer, while the flow of gas was measured with a Pitot probe. At 800 Pa, the γ of PM1000 increased from 0.17 to 0.21 in the temperature range from 1500 to 1610 K.

A later study by Steinbeck et al. [110], using the same facilities and techniques as Herdrich et al. [109], determined γ for pre-oxidized tungsten, PM1000, and its preoxidized form, SiC, and preoxidized SiC. At 83 Pa and 1371 K, the γ for pre-oxidized tungsten was 0.035. PM1000 in the temperature range 1499–1611 K at similar pressures exhibited a slight increase in γ from 0.206 to 0.233. Under the same conditions, an even higher $\gamma = 0.313$ was observed for pre-oxidized PM1000. Quartz glass exhibited a two-times increase in γ when temperature increased from 1180 to 1650. With SiC, γ seemed to drop with increasing temperature (1300–2000 K) from 0.085 to 0.009, but remained more or less the same in that temperature range for pre-oxidized SiC, albeit with a slightly higher value of $\gamma_{oxid.\ SiC} = 0.114$.

Park [86] used calorimetry in conjunction with a mathematical model to determine the γ of neutral oxygen atoms on copper and cupric oxide in a gas mixture of oxygen and argon. In his experiments, a thin film heat-transfer gauge was used to measure the heat transferred from plasma to the material through heterogenous surface recombination. The experiment was performed at a higher pressure (14,000 Pa) and room temperature, with the results providing $\gamma_{Cu} = 0.4$ and $\gamma_{CuO} = 0.0029$. The use of the same facilities to determine γ for copper at atomic oxygen partial pressures from 13,410 Pa to 25,620 Pa and at room temperature was described by Yang et al. [40]. γ decreased with rising pressure from 0.0022 to 0.0213.

3.2. Emission Spectroscopy

In methods utilizing emission spectroscopy, the relaxation of excited plasma particles is monitored. All particles tend towards their lowest possible energy, which is at their ground state. Excited particles, which are created in the plasma discharge, sooner or later de-excite to their ground states, releasing energy. Some of that energy is released through photons, which are usually in the optical or VUV range [96]. The schematic of this technique is shown in Figure 8.

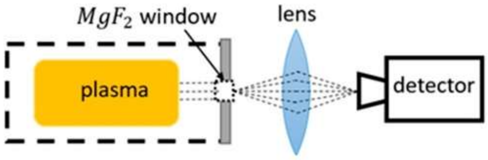

Figure 8. Schematic of an emission spectroscopy technique.

Mange et al. [111] utilized the VUV emission spectroscopy in measuring the γ of Pyrex in the pressure range of 3–667 Pa. The decay of oxygen atoms along a Pyrex tube at room temperature was measured through a MgF_2 window positioned in the afterglow, resulting in $\gamma_{pyrex} = 0.0024$. This was possible due to the high intensity of the three resonant atomic triplet lines which were analyzed in the range of wavelengths from 120 to 210 nm.

In a series of articles by Cartry et al., time-resolved VUV absorption spectroscopy was used to determine γ of quartz in oxygen discharges [44], and the experimental data was later used in a mathematical model [45]. Three atomic oxygen lines at 130.217 nm, 130.487, and 130.604 were monitored. At 133 Pa and room temperature, γ_{quartz} was experimentaly determined to be around 0.0001–0.0004, with a very similar value of 0.0005 provided by the mathematical model.

3.3. Actinometry

Actinometry utilizes optical emission spectroscopy to measure neutral atom densities. A known and low quantity of an actinometer, which is usually a noble gas (argon is used most frequently), is introduced into the experimental system where oxygen plasma is sustained. In the optical spectra, the intensity of the actinometric lines is compared to the intensity of the studied gas lines. Since the quantity of the actinometer is known, the ratio of intensities can be linked to the neutral atom density of the studied gas. A prerequisite for this method to work is that the emitting state of the actinometer needs to be at around the same energy as the emitting state of the gas in question.

In a study by Cartry et al. [77], the γ for oxygen atom recombination on a quartz glass surface was determined. Interestingly, two two sets of values were presented, one set for the fast-decaying atoms inside the discharge and one set for the slow-decaying atoms in the afterglow. Both sets were operated at pressures of 67, 133, and 267 Pa. The coefficients were measured for the quartz glass surface at room temperature. Measurements in the discharge provided higher values of $\gamma_{quartz} = 0.04 - 0.028$, which decreased with increasing pressure. On the other hand, afterglow measurements provided $\gamma_{quartz} = 0.00019 - 0.0005$, which increased with increasing pressure. The discrepancy was explained by the creation of additional active recombination sites on quartz through ion bombardment in the discharge area. This is one of a few scientific articles which addresses the role of charged particles (and perhaps also VUV radiation) on the surface recombination of oxygen atoms.

Krištof et al. [112] used actinometry for the determination of γ for quartz (0.0039), PET (0.00093), PTFE (0.00066), and mica (0.0012) at room temperature and pressures 150–350 Pa. Argon was used as the actinometer and emissions were observed along a 10 cm long afterglow chamber, with light being focused by a lens into an optic fiber connected to a spectrometer.

Booth and Sadeghi [69] used actinometry to study plasmas of pure oxygen and mixtures of oxygen and fluorine. Although they did not determine γ, they did determine the sticking coefficient (α) of oxygen atoms on the reactor wall, made of stainless steel. Their results show that in pure oxygen plasma, $\alpha_{O,\ SS} = 0.5$, but is significantly lowered to $\alpha_{O+F,SS} = 0.09$ in mixtures of oxygen and fluorine. Their experiments were performed at 3 Pa, and the reactor walls were at room temperature. The emission of oxygen atoms was observed at 844 nm and compared to the emission of argon atoms at 750 nm.

Pagnon et al. [113] measured the γ for quartz at room temperature, and observed an increase from 0.00002 to 0.0024 with increasing pressure from 50 to 300 Pa. Two spectral lines of oxygen, one at 844 nm and the other at 777 nm, were monitored along with the 750 nm argon line. The results of the actinometric method were also compared to those achieved using VUV spectroscopy, with a high degree of agreement between the two methods.

In a series of papers by Balat-Pichelin et al. [79–84], actinometry was utilized in conjunction with other methods to determine the γ of various materials. The 844 nm oxygen line and the 824 nm argon line were monitored in the discharge area. The studied materials included different steel alloys, aluminum oxide and its alloys, quartz, β-cristobalite quartz, SiC, a mixture of quartz and SiC chromium oxide, and various exotic alloys of zirconium (namely Y_2O_3 stabilized zirconia (YSZ), CaO stabilized zirconia (CSZ), MgO stabilized zirconia (MSZ), and ZrB_2-based materials). All of the listed materials were tested at pressures ranging from 100 to 1000 Pa and at relatively high surface temperatures (from 1000 to 2000 K), and all of the materials exhibited a rise in γ with increasing surface temperature, allthough in various amounts. All materials were studied as potential candidates for thermal shielding of spacecraft during planetary reentry. Therefore, to reach higher temperatures, the materials were heated using a solar furnace, and their temperature was monitored with an IR pyrometer. A calorimetric probe was used in the absence of materials to measure neutral atom densities at the same spot under the same experimental conditions. The results of the studies showed that aluminum-based alloys were the best catalysts, followed by steel alloys as well as zirconium alloys. Chromium oxide behaved similarly to quartz glass and SiC-based materials, remaining inert, with γ growing considerably at the high end of the temperature range (around 2000 K).

Guyon et al. [65,66] used actinometry along with NO titration to measure γ for various semiconductors at 110 Pa from their room temperature to the upper limit, where the materials would remain stable. A heater cartridge was used to heat the materials. The emission was observed through a collimator connected to a spectrophotometer through an optical fiber. A linear correlation between activation energy needed for heterogenous surface recombination and the energy gap of p-type oxide semiconductors was discovered upon studying MnO, CoO, PbO, and Sb_2O_3. An increase in γ was also noticed with the decreasing energy gap of p-type oxide semiconductors. However, no correlation was found between the gap energy of n-type semiconductors (WO_3, $BaTiO_3$, TiO_2, $CaTiO_3$, Al_2O_3, SiO_2, Fe_3O_4, and SiC + SiO_2) and γ. A logarithmic correlation between the activation energy of heterogenous neutral oxygen atom recombination and the density of active sites on n-type semiconductors was reported. All of the studied semiconductors exhibited an increase in γ with increased surface temperature [65,66].

A time-resolved actinometric method for the determination of heterogeneous loss of O, H, F, and CF_2 radicals on a quartz surface was proposed by Lopaev and Smirnov [43] and expanded upon by Lopaev et al. [42]. The loss of oxygen atoms was measured from the radial variation of the dissociation degree of oxygen. At higher pressures, the actinometric method had to be corrected, which required the spatial distribution of the reduced electric field to be known. In their findings, room-temperature quartz glass was examined first in the pressure range of 13 to 400 Pa [43] and later from 600 to 6600 Pa [42]. The results for the first pressure range provided a constant $\gamma_{quartz} = 0.00205$, while γ_{quartz} grew to 0.003 at higher pressures.

Macko et al. [47] also employed the time-resolved actinometric method to determine the γ of Pyrex in respect to the surface temperature in a pulsed discharge system. The decay of oxygen atom density after each pulse of the discharge was studied to determine the γ of the Pyrex walls of the reactor. Argon was used as the actinometer, and the line at 750 nm was monitored along with two oxygen lines at 777 and 844 nm. In the temperature range from 77 to 460 K, γ increased by two orders of magnitude, from 0.0004 to 0.016. In order to achieve lower temperatures, the tube was cooled with liquid nitrogen. Higher temperatures were obtained using a resistance heater. No pressure dependence of γ was observed in the range from 66 to 626 Pa.

Another use of the time-resolved actinometric method was documented by Bousquet et al. [114] when determining the γ of stainless steel plasma reactor walls. Along with that, a Langmuir probe was used to measure electron density and electron energy distribution. A gas mixture of oxygen and hexamethyldisiloxane (HMDSO) was used, along with pure oxygen, CO_2, and H_2O. The γ of oxygen atoms was found to be around five times higher in pure oxygen plasma (0.09) than in pure CO_2 plasma (0.02), which was attributed to the competition of CO and O radicals for the same surface adsorption sites. In pure H_2O and mixed oxygen and HMDSO plasmas, the recombination of oxygen atoms was further diminished by the adsorption of OH radicals onto the wall surface. Ion bombardment during the treatment seemed to create more adsorption sites, which increased γ. This observation is similar to that proposed in the paper by Cartry et al. [77].

Rakhimova et al. [54] used actinometry to determine atom loss coefficients of hydrogen and oxygen atoms on nanoporous dielectrics, quartz, and PTFE. Dielectric materials used were SiOCH with porosity between 24 and 33%. Experiments were performed at pressures of 400 Pa and 1300 Pa, and all the materials were kept at room temperature. The hydrogen line at 656 nm and the oxygen line at 777 nm were monitored, along with the argon line at 750 nm. After exposure to plasma, the amount of oxygen and hydrogen atoms absorbed into the sample surface was determined by Fourier-transform infrared (FTIR) spectroscopy. Atomic oxygen was shown to be a prominent remover of CH_3 groups from the surface of SiOCH, while hydrogen failed to break the $Si - CH_3$ bonds, limiting the damage of hydrogen plasma to the samples. The γ of oxygen atoms was calculated to be 0.0006 for PTFE, 0.0012 for quartz, 0.0038 for the SiOCH with 24% porosity, and 0.0044 for the SiOCH sample with 33% porosity. Therefore, the larger porosity increased the recombination coefficient.

Another study of stainless steel reactor walls and their interaction with oxygen plasma was reported by Tsutsumi et al. [51]. Using energy-resolved actinometry, they determined $\gamma_{SS} = 0.01$ at 40 Pa and 300 K. The use of energy-resolved actinometry allowed simultaneous measurements of the radial distribution of oxygen dissociation degree and electron temperature. Two oxygen lines at 777 and 844 nm were monitored along with the 750 nm argon line using phase-resolved optical emission spectroscopy to determine the radially resolved oxygen dissociation degree and the electron temperature.

Morillo-Candas et al. [115] compared the actinometric method with the high-resolution two-photon absorption laser-induced fluorescence for the determination of γ for oxygen atoms on Pyrex. Plasmas were sustained either in O_2 or CO_2 discharges. The latter method will be explained in the next section of this chapter. Pressures ranged from 27 to 667 Pa, while the surface temperature of Pyrex was kept between room temperature and 410 K. The increase in gas temperature was shown to increase γ, which was twice as high in pure oxygen plasma (0.00034–0.0011) compared to the γ of CO_2 plasma (0.00022–0.00065). Good agreement between the two complementary techniques was reported [115].

3.4. Laser-Induced Fluorescence

Laser-induced fluorescence (LIF) utilizes selective excitation of ground-state atoms with a laser. Once excited by the laser, the atoms release photons through fluorescence and assume a lower excited state. A laser set to 130 nm is used to excite the oxygen atoms from the ground state ($2p^4 3P$) to the excited state (3p3P), and the fluorescence deexcitation of oxygen atoms at 845 nm causes the atom to relax to the state $3p^3S$ [116]. The density of neutral atoms in the ground state can be determined by measuring the absorption of laser light and fluorescence.

Since lasers of such short wavelengths are not feasible [116], some workaround solutions must be incorporated. If two photons of larger wavelengths are absorbed simultaneously, laser-induced fluorescence can be achieved. This method is called the two-photon absorption laser-induced fluorescence (TALIF). In the case of oxygen, two photons with a wavelength of 226 nm are absorbed (Figure 9), while for hydrogen, two photons with a wavelength of 205 are needed to achieve fluorescence at 656 nm (Balmer α). Since the collisional cross-section of two-photon absorption is much smaller than for a single photon, a stronger laser source is required. While offering good spatial and temporal resolutions, TALIF is an expensive and rather impractical experimental method.

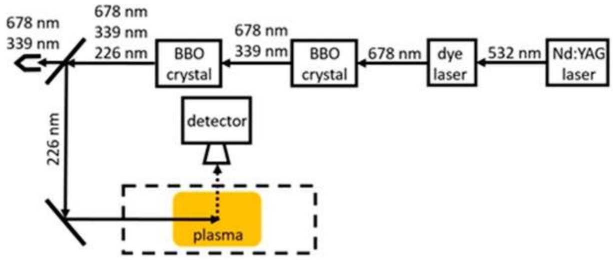

Figure 9. Schematic of a typical TALIF setup for measurements in oxygen plasma. Firstly, an Nd:YAG laser (in this case, with its second harmonic at 532 nm) is used to pump a continuum dye laser. This laser light is frequency doubled and tripled using two beta-barium borate (BBO) crystals. Lastly, the laser light is filtered and focused on the plasma, with the detector for the fluorescent light at a right angle.

In a study determining the spatial distribution and temporal evolution of oxygen atoms, TALIF was utilized by Tserepi and Miller [52]. Absolute densities were determined beforehand with NO titration. The spatial distribution of oxygen atoms between parallel plates of an RF discharge proved to be uniform (or very close to). The decay of oxygen atoms was studied to determine γ of stainless steel reactor walls. The 226 nm wavelength of the laser was achieved with an Nd/YAG laser with a wavelength of 1064 nm, which was used to pump a dye laser. That laser light was frequency tripled and focused using a quartz lens. A mathematical model was used along with the experimental results to determine γ_{SS}, which, at room temperature, gradually decreased from 0.013 to 0.005 at pressures ranging from 10 to 400 Pa.

Matsushita et al. [62] employed TALIF to determine the sticking coefficient (α) of oxygen atoms to a stainless steel surface at room temperature. The sticking coefficient must not be confused with the recombination coefficient, as sticking is only one part of the recombination process. At lower pressures (2 Pa), α was considerably higher (0.4) than at higher pressures of 10 Pa, where $\alpha = 0.1$. The required 226 nm wavelength was produced by the second harmonic generation of a 451 nm dye laser pumped with a XeCl excimer laser.

Another study of gaseous mixtures of nitrogen and oxygen used in plasma discharges was presented by Dilecce and De Benedictis [117]. In their study, TALIF was utilized to measure neutral atom densities and their loss rates, which, in conjunction with a kinetic model, provided the γ for stainless steel. Again, an Nd/YAG laser was used to pump a dye laser to achieve the proper wavelength of laser radiation. The results at room temperature for stainless steel showed a decrease in γ_{SS} from 0.006 to 0.002 with rising pressure from 133 to 267 Pa.

Gomez et al. [50] studied the γ of stainless steel, aluminium, silicon, quartz, and polypropylene (PP) using TALIF. A second harmonic at 532 nm from a pulsed Nd/YAG laser was used to pump a dye laser at 572 nm. Afterward, the dye laser output was frequency tripled to produce a 225.5 nm laser light. With temperatures from 400 to 600 K and pressures ranging from 1 to 100 Pa, the γ was calculated for several materials. For stainless steel, $\gamma_{SS} = 0.35 - 0.02$ decreased with increasing pressure. The same results were reported for aluminum, with $\gamma_{Al} = 0.3 - 0.01$ and almost identical results for quartz. On the other hand, the γ for silicon and PP increased with increasing pressure as $\gamma_{Si} = 0.02 - 0.2$, and $\gamma_{PP} = 0.02 - 0.3$. The rather large value of the recombination coefficient for polypropylene might be due to high temperature. Namely, the melting point of polypropylene is just above 400 K.

In a report by Marschall [118], along with reviewing different measurement methods, the side-arm method was used, with TALIF determining the profile of the decay of atoms along the side-arm. Decay was also simulated, and the results were compared. Experiments were performed at 40 Pa with materials remaining at room temperature. The determined γ was 0.016 for stainless steel (SS 304), 0.046 for a constantan alloy with a 45% amount of nickel, 0.0068 for chrome with a 10% amount of chromium, and 0.0053 for platinum.

3.5. NO Titration

NO titration is the process of adding gaseous NO to the reactor in the afterglow region (Figure 10). In the oxygen afterglow, NO is highly reactive and produces NO_2^* exciplex molecules. The resulting NO_2^* molecules are highly reactive with *O*-atoms, producing NO_2 molecules and releasing energy via chemiluminescence. The NO_2 can again dissociate into NO, which can repeat the entire cycle. Due to this process, even a small amount of NO is enough for the rapid depletion of atomic oxygen in the afterglow, and the yellow–green glow due to chemiluminescence can be monitored and linked to the oxygen atom density. A major drawback of NO titration is the poisoning of the reactor with NO and NO_2 gases. Due to safety reasons, a mixture of argon (around 2%) is used in many practical cases.

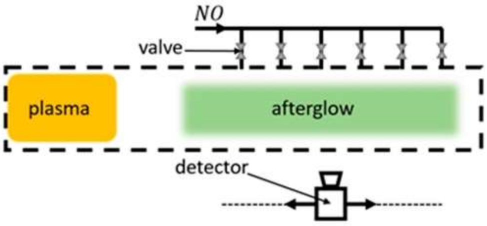

Figure 10. Schematic of a plasma system utilizing measurements with NO titration. NO gas is introduced to the system through a series of valves, and a movable detector monitors the afterglow.

In two studies by Kaufman [71,72], the γ for quartz and Pyrex surfaces at room temperature was determined using NO titration. The light intensities in the titration region were measured with movable photomultipliers, which provided the neutral atom density profile along the titration region. For quartz at 67 Pa, γ was determined to be 0.00002, a value much lower than determined in contemporary literature. As for Pyrex, the same value of γ was determined, again low compared to other sources.

In a report by Rosner et al. [119], a study of candidate materials for space shuttle thermal protection systems was carried out. Of particular interest was nickel oxide, with $\gamma_{NiO} = 0.1$ at room temperature. Regrettably, the pressure was not reported. One can speculate the pressure was similar to pressures in experimental setups of other authors utilizing NO titration. With that in mind, the pressure in the plasma system could have been between 50–1000 Pa.

Brake et al. [74,75] used NO titration along with a theoretical model when determining the γ of quartz at room temperature. NO gas was introduced into the system through eight pinholes forming a ring in a single cross-sectional plane of the titration chamber, meeting oxygen in a crossflow pattern. A one-dimensional, temperature-dependent mathematical model was in agreement with the experimentally determined oxygen atom density. However, the resulting γ_{quartz} provided two different values separated by a whole order of magnitude. From the experimental data, $\gamma_{quartz} = 0.0005$, while from theoretical calculations, $\gamma_{quartz} = 0.00005$.

A great example of NO poisoning of the reactor due to NO titration was demonstrated by Wickramanayaka et al. [60], with observable changes in γ due to NO poisoning of the surfaces of different materials. At the pressure of 133 Pa and room temperature, the γ of several materials in their original and poisoned state was determined. The γ of poisoned materials was generally lower than before NO poisoning. Results for γ were provided for stainless steel (clean at 0.099 and poisoned at 0.0064), aluminum (clean at 0.0044 and poisoned at 0.0029), aluminum with a layer of Ni + Cr_2O_3 (clean at 0.0036 and poisoned at 0.0035), aluminum with a PTFE layer (clean and poisoned at 0.002), copper (clean at 0.026 and poisoned at 0.019), platinum (clean at 0.0027 and poisoned at 0.0016), gold (clean at 0.0032 and poisoned at 0.0019), magnesium (clean at 0.0023 and poisoned at 0.0012), Pyrex (clean at 0.000092 and poisoned at 0.000056), and PTFE (clean at 0.000073 and poisoned at 0.000064). Based on these results, one must take the data obtained by *NO* titration with some precaution. Namely, titration experiments are often time-consuming, so ample time must be available to poison the reactor walls in the afterglow region.

3.6. Wrede–Harteck Gauge

Another method used to determine neutral atom densities, and, consequently, γ, is using the Wrede–Harteck gauge. The Wrede–Harteck gauge uses a manometer to measure pressure in a separate chamber connected to the plasma reactor through a small orifice, which allows atoms to pass through. As a result of dissociation, the pressure inside the gauge where atoms are present is larger than in the segment of the gauge where the atoms recombine into molecules because of the presence of the catalytic materials. When in equilibrium, the amount of atoms entering the gauge is balanced by the amount of molecules leaving the gauge. The difference in pressure between the gauge and the system can help us determine the neutral atom density inside the reactor, as shown in Figure 11.

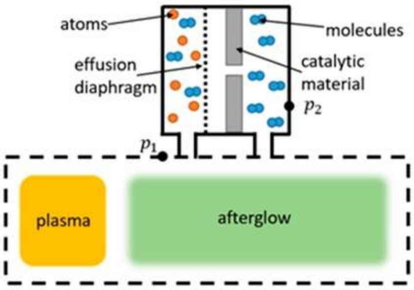

Figure 11. Schematic of a Wrede–Harteck gauge, where p_1 and p_2 are pressures measured inside the plasma chamber and inside the Wrede-Harteck gauge, respectively.

The use of Wrede–Harteck gauges to determine γ was described in the works by Greaves and Linnett [70,120], where the gauge was lined with different materials, and pressure was measured at both ends of the lined gauge using Pirani gauges. At a moderately low pressure of 650 Pa, the γ of several oxides was determined at room temperature. CuO exhibited the highest value at 0.043, while B_2O_3 and Sb had the lowest values of 0.000063 and 0.000081, respectively [120]. Quartz glass was examined more closely, with $\gamma_{SiO_2} = 0.00016 - 0.014$ growing with rising temperatures from 300 to 900 K and at 16 Pa [70].

Another seminal work for the determination of γ, by Melin and Madix [55], also utilized Wrede–Harteck gauges in conjunction with isothermal calorimetric filaments. Weak temperature dependence of γ was observed for silver and copper, with silver once again proving to be the best catalytic material for oxygen. Cobalt came in next with $\gamma_{C_O} = 0.075$ at room temperature, followed by copper and its oxide and nickel. Experiments were performed at relatively low pressures ranging from 1 to 4 Pa.

Sabadil and Pfau [121] measured the oxygen dissociation degree in a quartz glass tube at a pressure of 66 Pa using the Wrede–Harteck gauge along with the ozone method, with both methods in good agreement. The ozone method utilizes the association of atomic oxygen with molecular oxygen on a surface cooled with liquid nitrogen into an ozone molecule. The difference in pressure during ozone creation can be linked with the neutral oxygen atom density and, conversely, with γ. For quartz, γ was determined to be around 0.00048.

3.7. Mass Spectrometry

This method measures the mass-to-charge ratio of ions. As the gas from the reactor is pumped into a mass spectrometer, the neutral particles are ionized, and the resulting ions are analyzed via separation by mass-to-charge ratio. Examples of mass spectrometers include time-of-flight, magnetic sector, and quadrupole.

In a study by Sjolander [85], the probabilities for reflection, recombination, general surface reaction, and occlusion were calculated for the following materials: gold, nichrome V, aluminum, titanium, silver, and platinum. Measurements were performed at 40 Pa and at room temperature (due to the low density of *O*-atoms), and the probabilities were calculated using a mathematical model with experimental data as input parameters. The materials were exposed to the oxygen plasma for up to 10 h, which altered their γ. Stainless steel and titanium exhibited an identical rise in γ from 0.04 to 0.16 with increased exposure time to the oxygen plasma, as did silver (from 0.01 to 0.06) and gold (from 0.03 to 0.2). While not explicitly stated as the cause, surface reflectivity of *O*-atoms decreased with exposure time, which might be due to the surface being slowly cleaned of inert impurities by the force of impact of incident *O*-atoms.

Singh et al. [122] studied the surface recombinations of oxygen and nitrogen atoms on a stainless steel surface in pure oxygen and nitrogen plasmas with the help of a mathematical model. The input parameters were determined experimentally; the radical and molecule densities were measured with a quadrupole mass spectrometer, while the electron energy distribution function was measured with a Langmuir probe. Appearance potential mass spectrometry was used to ionize and detect either radicals or parent molecules selectively. At the surface temperature of 330 K and a pressure of 5 Pa, the γ for oxygen and nitrogen atoms was determined to be 0.17 and 0.07, respectively.

Another use of experimental data acquired with mass spectroscopy as input parameters in a simulation was presented by Kiehlbauch and Graves [123]. Again, a Langmuir probe was used to determine the electron energy distribution function, along with two separate quadrupole mass spectrometers for the composition of ions and neutral particles. Mass spectrometers were calibrated with argon beforehand, ensuring absolute values of neutral atom densities. Additionally, an optical spectrometer was used to measure the rotational temperature of neutral molecules. In the pressure range from 1 to 15 Pa and surface temperature ranging from 300 to 400 K, the γ of stainless steel reactor walls was determined at a constant value of 0.14.

Kurunczi et al. [124] studied the γ of oxygen atoms on an anodized aluminium surface of the reactor walls. The spinning wall method was employed. The spinning substrate was rapidly rotated (at 40,000 rpm) and periodically exposed to oxygen plasma. The substrate chamber was connected to a mass spectrometer, which analyzed the composition of gas in the system immediately after the interaction of the substrate with the gaseous particles. By varying rotation frequencies, the exposure time of the substrate and the time between exposure and detection by the mass spectrometer were controlled. At 1 Pa and room temperature, the γ of anodized aluminum decreased with increasing rotation speeds from 0.6 to 0.4. These values are very large compared to other reports and could be explained by the very rich morphology of anodized aluminum.

Another study of γ for stainless steel and aluminum surfaces was reported by Hsu et al. [125] in pure argon, mixed argon, and oxygen, as well as mixed argon, oxygen, and chlorine gaseous plasmas. Experimental results complemented a theoretical model. An ion flux probe was utilized to measure the flux of ions to the walls of the reactor, while a Langmuir probe measured electron density and the electron energy distribution function. Separate mass spectrometers were used to measure the composition of ions and neutral plasma particles. In the temperature range from 300 to 400 K and pressures from 1 to 11 Pa, the γ of stainless steel and aluminum were determined to be 0.3 and 0.0001, respectively.

Guha et al. studied the γ of anodized aluminum [126] and performed a separate study of γ for pure and copper-contaminated silicon surfaces [127]. The spinning wall method was utilized along with mass spectrometry and Auger electron spectroscopy (AES) for the detection of desorbing species. The rotation velocity of the spinning wall allowed the control of oxygen atom flux to the surface. At room temperature and pressures of around 1 Pa, the γ of aluminum decreased with increasing oxygen atom flux from 0.06 to 0.04. In the second study, the effect of copper contamination on silicon wafers was studied as well. The reason behind this study is the sputtering of copper to silicon reactor walls during plasma etching of dielectrics. A noticeable decrease in etching rates after some time was linked to an increased oxygen atom sink on the reactor walls due to the catalytic activity of deposited copper. At room temperature and 0.2 Pa, $\gamma_{Si} = 0.043$ was noticeably lower than $\gamma_{Si+Cu} = 0.069$.

Another use of the spinning wall method was employed by Stafford et al. in combination with a mathematical model to determine γ for oxygen atoms on stainless steel [61] and in a separate study of oxygen and chlorine plasmas and γ for oxygen and chlorine on stainless steel and aluminium reactor walls [128]. In both studies, the use of AES and line-of-sight mass spectrometry helped determine electron density and energy distribution function and the composition of ions and neutral particles. At room temperature and pressure of 0.2 to 3 Pa, the γ of stainless steel was 0.13 for oxygen atoms and decreased with exposure time to 0.09. This was due to the deposition of silicon particles on the material due to the slow etching of the reactor walls. In the second study, $\gamma_{SS} = 0.09$ and $\gamma_{Al} = 0.05$ were determined under the same temperature and pressure as before. The materials were again coated in a silicon-oxide-based layer, which is the main culprit for lower values of γ for stainless steel.

Donnelly et al. [38] reviewed the methods for studying surface reactions of atoms and molecules. They utilized the spinning wall method to determine $\gamma_{Cu} = 0.07$ at 0.02 Pa and room temperature. As with the previously described methods, AES and mass spectrometry were employed for the analysis of electrons, ions, and neutral particles. The experimentally obtained data were used in simulations to calculate γ.

3.8. Paramagnetic Resonance

Paramagnetic resonance utilizes the Zeeman effect, the splitting of energies of electronic states in a magnetic field (Figure 12). With an electromagnetic wave with the correct wavelength, electronic transitions can occur between different electronic states. These transitions usually happen in the GHz range of frequencies (wavelengths in the range of centimeters). The relative determination of neutral atom density is possible by monitoring the intensities of the peak in the absorption spectrum. Absolute densities are, however, much harder to determine using this method.

The first study of oxygen recombinations utilizing paramagnetic resonance was demonstrated by Krongelb and Strandberg [129]. They reported a strong paramagnetic-resonance absorption of oxygen atoms. Reactions in the plasma system were monitored by observing the intensity of the absorption. At room temperature and pressures ranging from 100 to 300 Pa, the γ of quartz for neutral oxygen atoms was determined to be 0.00032.

Hacker et al. [73] used paramagnetic resonance along with an isothermal calorimetric detector to determine the γ of quartz glass and platinum. This was conducted by measuring the decay of neutral atom concentration along the flow, which allowed the determination of recombination kinetics. At room temperature and pressures between 150 and 220 Pa, the γ for oxygen atoms on a quartz surface was 0.00004. For platinum, γ increased with temperature from 0.01 to 0.1 in the temperature range of 300–1100 K.

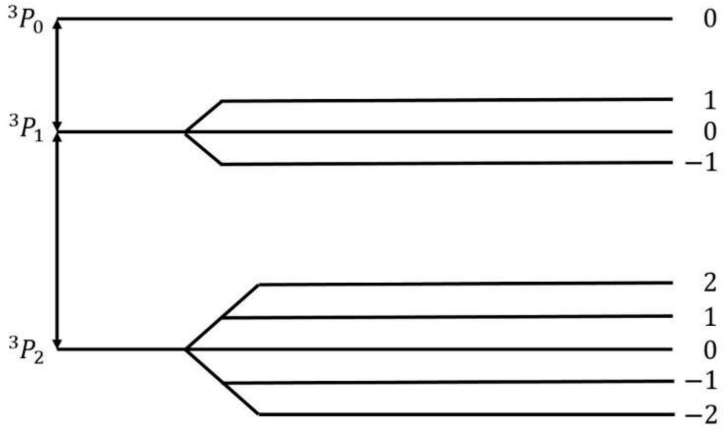

Figure 12. Splitting of the energy levels of an oxygen atom in a magnetic field.

In the paper by Marshall [130], the γ of room temperature Pyrex for oxygen, hydrogen, and nitrogen atoms was studied in the pressure ranges from 133 to 1330 Pa. The γ of Pyrex for oxygen atoms (0.0005) was observed to be almost twice as high as γ for nitrogen atoms (0.0003). Both remained constant throughout the entire pressure range.

Hogan and Burch [131] examined three-body collisions of oxygen atoms and molecules in the gas volume along with the wall recombinations on room-temperature reactor walls coated with a metaphosphoric acid-sodium metaphosphate (NaO_3P) mixture. The recombinations were monitored with a paramagnetic resonance spectrometer for pressures between 30 and 147 Pa. A liquid-nitrogen trap improved oxygen purity, which reduced the amount of water, CO_2, and NO_2 in the system. NaO_3P was not a very efficient recombinator, with $\gamma_{NaO_3P} = 0.0000091$ across the entire pressure range.

3.9. Theoretical Models

Various authors used different approaches when simulating the recombination of neutral atoms on the surface of materials. Some authors tested these models in experimental setups. We briefly examine some of the works of a few authors and present their results.

In a paper by Hardy and Linnett [37], simulations were based on the semiconductor theory. A connection between γ and conductivity was proposed and the model was applied to three tungsten-oxide-based materials at room temperature. Results show: $\gamma_{Li_2WO_3} = 0.022 - 0.052$, $\gamma_{Na_2WO_3} = 0.005 - 0.047$, and $\gamma_{K_2WO_3} = 0.022 - 0.48$. The method is promising, but not practical for the exact determination of γ.

Seward and Jumper [89,132] used a kinetic model to predict the γ of quartz and reaction cured glass (RCG), which were considered appropriate materials for thermal protection systems of space shuttles during planetary reentry. The results of the model show γ taking a complex form, which was an evolution of Equation (4). The resulting γ_{SiO_2} showed strong temperature dependence, rising with temperature from 0.0001 at room temperature until a peak of 0.02 at around 1000 K, and then decreasing with increased temperature. This result was reproduced in a separate model, along with similar behavior of RCG with a peak at 1000 K and $\gamma_{RCG} = 0.0004 - 0.01$. The results were in agreement with experimental work reported by other authors.

In the paper by Shibata et al. [53], a relaxation continuum model was used in the numerical analysis of oxygen plasma in a reactor with walls made of stainless steel. The numerical methods were accompanied by experimental results in a CCP discharge at room temperature and 66 Pa. Many values of γ were considered, with two extremes at 0.0001 and 0.5, but the best agreement between the model and the measurements was possible when γ of stainless steel was set at 0.015.

Daiss et al. [133] studied catalytic reactions of oxygen and nitrogen on quartz surfaces. A detailed surface chemistry model for the reactions (adsorption, desorption, and recombination) of plasma particles on the quartz surface was compiled and implemented into Navier–Stokes code. The predicted γ was compared with experimental results of Dickens and Sutcliffe [57], Stewart [103], Scott [100], and Kolodziej et al. [134]. The experimental results were in good agreement with the numerical results, showing an increase in γ with increasing surface temperature up to a peak at around 1000 K and then decreasing rapidly with further increases in temperature.

Quartz was also studied in low-pressure flowing discharges of oxygen and nitrogen by Gordiets and Ferreira [135], who proposed a self-consistent model for bulk and surface kinetic processes. The model was one-dimensional and only applied to DC discharges and afterglows. Kinetics of free electrons, electronic states, chemical and vibrational kinetics, as well as interactions with the wall with respect to gas and wall temperatures were all considered in this model. It was discovered that the γ for oxygen atoms increased with wall temperature and percentage of gaseous oxygen in oxygen–nitrogen mixtures. For nitrogen recombination, γ was shown to decrease with increasing temperatures up to 500 K and then rose with increasing wall temperature.

Cacciatore et al. [136] devised two separate semiclassical models, one for the Eley–Rideal recombination mechanism and the other for the Langmuir–Hinshelwood recombination mechanism. Under the same conditions (wall temperatures from 600 to 1000 K), the theoretical prediction was that the γ of quartz glass would achieve higher values than recombinations that adhered to the rules of the Eley–Rideal mechanism when compared to γ for the Langmuir–Hinshelwood mechanism.

A global volume-averaged model was used to study discharges in a gaseous mixture of oxygen and argon by Gudmundsson and Thorsteinsson [90]. Increasing argon content in the discharge increased the electron temperature, which in turn increased the dissociation of oxygen molecules. The recombination of oxygen on a stainless steel surface was also studied. γ seemed to decrease with increasing pressure (0.1 to 20 Pa) from 0.5 to 0.1. This seemingly supports the theory that γ is negatively impacted by increasing pressure in the system.

Marinov et al. [88] utilized two approaches when modeling surface reactions of gaseous plasmas: the coarse-grained deterministic and the kinetic Monte Carlo methods. It was found that the kinetic Monte Carlo method produced more reliable results but was computationally more demanding. Both the Eley–Rideal and the Langmuir–Hinshelwood mechanisms were incorporated into the models, with γ depending on the total number 1 of active sites on the material surface. In the temperature range from 200 to 400 K, the γ of quartz was determined to decrease from 0.079 to 0.00039.

Experimental results demonstrating a high degree of vibrational excitation of oxygen molecules in oxygen plasmas piqued the interest of Annušova et al. [137], who performed experiments and devised a self-consistent zero-dimensional global kinetic model. The model incorporated electron impacts on ground-state oxygen molecules, the chemistry in the gas phase and the interactions of plasma with the surface. The γ of aluminum was determined at room temperature and pressures from 1 to 10 Pa at a constant value of 0.15, which was considerably higher than most contemporary studies. No surface finish of the aluminum samples was reported.

The results explained throughout the chapter are summarized in Table 2. With all the methods by various authors described, we can now compare the results of their work for various surfaces, which can help us categorize the materials. A comparison of the average γ for oxygen atoms on the material surface, determined using different methods, is shown in Figure 13. Apart from the γ for silver obtained by the Wrede–Harteck method, the largest values were, on average, reported using calorimetry, which is also the most commonly used experimental method. Larger values were also reported in works using LIF and mass spectrometry techniques. Based on Figures 6 and 13, the results thus show that the measured values may depend on the type of discharge system used and on the applied method of measurement. A brief overview of the advantages and disadvantages of the aforementioned measurement methods is presented in Table 3.

Table 2. List of recombination coefficients (γ) determined with different methods for various materials in different plasma systems at a given pressure (p) and surface temperature (T). In all cases, the samples for which γ was determined were kept at a floating potential. Values of γ in parenthesis were reported for «NO-poisoned» surfaces.

Material	γ	*p* [Pa]	*T* [K]	Plasma	Method	Ref.
Ag	0.21	10	300	ICP RF	thermocouple probe	[56]
	0.01–0.06	40	300	atomic beam	mass spectrometry	[85]
	0.11	760	300	pulsed RF	thin film resistance thermometer + NO titration	[63]
	0.1	0.0000001	373–673	MW	silver filament thermal resistance	[108]
	0.24–0.38	1–4	310–435	ICP RF	Wrede–Harteck gauge + NO titration	[55]
	0.22–0.29	1–2	298–375	ICP RF	thermal resistivity + effusion	[99]
	0.015	300	313–423	MW	NO-titration + thermal resistivity	[106]
	0.037	400–1300	300	pulsed RF	thin-film heat transfer gauge	[64]
Ag_2O	0.15	7–15	300	ICP RF	thin film heat-transfer gauge	[98]
	0.1	0.0000001	373–673	MW	silver filament thermal resistance	[108]
Al	0.3–0.01	1–100	400–600	ICP&CCP RF	TALIF	[50]
	0	40	300	atomic beam	mass spectrometry	[85]
	0.06–0.04	0.2–3	300	ICP RF	spinning wall desorption mass spectrometry	[126]
	0.0068	750		pulsed RF	thin film resistance thermometer + NO titration	[63]
	0.0001	1–11	300–400	ICP RF	mass spectrometry + Langmuir probe + ion flux probe	[125]
	0.05	0.2–3	310	ICP RF	Langmuir probe + actinometry + mass spectrometry	[128]
	0.0044 (0.0029)	133	300	ICP RF	NO-titration	[60]
	0.15	1–10	300	ICP RF	model	[137]
	0.4–0.6	1	300	ICP RF	spinning wall desorption mass spectrometry	[124]
Al foil	0.00042	40–180	300	ICP RF	side-arm + fiber optic catalytic probe	[95]
	0.00048	30–280	300	ICP RF	side-arm + fiber optic catalytic probe	[96]
C coated Al foil	0.0016	40–180	300	ICP RF	side-arm + fiber optic catalytic probe	[95]

Table 2. *Cont.*

Material	γ	p [Pa]	T [K]	Plasma	Method	Ref.
Al_2O_3	0.0018–0.0034	10	300	ICP RF	thermocouple probe	[56]
	0.01	7–15	300	ICP RF	thin film heat-transfer gauge	[98]
	0.0021	650	300	ICP RF	Wrede–Harteck gauge	[120]
	0.014–0.031	110	313–773	pulsed RF	actinometry	[65]
	0.0097–0.061	110	300–773	pulsed RF	actinometry + NO titration	[66]
	0.085	200	940	MW	actinometry + pyrometry	[79]
	0.0017 (0.0013)	133	300	ICP RF	NO-titration	[60]
Al_2O_3F	0.018–0.57	200	800–2300	MW	OES + actinometry + pyrometry	[80]
Al_2O_3SiK	0.038–0.24	200	800–2030	MW	OES + actinometry + pyrometry	[80]
Al_2O_3SiK fused	0.26	200	2330–2430	MW	OES + actinometry + pyrometry	[80]
Al_2O_3AlN	0.0035–0.15	200	800–2000	MW	OES + actinometry + pyrometry	[80]
Al + Ni + Cr_2O_3	0.0036 (0.0035)	133	300	ICP RF	NO-titration	[60]
Al + PTFE	0.002 (0.002)	133	300	ICP RF	NO-titration	[60]
As	0.00046	10	300	ICP RF	thermocouple probe	[56]
	0.000081	650	300	ICP RF	Wrede–Harteck gauge	[120]
Au	0.0052	10	300	ICP RF	thermocouple probe	[56]
	0.03–0.2	40	300	atomic beam	mass spectrometry	[85]
	0.0047	750		pulsed RF	thin film resistance thermometer + NO titration	[63]
	0.008	1–4	300	ICP RF	Wrede–Harteck gauge + NO titration	[55]
	0.0061–0.012	1–2	305–347	ICP RF	thermal resistivity + effusion	[99]
	0.005	300	313	MW	NO-titration + thermal resistivity	[106]
	0.0032 (0.0019)	133	300	ICP RF	NO-titration	[60]
	0.02	400–1300	300	pulsed RF	thin-film heat transfer gauge	[64]
B_2O_3	0.000063	650	300	ICP RF	Wrede–Harteck gauge	[120]
	0.00028	10	300	ICP RF	thermocouple probe	[56]
$BaCl_2$	0.00057–0.0019	10	300	ICP RF	thermocouple probe	[56]
$BaTiO_3$	0.012–0.078	110	313–773	pulsed RF	actinometry	[65]
Bi	0.0022	650	300	ICP RF	Wrede–Harteck gauge	[120]
C	0.0005	40–180	300	ICP RF	side-arm + fiber optic catalytic probe	[94]
	0.001	30–280	300	ICP RF	side-arm + fiber optic catalytic probe	[96]

Table 2. *Cont.*

Material	γ	p **[Pa]**	T **[K]**	**Plasma**	**Method**	**Ref.**
C-CAT ACC-4 SiC	0.013–0.03	500–3500	1200–1368	arc-jet	heat-flux + thermocouple + pyrometry + LIF	[104]
	0.030–0.00041	500–3500	1368–2000	arc-jet	heat-flux + thermocouple + pyrometry + LIF	[104]
CaO	0.00016	650	300	ICP RF	Wrede–Harteck gauge	[120]
CaO + ZrO_2	0.036–0.202	200	900–2500	MW	thermocouple probe + OES + actinometry	[84]
$CaTiO_3$	0.0097–0.061	110	313–773	pulsed RF	actinometry	[65]
	0.013–0.028	110	300–773	pulsed RF	actinometry + NO titration	[66]
CdO	0.001–0.27	4	295–625	ICP RF	side-arm thermocouple probe	[57]
chromel	0.0068	40	300	MW	side-arm + LIF	[118]
CNW	0.59	50	300	ICP and CCP RF	catalytic probe	[49]
Co	0.075	1–4	300	ICP RF	Wrede–Harteck gauge + NO titration	[55]
	0.14–0.08	10–400	750	ICP RF	Langmuir probe + fiber optic catalytic probe	[93]
CoO	0.029–0.034	110	300–473	pulsed RF	actinometry	[65]
Co_3O_4	0.0018–0.25	4	300–625	ICP RF	side-arm thermocouple probe	[57]
	0.00049	650	300	ICP RF	Wrede–Harteck gauge	[120]
constantan	0.046	40	300	MW	side-arm + LIF	[118]
Cr	0.06	1–2	308–356	ICP RF	thermal resistivity + effusion	[99]
Cr_2O_3	0.0002	4	300–650	ICP RF	side-arm thermocouple probe	[57]
	0.00025	650	300	ICP RF	Wrede–Harteck gauge	[120]
	0.023–0.072	300, 1000	850–1650	MW	actinometry + OES	[82]
CsCl	0.00034–0.0016	10	300	ICP RF	thermocouple probe	[56]
Cu	0.17	10	300	ICP RF	thermocouple probe	[56]
	0.07	0.02	300	ICP RF	spinning wall desorption mass spectrometry	[38]
	0.00217	25620	300	shock tube	thin film heat-transfer gauge	[40]
	0.00899	18400	300	shock tube	thin film heat-transfer gauge	[40]
	0.0213	13410	300	shock tube	thin film heat-transfer gauge	[40]
	0.016	1400	300	shock tube	thin film heat-transfer gauge	[86]
	0.4	1400	300	shock tube	thin film heat-transfer gauge	[87]

Table 2. *Cont.*

Material	γ	p **[Pa]**	T **[K]**	**Plasma**	**Method**	**Ref.**
Cu	0.031	760		pulsed RF	thin film resistance thermometer + NO titration	[63]
	0.015–0.024	1–4	300–370	ICP RF	Wrede–Harteck gauge + NO titration	[55]
	0.225	10–400	800	ICP RF	Langmuir probe + fiber optic catalytic probe	[93]
	0.070–0.11	1–2	298–375	ICP RF	thermal resistivity + effusion	[99]
	0.025	300	313	MW	NO-titration + thermal resistivity	[106]
	0.026 (0.019)	93	300	ICP RF	NO-titration	[60]
	0.23	100	55 0	ICP RF	thermocouple probe + OES + NO titration + Langmuir probe	[92]
CuO	0.0026–0.0032	14000	300	shock tube	thin film heat-transfer gauge	[86]
	0.034–0.18	4	295–485	ICP F	side-arm thermocouple probe	[57]
	0.043	650	300	ICP RF	Wrede–Harteck gauge	[120]
	0.02	10	300	ICP RF	thermocouple probe	[56]
Cu_2O	0.1–0.34	4	300–540	ICP RF	side-arm thermocouple probe	[57]
Fe	0.036	10	300	ICP RF	thermocouple probe	[56]
	0.018	750		pulsed RF	thin film resistance thermometer + NO titration	[63]
	0.01	1–4	300	ICP RF	Wrede–Harteck gauge + NO titration	[55]
	0.41	100	550	ICP RF	2007	
Fe_2O_3	0.0082	10	300	ICP RF	thermocouple probe	[56]
	0.0046–0.15	4	290–625	ICP RF	side-arm thermocouple probe	[57]
	0.0052	650	300	ICP RF	Wrede–Harteck gauge	[120]
Fe_3O_4	0.015–0.028	110	300–873	pulsed RF	actinometry + NO titration	[66]
graphite polished	0.05	30–280	300	ICP RF	side-arm + fiber optic catalytic probe	[96]
Ga_2O_3	0.00013	650	300	ICP RF	Wrede–Harteck gauge	[120]
GeO_2	0.00013	650	300	ICP RF	Wrede–Harteck gauge	[120]
H_3PO_4	0.00012	650	300	ICP RF	Wrede–Harteck gauge	[120]
Inconel 617 alloy	0.0014–0.18	36, 500–3500	260–1510	arc jet	side-arm + LIF	[46]
KBr	0.0013	10	300	ICP RF	thermocouple probe	[56]

Table 2. *Cont.*

Material	γ	p [Pa]	T [K]	Plasma	Method	Ref.
KCl	0.00078	10	300	ICP RF	thermocouple probe	[56]
	0.0001–0.015	10	300–700	ICP RF	catalytic probe	[58]
KF	0.00092	10	300	ICP RF	thermocouple probe	[56]
KI	0.00074–0.0035	10	300	ICP RF	thermocouple probe	[56]
K_2WO_3	0.022–0.48		300		semiconductor theory (conductivity, Fermi levels)	[37]
LiCl	0.0019	10	300	ICP RF	thermocouple probe	[56]
	0.00013–0.01	10	300–700	ICP RF	catalytic probe	[58]
Li_2WO_3	0.022–0.052		300		semiconductor theory (conductivity, Fermi levels)	[37]
LVP SiC - SiB + ZrO_2	0.0075–0.03	500–3500	1200–1500	arc-jet	heat-flux + thermocouple + pyrometry + LIF	[104]
	0.030–0.0016	500–3500	1500–2000	arc-jet	heat-flux + thermocouple + pyrometry + LIF	[104]
Mg	0.0026	10	300	ICP RF	thermocouple probe	[56]
	0.0023 (0.0012)	133	300	ICP RF	NO-titration	[60]
MgO	0.0035	10	300	ICP RF	thermocouple probe	[56]
	0.0089–0.022	4	295–415	ICP RF	side-arm thermocouple probe	[57]
	0.0025	650	300	ICP RF	Wrede–Harteck gauge	[120]
MgO + ZrO_2	0.073–0.109	200	900–1600	MW	thermocouple probe + OES + actinometry	[84]
$MgAl_2O_4$ (spinel)	0.071–0.09	800	1520–1780	ICP wind tunnel PWK3	pyrometry + calorimetry + Pitot probe	[109]
	0.15	7–15	300	ICP RF	thin film heat-transfer gauge	[98]
mica	0.0012	150–350	300	double pulse DC	discharge-induced emission spectroscopy + actinometry	[112]
MnO	0.017–0.025	110	300–473	pulsed RF	actinometry	[65]
MnO_2	0.013	650	300	ICP RF	Wrede–Harteck gauge	[120]
Mn_2O_3	0.0012–0.299	4	295–620	ICP RF	side-arm thermocouple probe	[57]
Mo	0.0048	10000	300	ICP RF	stagnation point heat flux + model	[105]
MoO_3	0.02–0.007	10	300–700	ICP RF	catalytic probe	[58]
	0.001	650	300	ICP RF	Wrede–Harteck gauge	[120]
NaCl	0.00094	10	300	ICP RF	thermocouple probe	[56]
NaO_3P	0.0000091	30–147	300	MW	electron paramagnetic resonance spectrometer	[131]
Na_2WO_3	0.005–0.047		300		semiconductor theory (conductivity, Fermi levels)	[37]

Table 2. *Cont.*

Material	γ	p [Pa]	T [K]	Plasma	Method	Ref.
Nb	0.02–0.09	10–400	600	ICP RF	Langmuir probe + fiber optic catalytic probe	[93]
	0.09	100–400	420–620	ICP RF	Langmuir probe + fiber optic catalytic probe	[91]
	0.09	100	550	ICP RF	thermocouple probe + OES + NO titration + Langmuir probe	[91]
Nb nanostructured	0.8	100	550	ICP RF	thermocouple probe + OES + NO titration + Langmuir probe	[91]
Ni	0.028	10	300	ICP RF	thermocouple probe	[56]
	0.27	10–100	500–1100	ICP RF	thermocouple probe	[107]
	0.0085	750		pulsed RF	thin film resistance thermometer + NO titration	[63]
	0.017	1–4	300	ICP RF	Wrede–Harteck gauge + NO titration	[55]
	0.27	10–400	800	ICP RF	Langmuir probe + fiber optic catalytic probe	[93]
	0.27	100	550	ICP RF	thermocouple probe + OES + NO titration + Langmuir probe	[92]
	0.28	30–280	300	ICP RF	side-arm + fiber optic catalytic probe	[96]
NiO	0.0077	10	300	ICP RF	thermocouple probe	[56]
	0.04	7–15	300	ICP RF	thin film heat-transfer gauge	[98]
	0.0008–0.056	4	295–620	ICP RF	side-arm thermocouple probe	[57]
	0.1	4	300	ICP RF	NO titration	[119]
	0.00089	650	300	ICP RF	Wrede–Harteck gauge	[120]
PbO	0.0058	10	300	ICP RF	thermocouple probe	[56]
	0.00063	650	300	ICP RF	Wrede–Harteck gauge	[120]
	0.015–0.09	10	300–700	ICP RF	catalytic probe	[58]
	0.013–0.018	110	300–473	pulsed RF	actinometry	[65]
Pd	0.00038	400–1300	300	pulsed RF	thin-film heat transfer gauge	[64]
PET	0.0024	8–200	320	MW surfatron	catalytic probe	[76]
	0.00083	150–350	300	double pulse DC	discharge-induced emission spectroscopy + actinometry	[112]
PM1000	0.17–0.21	800	1500–1610	ICP wind tunnel PWK3	pyrometry + calorimetry + Pitot probe	[109]
	0.206–0.233	72–93	1499–1611	ICP wind tunnel PWK3	thermocouple + Pitot probe	[110]
	0.0003–0.16	36, 500–3500	105–1061	arc jet	side-arm + LIF	[46]

Table 2. *Cont.*

Material	γ	p **[Pa]**	T **[K]**	**Plasma**	**Method**	**Ref.**
PM1000	0.046–0.19	300, 1000	850–1650	MW	actinometry + OES	[82]
	0.019–0.057	300, 1000	850–1650	MW	actinometry + OES	[82]
	0.003–0.011	300, 1000	850–1650	MW	actinometry + OES	[82]
PM 1000 sol-gel	0.003–0.49	36, 500–3500	280–1220	arc jet	side-arm + LIF	[46]
PM1000 oxidized	0.313	64	1559	ICP wind tunnel PWK3	thermocouple + Pitot probe	[110]
PP	0.02–0.3	1–100	400–600	ICP&CCP RF	TALIF	[50]
PS	0.0022	8–200	320	MW surfatron	catalytic probe	[76]
Pt	0	40	300	atomic beam	mass spectrometry	[85]
	0.014	1–4	300	ICP RF	Wrede–Harteck gauge + NO titration	[55]
	0.01–0.1	150–220	300–1100	MW	paramagnetic resonance absorption spectrometer + isothermal calorimetric detector	[73]
	0.0053	40	300	MW	side-arm + LIF	[118]
	0.0027 (0.0016)	133	300	ICP RF	NO-titration	[60]
	0.00055	400–1300	300	pulsed RF	thin-film heat transfer gauge	[64]
PtO_2	0.004	7–15	300	ICP RF	thin film heat-transfer gauge	[98]
PTFE	0.0011	8–200	320	MW surfatron	catalytic probe	[76]
	0.00066	150–350	300	double pulse DC	discharge-induced emission spectroscopy + actinometry	[112]
	0.000073 (0.000064)	133	300	ICP RF	NO-titration	[60]
	0.0006	400, 1300	300	CCP RF	actinometry + FTIR + model	[54]
	0.0004	30–280	300	ICP RF	side-arm + fiber optic catalytic probe	[96]
Pyrex (SiO_2 +B_2O_3)	0.000033–0.00012	10	300	ICP RF	thermocouple probe	[56]
	0.00019	10–100	300	ICP RF	thermocouple probe	[107]
	0.000077	10–400	300	MW	thermocouple probe	[97]
	0.0001	7–15	300	ICP RF	thin film heat-transfer gauge	[98]
	0.00013	1–4	300	ICP RF	Wrede–Harteck gauge + NO titration	[55]
	0.000031–0.000045	650	300	ICP RF	Wrede–Harteck gauge	[120]
	0.00012–0.0003	10–13	300–700	electrode + electrodeless	thermocouple probe	[58]
	0.00034–0.0011	25–660	335–410	DC glow	TALIF + actinometry + FTIR (Fourier transform IR)	[115]
	0.0004–0.016	66–626	77–460	double pulse DC	time-resolved actinometry	[47]

Table 2. *Cont.*

Material	γ	p [Pa]	T [K]	Plasma	Method	Ref.
Pyrex	0.0039	150–350	300	double pulse DC	discharge-induced emission spectroscopy + actinometry	[112]
	0.00041–0.0052	266	300–400	DC glow	model + MW cavity + electrostatic + thermocouple probe	[102]
	0.00011–0.000061	133	300	ICP RF	NO titration	[60]
	0.0012–0.026	27; 500–3500	300–1640	arc jet	thermocouple + pyrometer + side arm	[103]
	0.000092 (0.000056)	133	300	ICP RF	NO-titration	[60]
	0.00002	26–213	300	MW magnetron	NO-titration + photometry	[72]
	0.0024	3–667	300	pulsed DC	VUV resonant absorption spectroscopy	[111]
	0.00044–0.00051	66–120	300	DC	Wrede–Harteck gauge + ozone detection	[121]
	0.006–0.05	810–2840	1435–1845	hypersonic arc jet	calorimetry + pyrometry	[134]
	0.0003–0.0036	100–1333	285–430	DC glow	time-resolved actinometry	[138]
	0.00002–0.0024	50–300	300	DC glow	actinometry + model	[113]
	0.0005	133–1330	300	MW	paramagnetic resonance	[130]
Pyrex coating	0.0058–0.0047	10000	1600–1800	ICP RF	stagnation point heat flux + model	[105]
Pyromark 2500	0.0012–0.20	36, 500–3500	465–1040	arc jet	side-arm + LIF	[46]
RbCl	0.00045–0.0024	10	300	ICP RF	thermocouple probe	[56]
RCG	0.008–0.023	400–2600	1400–1650	arc jet	stagnation point heat flux measurements + model	[100]
	0.0004–0.01	13–1330	300–1000	planetary reentry	kinetic model	[132]
Sb	0.00082	10	300	ICP RF	thermocouple probe	[56]
	0.00027	650	300	ICP RF	Wrede–Harteck gauge	[120]
Sb_2O_3	0.0082–0.021	110	300–473	pulsed RF	actinometry	[65]
Se	0.00017	10	300	ICP RF	thermocouple probe	[56]
Si	0.02–0.2	1–100	400–600	ICP&CCP RF	TALIF	[50]
	0.043	0.2	298–307	ICP RF	mass spectrometry + actinometry + thermal resistivity	[127]
Si + Cu	0.069	0.2	298–307	ICP RF	mass spectrometry + actinometry + thermal resistivity	[127]

Table 2. *Cont.*

Material	γ	p [Pa]	T [K]	Plasma	Method	Ref.
SiC	0.004–0.041	110	313–773	pulsed RF	actinometry	[65]
	0.004–0.0093	110	300–773	pulsed RF	actinometry + NO titration	[66]
	0.0003–0.46	27; 500–3500	300–1320	arc jet	thermocouple + pyrometer + side arm	[103]
	0.066–0.043	800	1230–1870	ICP wind tunnel PWK3	pyrometry + calorimetry + Pitot probe	[109]
	0.085–0.009	80–902	1236–2000	ICP wind tunnel PWK3	thermocouple + Pitot probe	[110]
	0.008	200	870	MW	actinometry + pyrometry	[79]
CVD-SiC	0.003–0.03	110	300–773	pulsed RF	actinometry + NO titration	[66]
SiC oxidized	0.113–0.114	78–607	1328–1964	ICP wind tunnel PWK3	thermocouple + Pitot probe	[110]
SiC + $HfBr_2$	0.052–0.0003	500–3500	1250–2000	arc-jet	heat-flux + thermocouple + pyrometry + LIF	[104]
SiO_2	0.00071	10	300	ICP RF	thermocouple probe	[56]
	0.3–0.01	1–100	300	ICP&CCP RF	TALIF	[50]
	0.0001–0.0004	30	300–1200	MW	thermocouple probe inside tube	[101]
	0.000008	30	194	MW	thermocouple probe inside tube	[101]
	0.0001	7–15	300	ICP RF	thin film heat-transfer gauge	[98]
	0.00012	10	300	ICP RF	catalytic probe	[58]
	0.00028–0.0029	4	300–500	ICP RF	side-arm thermocouple probe	[57]
	0.0001–0.003	600–6600	300	DC glow	time-resolved actinometry	[42]
	0.0005	133	300	pulsed DC	VUV absorption spectroscopy + model	[45]
	0.000086–0.0004	133	300	pulsed DC	time-resolved VUV absorption spectroscopy	[44]
	0.003	10000	300	plasmatron MW	heat transfer + TPM (tethered particle motion) model	[78]
	0.00004	150–220	300	MW	paramagnetic resonance absorption spectrometer + isothermal calorimetric detector	[73]
	0.0004–0.01	133	300–1000	planetary reentry	kinetic model	[132]
	0.00016	650	300	ICP RF	Wrede–Harteck gauge	[120]
	0.0016–0.011	10000	570–870	ICP RF	stagnation point heat flux + model	[105]
	0.039–0.104	200	1000–1770	MW	optical pyrometry + model	[83]

Table 2. *Cont.*

Material	γ	p **[Pa]**	T **[K]**	**Plasma**	**Method**	**Ref.**
SiO_2	0.00016–0.014	15–16	300–900	MW	Wrede–Harteck gauge	[70]
	0.00205	13–400	300	DC glow	time-resolved modulation actinometry	[43]
	0.004–0.041	110	313–773	pulsed RF	actinometry	[65]
	0.004–0.0093	110	300–773	pulsed RF	actinometry + NO titration	[66]
	0.005–0.014	200	846–1435	MW	OES + actinometry	[81]
	0.0049–0.014	200	850–1430	MW	OES + actinometry + pyrometry	[80]
	0.00016–0.0057	266	285–1960	DC glow	model	[135]
	0.053–0.108	82–300	1180–1650	ICP wind tunnel PWK3	thermocouple + Pitot probe	[110]
	0.079–0.00039		200–400		model	[88]
	0.000098	40	300	MW	side-arm + LIF	[118]
	0.0005	1000–2000	300	MW	NO-titration	[74]
	0.00005	1000	300	MW	NO-titration	[75]
	0.0012	400, 1300	300	CCP RF	actinometry + FTIR + model	[54]
	0.00002	67	300	MW	NO-titration	[71]
	0.04, 0.03, 0.028	67, 133, 267	300	MW	pulsed induced fluorescence	[77]
	0.00019, 0.0004, 0.0005	67, 133, 267	300	MW	pulsed induced fluorescence	[77]
	0.033–0.029		600–1000		semiclassical collisional model	[136]
	0.0046–0.0023		600–1000		semiclassical collisional model	[136]
	0.0006–0.01	10–10000	300–1250		model	[133]
	0.0001–0.02		300–1250		model	[89]
	0.00032	100–300	300	MW	paramagnetic resonance absorption spectrometer + isothermal calorimetric detector	[129]
	0.0016	30–280	300	ICP RF	side-arm + fiber optic catalytic probe	[96]
SiO_2 β-cristobalite	0.01–0.09	200	850–1820	MW	OES + actinometry	[81]
	0.0094–0.1	200	800–1830	MW	OES + actinometry + pyrometry	[80]
SiO_2 + SiC	0.01	200	850	MW	actinometry + pyrometry	[79]
SiOCH nanoporous	0.0038	400, 1300	300	CCP RF	actinometry + FTIR + model	[54]
	0.004	400, 1300	300	CCP RF	actinometry + FTIR + model	[54]
	0.0044	400, 1300	300	CCP RF	actinometry + FTIR + model	[54]

Table 2. *Cont.*

Material	γ	p **[Pa]**	T **[K]**	**Plasma**	**Method**	**Ref.**
SnO_2	0.001	650	300	ICP RF	Wrede–Harteck gauge	[120]
soda glass	0.00034	10	300	ICP RF	thermocouple probe	[56]
stainless steel	0.09	1	300	pulsed RF	actinometry	[114]
	0.35–0.02	1–100	400–600	ICP&CCP RF	TALIF	[50]
	0.17	5	330	ICP RF	neutral mass spectrometry and Langmuir probe	[122]
	0.07	10–100	400–700	ICP RF	thermocouple probe	[59]
	0.04–0.16	40	300	atomic beam	mass spectrometry	[85]
	0.09	0.2–3	300	ICP RF	spinning wall desorption mass spectrometry	[61]
	0.1–0.4	2–10	300	pulsed RF	TALIF	[62]
	0.5	3	300	MW	actinometry	[69]
	0.01	40	300	CCP RF	energy resolved actinometry (fitting)	[51]
	0.013–0.005	10–400	300	CCP RF	TALIF (fitting)	[52]
	0.14	1–15	300–400	ICP RF	Langmuir probe + simulation	[123]
	0.3	1–11	300–400	ICP RF	mass spectrometry + Langmuir probe + ion flux probe	[125]
	0.09	0.2–3	310	ICP RF	Langmuir probe + actinometry + mass spectrometry	[128]
	0.5–0.1	0.1–20	300	model	model	[90]
	0.015	66	300	CCP RF	model	[53]
	0.0099 (0.0064)	133	300	ICP RF	NO-titration	[60]
	0.006–0.002	133–267	300	pulsed RF	LIF + TALIF + PIE (plasma-induced emission)	[117]
	0.07	100	550	ICP RF	thermocouple probe + OES + NO titration + Langmuir probe	[92]
	0.016	40	300	MW	side-arm + LIF	[118]
steel	0.0071	300	313	MW	NO-titration + thermal resistivity	[106]
TiO_2	0.013–0.028	110	313–773	pulsed RF	actinometry	[65]
	0.014–0.031	110	300–773	pulsed RF	actinometry + NO titration	[66]
V_2O_5	0.00048	650	300	ICP RF	Wrede–Harteck gauge	[120]
W	0.013	1–4	300	ICP RF	Wrede–Harteck gauge + NO titration	[55]
WO_3	0.017	650	300	ICP RF	Wrede–Harteck gauge	[120]
	0.012–0.078	110	313–773	pulsed RF	actinometry	[65]
W oxidized	0.035	83	1371	ICP wind tunnel PWK3	thermocouple + Pitot probe	[110]

Table 2. *Cont.*

Material	γ	p [Pa]	T [K]	Plasma	Method	Ref.
Zn	0.0043	300	313	MW	NO-titration + thermal resistivity	[106]
ZnO	0.00034–0.1	4	295–620	ICP RF	side-arm thermocouple probe	[57]
	0.00044	650	300	ICP RF	Wrede–Harteck gauge	[120]
ZrB_2 + 15SiC + $2MoSi_2$	0.01–0.1	200	770–1820	MW	thermocouple probe + OES + actinometry	[84]
ZrB_2 + 15SiC + $2MoSi_2$	0.0073–0.03	200	770–2000	MW	thermocouple probe + OES + actinometry	[84]
ZrB_2 + $10HfB_2$ + 15SiC + $2MoSi_2$	0.019–0.135	200	1000–1820	MW	thermocouple probe + OES + actinometry	[84]
ZrB_2 + $10HfB_2$ + 15SiC + $2MoSi_2$	0.023–0.096	200	830–1820	MW	thermocouple probe + OES + actinometry	[84]
ZrO_2 + Y_2O_3	0.04–0.21	200	900–2300	MW	thermocouple probe + OES + actinometry	[84]

Table 3. Advantages and disadvantages of various types of measuring methods for determination of the neutral atom density and recombination coefficient.

Measurement Method	Advantages	Disadvantages
Calorimetry	Simple, cheap, reliable	Slow method, slight changes of plasma conditions around detector
Emission spectroscopy	Quick, non-intrusive method	Only measurable in glow region, unreliable interpretation of data
Actinometry	Quick, non-intrusive method	Only measurable in glow region, unreliable interpretation of data
LIF	Non-intrusive method, good spatial and temporal resolution	Expensive, complicated interpretation of data
NO titration	Simple method, quick determination	Poisoning of reactor, introduction of reactive gas
Wrede–Harteck	Simple setup, only pressure detectors needed	Works only in the afterglow, needs a complimentary method
Mass spectrometry	Non-intrusive method	Complicated setup, needs simulation to interpret results
Paramagnetic resonance	Non-intrusive method	Absolute densities harder to determine, needs a complimentary method

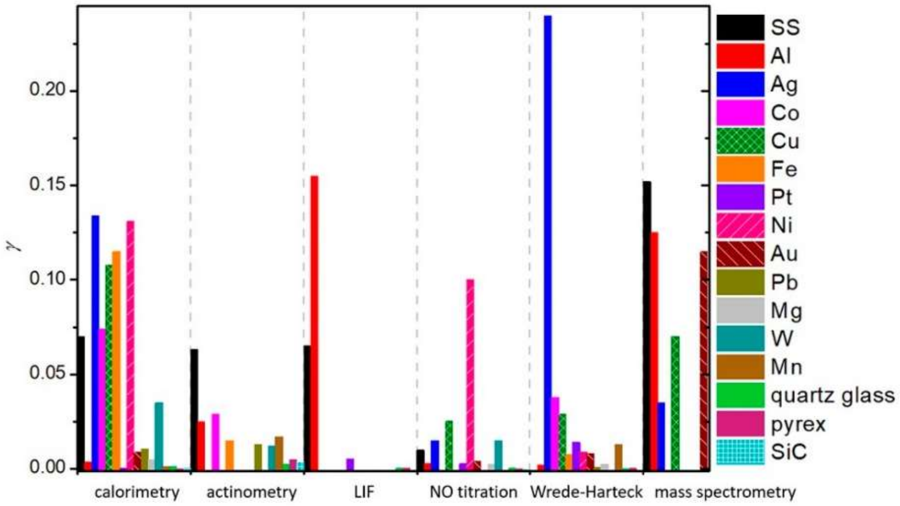

Figure 13. Comparison of average γ determined using different measuring techniques.

4. Material Categorization

As explained in previous chapters, different authors used different experimental conditions to determine the recombination coefficients. Some authors reported values for pristine materials, but most for oxidized materials. Many materials will form a thin oxide film upon exposure to oxygen, so it is difficult to ensure an oxygen-free surface. Not surprisingly, the reported results are scattered, sometimes over an order of magnitude or more. The average values are shown in Table 4, which also shows the lowest and largest reported values as well as average values at different temperatures.

So much gathered data for γ enables meta-analysis of the reported results. The values reported for a few materials were compared in the hope of finding useful correlations. Based on the determined γ, we can divide the materials into three distinct groups. Materials exhibiting catalytic properties ($\gamma > 0.1$) were deemed catalytic, followed by semi-catalytic materials ($0.1 > \gamma > 0.01$), and the rest were deemed inert ($\gamma < 0.01$). Many of the materials were hard to categorize, with their γ evolving with varying parameters, making a material catalytic under certain conditions, only to become inert under different conditions. Therefore, the dividing lines between the categories of materials were mostly blurred and subject to one's opinion. Nevertheless, this categorization helps tidy up the long list of γ for various materials. A comparison of average reported values of γ for the most commonly studied materials is shown in Figure 14 for various plasma system configurations and in Figure 15 for different methods of measurement. In general, metals have higher γ, with glass materials (quartz glass and Pyrex) having much lower γ. First up, we will examine catalytic materials.

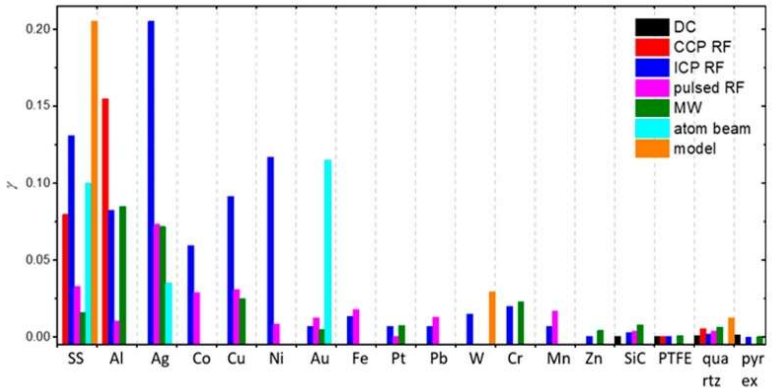

Figure 14. Comparison of average reported recombination coefficients for the most commonly studied materials in various plasma systems.

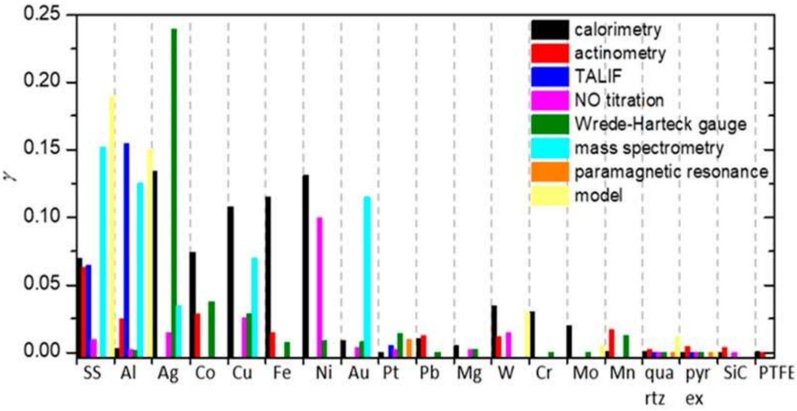

Figure 15. Comparison of average reported recombination coefficients for the most commonly studied materials for different measurement methods.

4.1. Catalytic Materials

The candidate materials most frequently declared as catalytic for oxygen atom recombinations are metals, with Ag, Cu, Ni consistently exhibiting the highest γ in various studies. In Figure 16, γ versus surface temperature is shown for a handful of catalytic materials, while in Figure 17, that same graph is repeated for materials tested at higher temperatures (above 1000 K). In general, γ increases with increasing surface temperature, at least in the range from room temperature to about 2000 K.

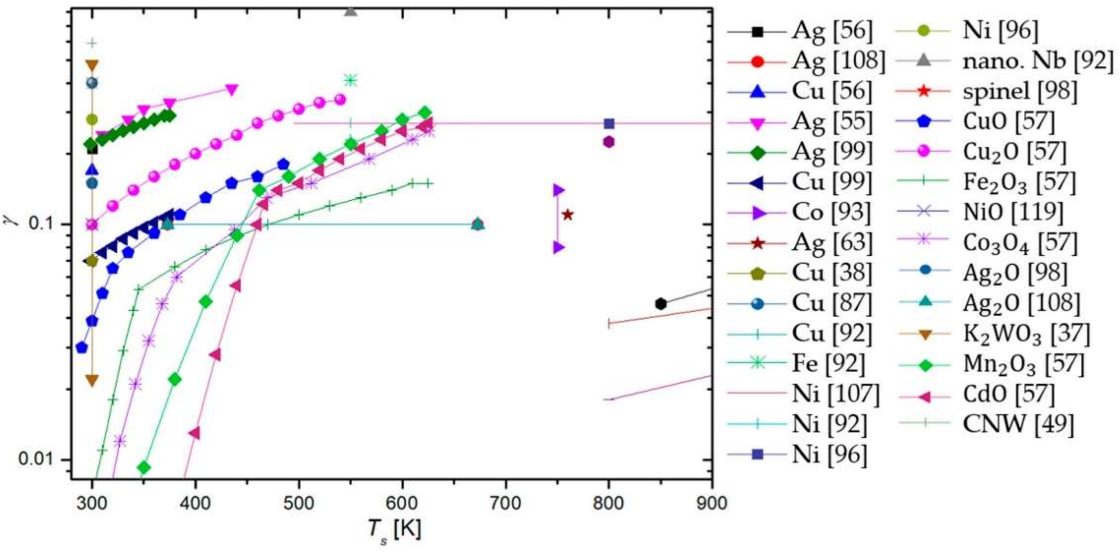

Figure 16. Recombination coefficient (γ) of neutral oxygen atoms versus surface temperature (T_s) for various catalytic surfaces.

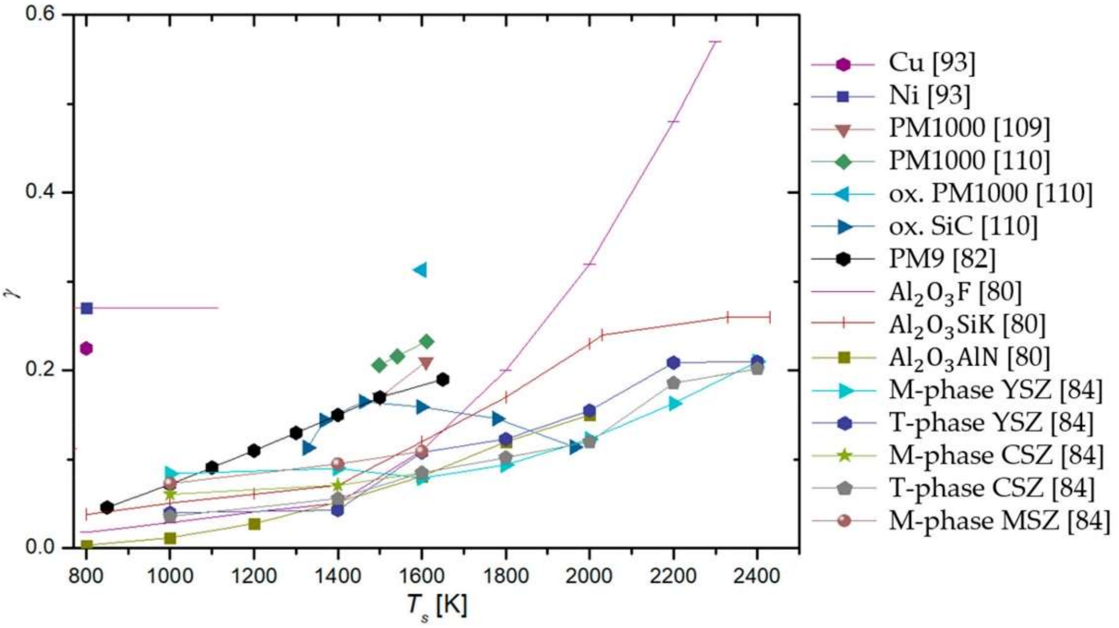

Figure 17. Recombination coefficient (γ) of neutral oxygen atoms versus surface temperature (T_s) for various catalytic surfaces at temperatures higher than 800 K.

Table 4. Recombination coefficient values reported for various materials and their composites. Along with the lowest and highest values reported, average values and standard deviations were calculated (where possible). Materials were grouped together with their oxides, as were certain alloys.

Material	Lowest Reported Value	Largest Reported Value	Average Value	Standard Deviation	Average Value (300 K)	Average Value (600 K)	Average Value (1000 K)
stainless steel	0.002 [117]	0.5 [90]	0.103	0.056	0.098	0.123	/
Al	0.0001 [125]	0.6 [124]	0.0948	0.308	0.068	0.101	0.233
Ag	0.015 [106]	0.38 [55]	0.148	0.385	0.114	0.079	0.037
Co	0.00049 [120]	0.25 [57]	0.0763	0.276	0.027	0.157	/
Cu	0.00217 [40]	0.4 [87]	0.0903	0.301	0.0604	0.244	/
Fe	0.0046 [57]	0.41 [92]	0.0685	0.262	0.0203	0.219	/
Pt	0.00055 [64]	0.1 [73]	0.0195	0.140	0.0161	0.0503	0.0503
Ni	0.0008 [57]	0.28 [96]	0.104	0.322	0.0593	0.199	0.270
Au	0.0032 [60]	0.2 [85]	0.029	0.057	0.0347	0.016	0.02
Nb	0.02 [93]	0.09 [91]	0.073	0.030	0.09	0.067	/
Pb	0.00063 [120]	0.09 [58]	0.024	0.030	0.0086	0.09	/
Mg	0.0023 [60]	0.022 [57]	0.00697	0.0835	0.00396	/	/
Cr	0.0002 [57]	0.072 [82]	0.0311	0.176	0.0202	0.0002	0.023
Mn	0.0012 [57]	0.299 [57]	0.071	0.052	0.0104	0.299	/
Zn	0.00034 [57]	0.01 [57]	0.0263	0.162	0.00169	0.01	/
Mo	0.001 [120]	0.02 [58]	0.0082	0.0906	0.0086	0.007	/
Mn	0.0012 [57]	0.299 [57]	0.071	0.267	0.0104	0.162	/
W alloys	0.005 [37]	0.48 [37]	0.0712	0.267	0.0744	0.078	0.035
Zr alloys	0.0073 [84]	0.21 [84]	0.078	0.065	/	0.0415	0.148
Ti alloys	0.0097 [65]	0.078 [65]	0.029	0.022	0.0123	0.0452	/
PM1000	0.0003 [82]	0.313 [110]	0.124	0.101	/	/	0.0718
quartz glass	0.000008 [101]	0.3 [50]	0.016	0.042	0.0111	0.0082	0.0226
quartz crystal	0.0094 [80]	0.1 [80]	0.052	0.043	/	/	0.0497
Pyrex	0.00002 [72]	0.05 [134]	0.0039	0.0097	0.00089	0.00095	0.00057
RCG	0.0004 [132]	0.023 [100]	0.0104	0.0081	0.0004	/	0.009
SiC	0.0003 [104]	0.46 [103]	0.047	0.100	0.00283	0.0268	0.146
PTFE	0.000073 [60]	0.0011 [76]	0.00057	0.00034	0.00057	/	/
carbon	0.0005 [94]	0.59 [49]	0.16	0.25	0.16	/	/

The increasing recombination coefficient revealed in Figures 16 and 17 may be explained by the increasing surface mobility of adsorbed oxygen atoms. As mentioned earlier, one model of surface recombination (Langmuir–Hinshelwood) predicts the association of two adsorbed atoms and the formation of a molecule, which is desorbed from the surface. The surface association of atoms to molecules requires close proximity of two atoms. The average internuclear distance in oxygen molecules in the ground vibrational state is about 0.12 nm. The intermolecular distance is much shorter than the distance between two neighboring atoms in the solid material. Namely, the surface density of atoms in the solid material is roughly 10^{19} m^{-2}, so the average distance between two atoms in the solid material is roughly 0.3 nm. It is reasonable to assume at most one adsorbed oxygen atom per atom of solid material, so the distance between neighboring adsorbed oxygen atoms is a few times larger than the distance of oxygen atoms in a stable oxygen molecule. These are average values, and the atoms (both of the solid material and adsorbed O-atoms) oscillate on the surface due to phonon excitations. The oscillation amplitude increases with increasing surface temperature, and thus the probability for association following the Langmuir–Hinshelwood mechanism. Unfortunately, the effect is yet to be addressed by theoreticians who may be able to provide a scientifically spotless model for increasing surface recombination due to increasing oscillations. Equation (4) predicts an exponential increase in the recombination coefficient with increasing surface temperature, but the general behavior, as deduced from Figures 16 and 17, only partially confirms such a behavior.

The discrepancy between the simple theory, as in Equation (4), and the experimental results, as in Figure 1 or Figure 2, may be because of numerous reasons. One trivial explanation is the existence of the Eley–Rideal mechanism, whose temperature behavior is difficult to predict. In general, both mechanisms should be responsible for catalytic surface recombination, but the intensity of surface reactions depends on numerous parameters, such as the density of surface adsorption sites and the surface morphology on the nanometer scale.

It is worth stressing that the surface morphology of many catalytic materials depends on their history, particularly the temperature of materials upon exposure to oxygen plasma. It is known that many metals form nanostructures upon oxidation [139]. The oxidation obviously depends on the surface temperature. The richer morphology on the nanometer or sub-micrometer scale will result in a larger recombination coefficient. The establishment of the rich morphology of surface oxides formed upon treatment of catalytic materials with oxygen plasma is often irreversible. Unfortunately, very few authors reported on the history of the samples before measuring the recombination coefficient for oxygen atoms.

Apart from studying the temperature dependence of γ, we are also interested in the effects of pressure on γ. In Figure 18, the γ of catalytic materials is shown with respect to pressure. However, no discernable trend is noticeable.

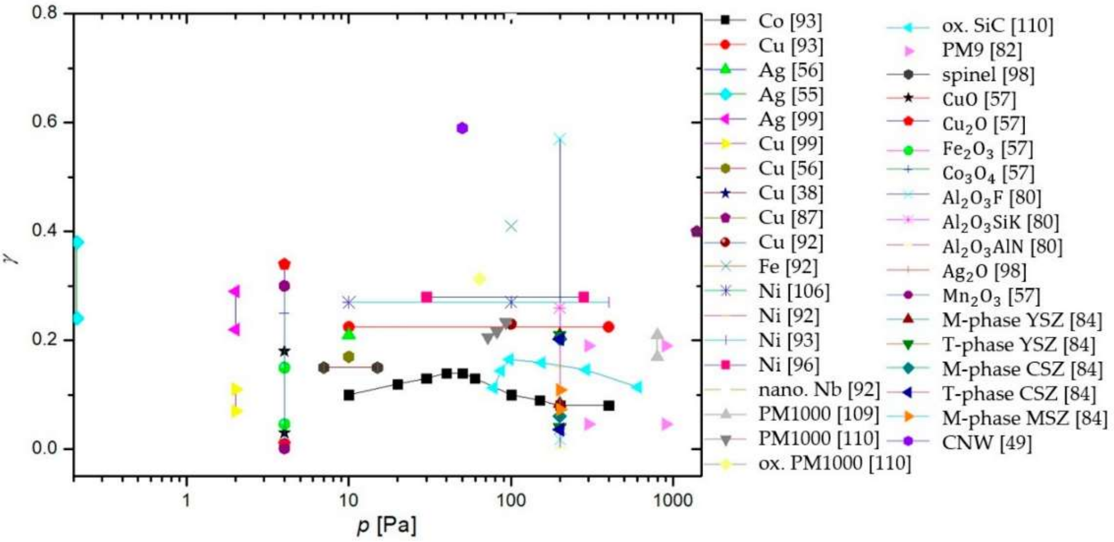

Figure 18. Recombination coefficient (γ) of neutral oxygen atoms versus pressure (p) for various catalytic surfaces.

4.2. Semi-Catalytic Materials

Semi-catalytic materials are the most varied category, with materials ranging from various metals and their alloys to different types of glass. This is partly due to semi-catalytic materials being the middle category, with overlap from both catalytic and inert materials. When looking at the surface temperature dependence of γ in Figure 19, it is clear that the relationship is not straightforward. While some materials exhibit a rise in γ with rising surface temperature, others do the opposite, and still, other materials, such as SiC [109,110], C-CAT [104], and spinel [109], behave in more complex ways.

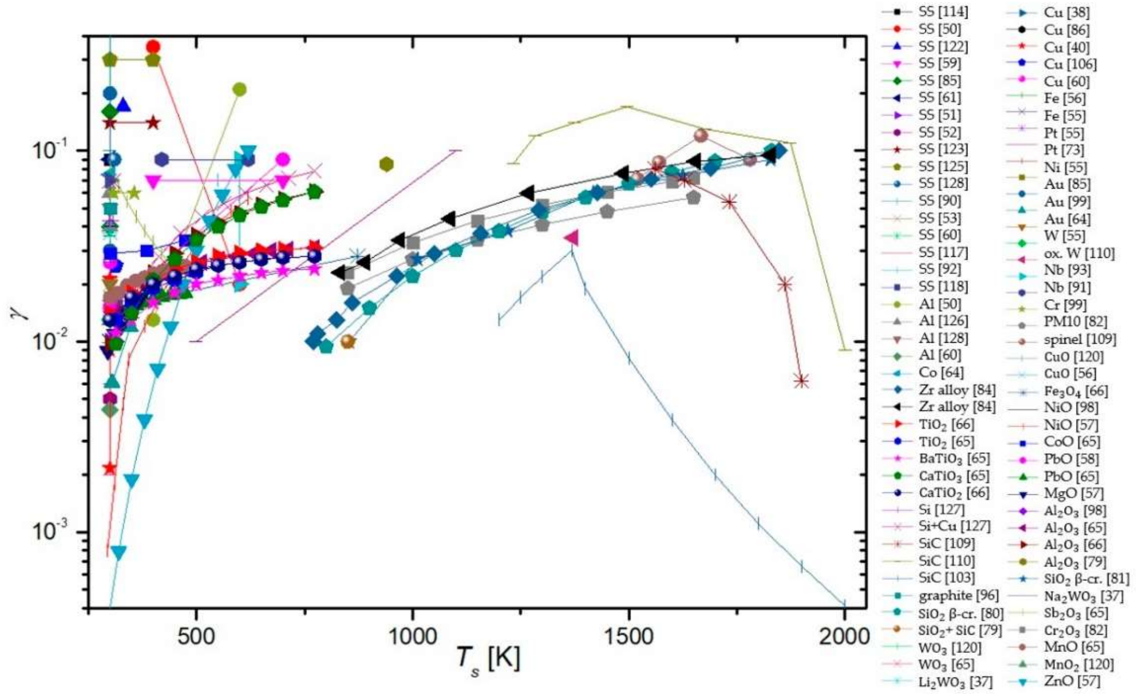

Figure 19. Recombination coefficient (γ) of neutral oxygen atoms versus surface temperature (T_s) for various semi-catalytic surfaces.

Regarding pressure dependence, the γ of some semi-materials seems to decrease with increasing pressure, but in general, we fail to observe any overarching trends. The results are shown in Figure 20.

4.3. Inert Materials

Materials that have little-to-no interactions with neutral oxygen atoms are categorized as inert. With such γ, only up to 1% of incident neutral atoms recombine. In this category, we also have two of the most-researched materials when it comes to γ: quartz and Pyrex. In Figure 21, the γ of glass-based materials, including quartz glass and Pyrex, is shown as determined by various researchers with respect to surface temperature. In a separate graph in Figure 22, the same results are shown with respect to pressure. As evident from Figure 21, some parallels can be drawn from different researchers as to the behavior of γ of glass-based surfaces in respect of temperature. Regrettably, the same is not true for the pressure dependence of γ Figure 22.

For the rest of the inert materials, Figures 23 and 24 show the evolution of γ versus temperature and pressure, respectively. Some common behavior of different materials can be seen: γ seems to increase with surface temperature. Again, nothing conclusive can be determined regarding the pressure dependence of γ.

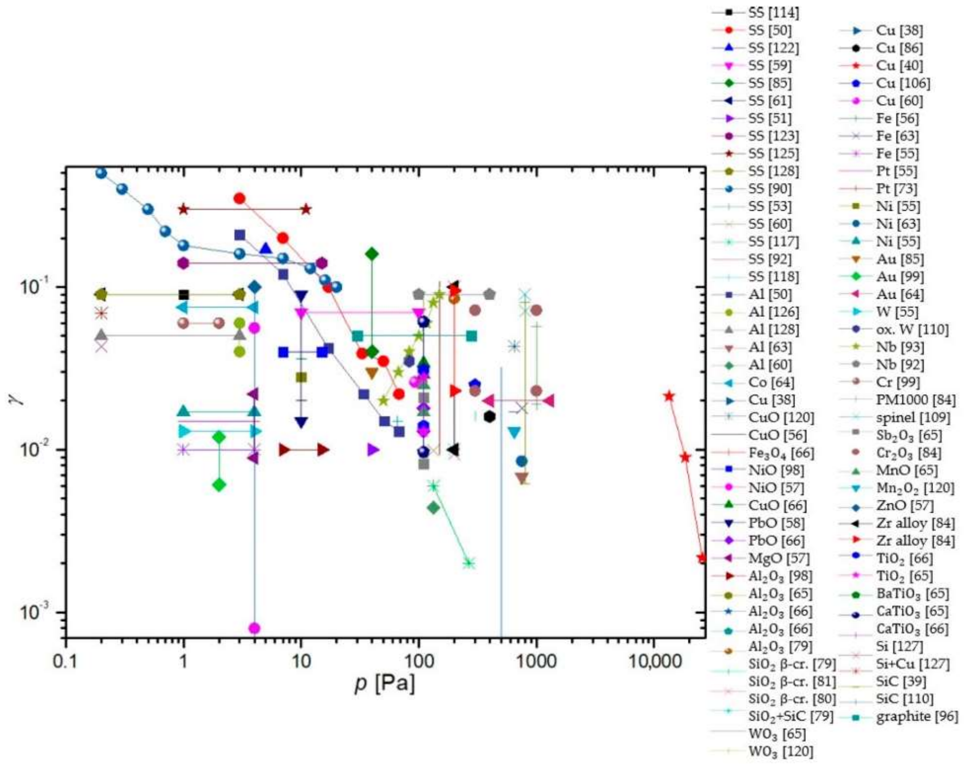

Figure 20. Recombination coefficient (γ) of neutral oxygen atoms versus pressure (p) for various semi-catalytic surfaces.

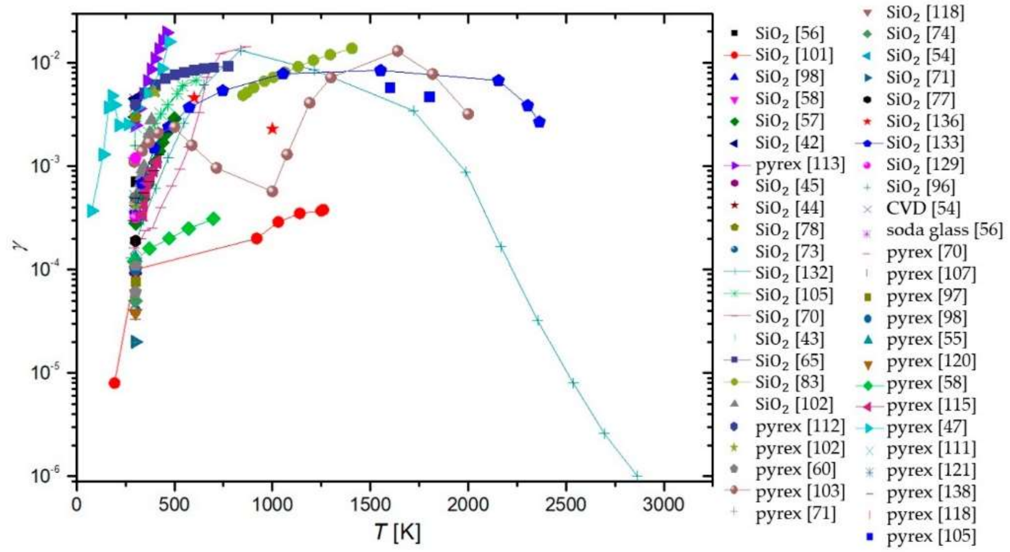

Figure 21. Recombination coefficient (γ) of neutral oxygen atoms versus surface temperature (T_s) for glass surfaces.

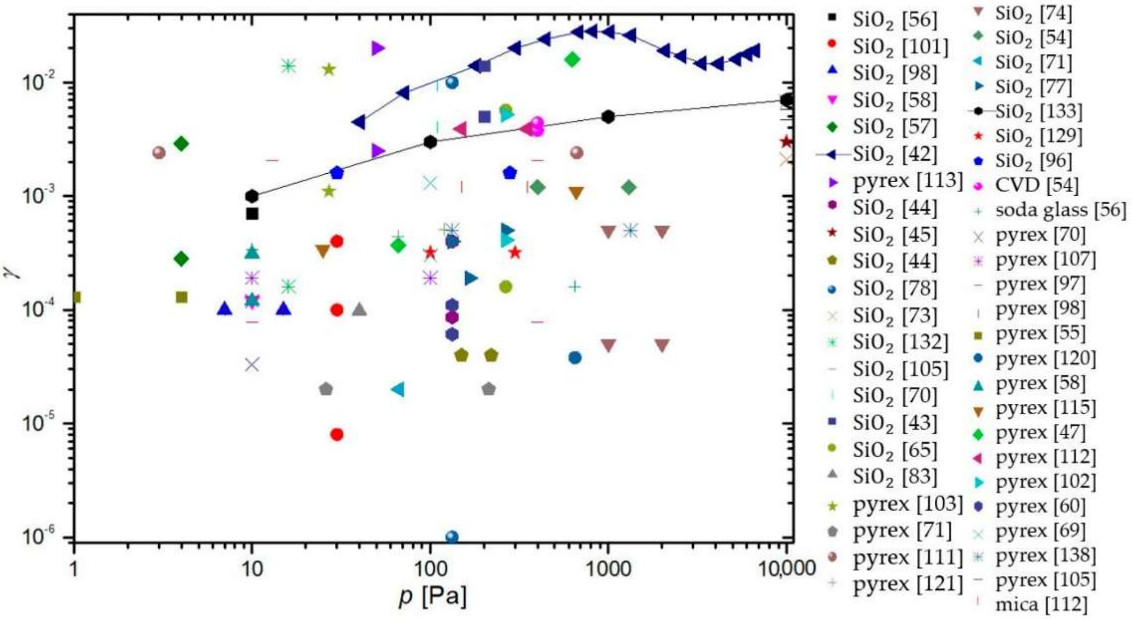

Figure 22. Recombination coefficient (γ) of neutral oxygen atoms versus pressure (p) for glass surfaces.

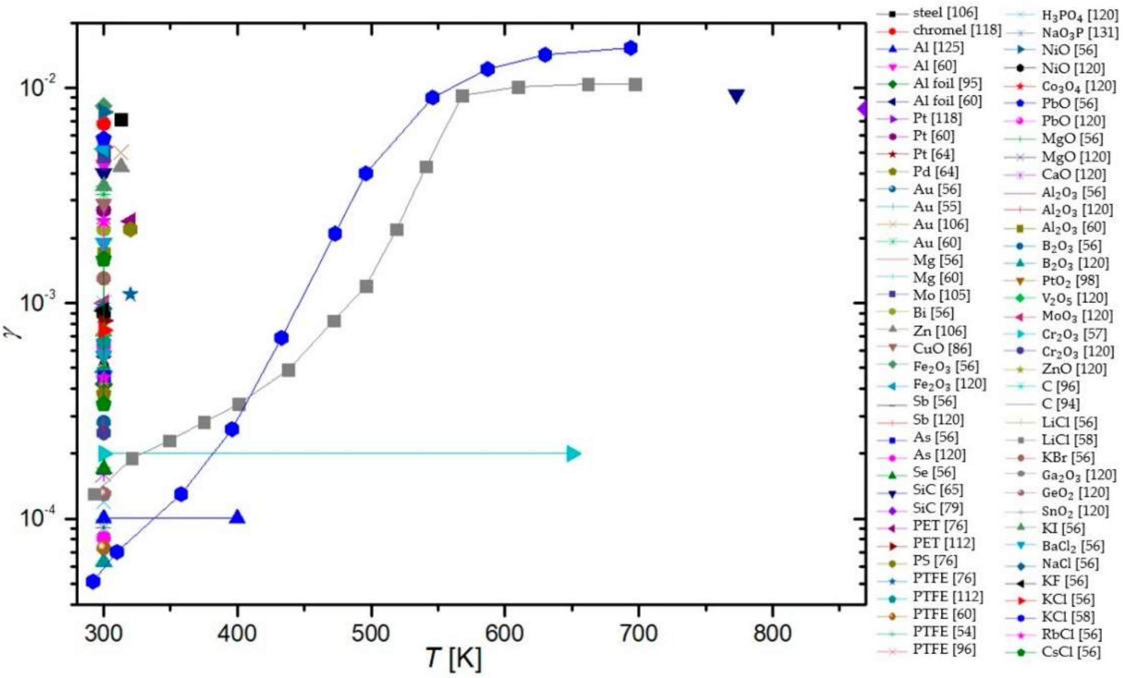

Figure 23. Recombination coefficient (γ) of neutral oxygen atoms versus surface temperature (T_s) for various inert surfaces.

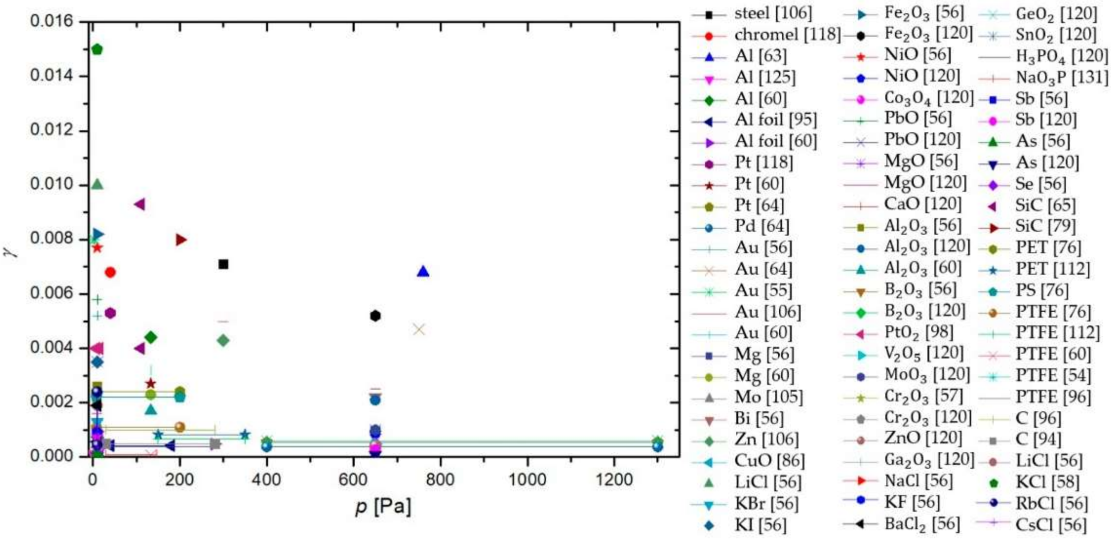

Figure 24. Recombination coefficient (γ) of neutral oxygen atoms versus pressure (p) for various inert surfaces.

5. Authors' Remarks

As reported by various authors, the recombination coefficients for the same (or similar) materials differ significantly. The reasons may be due to experimental errors (which were rarely reported by the authors) but also because of other effects tackled by a few authors. They include:

- The purity of materials and their surfaces, poisoning with adsorbed gaseous species.
- The presence of other species in the gas phase and synergies between atom recombination, irradiation with photons, bombardments with positively charged ions, and surface relaxation of metastables.
- The influence of surface morphology.

The most trivial one is the purity of materials. Most materials, in particular metals, are of limited purity. The foreign atoms will enable sites for *O*-atom adsorption of different bunding energy than the surface atoms of the investigating materials. Furthermore, the impurity atoms may segregate on surfaces causing the formation of a very thin layer of oxide, which is chemically different from the oxides of parent materials. This effect is particularly relevant for alloys. For example, stainless steel will form various surface oxides upon exposure to oxygen plasma. The native oxide film on stainless steel is iron oxide, but the most stable is chromium oxide which forms a passive film, and this prevents further oxidation and makes stainless steel oxidation-resistant. Other oxides may be formed on the stainless steel surface as well.

As mentioned above, the surface recombination of *O*-atoms to parent molecules requires adsorption on surfaces. The number of adsorption sites is limited and governs the recombination coefficient. The number of adsorption sites depends on the chemical composition and structure of the material surface, and this property will depend on the irradiation with energetic particles. The synergy with ions (which bombard the surface with a kinetic energy that depends on the surface-to-plasma potential) and VUV radiation (which breaks bonds in the surface film of thickness equal to the penetration depth of the energetic photons) is likely to occur but was not addressed by many authors. Furthermore, the energy brought by these particles will be dissipated on the surface, and this facilitates the surface mobility of atoms. The synergy may explain the much larger coefficient measured by Cartry et al. [77] for the case treatment in glowing plasma and oxygen plasma afterglow. The kinetics of recombination versus the fluxes and/or energy of ions and photons is yet to be elaborated. The same applies to the surface relaxation of metastables and its contribution to the recombination probability. In Figure 25, measurements of γ for quartz glass (the most commonly studied material) in the plasma glow and afterglow are compared. In general, the measured γ is lower in the afterglow, although not without a few outliers.

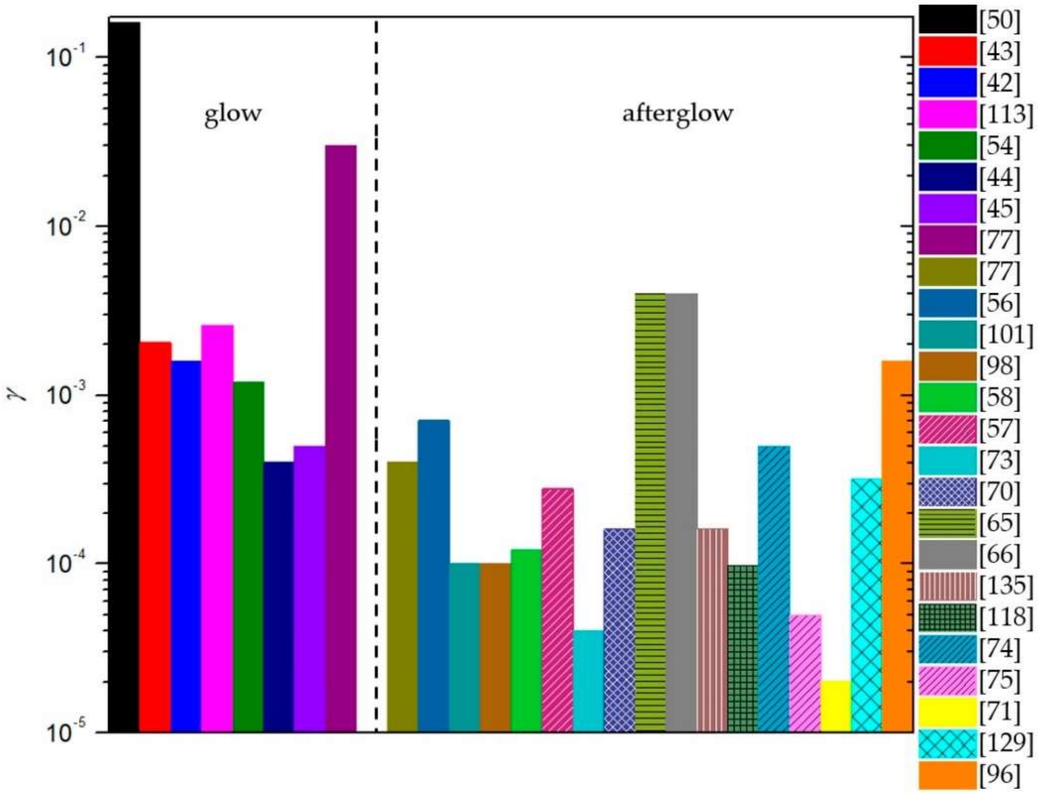

Figure 25. Compendium of γ of quartz glass measured at room temperature. Measurements in the glowing region of plasma are separated from the measurements in the afterglow.

Surface morphology was rarely reported in articles dealing with heterogeneous surface recombination of *O*-atoms. The effect of surface morphology on the measured recombination coefficient is evident in Figure 26. The atoms arriving from the gas phase enter the gaps in the surface of the solid material and experience numerous elastic collisions with the surface. There is a certain probability for adsorption and recombination at each collision, so the measured recombination coefficient depends on the number of collisions within the gap. In the limiting case of infinitely thin walls and infinitely long gaps, the measured recombination coefficient should approach 1, irrespective of the catalyticity of the smooth materials. The *O*-atoms are trapped in the material of such morphology, so they cannot leave the gap without recombining to form the parent molecules. This effect may explain the huge value of the recombination coefficient on anodized aluminum, as reported by Kurunczi et al. [124]. Namely, anodized aluminum may form a very porous structure. In fact, one of the largest coefficients was reported for carbon nanowalls [49], although amorphous carbon (or even smooth graphite) is far from being catalytic. Furthermore, the exposure of many materials to oxygen plasma at elevated temperatures may cause nanostructuring of the surface, and this increases the recombination coefficient. The influence of morphology is yet to be studied systematically.

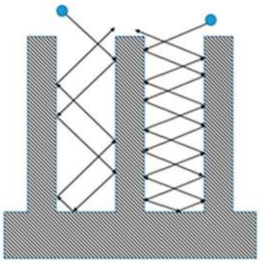

Figure 26. An illustration of the effect of surface morphology on the measured recombination coefficient. The arrows represent the path of atoms within the gaps in the approximation of elastic collisions with the walls.

6. Conclusions

In this review article, we examined various publications that reported the coefficient for heterogeneous surface recombination of oxygen atoms (γ). Special emphasis was put on finding how it changes with two key parameters: the surface temperature of the material and the pressure in the system. Knowing γ is of great importance when working with plasma since it governs our choice of materials for any given plasma-related task. If we are constructing a plasma reactor, we will search for inert materials as building blocks. On the other hand, if we want to measure plasma with a calorimetric method, we would utilize a catalytic material to increase the responsiveness of our probe. There are countless uses of oxygen plasma, and with that come countless choices of the use of proper materials.

Surface recombination may depend on the choice of material, but it still follows one of two proposed mechanisms: the Langmuir–Hinshelwood mechanism or the Eley–Rideal mechanism. The characteristic property of surface recombination is γ, which, in its purest form, is the ratio between the flux of incident neutral atoms and the flux of molecules leaving the surface. For this article, we limited ourselves to neutral oxygen surface recombinations and created a compendium of γ, determined by various authors for different materials. Experimental conditions such as the type of discharge and methods used for the evaluation of γ were also reviewed to find any possible influence on the measured γ. Discharges used by various authors can be categorized into four groups in this paper: DC, RF, MW, and other types of discharges, such as the shock tube and atomic beam discharges. γ was mostly determined using the following methods, which are also briefly explained in the paper: calorimetry, emission spectroscopy, actinometry, LIF, *NO* titration, Wrede–Harteck gauges, mass spectrometry, paramagnetic resonance, and numerical methods. It was found that the reported values of γ may differ by several orders of magnitude for the same material. It was difficult to draw any clear correlations because some data were not statistically significant enough. Nevertheless, the highest reported values were found for RF-ICP systems and the calorimetric method, which were the most often used by researchers.

A comparison of γ for various materials between different publications clearly demonstrates that it can be divided into three distinct categories: catalytic, semi-catalytic, and inert. For each category, we examined the dependence of γ on the surface temperature of the material and the pressure inside the experimental systems. We noticed a number of publications agreeing on the connection between surface temperature and γ. However, that was not always the case. For catalytic materials, a general increase in γ with increasing surface temperature was observed. No conclusions could be taken regarding the dependence of γ on pressure for all categories of materials. Semi-catalytic materials exhibited a variety of behaviors when examining the evolution of γ with surface temperature. However, a general rise of γ with increasing surface temperature could not be attributed to all the materials. Data on γ for inert materials was the most common across all publications due to extensive research on quartz glass and Pyrex. Inert glass materials exhibited complex behavior of γ with respect to surface temperature, while other inert materials exhibited a general rise in γ with increasing surface temperature.

This review article will serve as our basis for further research into γ of various materials, and the gathered publications as a great point of reference in further studies of surface recombinations.

Author Contributions: Conceptualization, R.Z. and D.P.; methodology D.P.; validation, R.Z. and D.P.; formal analysis, D.P. and A.V.; investigation, D.P. and A.V.; resources, R.Z. and D.P.; data curation, D.P.; writing—original draft preparation, D.P.; writing—review and editing, M.M. and A.V.; visualization, D.P., R.Z. and M.M.; supervision, R.Z.; project administration, M.M., G.P. and D.Đ.; funding acquisition, M.M., G.P. and D.Đ. All authors have read and agreed to the published version of the manuscript.

Funding: This research was funded by the Slovenian Research Agency, grant number P2-0082 and L2-4487.

Institutional Review Board Statement: Not applicable.

Informed Consent Statement: Not applicable.

Data Availability Statement: All collected and analyzed data are presented in this manuscript.

Conflicts of Interest: The authors declare no conflict of interest. The funders had no role in the design of the study; in the collection, analyses, or interpretation of data; in the writing of the manuscript; or in the decision to publish the results.

References

1. Mandal, R.; Singh, A.; Singh, A.P. Recent developments in cold plasma decontamination technology in the food industry. *Trends Food Sci. Technol.* **2018**, *80*, 93–103. [CrossRef]
2. Oliveira, M.; Fernandez-Gomez, P.; Alvarez-Ordonez, A.; Prieto, M.; Lopez, M. Plasma-activated water: A cutting-edge technology driving innovation in the food industry. *Food Res. Int.* **2022**, *156*, 111368. [CrossRef] [PubMed]
3. Abou Saoud, W.; Assadi, A.A.; Kane, A.; Jung, A.-V.; Le Cann, P.; Gerard, A.; Bazantay, F.; Bouzaza, A.; Wolbert, D. Integrated process for the removal of indoor VOCs from food industry manufacturing: Elimination of Butane-2,3-dione and Heptan-2-one by cold plasma-photocatalysis combination. *J. Photochem. Photobiol. A Chem.* **2020**, *386*, 112071. [CrossRef]
4. Schettgen, T.; Esser, A.; Kraus, T.; Ziegler, P. Plasma levels of unintentionally produced non-Aroclor polychlorinated biphenyl (PCB) congeners in workers from the silicone rubber industry. *Chemosphere* **2022**, *291*, 132722. [CrossRef] [PubMed]
5. Sauvageau, J.-F.; Fortin, M.-A. Recovery of Noble metal elements from effluents of the semiconductor industry as nanoparticles, by dielectric barrier discharge (DBD) plasma treatment. *Hydrometallurgy* **2020**, *197*, 105483. [CrossRef]
6. Elfa, R.R.; Nayan, N.; Ahmad, M.K.; Wibowo, K.M.; Soon, C.F.; Sahdan, M.Z.; Mamat, M.H.; Ahmad, M.Y.; Aldalbahi, A. Atmospheric pressure plasma needle jet treated on aluminium thin film for semiconductor industries. *Mater. Today-Proc.* **2019**, *7*, 715–720. [CrossRef]
7. Zhu, L.; Xiao, C.Q.; Teng, X.; Xu, M.Z.; Yin, L.H. An inductively coupled plasma mass spectrometry method for the determination of elemental impurities in calcium carbonate mineral medicine. *Spectrochim. Acta Part B At. Spectrosc.* **2022**, *192*, 106429. [CrossRef]
8. Bonzanini, A.D.; Paulson, J.A.; Graves, D.B.; Mesbah, A. Toward Safe Dose Delivery in Plasma Medicine using Projected Neural Network-based Fast Approximate NMPC. *IFAC Pap.* **2020**, *53*, 5279–5285. [CrossRef]
9. Setsuhara, Y. Low-temperature atmospheric-pressure plasma sources for plasma medicine. *Arch. Biochem. Biophys.* **2016**, *605*, 3–10. [CrossRef]
10. Rajeshkannan, A.; Ali, M.; Prakash, R.; Prasad, R.; Jeevanantham, A.K.; Jayaram, K. Optimizing the Process Parameters in Plasma Arc Cutting using Taguchi Approach for the Case Industry in Fiji. *Mater. Today Proc.* **2020**, *24*, 1122–1131. [CrossRef]
11. Mavrin, A.A. Improved fits of coronal radiative cooling rates for high-temperature plasmas. *Radiat. Eff. Defects Solids* **2018**, *173*, 388–398. [CrossRef]
12. Chen, P.; Li, D.; Zuo, C.; Li, Z.S.; Chen, D.Z. A method to evaluate the plasma equivalent resistance of fusion relevant RF ion sources. *Fusion Eng. Des.* **2021**, *173*, 112926. [CrossRef]
13. Recek, N.; Mozetic, M.; Jaganjac, M.; Milkovic, L.; Zarkovic, N.; Vesel, A. Improved proliferation of human osteosarcoma cells on oxygen plasma treated polystyrene. *Vacuum* **2013**, *98*, 116–121. [CrossRef]
14. Mozetič, M.; Primc, G.; Vesel, A.; Zaplotnik, R.; Modic, M.; Junkar, I.; Recek, N.; Klanjšek-Gunde, M.; Guhy, L.; Sunkara, M.K.; et al. Application of extremely non-equilibrium plasmas in the processing of nano and biomedical materials. *Plasma Sources Sci. Technol.* **2015**, *24*, 015026. [CrossRef]
15. Brovko, A.; Amzallag, O.; Adelberg, A.; Chernyak, L.; Raja, P.V.; Ruzin, A. Effects of oxygen plasma treatment on Cd1-xZnxTe material and devices. *Nucl. Instrum. Methods Phys. Res. Sect. Accel. Spectrometers Detect. Assoc. Equip.* **2021**, *1004*, 165343. [CrossRef]

16. Donate, R.; Aleman-Dominguez, M.E.; Monzon, M. On the Effectiveness of Oxygen Plasma and Alkali Surface Treatments to Modify the Properties of Polylactic Acid Scaffolds. *Polymers* **2021**, *13*, 1643. [CrossRef] [PubMed]
17. Lojen, D.; Zaplotnik, R.; Primc, G.; Mozetic, M.; Vesel, A. Optimization of surface wettability of polytetrafluoroethylene (PTFE) by precise dosing of oxygen atoms. *Appl. Surf. Sci.* **2022**, *598*, 153817. [CrossRef]
18. Boscariol, M.R.; Moreira, A.J.; Mansano, R.D.; Kikuchi, I.S.; Pinto, T.J. Sterilization by pure oxygen plasma and by oxygen-hydrogen peroxide plasma: An efficacy study. *Int. J. Pharm.* **2008**, *353*, 170–175. [CrossRef]
19. Primc, G.; Lojen, D.; Vesel, A.; Mozetic, M.; Zaplotnik, R. Oxygen atom density in a large reactor powered by four inductively coupled plasma sources. *Vacuum* **2022**, *199*, 110964. [CrossRef]
20. Zhang, B.; Zhang, X. Modeling of plasma density, argon ion energy and ion velocity functions in a dipolar electron cyclotron resonance plasma source. *Vacuum* **2020**, *174*, 109215. [CrossRef]
21. Gajo, T.; Mijatović, Z.; Djurović, S. Plasma temperature determination based on the ratio of plasma electron densities obtained from hydrogen Hα and Hβ spectral lines. *Spectrochim. Acta Part B At. Spectrosc.* **2022**, *194*, 106484. [CrossRef]
22. Gong, C.M.; Yi, L.; Wang, K.; Huang, K.; Liu, F.H. Numerical study on electron energy distribution characteristics and evolution of active particles of methanol-air mixture by non-equilibrium plasma. *Energy* **2020**, *193*, 1258–1267. [CrossRef]
23. Proch, J.; Niedzielski, P. Recent applications of continuous flow chemical vapor and hydride generation (CVG, HG) coupled to plasma–based optical emission spectrometry (ICP OES, MIP OES). *Talanta* **2022**, *243*, 123372. [CrossRef]
24. Mehrabian, S.; Ostrikov, K. Relativistic air-plasma far-infrared radiation effects by ultrashort laser pulses in air. *High Energy Density Phys.* **2019**, *33*, 100708. [CrossRef]
25. Lojen, D.; Zaplotnik, R.; Primc, G.; Mozetic, M.; Vesel, A. Effect of VUV radiation and reactive hydrogen atoms on depletion of fluorine from polytetrafluoroethylene surface. *Appl. Surf. Sci.* **2020**, *533*, 147356. [CrossRef]
26. Ferreira, D.R.; Carvalho, P.J.; Carvalho, I.S.; Stuart, C.; Lomas, P.J. Monitoring the plasma radiation profile with real-time bolometer tomography at JET. *Fusion Eng. Des.* **2021**, *164*, 112179. [CrossRef]
27. Zhang, C.; Tadigadapa, S. Modified inductively coupled plasma reactive ion etch process for high aspect ratio etching of fused silica, borosilicate and aluminosilicate glass substrates. *Sens. Actuators A Phys.* **2018**, *273*, 147–158. [CrossRef]
28. Qin, S. High quality low thermal budget low cost SiO_2 film fabricated by O_2 plasma immersion ion implantation. *Thin Solid Films* **2022**, *756*, 139385. [CrossRef]
29. Resende, R.C.; Ribeiro, R.P.; Waldman, W.R.; Cruz, N.C.; Araujo, J.R.; Rangel, E.C. Improvement of thermoplastic elastomer degradation resistance by low-energy plasma immersion ion bombardment. *Mater. Chem. Phys.* **2020**, *242*, 122467. [CrossRef]
30. Ramaiya, N.; Goto, M.; Seguineaud, G.; Oishi, T.; Morita, S. Measurement of polarization in Lyman-α line caused by anisotropic electron collisions in LHD plasma. *J. Quant. Spectrosc. Radiat. Transf.* **2021**, *260*, 107430. [CrossRef]
31. Kurnaev, V.A.; Abramov, V.A.; Kadetov, V.A.; Mozgrin, D.V.; Sarytchev, D.V.; Savjolov, A.S.; Vizgalov, I.V.; Kolesnikov, V.N.; Presnyakov, L.P. Comparative studies of ionised and excited hydrogen atoms and molecules distributions for plasma-target interaction in a linear simulator machine. *J. Nucl. Mater.* **1999**, *266*, 412–416. [CrossRef]
32. Vesel, A.; Mozetic, M. New developments in surface functionalization of polymers using controlled plasma treatments. *J. Phys. D Appl. Phys.* **2017**, *50*, 293001. [CrossRef]
33. Brennan, D. Chapter 3 Heterogeneous Atomisation and Recombination. In *Reactions of Solids with Gases*; Bamford, C.H., Tipper, C.F.H., Compton, R.G., Eds.; Elsevier: Amsterdam, The Netherlands, 1984; Volume 21, pp. 151–234.
34. Bittencourt, J.A. *Fundamentals of Plasma Physics*; Springer: New York, NY, USA, 2004.
35. Vesel, A. Heterogeneous Surface Recombination of Neutral Nitrogen Atoms. *Mater. Tehnol.* **2012**, *46*, 7–12.
36. Guerra, V.; Tejero-del-Caz, A.; Pintassilgo, C.D.; Alves, L.L. Modelling N_2–O_2 plasmas: Volume and surface kinetics. *Plasma Sources Sci. Technol.* **2019**, *28*, 073001. [CrossRef]
37. Hardy, W.A.; Linnett, J.W. Mechanisms of atom recombination on surfaces. *Symp. Int. Combust.* **1967**, *11*, 167–179. [CrossRef]
38. Donnelly, V.M.; Guha, J.; Stafford, L. Critical review: Plasma-surface reactions and the spinning wall method. *J. Vac. Sci. Technol. A* **2011**, *29*, 010801. [CrossRef]
39. Herdrich, G.; Fertig, M.; Petkow, D.; Steinbeck, A.; Fasoulas, S. Experimental and numerical techniques to assess catalysis. *Prog. Aerosp. Sci.* **2012**, *48–49*, 27–41. [CrossRef]
40. Yang, Y.; Lee, S.; Park, S.H.; Park, G.; Kim, J.G.; Kim, I. Analysis of wall partial pressure-dependence on oxygen surface catalytic recombination with shock-heated flow. *Case Stud. Therm. Eng.* **2021**, *28*, 101600. [CrossRef]
41. Piel, A. Plasma generation. In *Plasma Physics*; Springer: Berlin/Heidelberg, Germany, 2010.
42. Lopaev, D.V.; Malykhin, E.M.; Zyryanov, S.M. Surface recombination of oxygen atoms in O2plasma at increased pressure: I. The recombination probability and phenomenological model of surface processes. *J. Phys. D Appl. Phys.* **2011**, *44*, 015201. [CrossRef]
43. Lopaev, D.V.; Smirnov, A.V. Diagnostics of heterogeneous processes with the participation of radicals by time-resolved actinometry. *Plasma Phys. Rep.* **2004**, *30*, 882–893. [CrossRef]
44. Cartry, G.; Magne, L.; Cernogora, G. Atomic oxygen recombination on fused silica: Experimental evidence of the surface state influence. *J. Phys. D Appl. Phys.* **1999**, *32*, L53–L56. [CrossRef]
45. Cartry, G.; Magne, L.; Cernogora, G. Atomic oxygen recombination on fused silica: Modelling and comparison to low-temperature experiments (300 K). *J. Phys. D Appl. Phys.* **2000**, *33*, 1303–1314. [CrossRef]
46. Stewart, D.; Bouslog, S. Surface characterization of candidate metallic TPS for RLV. In Proceedings of the 33rd Thermophysics Conference, Norfolk, VA, USA, 28 June–1 July 1999.

47. Macko, P.; Veis, P.; Cernogora, G. Study of oxygen atom recombination on a Pyrex surface at different wall temperatures by means of time-resolved actinometry in a double pulse discharge technique. *Plasma Sources Sci. Technol.* **2004**, *13*, 251–262. [CrossRef]
48. Bogaerts, A.; Gijbels, R. Similarities and differences between direct current and radio-frequency glow discharges: A mathematical simulation. *J. Anal. At. Spectrom.* **2000**, *15*, 1191–1201. [CrossRef]
49. Mozetic, M.; Vesel, A.; Stoica, S.D.; Vizireanu, S.; Dinescu, G.; Zaplotnik, R. Oxygen atom loss coefficient of carbon nanowalls. *Appl. Surf. Sci.* **2015**, *333*, 207–213. [CrossRef]
50. Gomez, S.; Steen, P.G.; Graham, W.G. Atomic oxygen surface loss coefficient measurements in a capacitive/inductive radio-frequency plasma. *Appl. Phys. Lett.* **2002**, *81*, 19–21. [CrossRef]
51. Tsutsumi, T.; Greb, A.; Gibson, A.R.; Hori, M.; O'Connell, D.; Gans, T. Investigation of the radially resolved oxygen dissociation degree and local mean electron energy in oxygen plasmas in contact with different surface materials. *J. Appl. Phys.* **2017**, *121*, 143301. [CrossRef]
52. Tserepi, A.D.; Miller, T.A. Spatially and Temporally Resolved Absolute O-Atom Concentrations in Etching Plasmas. *J. Appl. Phys.* **1995**, *77*, 505–511. [CrossRef]
53. Shibata, M.; Nakano, N.; Makabe, T. Effect of $O_2(a^1\Delta g)$ on plasma structures in oxygen radio frequency discharges. *J. Appl. Phys.* **1996**, *80*, 6142–6147. [CrossRef]
54. Rakhimova, T.V.; Braginsky, O.V.; Kovalev, A.S.; Lopaev, D.V.; Mankelevich, Y.A.; Malykhin, E.M.; Rakhimov, A.T.; Vasilieva, A.N.; Zyryanov, S.M.; Baklanov, M.R. Recombination of O and H Atoms on the Surface of Nanoporous Dielectrics. *IEEE Trans. Plasma Sci.* **2009**, *37*, 1697–1704. [CrossRef]
55. Melin, G.A.; Madix, R.J. Energy accommodation during oxygen atom recombination on metal surfaces. *Trans. Faraday Soc.* **1971**, *67*, 198–211. [CrossRef]
56. Greaves, J.C.; Linnett, J.W. The recombination of oxygen atoms at surfaces. *Trans. Faraday Soc.* **1958**, *54*, 1323–1330. [CrossRef]
57. Dickens, P.G.; Sutcliffe, M.B. Recombination of oxygen atoms on oxide surfaces. Part 1.—Activation energies of recombination. *Trans. Faraday Soc.* **1964**, *60*, 1272–1285. [CrossRef]
58. Linnett, J.W.; Marsden, D.G.H. The recombination of oxygen atoms at salt and oxide surfaces. *Proc. R. Soc. Lond. Ser. A Math. Phys. Sci.* **1956**, *234*, 504–515.
59. Mozetič, M.; Zalar, A. Recombination of neutral oxygen atoms on stainless steel surface. *Appl. Surf. Sci.* **2000**, *158*, 263–267. [CrossRef]
60. Wickramanayaka, S.; Meikle, S.; Kobayashi, T.; Hosokawa, N.; Hatanaka, Y. Measurements of catalytic efficiency of surfaces for the removal of atomic oxygen using NO^*_2 continuum. *J. Vac. Sci. Technol. A Vac. Surf. Film.* **1991**, *9*, 2999–3002. [CrossRef]
61. Stafford, L.; Guha, J.; Donnelly, V.M. Recombination probability of oxygen atoms on dynamic stainless steel surfaces in inductively coupled O_2 plasmas. *J. Vac. Sci. Technol. A Vac. Surf. Film.* **2008**, *26*, 455–461. [CrossRef]
62. Matsushita, J.; Sasaki, K.; Kadota, K. Dynamic Variation of the Sticking Coefficient of Oxygen Atoms in Helicon-Wave Excited High-Density Oxygen Plasmas. *Jpn. J. Appl. Phys.* **1997**, *36*, 4747. [CrossRef]
63. Myerson, A.L. Exposure-Dependent Surface Recombination Efficiencies of Atomic Oxygen. *J. Chem. Phys.* **1969**, *50*, 1228–1234. [CrossRef]
64. Myerson, A.L. Mechanisms of surface recombination from stepfunction flows of atomic oxygen over noble metals. *J. Chem. Phys.* **1965**, *42*, 3270–3276. [CrossRef]
65. Guyon, C.; Cavadias, S.; Amouroux, J. Heat and mass transfer phenomenon from an oxygen plasma to a semiconductor surface. *Surf. Coat. Technol.* **2001**, *142*, 959–963. [CrossRef]
66. Guyon, C.; Cavadias, S.; Mabille, I.; Moscosa-Santillan, M.; Amouroux, J. Recombination of oxygen atomic excited states produced by non-equilibrium RF plasma on different semiconductor materials: Catalytic phenomena and modelling. *Catal. Today* **2004**, *89*, 159–167. [CrossRef]
67. Moisan, M.; Wertheimer, M.R. Comparison of microwave and r.f. plasmas: Fundamentals and applications. *Surf. Coat. Technol.* **1993**, *59*, 1–13. [CrossRef]
68. Fridman, A.A.; Kennedy, L.A. *Plasma Physics and Engineering*; Taylor & Francis Routledge: Abingdon-on-Thames, UK, 2004.
69. Booth, J.P.; Sadeghi, N. Oxygen and Fluorine Atom Kinetics in Electron-Cyclotron Resonance Plasmas by Time-Resolved Actinometry. *J. Appl. Phys.* **1991**, *70*, 611–620. [CrossRef]
70. Greaves, J.C.; Linnett, J.W. Recombination of atoms at surfaces. Part 6—Recombination of oxygen atoms on silica from 20 °C to 600 °C. *Trans. Faraday Soc.* **1959**, *55*, 1355–1361. [CrossRef]
71. Kaufman, F.; Norrish, R.G.W. The air afterglow and its use in the study of some reactions of atomic oxygen. *Proc. R. Soc. Lond. Ser. A Math. Phys. Sci.* **1958**, *247*, 123–139.
72. Kaufman, F. Air Afterglow and Kinetics of Some Reactions of Atomic Oxygen. *J. Chem. Phys.* **1958**, *28*, 352–353. [CrossRef]
73. Hacker, D.S.; Marshall, S.A.; Steinberg, M. Recombination of Atomic Oxygen on Surfaces. *J. Chem. Phys.* **1961**, *35*, 1788–1792. [CrossRef]
74. Brake, M.; Hinkle, J.; Asmussen, J.; Hawley, M.; Kerber, R. Dissociation and recombination of oxygen atoms produced in a microwave discharge. Part I. Experiment. *Plasma Chem. Plasma Process.* **1983**, *3*, 63–78. [CrossRef]
75. Brake, M.L.; Kerber, R.L. Dissociation and recombination of oxygen atoms produced in a microwave discharge. Part II. Theoretical calculations. *Plasma Chem. Plasma Process.* **1983**, *3*, 79–95. [CrossRef]
76. Zaplotnik, R.; Vesel, A.; Mozetic, M. Atomic oxygen and hydrogen loss coefficient on functionalized polyethylene terephthalate, polystyrene, and polytetrafluoroethylene polymers. *Plasma Process. Polym.* **2018**, *15*, 1800021. [CrossRef]
77. Cartry, G.; Duten, X.; Rousseau, A. Atomic oxygen surface loss probability on silica in microwave plasmas studied by a pulsed induced fluorescence technique. *Plasma Sources Sci. Technol.* **2006**, *15*, 479–488. [CrossRef]

78. Kolesnikov, A.F. Combined measurements and computations of high enthalpy and plasma flows for determination of TPM surface catalycity, RTO AVT Course on "Measurement techniques for high enthalpy and plasma flows. In Proceedings of the RTO AVT Course Measurement Techniques for High Enthalpy and Plasma Flows, Rhode-Saint-Genese, Belgium, 25–29 October 1999.
79. Balat, M.; Czerniak, M.; Badie, J.M. Thermal and chemical approaches for oxygen catalytic recombination evaluation on ceramic materials at high temperature. *Appl. Surf. Sci.* **1997**, *120*, 225–238. [CrossRef]
80. Balat-Pichelin, M. *Interactions of Reactivegas Flows and Ceramics at High Temperature—Experimental Methods for the Measurements of Species Recombination during Planetary Entry*; Defense Technical Information Center: Fort Belvoir, VA, USA, 2007.
81. Balat-Pichelin, M.; Badie, J.M.; Berjoan, R.; Boubert, P. Recombination coefficient of atomic oxygen on ceramic materials under earth re-entry conditions by optical emission spectroscopy. *Chem. Phys.* **2003**, *291*, 181–194. [CrossRef]
82. Balat-Pichelin, M.; Beche, E. Atomic oxygen recombination on the ODS PM 1000 at high temperature under air plasma. *Appl. Surf. Sci.* **2010**, *256*, 4906–4914. [CrossRef]
83. Balat-Pichelin, M.; Kovalev, V.L.; Kolesnikov, A.F.; Krupnov, A.A. Effect of the incomplete accommodation of the heterogeneous recombination energy on heat fluxes to a quartz surface. *Fluid Dyn.* **2008**, *43*, 830–838. [CrossRef]
84. Balat-Pichelin, M.; Pascarelli, M.; Scatteia, L.; Alfano, D. Catalycity of zirconia nad of $ZrBr_2$-based ultra-high temperature ceramics. In Proceedings of the 6th European Symposium on Aerothermodynamics for Space Vehicles, Noordwijk, The Netherlands, 17–19 May 2009.
85. Sjolander, G.W. Atomic oxygen-metal surface studies as applied to mass spectrometer measurements of upper planetary atmospheres. *J. Geophys. Res.* **1976**, *81*, 3767–3770. [CrossRef]
86. Park, G. Oxygen Catalytic Recombination on Copper Oxide in Tertiary Gas Mixtures. *J. Spacecr. Rocket.* **2013**, *50*, 540–555. [CrossRef]
87. Goulard, R. On Catalytic Recombination Rates in Hypersonic Stagnation Heat Transfer. *J. Jet Propuls.* **1958**, *28*, 737–745. [CrossRef]
88. Marinov, D.; Teixeira, C.; Guerra, V. Deterministic and Monte Carlo methods for simulation of plasma-surface interactions. *Plasma Process. Polym.* **2017**, *14*, 1600175. [CrossRef]
89. Seward, W.A.; Jumper, E.J. Model for Oxygen Recombination on Silicon-Dioxide Surfaces. *J. Thermophys. Heat Transf.* **1991**, *5*, 284–291. [CrossRef]
90. Gudmundsson, J.T.; Thorsteinsson, E.G. Oxygen discharges diluted with argon: Dissociation processes. *Plasma Sources Sci. Technol.* **2007**, *16*, 399–412. [CrossRef]
91. Mozetič, M.; Zalar, A.; Cvelbar, U.; Poberaj, I. Heterogeneous recombination of neutral oxygen atoms on niobium surface. *Appl. Surf. Sci.* **2003**, *211*, 96–101. [CrossRef]
92. Mozetič, M.; Cvelbar, U. Heterogeneous recombination of O atoms on metal surfaces. *Int. J. Nanosci.* **2007**, *6*, 121–124. [CrossRef]
93. Cvelbar, U.; Mozetic, M.; Ricard, A. Characterization of oxygen plasma with a fiber optic catalytic probe and determination of recombination coefficients. *IEEE Trans. Plasma Sci.* **2005**, *33*, 834–837. [CrossRef]
94. Drenik, A.; Vesel, A.; Mozetic, M.; Panjan, P. Recombination of atomic oxygen and hydrogen on amorphous carbon. *J. Nucl. Mater.* **2013**, *442*, S751–S754. [CrossRef]
95. Drenik, A.; Vesel, A.; Mozetic, M.; Panjan, P. Influence of amorphous carbon deposition on the probability for recombination of neutral oxygen atoms on aluminium surfaces. In Proceedings of the 20th International Conference Nuclear Energy for New Europe, Bovec, Slovenia, 12–15 September 2011.
96. Drenik, A. The Probability of Heterogeneous Recombination of Hydrogen and Oxygen Atoms on the Surfaces of Fusion-Relevant Materials. Ph.D. Thesis, Jožef Stefan International Postgraduate School, Ljubljana, Slovenia, 2009.
97. Elias, L.; Ogryzlo, E.A.; Schiff, H.I. The study of electrically discharged O_2 by means of an isothermal calorimetric detector. *Can. J. Chem.* **1959**, *37*, 1680–1689. [CrossRef]
98. Hartunian, R.A.; Thompson, W.P.; Safron, S. Measurements of Catalytic Efficiency of Silver for Oxygen Atoms and the $O–O_2$ Diffusion Coefficient. *J. Chem. Phys.* **1965**, *43*, 4003–4006. [CrossRef]
99. May, J.W.; Linnett, J.W. Recombination of atoms at surfaces: An effusion method applied to oxygen atom recombination. *J. Catal.* **1967**, *7*, 324–341. [CrossRef]
100. Scott, C.D. Catalytic recombination of nitrogen and oxygen on hight-temperature reusable surface insulation. In Proceedings of the AIAA 15th Thermophysics Conference, Snowmass, CO, USA, 14–16 July 1980; pp. 192–212.
101. Kim, Y.C.; Boudart, M. Recombination of oxygen, nitrogen, and hydrogen atoms on silica: Kinetics and mechanism. *Langmuir* **1991**, *7*, 2999–3005. [CrossRef]
102. Gordiets, B.; Ferreira, C.M.; Nahorny, J.; Pagnon, D.; Touzeau, M.; Vialle, M. Surface kinetics of N and O atoms in discharges. *J. Phys. D Appl. Phys.* **1996**, *29*, 1021–1031. [CrossRef]
103. Stewart, D. Determination of surface catalytic efficiency for thermal protection materials—Room temperature to their upper use limit. In Proceedings of the 31st Thermophysics Conference, New Orelans, LA, USA, 17–20 June 1996.
104. Stewart, D.A. Surface Catalytic Efficiency of Advanced Carbon Carbon Candidate Thermal Protection Materials for SSTO Vehicles. NASA Technical Memorandum 110383. 1996. Available online: https://ntrs.nasa.gov/citations/19960015940 (accessed on 8 January 2023).
105. Bykova, N.G.; Vasil'evskii, S.A.; Gordeev, A.N.; Kolesnikov, A.F.; Fershin, I.S.; Yakushin, M.I. Determination of the Effective Probabilities of Catalytic Reactions on the Surfaces of Heat Shield Materials in Dissociated Carbon Dioxide Flows. *Fluid Dyn.* **1997**, *32*, 876–886. [CrossRef]

106. Cauquot, P.; Cavadias, S.; Amouroux, J. Thermal energy accommodation from oxygen atoms recombination on metallic surfaces. *J. Thermophys. Heat Transf.* **1998**, *12*, 206–213. [CrossRef]
107. Šorli, I.; Ročak, R. Determination of atomic oxygen density with a nickel catalytic probe. *J. Vac. Sci. Technol. A Vac. Surf. Film.* **2000**, *18*, 338–342. [CrossRef]
108. Zheludkevich, M.L.; Gusakov, A.G.; Voropaev, A.G.; Vecher, A.A.; Kozyrski, E.N.; Raspopov, S.A. Oxidation of silver by atomic oxygen. *Oxid. Met.* **2004**, *61*, 39–48. [CrossRef]
109. Herdrich, G.; Auweter-Kurtz, M.; Fertig, M.; Fischer, W.; Muylaert, J.-M.; Pidan, S.; Schüssler, M.; Trabandt, U. Catalysis of candidate TPS Materials for EXPERT—A Basis for TPS Design and Catalysis based in-flight Instrumentations. In Proceedings of the Thermal Protection Systems and Hot Structures, Noordwijk, The Netherlands, 1 August 2006; p. 42.
110. Steinbeck, A.; Fertig, M.; Herdrich, G.; Roeser, H.-P. Enhanced evaluation of recombination coefficient measurements in plasma wind tunnels. In Proceedings of the 41st AIAA Thermophysics Conference, San Antonio, TX, USA, 22–25 June 2009.
111. Magne, L.; Coitout, H.; Cernogora, G.; Gousset, G. Atomic Oxygen Recombination at the Wall in a Time Afterglow. *J. Phys. III* **1993**, *3*, 1871–1889. [CrossRef]
112. Krištof, J.; Macko, P.; Veis, P. Surface loss probability of atomic oxygen. *Vacuum* **2012**, *86*, 614–619. [CrossRef]
113. Pagnon, D.; Amorim, J.; Nahorny, J.; Touzeau, M.; Vialle, M. On the use of actinometry to measure the dissociation in O2DC glow discharges: Determination of the wall recombination probability. *J. Phys. D Appl. Phys.* **1995**, *28*, 1856–1868. [CrossRef]
114. Bousquet, A.; Cartry, G.; Granier, A. Investigation of O-atom kinetics in O_2, CO_2, H_2O and O_2/HMDSO low pressure radiofrequency pulsed plasmas by time-resolved optical emission spectroscopy. *Plasma Sources Sci. Technol.* **2007**, *16*, 597–605. [CrossRef]
115. Morillo-Candas, A.S.; Drag, C.; Booth, J.P.; Dias, T.C.; Guerra, V.; Guaitella, O. Oxygen atom kinetics in CO_2 plasmas ignited in a DC glow discharge. *Plasma Sources Sci. Technol.* **2019**, *28*, 075010. [CrossRef]
116. Zhang, Z.; Kushimoto, M.; Sakai, T.; Sugiyama, N.; Schowalter, L.J.; Sasaoka, C.; Amano, H. A 271.8 nm deep-ultraviolet laser diode for room temperature operation. *Appl. Phys. Express* **2019**, *12*, 124003. [CrossRef]
117. Dilecce, G.; Benedictis, S.D. Experimental studies on elementary kinetics in N_2-O_2 pulsed discharges. *Plasma Sources Sci. Technol.* **1999**, *8*, 266–278. [CrossRef]
118. Marschall, J. *Laboratory Determination of Thermal Protection System Materials Surface Catalytic Properties*; NASA: Menlo Park, CA, USA, 2007; pp. 11-11–11-32.
119. Breen, J.A.; Rosner, D.E.; Delgass, W.N.; Nordine, P.C.; Cibrian, R.; Krishnan, N.G. *Catalysis Study for Space Shuttle Vehicle Thermal Protection Systems*; NASA: Menlo Park, CA, USA, 1973.
120. Greaves, J.C.; Linnett, J.W. Recombination of atoms at surfaces. Part 5—Oxygen atoms at oxide surfaces. *Trans. Faraday Soc.* **1959**, *55*, 1346–1354. [CrossRef]
121. Sabadil, H.; Pfau, S. Measurements of the Degree of Dissociation in Oxygen Dc Discharges—Comparison of the Ozone Method with the Wrede-Harteck Method. *Plasma Chem. Plasma Process.* **1985**, *5*, 67–79. [CrossRef]
122. Singh, H.; Coburn, J.W.; Graves, D.B. Recombination coefficients of O and N radicals on stainless steel. *J. Appl. Phys.* **2000**, *88*, 3748–3755. [CrossRef]
123. Kiehlbauch, M.W.; Graves, D.B. Inductively coupled plasmas in oxygen: Modeling and experiment. *J. Vac. Sci. Technol. A* **2003**, *21*, 660–670. [CrossRef]
124. Kurunczi, P.F.; Guha, J.; Donnelly, V.M. Recombination reactions of oxygen atoms on an anodized aluminum plasma reactor wall, studied by a spinning wall method. *J. Phys. Chem. B* **2005**, *109*, 20989–20998. [CrossRef]
125. Hsu, C.-C.; Nierode, M.A.; Coburn, J.W.; Graves, D.B. Comparison of model and experiment for Ar, Ar/O_2 and Ar/O_2/Cl_2 inductively coupled plasmas. *J. Phys. D Appl. Phys.* **2006**, *39*, 3272–3284. [CrossRef]
126. Guha, J.; Kurunczi, P.; Stafford, L.; Donnelly, V.M.; Pu, Y.-K. In-Situ Surface Recombination Measurements of Oxygen Atoms on Anodized Aluminum in an Oxygen Plasma. *J. Phys. Chem. C* **2008**, *112*, 8963–8968. [CrossRef]
127. Guha, J.; Khare, R.; Stafford, L.; Donnelly, V.M.; Sirard, S.; Hudson, E.A. Effect of Cu contamination on recombination of O atoms on a plasma-oxidized silicon surface. *J. Appl. Phys.* **2009**, *105*, 113309. [CrossRef]
128. Stafford, L.; Guha, J.; Khare, R.S.; Mattei, S.; Boudreault, O.; Clain, B.; Donnelly, V.M. Experimental and modeling study of O and Cl atoms surface recombination reactions in O_2 and Cl_2 plasmas. *Pure Appl. Chem.* **2010**, *82*, 1301–1315. [CrossRef]
129. Krongelb, S.; Strandberg, M.W.P. Use of Paramagnetic-Resonance Techniques in the Study of Atomic Oxygen Recombinations. *J. Chem. Phys.* **1959**, *31*, 1196–1210. [CrossRef]
130. Marshall, T.C. Studies of Atomic Recombination of Nitrogen, Hydrogen, and Oxygen by Paramagnetic Resonance. *Phys. Fluids* **1962**, *5*, 743–753. [CrossRef]
131. Hogan, L.; Burch, D.S. A measurement of the rate constant for the reaction $O + O_2 + O_2 \rightarrow O_3 + O_2$. *J. Chem. Phys.* **1976**, *65*, 894–900. [CrossRef]
132. Jumper, E.J. *Recombination of Oxygen and Nitrogen on Silica-Based Thermal Protection Surfaces: Mechanism and Implications*; Springer: Berlin/Heidelberg, Germany, 1996.
133. Daiss, A.; Fruhauf, H.H.; Messerschmid, E.W. Modeling of catalytic reactions on silica surfaces with consideration of slip effects. *J. Thermophys. Heat Transf.* **1997**, *11*, 346–352. [CrossRef]
134. Kolodziej, P.; Stewart, D.A. Nitrogen recombination on high-temperature reusable surface insulation and the analysis of its effect on surface catalysis. In Proceedings of the 22nd Thermophysics Conference AIAA, Honolulu, HI, USA, 8–10 June 1987; pp. 87–1637.
135. Gordiets, B.F.; Ferreira, C.M. Self-consistent modeling of volume and surface processes in air plasma. *AIAA J.* **1998**, *36*, 1643–1651. [CrossRef]

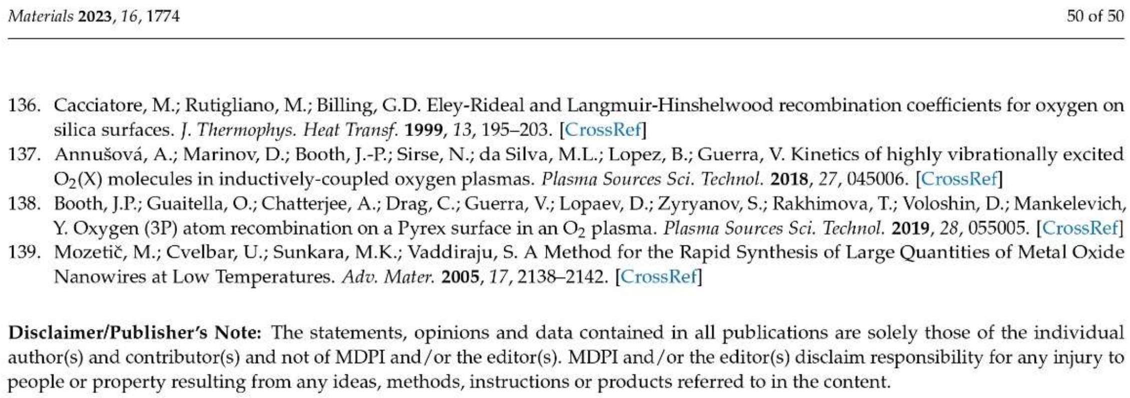

136. Cacciatore, M.; Rutigliano, M.; Billing, G.D. Eley-Rideal and Langmuir-Hinshelwood recombination coefficients for oxygen on silica surfaces. *J. Thermophys. Heat Transf.* **1999**, *13*, 195–203. [CrossRef]
137. Annušová, A.; Marinov, D.; Booth, J.-P.; Sirse, N.; da Silva, M.L.; Lopez, B.; Guerra, V. Kinetics of highly vibrationally excited O_2(X) molecules in inductively-coupled oxygen plasmas. *Plasma Sources Sci. Technol.* **2018**, *27*, 045006. [CrossRef]
138. Booth, J.P.; Guaitella, O.; Chatterjee, A.; Drag, C.; Guerra, V.; Lopaev, D.; Zyryanov, S.; Rakhimova, T.; Voloshin, D.; Mankelevich, Y. Oxygen (3P) atom recombination on a Pyrex surface in an O_2 plasma. *Plasma Sources Sci. Technol.* **2019**, *28*, 055005. [CrossRef]
139. Mozetič, M.; Cvelbar, U.; Sunkara, M.K.; Vaddiraju, S. A Method for the Rapid Synthesis of Large Quantities of Metal Oxide Nanowires at Low Temperatures. *Adv. Mater.* **2005**, *17*, 2138–2142. [CrossRef]

1.4 Hypothesis

Going forward based on the gathered data, a few hypotheses are given:

1. The use of the Šorli-Ročak method, a calorimetric method similar to the use of catalytic probes, will enable us to measure the absolute density of neutral oxygen atoms independent of the recombination coefficient of the material, from which our probe is made. To confirm this, several tubes made from different materials will be used, and the results of the measurements with different materials should be the same.
2. The recombination coefficient of a given material is not a constant value and should change if we alter certain surface properties, such as the temperature of the surface of the material, the surface chemistry, and the surface morphology of the material.
3. The recombination coefficient of a given material should increase with increasing temperature of the material since an elevated temperature increases the mobility of adsorbed atoms on the surface of the material.
4. At elevated pressures inside a plasma system, there is an increased number of molecules, which can screen the available bonding sites for atoms on the surface of a given material, effectively shielding the surface of a material from neutral atom adsorption. Since those sites are no longer available for the adsorption of neutral atoms, less neutral atoms are adsorbed to the surface of a material, thus lowering the recombination coefficient.
5. The surface roughness of a given material has profound effects on the recombination coefficient. A material with a higher surface roughness can trap neutral atoms created in the plasma discharge into a geometrical trap (as shown schematically in Figure 5) where the neutral atoms undergo several collisions with the surface of the material, each collision having a certain probability to result in the adsorption of the neutral atom to the surface of the material. The adsorbed neutral atom can then recombine with other neutral atoms, which increases the recombination coefficient.

The given hypotheses will be scientifically tested using experimental methods described in the proceeding chapters.

Chapter 2

Recombination of Oxygen Atoms on Oxidized Surfaces

Before we can determine the recombination coefficient of a given material using calorimetry, we first need a method to determine the absolute number density of neutral atoms. One such method is the Šorli-Ročak method [58], which uses a metallic tube as an element that recombines all atoms passing it. The major requirement for this method is that the large majority of neutral atoms recombine on the metallic tube successfully. Metallic materials are used because they are generally more efficient at recombining neutral oxygen atoms than dielectrics.

Let us start with a metallic tube with a certain mass (m_{tube}) and specific heat ($c_{p(tube)}$). If we place this metallic tube near an orifice with similar dimensions (Figure 9), ignite a plasma discharge at the other side of the orifice, and pump the gas through the orifice and the metallic tube, all the neutral atoms pass through the metallic tube. The number of neutral atoms reaching the metallic tube in a unit of time is equal to the product of the number density of neutral atoms (n) and the effective pumping speed (ϕ). If a vast majority of neutral atoms recombine on the surface of the metallic tube, the tube heats up, and the heating power (P_H) is:

$$P_H = \phi \, n \frac{W_D}{2} \, . \tag{2.1}$$

Factor 2 in equation (2.5) takes into account that it takes two oxygen atoms to recombine into an oxygen molecule (O_2). The metallic tube also dissipates heat at the rate of the dissipating power (P_D):

$$P_D = m \, c_p \frac{dT}{dt}(tube) \tag{2.2}$$

where $dT/dt(tube)$ is the absolute value of the first derivative of the temperature of the metallic tube over time. Similarly, as with the standard catalytic probe (equations (1.7), (1.10), and (1.11)), we can equate the heating and cooling power once the metallic tube reaches an equilibrium temperature and get the following relation:

$$n = \frac{2 m_{tube} c_{p(tube)}}{W_D \phi} \frac{dT}{dt}(tube) \; . \tag{2.3}$$

The relation in equation (2.3) differs from the one in equation (1.11) in one key aspect: there is no need to know the recombination coefficient of the material. This is the key advantage of the Šorli-Ročak method. The idea is to measure the absolute number density of neutral atoms using this method and later replace the metallic tube with a catalytic probe with a tip made of a chosen material. Of course, another requirement for this to work is that the metallic tube does not significantly alter the volumetric flow of the gas inside the system.

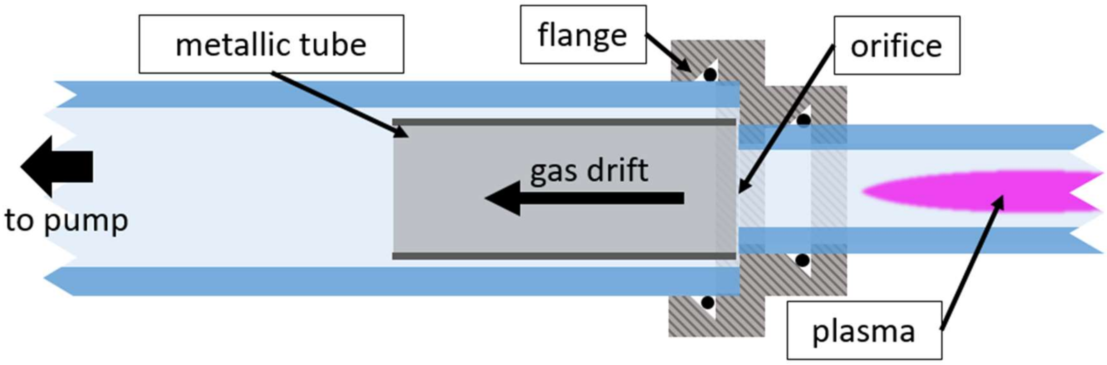

Figure 9: Schematic of a metallic tube positioned at a similarly sized orifice downstream of a plasma discharge so that all the neutral atoms have to pass through the metallic tube.

2.1 Recombination of Oxygen Atoms on the Surface of Oxidized Polycrystalline Nickel – Temperature and Pressure Dependences

In the proceeding article [20], we utilize the Šorli-Ročak method to measure the absolute neutral atom density inside a low-pressure microwave plasma system (Figure 10). Gas enters the system on one side through the mass flow controller (MFC), and is pumped by a two-stage rotary pump on the other side. Plasma is sustained inside the glow chamber by a microwave generator (MW) operating in the surfatron mode [59], [60], [61]. Both the metallic tubes and the catalytic probe, which are in the afterglow chamber, are connected to a voltmeter so that we can measure the temperature of the catalytic probe tip and the metallic tube. A pressure gauge is also installed to monitor the pressure inside the afterglow chamber.

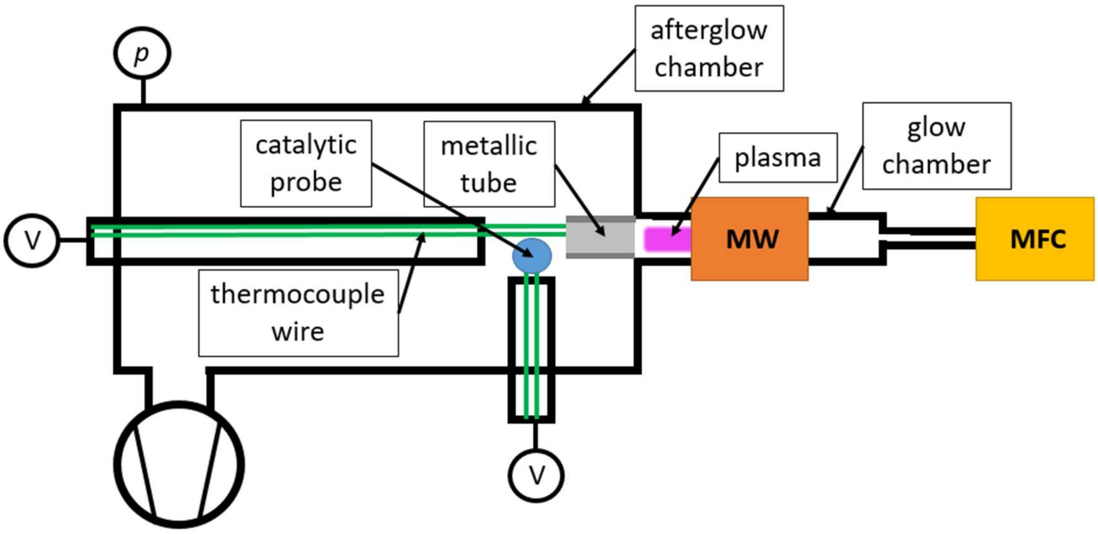

Figure 10: Schematic of the experimental setup using the low-pressure microwave plasma system.

The glow chamber is made of quartz glass which does not represent a significant sink of oxygen atoms due to a very low recombination coefficient of quartz glass [62], [63], [64], [65]. The recombination of oxidized polycrystalline nickel is determined by first employing the Šorli-Ročak method to measure the neutral atom density in the afterglow chamber and later replaced by a catalytic probe with a nickel tip. Metallic tubes of three different materials were used: nickel, iron, and cobalt. The results of the measurements with all three tubes are the same, confirming one of our hypotheses.

The recombination coefficient of nickel samples has already been studied by other authors [28], [66], [67], [68], [69], [70] but there is little-to-no agreement between the results. The article aims to clear this up and systematically measure the recombination coefficient of oxidized polycrystalline nickel while also providing an empirical formula for the dependence of the recombination coefficient on the temperature of the nickel sample as well as the pressure inside the experimental system.

Along with that, atomic force microscopy (AFM) measurements are performed on nickel samples oxidized at different temperatures. While not explicitly stated in the article, the surface roughness increases with increasing sample temperature during oxidation with oxygen plasma (Figure 11). The surface roughness increases almost linearly with increasing temperature. Additionally, a time-of-flight secondary ion mass spectrometry (ToF-SIMS) measurement [71] is performed on the oxidized nickel sample used as the tip of the catalytic probe. The results show that a 50 µm thick nickel sample has a 10 µm thick layer of oxide on each side, which is far thicker than an oxide layer formed on a metallic surface naturally at room temperature [72].

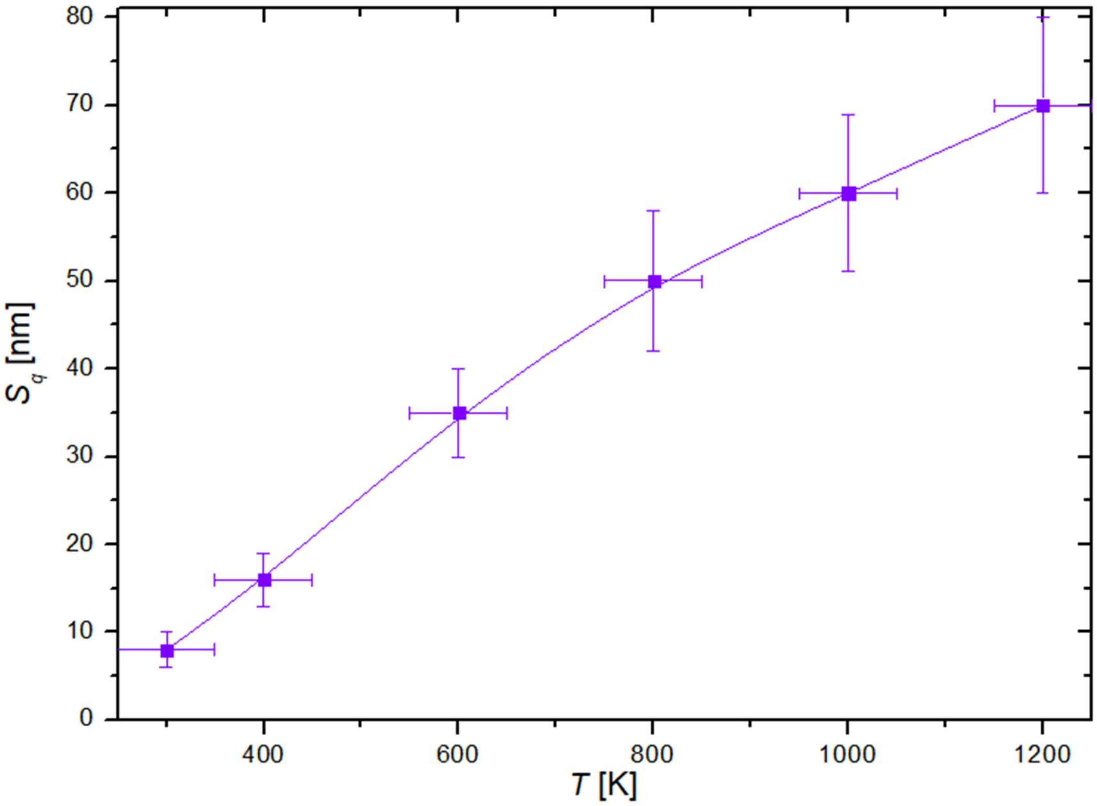

Figure 11: The root-mean-square surface roughness (S_q) of nickel samples oxidized at different temperatures (T) in oxygen plasma.

More importantly, the proceeding article demonstrates that the recombination coefficient of an oxidized polycrystalline nickel sample varies with the temperature of the sample, and with the pressure inside the system, confirming our hypothesis. The recombination coefficient increased with increasing temperature similar to an Arrhenius plot [66] but decreased with increasing pressure, resulting in the following empirical formula:

$$\gamma(p,T) = \frac{A}{\sqrt{p}} e^{-B/T} \tag{2.4}$$

where $A = 17$ $\mathrm{Pa}^{1/2}$ and $B = 1400$ K are fitting parameters. This empirical function aligns well with our experimental results which were done in the temperature range between 370 to 750 K and the pressure range between 40 and 220 Pa, the latter commonly used in industrial applications [73]. The results are in agreement with the results of some previous authors [66], [70], [74]. Additionally, several authors have already reported a similar temperature dependence of the recombination coefficient for different materials [75], [76], [77], [78], [79], [80], [81], [82], [83], [84], [85]. A few authors also reported a similar pressure dependence of the recombination coefficient for different materials [86], [87], [88].

OPEN ACCESS
IOP Publishing
Plasma Sources Science and Technology
Plasma Sources Sci. Technol. **32** (2023) 075001 (13pp)
https://doi.org/10.1088/1361-6595/ace129

Recombination of oxygen atoms on the surface of oxidized polycrystalline nickel—temperature and pressure dependences

Domen Paul[1,2,*], Miran Mozetič[1], Rok Zaplotnik[1], Jernej Ekar[1,2], Alenka Vesel[1], Gregor Primc[1] and Denis Đonlagič[3]

[1] Jozef Stefan Institute, Jamova cesta 39, 1000 Ljubljana, Slovenia
[2] Jozef Stefan International Postgraduate School, Jamova cesta 39, 1000 Ljubljana, Slovenia
[3] Faculty of Electrical Engineering and Computer Science, University of Maribor, Koroska cesta 46, 2000 Maribor, Slovenia

E-mail: domen.paul@ijs.si

Received 26 April 2023, revised 15 June 2023
Accepted for publication 23 June 2023
Published 6 July 2023

Abstract

The recombination of neutral oxygen atoms in the ground state on the oxidized nickel samples was studied experimentally in the range of pressures where the maximum density occurs in weakly ionized low-pressure oxygen plasma, i.e. between 40 and 200 Pa. The recombination coefficient was determined in the flowing afterglow. The source of oxygen atoms was plasma sustained in a quartz tube of inner diameter 4.7 mm by a microwave discharge in the surfatron mode. The recombination coefficient was determined in the afterglow chamber, which was a Pyrex tube with an inner diameter of 36 mm. The density of oxygen atoms in the afterglow chamber was varied by adjusting the discharge power, the gas flow, the pressure, and the position of a recombinator. Such flexibility of the experimental system enabled adjustment of the temperature of the oxidized nickel samples independently from the O-atom density in its vicinity or other parameters. The density of oxygen atoms in the afterglow chamber at various system parameters was determined by the Šorli method, which is reliable, and has an accuracy of about 20%. The recombination coefficient was determined by calorimetry. The coefficient was inversely proportional to the square root of the pressure and exponentially to the sample temperature. Systematic measurements performed at various pressures and temperatures enabled empirical formula, which were explained qualitatively by recombination kinetics.

Keywords: heterogenous surface recombination, recombination coefficient, nickel, nickel oxide, temperature dependence, pressure dependence

(Some figures may appear in colour only in the online journal)

---

[*] Author to whom any correspondence should be addressed.

1361-6595/23/075001+13$33.00 Printed in the UK

1. Introduction

The interaction of neutral oxygen atoms with the surfaces of solid materials has attracted the attention of numerous authors involved in the basic phenomena as well as technological aspects of controlled surface oxidation [1–7]. Surface oxidation should often be achieved at low temperatures, sometimes even at room temperature. Namely, the bulk properties of materials should be preserved despite the exothermic character of the surface reactions. Keeping a low (preferable room) temperature is particularly important when delicate materials like polymers are to be oxidized. Oxidation with molecular oxygen is usually not feasible because many materials will not form oxides unless heated to elevated temperatures. The best examples are polymers. The surface oxidation of both synthetic and natural polymers with molecular oxygen usually occurs at temperatures above the glass transition point or even the melting point.

In cases where low-temperature oxidation should be achieved, molecular oxygen has to be replaced with oxygen of higher oxidation potential. Ozone is often chosen, but it may be impractical and rather expensive for the oxidation of large quantities of organic materials. An alternative to ozone is oxygen atoms. They are perfectly stable in the gas phase as long as the pressure is low enough to ensure a negligible association of O atoms to parent molecules in the gas phase. The shelf time of oxygen atoms will decrease with increasing pressure because the probability of three-body collisions increases as a square of the pressure. At low pressures, the loss of oxygen atoms is predominantly on the surfaces of materials.

The surface recombination coefficient depends on the type of material, in particular on the ability of a material to provide a large density of surface adsorption sites. Many materials exhibit a very low recombination coefficient, among them glasses, some types of ceramics, and many polymers [8]. On the other hand, metal oxides will enable a large coefficient as long as oxygen is not firmly bound to metallic atoms in the metal oxide. Especially transition metals will form oxides, which are semi-conductive and provide recombination sites for O atoms arriving from the gas phase [9, 10].

The surface recombination of atoms attracted the attention of early authors, who illustrated the basic mechanisms. Nowadays, there are numerous theories on surface recombination, but there are two distinguished models: the Langmuir–Hinshelwood and Eley–Rideal. The first one predicts the adsorption of atoms on the surface of the solid material, surface oscillations or migration, and the association of two atoms on the surface to the parent molecule. The molecule is obviously in thermal equilibrium with the surface, so it will leave the surface with negligible kinetic or potential energy. The second model predicts the direct interaction of a gas phase atom impinging the surface with an atom already bound on the surface. The potential energy of an oxygen atom in the gas phase is usually taken as half of the binding energy of oxygen molecules, i.e. 2.6 eV. Since the interaction is immediate, there is no time for surface accommodation of the impinging atom, and the resulting molecule may leave the surface with significant potential energy (i.e. vibrationally excited).

The Eley–Rideal model does not involve surface migration, so the recombination probability will be large even at low temperatures. On the other hand, the recombination probability of the Langmuir–Hinshelwood model will increase with increasing surface mobility of atoms, i.e. increasing temperature.

These two models only illustrate the mechanisms, which are still not well understood. The probability of surface recombination will definitely depend on the type of material and its morphology on both the nanometer and micrometer scales. The type of material will dictate the availability of surface recombination sites, whereas the roughness will enable various collisions of an atom trapped in a gap on the material surface. In fact, the largest recombination coefficient for a particular material was measured on vertically oriented nanosheets [11]. The recombination coefficient may also depend on the concentration of any other gaseous species adsorbed on the surface. Namely, other species but atoms will shade the surface sites, so they may not be available for the adsorption of oxygen atoms. Taking into account the upper discussion, the recombination coefficient is likely to depend on the material temperature.

The surface recombination coefficient will dictate the density of atoms in a processing chamber and, thus, the flux of atoms on the material, which should be processed with the atoms. In many practical cases, keeping the flux as constant as possible and as laterally homogeneous as possible is useful [12]. This is not always possible because of the edge effects and also because the density of atoms changes with time without changing the discharge parameters [13]. The variation in the O-atom density may be a consequence of the temperature dependence of the surface loss coefficient. This is especially a severe concern for industrial plasma systems operating in batch mode and loaded with different amounts of different products. Based on these considerations, it is useful to know the variation of the recombination coefficient with the temperature and the pressure.

One of the first reports on the recombination of oxygen atoms at various surfaces was provided by Greaves and Linnett in 1958 [10]. They used a flowing system and measured the density of oxygen atoms along a continuously pumped tube made of or coated with different materials. They kept the temperature of these materials constant (close to room temperature) and reported the coefficients for different metals, metal oxides, as well as some other materials. They did not report how they enabled oxygen-free metallic samples in an atmosphere rich in oxygen atoms. The fluxes of any other species likely present in gaseous plasma, such as charged particles and UV photons, were negligible because they used a sidearm. They reported the recombination coefficient for transition metals like iron and nickel about $3 \cdot 10^{-2}$, whereas the coefficient on these metal oxides was as low as about $8 \cdot 10^{-3}$. They did not report any morphological properties of the materials.

Myerson [14] performed similar experiments but used a pulsed radio-frequency discharge for the dissociation of oxygen molecules. He added argon to the source gas to increase the dissociation fraction. He used NO titration to measure the density of O atoms in the processing chamber. Myerson is probably the first author who reported the initial effects upon exposure of metallic foils to oxygen atoms. The recombination coefficient was found to be a complex function of the exposure time for low exposure times. The results are explained by the formation of oxide film as well as possible nanostructuring, which is likely to occur upon prolonged exposure of metal foils to oxygen atoms [15]. In any case, the coefficient stabilized after prolonged exposure, and the coefficients were found to be 0.018 for iron and 0.0085 for nickel. The results are different from Greaves and Linnett, who reported values of about 0.03 for both metals. The discrepancy between the results could be explained by various factors, including the accuracy of the measuring technique, different pressures used by different authors, and unknown surface morphology.

Melin and Madix [16] performed both theoretical and experimental work to determine the recombination coefficient for various materials. Apart from the recombination coefficient, they also evaluated the energy accommodation coefficient (β), which is defined as:

$$\beta = \frac{8 N_\mathrm{A} P_\mathrm{input}}{4.186\ \bar{v} n\ S \gamma\ W_\mathrm{D}}, \tag{1}$$

where N_A is the Avogadro number, P_input is the measured input power to the isothermal calorimeter, $\bar{v}$ is the mean free velocity of atoms, n is the number density of atoms near the surface of the material, S is the surface area of the material, γ is the recombination coefficient of the material, and W_D is the dissociation energy of the parent molecule. Unlike previous authors, they found the recombination coefficient for nickel larger than that of iron, in particular, 0.017 and 0.010, respectively. They also reported the recombination coefficient for another transition metal—cobalt. The recombination coefficient for cobalt was several times larger at 0.075. All these values were supposed to be measured at room temperature of the metallic samples. Melin and Madix also reported highly vibrationally excited molecules leaving the surface. They found an exponential increase in the recombination coefficient with increasing temperature and provided an empirical formula. They measured the temperature dependence of the recombination coefficient in the range of about 300–500 K.

Another breakthrough was achieved by Šorli and Ročak [17]. They constructed a simple experimental setup, which enabled a rather precise determination of oxygen atom density in the measuring chamber. They measured the heat dissipated on a highly recombinative metallic tube mounted between the plasma source of atoms and the measuring chamber. They assured almost zero transmitivity of the metallic tubes for neutral oxygen atoms. They measured the recombination coefficient for nickel in a range of temperatures from 500 to 1100 K and found a rather constant value at about 0.27. They also provided the dissociation fraction of oxygen atoms measured with a probe by considering this value of the recombination coefficient and disclosed values between about 10% and 20%. They discussed the accuracy of their method for the determination of the recombination coefficient and argued that the dissociation fraction would be over 100% if the recombination coefficients provided by Greaves and Linnett were taken into account. Namely, the nickel catalytic material used by Šorli and Ročak was oxidized, and Greaves and Linnett reported values below 0.01 for oxidized nickel surfaces. Šorli and Ročak measured the recombination coefficient in the range of pressures between 10 and 100 Pa. The temperature of the nickel material was about 600 K at 10 Pa and 1100 K at 60 Pa.

Later, the recombination coefficient was measured by other authors. For example, Mozetič and Cvelbar [18] measured the coefficient on the nickel surface and found the same value as Šorli and Ročak. However, they were probably the first authors who reported serious deviation of the recombination coefficient because of the formation of a thick oxide film of rich morphology. In another paper, the same group measured the recombination coefficient versus the pressure in the processing chamber [19]. They found the coefficient for copper practically independent from the pressure, whereas the recombination coefficient for cobalt was maximal at the pressure of about 20 Pa, decreased rapidly with decreasing pressure and slowly with increasing pressure. A completely different behavior was reported for niobium, where the coefficient increased linearly from 40 to 120 Pa and remained constant thereafter. Such a rather unexpected result may be explained by the fact that the material temperature upon surface recombination of oxygen atoms depends on the pressure. Different materials form different oxides of different morphologies. Unfortunately, these effects were not addressed by [18, 19].

Poberaj *et al* [20] did not measure the recombination coefficient but reported interesting results, which may indicate the temperature dependence of the recombination coefficient. They measured O atom density with catalytic probes. One probe was always kept at a rather high temperature, while the other was sometimes kept at a high temperature but sometimes at a low temperature. They reported good agreements between the results obtained by catalytic probes when immersed in an oxygen atmosphere with a high density of neutral oxygen atoms. At low O atom density, however, there was a serious discrepancy. The discrepancy was explained by the fact that one probe always operated at a rather high temperature, while the other probe also operated at a low temperature when the O density was lower. Implicitly, Poberaj *et al* reported a lower value of recombination coefficient for a nickel at a lower nickel temperature.

The above literature survey leads to the assumption of the pressure and/or temperature dependence of the recombination coefficient. In order to clarify both dependences, we performed systematic measurements of the recombination coefficient at various fluxes of both oxygen atoms and molecules, various pressures, and temperatures of the nickel catalyst. We selected the range of pressures between 40 and 200 Pa because the O-atoms density often reaches the maximum in this pressure range in weakly ionized plasmas sustained in discharge chambers made from a material of low surface loss probability. The knowledge of the temperature and pressure dependence of the recombination coefficient is absolutely necessary when using calorimetry (including advanced versions of catalytic probes) for measuring the O-atom density in plasma systems for controlled oxidation of heat-sensitive objects, including biological samples. Namely, the surface finish (hydrophilicity, wettability, printability, biocompatibility, etc) depends on the doses of O-atoms, so it is important to determine the flux as accurately as possible. The lack of knowledge on the temperature dependence of the recombination coefficient could lead to a misinterpretation of the range of fluences useful for optimal surface finish of delicate materials.

2. Methods

2.1. Experimental setup

We adopted the experimental technique proposed by Šorli and Ročak to determine any temperature or pressure dependence of the recombination coefficient. A schematic of the experimental setup is shown in figure 1. The gas was introduced into the system via the mass flow controller, and passed through a narrow quartz tube. The gaseous plasma, which was the source of oxygen atoms, was ignited and sustained in the microwave (MW) cavity inside the narrow quartz tube of inner diameter 4.7 mm by a MW discharge in the surfatron mode. Details about the operation of such a discharge were reported elsewhere [21]. The MW discharge sustained plasma in a rather small volume inside the MW cavity. Oxygen molecules were partially dissociated, ionized, and excited upon plasma conditions. The gas speed through the narrow quartz tube was large, typically more than 100 ms at the exhaust of the narrow tube to a wider tube [22]. The large speed was a consequence of a pressure gradient along the glass tube. A typical ratio of pressures on the inlet and outlet side of the tube was 10 or more [23].

We placed a movable recombinator inside the narrow tube for some of the measurements in order to obtain lower densities of neutral atoms. The recombinator was a titanium rod with a diameter of 2 mm. After the gas passed through the quartz tube, it entered a wider Pyrex tube. The Pyrex tube was pumped with a two-stage rotary pump, which also had an adjustable valve to control the effective pumping speed. The pressure inside the Pyrex tube was measured with a baratron.

Charged particles effectively recombined on the glass surface on the way from the MW cavity to the exhaust from the glass tube. The recombination coefficient for oxygen atoms on quartz glass is of the order of 10^{-4} [24–27], so the loss of atoms was negligible. The gas entering the afterglow chamber (Pyrex tube) thus contained only neutral oxygen atoms in the ground state and oxygen molecules.

The density of oxygen atoms in the ground state in the measuring chamber next to the exhaust of the quartz tube was determined using the Šorli method. A metallic tube made of catalytic material was mounted at the exhaust of the quartz tube, as shown in figure 1(b). Metallic tubes were made from three different materials, i.e. nickel, iron, or cobalt. The inner diameter and the length of the metallic tubes were 6 and 27 mm, respectively. The metallic tube was mounted in such a manner that it fitted tightly on the quartz glass tube, as shown in figure 1(b). Each metallic tube was connected to a thermocouple to enable measuring its temperature. The oxygen atoms arriving from the quartz tube effectively recombined on the surface of the metallic tube by heterogenous surface recombination. The number of atoms entering the metallic tube in a unit of time ($\mathrm{d}N/\mathrm{d}t$) was calculated as follows:

$$\frac{\mathrm{d}N}{\mathrm{d}t} = \phi\, n, \tag{2}$$

where ϕ is the effective pumping speed (the volume flow at the exhaust of the narrow glass tube), and n is the number density of oxygen atoms entering the metallic tube. Each atom that recombined on the surface of the metallic tube brought half of the dissociation energy of oxygen molecules, i.e. 2.6 eV. The energy was spent on heating the metallic tube. After igniting the discharge, the temperature of the metallic tube started to rise, and after a prolonged time, it assumed a constant value. When the constant temperature of the metallic tube was reached, the discharge was turned off, and the metallic tube started to cool. Just after turning off the discharge, the cooling rate was equal to the heating when the discharge was on. Knowing the measured time derivative of the metallic tube temperature just after turning off the discharge enabled the estimation of the power dissipated on the surface of the metallic tube. The power is proportional to the number of atoms entering the metallic tube (equation (2)). We can calculate the number density of oxygen atoms at the exhaust of the quartz tube as:

$$n = \frac{2\, m_{\mathrm{tube}} c_{\mathrm{p(tube)}}}{W_{\mathrm{D}}\, \phi} \frac{\mathrm{d}T}{\mathrm{d}t}\left(\mathrm{tube}\right), \tag{3}$$

where W_{D} is the dissociation energy of oxygen molecules, and m_{tube}, $c_{\mathrm{p(tube)}}$, $\mathrm{d}T/\mathrm{d}t(\mathrm{tube})$ are the mass, specific heat, and the time derivative of the temperature of the metallic tube, respectively [17]. Equation (3) predicts that all atoms passing the metallic tube from the plasma source into the afterglow chamber (Pyrex tube) recombine to form parent molecules.

The Šorli method will give reliable results providing all the atoms entering metallic tube will actually recombine to form parent molecules. If this is true, the density of atoms in the afterglow chamber (at the position of the nickel disc, see figure 1(a)) when the metallic tube is present is negligible. Since nickel is catalytic for surface recombination of O atoms, the nickel disc mounted close to the exhaust from the quartz tube serves as a catalytic probe. The signal was actually below the detection limit of the probe, which is at the O-atom density of about 10^{19} m^{-3}, so it is possible to conclude that a vast majority of atoms actually recombine on the metal-

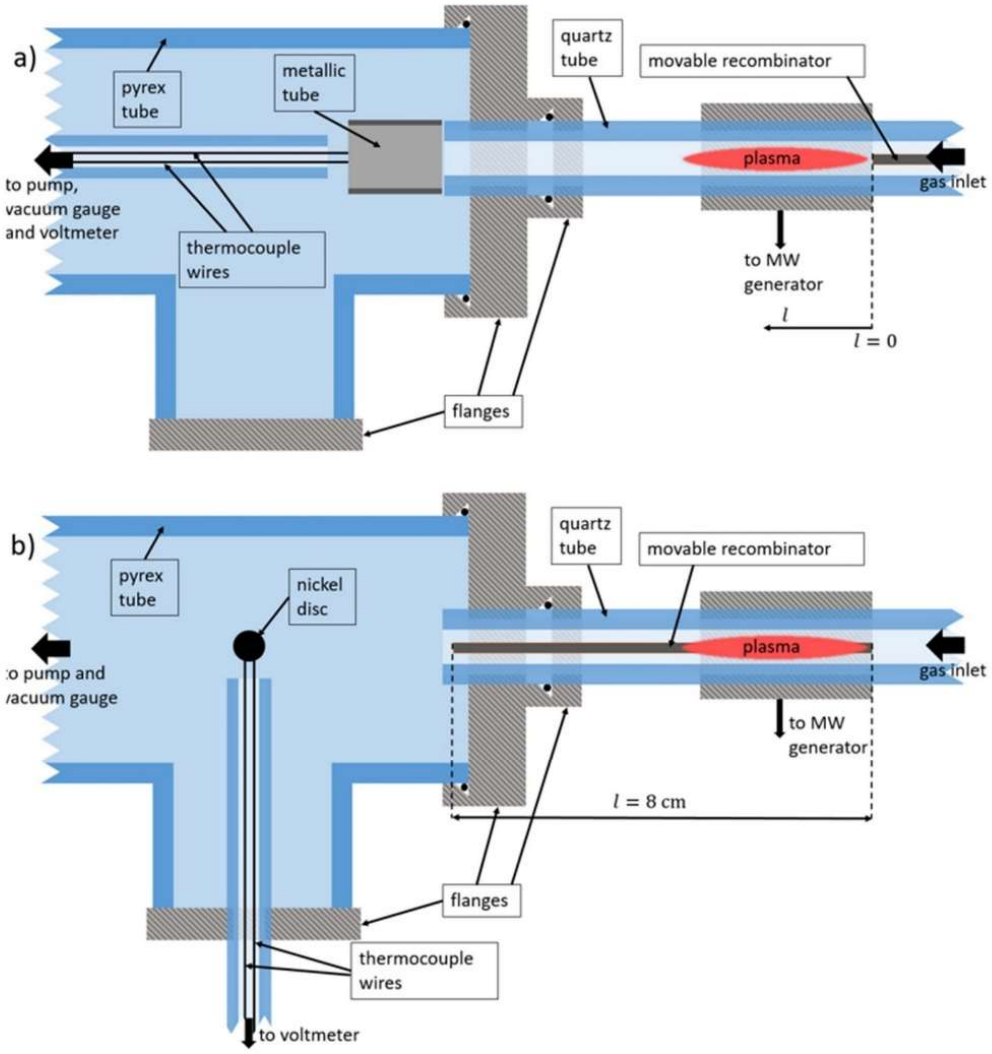

Figure 1. Experimental setup. (a) For measuring the recombination coefficient; (b) for measuring the atom density inside the Pyrex tube. The outer and inner diameters of the quartz tube are 6 and 4.7 mm, respectively, the metallic tube of diameter 6 mm is made from a thin metallic foil, and the movable recombinator is a titanium rod of diameter 2 mm. $l = 0$ marks the position of the movable recombinator just outside the MW cavity while $l = 8$ cm marks the leftmost position of the movable recombinator.

lic tube in the configuration of figure 1(b), so equation (2) is a reliable approximation. The probe signal became measurable only at elevated pressures. The correction factor at pressures up to 100 Pa is below a few %, whereas it is up to about 10% at the highest flow probed at our experiments, i.e. 3000 sccm.

The recombination coefficient of nickel was measured after removing the metallic tube from the experimental system, so in the configuration as shown in figure 1(a). Namely, when the metallic tube was absent (figure 1(a)), the flow of atoms into the afterglow chamber was practically the same as the flow into the metallic tube in the configuration as in figure 1(b).

A thin disc of high-purity nickel (99.99%) was placed into the afterglow chamber at the position marked as 'nickel disc' in figure 1. The disc was fixed to thermocouple wires. Before performing systematic measurements at various conditions, the disc was kept at a temperature of about 750 K for half an hour to enable the formation of a stable and thick oxide film. The surface roughness of the oxidized catalytic material was measured by atomic force microscopy and the thickness of the oxide film by ToF-SIMS after cutting the disc.

The recombination coefficient of the nickel disc was measured by calorimetry. Knowing the density of atoms at the position of the catalytic disc enables the calculation of the recombination coefficient:

$$\gamma = \frac{8\, m_{\mathrm{disc}}\, c_{\mathrm{p(disc)}}}{v\, W_{\mathrm{D}}\, \pi\, r_{\mathrm{disc}}^{2}\, n} \frac{\mathrm{d}T}{\mathrm{d}t}(\mathrm{disc}), \quad (4)$$

where m_{disc}, $c_{\mathrm{p(disc)}}$, r_{disc}, and $\mathrm{d}T/\mathrm{d}t\,(\mathrm{disc})$ are the mass, specific heat, radius, and the time derivative of the temperature of the catalytic disc, respectively [17]. Any temperature or pressure dependence of the recombination coefficient was determined by either keeping the catalytic disc temperature constant at different pressures or keeping the pressure constant but allowing different temperatures of the catalytic discs. The pressure in the system was kept constant at different disc temperatures by variation of the effective pumping speed and the inlet gas flow. By different combinations of these two parameters, it was possible to achieve different atom densities at the position of the catalytic disc at the selected pressure. The atom density was also adjusted by moving the titanium recombinator in the quartz tube, as shown schematically in figure 1.

2.2. AFM measurements

Atomic force microscopy (AFM) measurements were performed with the A100-AFM microscope produced by A.P.E. Research (Italy) with the NT-MDT silicon tips. Measurements were done in the contact mode with the recording frequency of 0.5 Hz. The resolution of the images was set to 256 × 256 pixels. Images were post-processed with the plane subtraction due to the sample inclination involving a second-order polynomial correction and with the correction of the horizontal scars caused by the rough surface and consequent errors due to the responsiveness of the tip.

2.3. ToF-SIMS measurements

The time-of-flight secondary ion emission spectroscopy (ToF-SIMS) analyses were performed on a TOF.SIMS 5 instrument produced by IONTOF (Germany). Micrographs were recorded using Bi^{+} ions with the energy of 30 keV while simultaneously performing sputtering with the second ion gun (dual beam) using Cs^{+} ions with the energy of 1 keV. The current of the Bi^{+} ions was approximately 0.2 pA and the current of the Cs^{+} ions was approximately 564 nA. The analyses with the Bi^{+} primary ions were performed over a 100 × 100 μm scanning area (512 × 512 pixels), located in the center of the 400 × 400 μm etching crater sputtered by the Cs^{+} ion beam. The lateral resolution of the Bi^{+} analysis beam was approximately 200 nm. Hydrogen gas was introduced into the analysis chamber via a capillary to close proximity of the analyzed region to reduce the matrix effect and enable better differentiation between layers of Ni and NiO [28]. The pressure of the H_2 atmosphere in the analysis chamber was 7×10^{-7} mbar. Secondary ions were analyzed in the *m/z* range 0–420. Only negative secondary ions were analyzed.

3. Results and discussion

3.1. Oxygen atom density and dissociation fraction in the measuring chamber

The experimental setup shown in figure 1 was first used to evaluate the density of atoms in the measuring chamber at the position where the catalytic discs was mounted (configuration as in figure 1(b)). Equation (3) indicates that the calculated number of atoms entering the afterglow chamber (Pyrex tube) in unit time is independent of the recombination coefficient of the material the metallic tube is made from. We placed three different metallic tubes made from nickel, cobalt, and iron at the exhaust of the quartz tube into the Pyrex tube as shown in figure 1(b). The density of O atoms in the afterglow chamber using these three metallic tubes is plotted in figure 2. There are small deviations from the standard curve, but all measured points are within the limits of the experimental error. The results in figure 2 therefore confirm that the density of atoms, as calculated from equation (3), does not depend on the recombination coefficient of the materials from which the metallic tubes are made. As mentioned earlier, this is because the surface recombination is large enough to transform practically all atoms into molecules when the partially dissociated gas passes through the metallic tube.

The error bars in figure 2 arise from several repetitions of the measurements (statistical error) as well as the uncertainty of the atom leakage through the metallic tubes. The latter increases with increasing pressure. As mentioned above, the uncertainty of the measured density of oxygen atoms depends on the efficiency of the metallic tubes to recombine atoms, and the efficiency slowly decreases when the pressure increases. Namely, the mean free path of gaseous species decreases with increasing pressure, so there is a certain probability that the atoms will pass the metallic tube without experiencing numerous collisions with the metallic tube surface at elevated pressures, which is necessary for efficient recombination.

Several effects explain the behavior of the O-atom density versus the pressure (figure 2). First, the number of available molecules for dissociation increases linearly with increasing pressure. When this effect prevails, the O atom density also increases linearly with increasing pressure. The linearity persists up to the pressure of about 80 Pa at conditions selected for figure 2. At elevated pressure, the dissociation of oxygen molecules in the plasma is not as efficient as at low pressures because the discharge power is limited. In the case of the results presented in figure 2, we used the discharge power of 180 W. As shown by some other authors, the dissociation of oxygen molecules at elevated power actually increases with increasing discharge power [23]. The measurements were repeated at various gas flows, pressures, and the position of the movable recombinator in order to determine the O-atom density in a broad range of discharge parameters useful for the determination of the recombination coefficients.

The movable recombinator serves for adjustment of the O-atom density in the Pyrex tube irrespective of the discharge power or pressure. Namely, some atoms formed upon

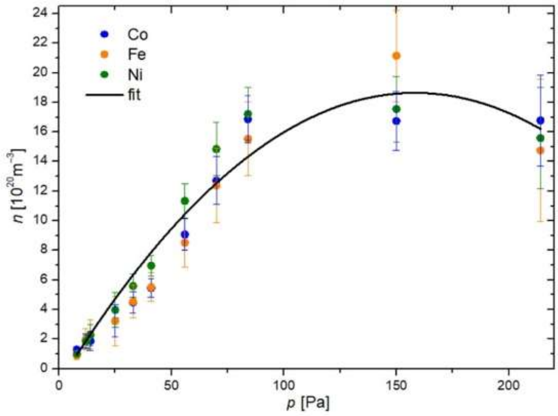

Figure 2. O atom density at the position of the catalyst discs versus the pressure in the measuring chamber at the effective pumping speed of up to 0.017 $m^3\ s^{-1}$ and gas inlet rates up to 3000 sccm.

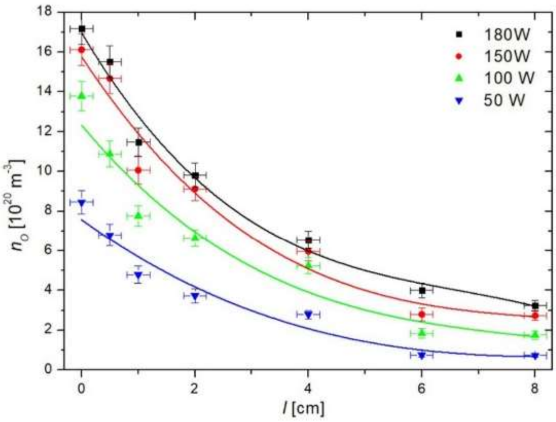

Figure 3. The O-atom density (n_O) in the Pyrex tube versus the position of the movable recombinator (l) at the gas pressure inside the Pyrex tube of 84 Pa and four different discharge powers.

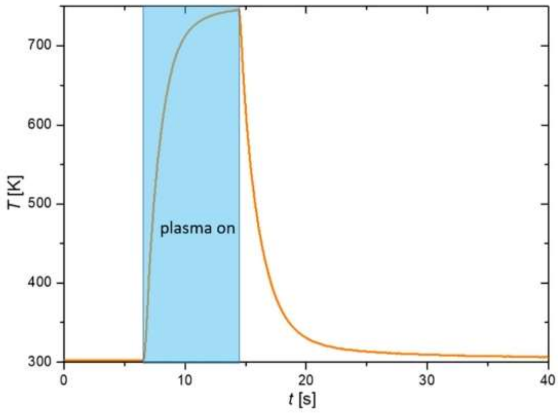

Figure 4. Typical measurement with a nickel disc catalytic probe. The graph shows the disc temperature (T) versus time (t).

dissociation of oxygen molecules in glowing plasma recombine on the surface of the titanium rod. The O-atom density in the Pyrex tube is plotted versus the position of the movable recombinator in figure 3. Position 0 in figure 3 corresponds to the right edge of the MW cavity in figure 1(a). As expected, the O-atom density decreases as the recombinator is moved inside the plasma.

3.2. The recombination coefficient

After measuring the atom density in the afterglow chamber at various conditions, the metallic tubes were removed from the experimental system shown in figure 1(b), and a nickel disc was mounted, as shown in figure 1(a). The disc was connected to very thin thermocouple wires, and the discs temperature was measured versus time at various experimental conditions. A typical example of a disc temperature is shown in figure 4. The discharge was switched on at $t = 7$ s, and switched off at $t = 14$ s. One can observe a behavior typical for heating a sample at a constant heating power. Soon after igniting the discharge, the temperature increases linearly with time because the heating power is constant (strictly, it is constant if the recombination coefficient does not depend on the temperature), and any cooling is negligible. As the temperature increases with increasing treatment time, a deviation of linearity is observed, and after about 10 s, the temperature stabilizes. When the temperature is constant, the heating and cooling rates are equal. Cooling depends on various mechanisms, including the grey body radiation, the thermal conductivity of the surrounding gas, cooling by gas drift, and cooling through

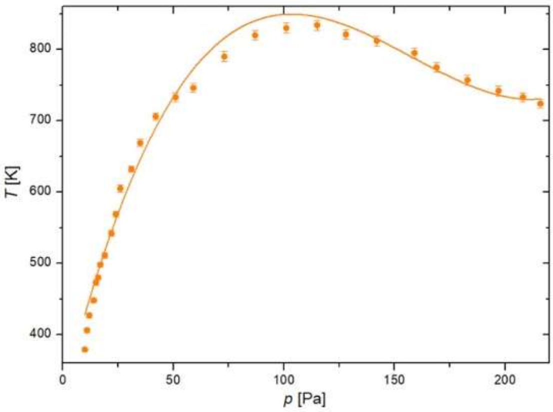

Figure 5. The maximum temperature ($T_{\max}$) of a nickel disc versus pressure (p) inside the system.

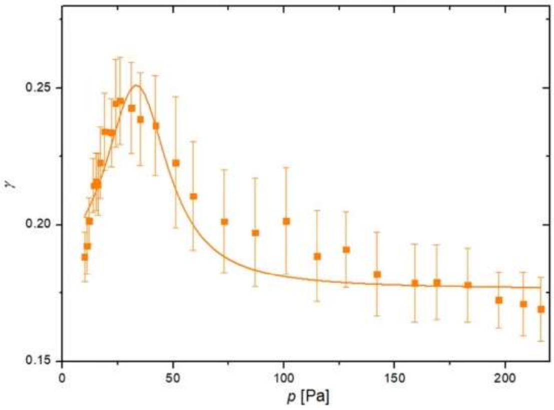

Figure 6. The recombination coefficient of a nickel catalytic disc versus the pressure in the measuring chamber at the fixed discharge power of 180 W, calculated from equation (4).

the thermocouple wires. The latter is negligible because of the very small mass of the wires (0.25 mm diameter). The maximum temperatures of a nickel disc are plotted in figure 5 versus the pressure at the discharge power of 180 W, a fully open butterfly valve, and the recombinator outside the quartz tube.

The recombination coefficient of the nickel disc is calculated from the time derivative of the disc temperature using equation (4), providing the O atom density in the vicinity of the catalytic disc is known and providing that the disc does not represent such a large sink of atoms so that the O-atom gradient would form around the disc. Numerous measurements were performed at various discharge conditions, which enabled various O-atom densities in the afterglow chamber. Results are shown in figure 6.

According to figure 6, the recombination coefficient increases steeply with the pressure in the range of 10–30 Pa. The coefficient is about 0.20 at 10 Pa and 0.25 at 30 Pa. Thereafter, the recombination coefficient starts decreasing with further pressure increase. At first glance, one may conclude that the recombination coefficient increases with increasing pressure up to about 30 Pa and decreases at elevated pressures. The observations arising from the behavior of the measured curve in figure 6, however, should be taken with precautions because not only is the pressure changing, but the temperature of the catalytic disc when turning off the discharge also depends on the pressure (figure 5). Figure 6 only indicates some dependencies, but it is unclear whether the dependence is directly due to pressure-related or temperature-related effects. Interestingly, very similar results were reported by Cvelbar *et al* for a cobalt catalyst [19].

Similar results as in figure 6 can be presented versus the maximum temperature of the catalytic disc. Results for nickel are shown in figure 7. In addition, we also provide the results of the calculated recombination coefficient at several discharge powers. We were changing the gas pressure in the same

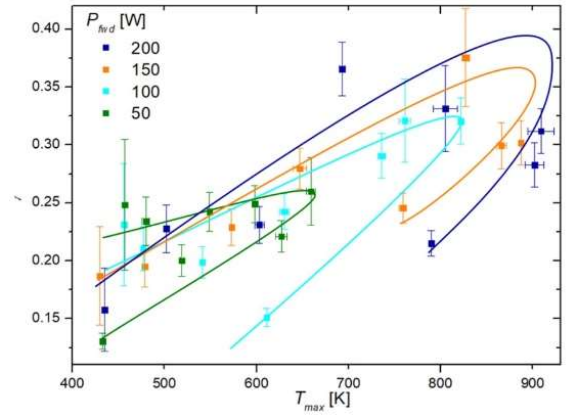

Figure 7. Calculated recombination coefficient (γ) of nickel at various maximum temperatures of the nickel disc for four different forward powers of the MW generator.

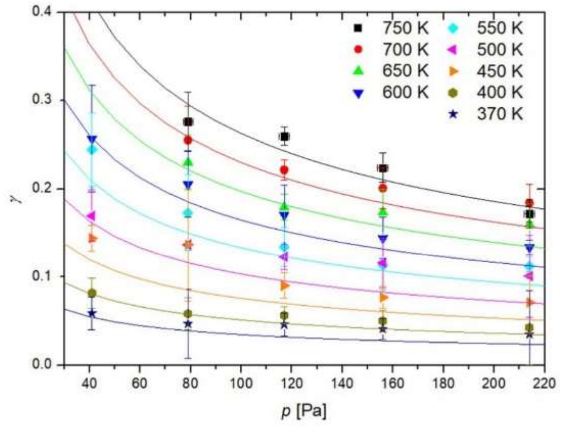

Figure 8. Recombination coefficient (γ) of nickel for oxygen atoms versus pressure (p) in the plasma system at nine fixed temperatures. Plotted lines represent the fitting of the function $\gamma(p,T) = A\,p^{-1/2}\,e^{-B/T}$ onto the measurements.

manner as for results shown in figure 5 at a constant pumping speed, but we calculated the recombination coefficient versus maximum temperature at various discharge powers. We see that all four curves in figure 7 exhibit a rather unexpected behavior. The recombination coefficient increases with increasing temperature up to about 800 K, but starts decreasing thereafter and assumes a rather low value when the temperature is decreased. The highly surprising results are explained by the fact that probe temperature does not only depend on atom density in the vicinity of the probe but also on the gas pressure. The turn in the curve in figure 7 indicates decreasing γ with increasing pressure. Taking into account the pressure, which was measured simultaneously, one may deduce that a rather high recombination coefficient is measured at low pressure, the highest measured at moderate pressure, whereas at large pressures, the recombination coefficient decreases again. The turning point in figure 7 is observed for all four discharge powers, but the absolute values are different. The differences are due to the increasing O-atom density with increasing discharge power. The larger O-atom density at a fixed pressure will cause a higher catalyst temperature because of the larger flux of oxygen atoms onto the catalyst surface, whereas the cooling through the gas at a fixed pressure remains the same, irrespective of the discharge power.

Considering figures 5 and 6, one can conclude either about pressure or temperature dependence of the recombination coefficient or both. In order to clarify, we performed measurements at fixed temperatures of the nickel sample and at several pressures. This was possible by changing the input power of the MW generator and the position of the movable recombinator (figure 1).

Figure 8 represents the recombination coefficients for a nickel disc kept at nine different temperatures, ranging from 370 K to 750 K, and at various pressures between 41 and 214 Pa. Such broad conditions were achieved by changing the flow of gas through the system and varying the

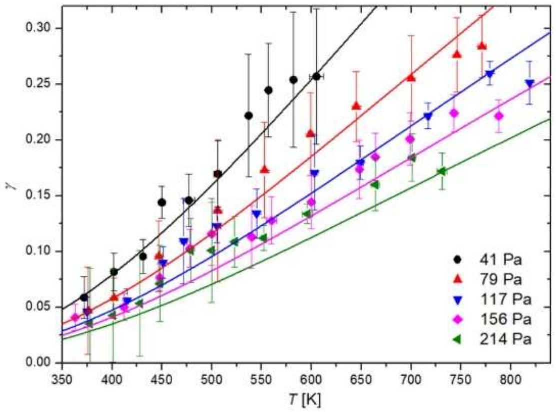

Figure 9. Recombination coefficient (γ) of oxidized nickel for oxygen atoms versus surface temperature (T) at five fixed pressures inside the afterglow chamber. Plotted lines represent the fitting of the function $\gamma\,(p,T) = A\,p^{-1/2}\mathrm{e}^{-B/T}$ onto the measurements.

discharge power. Furthermore, we were moving the titanium recombinator in the quartz tube (figure 1) to achieve lower densities of neutral atoms at large discharge powers, which allowed for measurements at temperatures of the nickel disc below the value that would be reached without the recombinator. One can observe a monotonous decrease in the recombination coefficient with increasing pressure in figure 8. These measurements clearly indicate that the gas pressure influences the recombination coefficient. The difference between the lowest and the highest pressure, however, is not dramatic—less than a factor of 2.

The lowest measurable point for 750, 700, and 650 K in figure 8 is at the pressure of about 79 Pa. Namely, the probe does not heat up to 650 K at lower pressures simply because O atom density is too low (see figure 5). Lower temperatures are achievable in our experimental system also at slightly lower pressures. The recombination coefficient decreases with increasing pressure and the differences are not large at elevated pressures. It was not possible to measure the curve at higher pressure because it was not possible to heat the catalyst to such a high temperature at elevated pressures.

The pressure dependence of recombination coefficients has already been mentioned by several authors [29–31]. A feasible explanation is the screening of the oxygen atom adsorption sites by oxygen molecules. This effect is, of course, more pronounced at elevated pressures simply because the flux of molecules on the surface increases linearly with increasing pressure. Still, the rather small slope of the curve at around 200 Pa indicates a significant number of recombination sites even at elevated pressures. Figure 8, therefore, indicates that recombination at various elevated temperatures remains relatively large even at high pressures (does not approach zero).

As mentioned earlier and according to figure 8, the recombination coefficient should also depend on the temperature because the mobility of surface adatoms increases with increasing temperature. The measured temperature dependence of the recombination coefficient for the nickel disc at the pressures of 41, 79, 117, 156, and 214 Pa is plotted in figure 9. The measured dots are somewhat scattered, but the general trend is obvious: the recombination coefficient increases with increasing surface temperature.

Several authors have reported a similar trend when it comes to the temperature dependence of the recombination coefficient [9, 16, 32–42]. Many agree that the dependence can be described with an Arrhenius plot in the form of:

$$\gamma\,(T) = A\,\mathrm{e}^{-B/T}, \tag{5}$$

where A and B are parameters usually gleaned from empirical results. Equation (5) was taken as a basis for our own empirical equation, but we also considered the pressure dependence. Several formulas were considered, with a few viable candidates. In the end, the best agreement for both pressure and temperature dependence of γ in the range of the probed pressures and temperatures was found to be in the form of:

$$\gamma\,(p,T) = \frac{A}{\sqrt{p}}\mathrm{e}^{-B/T}, \tag{6}$$

where $A = 17\ \mathrm{Pa}^{1/2}$ and $B = 1400$ K. While we could not find any data on the pressure dependence of γ for nickel, the exponential factor B is in agreement with Dickens and Sutcliffe when using the Arrhenius plot [9]. This exponential factor corresponds to an energy of 0.121 eV, which is significantly lower than the dissociation energy of an oxygen molecule.

The flexibility of the experimental system adopted for this research enabled variation of the nickel disc temperature irrespectively from the pressure in the afterglow chamber or the atom density near the catalyst. This is particularly important because the simultaneous variation of both the pressure and the catalyst temperature may lead to misinterpretation of the recombination coefficient dependence, as demonstrated in

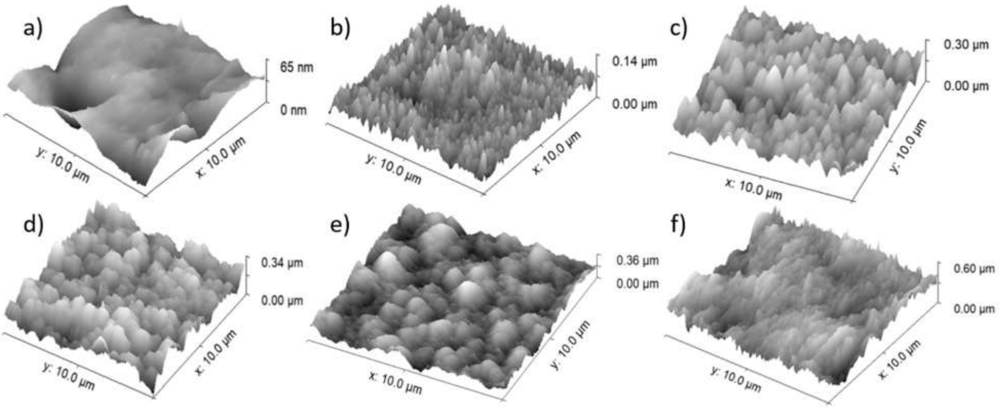

Figure 10. AFM images of $10 \times 10\ \mu\text{m}^2$ surface areas of nickel samples, starting with (a) a clean nickel sample with $S_q = 8$ nm, (b) nickel sample oxidized at 400 K with $S_q = 16$ nm, (c) nickel sample oxidized at 600 K with $S_q = 35$ nm, (d) nickel sample oxidized at 800 K with $S_q = 50$ nm, (e) nickel sample oxidized at 1000 K with $S_q = 60$ nm, and (f) nickel sample oxidized at 1200 K with $S_q = 70$ nm.

figures 5 and 6. The results presented in figures 7 and 8 are reliable, but not very accurate because a rather large scattering of measured points is observed. The scattering comes from the inaccuracy of measuring the density of oxygen atoms in the afterglow chamber (a few examples are shown in figure 2) as well as somehow arbitrary determination of the maximal catalyst temperature (figure 4). The latter is probably the effect of increasing gas temperature with increasing plasma duration.

The empirical formula obtained from measured points in figures 7 and 8 does not fit perfectly the measured values. It should be taken only as a recommended approximation for the range of probed pressures and temperatures of the oxidized nickel samples at turning off the discharge generator. Although similar temperature behavior was reported by numerous authors ([9, 16, 32–42]), the scientifically spotless explanation remains to be invented. Qualitatively, one can explain the temperature behavior by increasing mobility of surface adatoms with increasing temperature. As mentioned above, the Langmuir–Hinshelwood model predicts the association of two adatoms accommodated on the surface to a molecule, which is, contradictory to atoms, not trapped by rather strong chemical bonds, so it desorbs and leaves the surface. The association of neighboring adatoms will require close proximity because the average distance between oxygen atoms in the O_2 molecule is only about 0.12 nm [43], while the average distance between atoms on the surface of solid material is roughly $0.2 - 0.3$ nm [44]. Such proximity is more likely to occur at an increased amplitude of bonded O-atoms oscillation, and the amplitude increases with increasing temperature. Any discussion on the exact mechanisms at the atomic scale is beyond the scope of this article.

The formula (6) indicates the recombination inversely proportional to the square root of pressure. Obviously, the formula is void at low pressures, because the coefficient would approach infinity when the pressure will approach 0. The formula is valid only in the range of pressures used in this work. We selected the range of pressures between 40 and 200 Pa because the measurements were feasible in this range. In fact, many reactors employing weakly ionized oxygen plasma for tailoring surface properties of solid materials exhibit the maximum O-atom density within this range [45].

As already mentioned, metals form oxide films upon exposure to oxygen at elevated temperatures. The film thickness will increase with increasing temperature (and, to less extent, also the oxidation time). Even if the catalytic disc is polished, the oxide film will be rather rough. The recombination coefficient should depend on the roughness because the roughness increases the effective surface when compared to the geometrical surface area. All measurements of the recombination coefficient were performed after thorough oxidation of the nickel disc as explained above. AFM images of a nickel surface oxidized at different temperatures are shown in figure 10, progressing from a clean nickel surface (a), oxidation at 400 K (b), oxidation at 600 K (c), oxidation at 800 K (d), oxidation at 1000 K (e), and oxidation at 1200 K (f). The RMS surface roughness (S_q) increased with increasing oxidation temperature from 10 nm to 70 nm. The catalytic nickel disc, which was used in experiments after forming a stable oxide film at around 1000 K, is shown in figure 10(e). The roughness was estimated at $S_q = 60$ nm. The thickness of the oxide film after thorough oxidation of the nickel disc was determined by ToF-SIMS. As shown in figure 11, the thickness was about 10 μm.

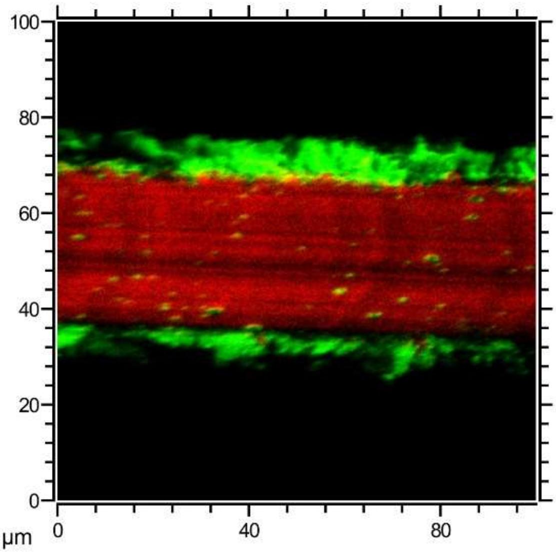

Figure 11. ToF-SIMS image of the cross section of the nickel disc. At around 30 μm thickness, the red section represents pure nickel, whereas the green sections represent nickel oxide with a thickness of about 10 μm on each side.

4. Conclusions

The coefficient for heterogenous recombination of O atoms on the surface of oxidized nickel disc to parent molecules was determined experimentally. First, the O atom density in the afterglow chamber was measured at various experimental conditions using the method originally proposed by Šorli and Ročak. Three different metallic tubes were probed in order to validate the reliability of the method. The same conditions were adopted for measuring the heating curves of a well-oxidized nickel disc. The heating curves enabled calculation of the recombination coefficient from known density of O atoms in the measuring chamber. Various gas flow rates, effective pumping speeds and O-atom densities enabled determination of the temperature and pressure variation of the recombination coefficient in the range of pressures between about 40 and 200 Pa, and the range of temperatures between about 370 and 750 K. The measured results were fitted with an empirical formula. The formula is useful at any attempt to use nickel as the catalytic material in advanced probes for sensing the density of oxygen atoms in devices for oxidation of delicate materials in a highly controllable manner.

Data availability statement

The data cannot be made publicly available upon publication because they are not available in a format that is sufficiently accessible or reusable by other researchers. The data that support the findings of this study are available upon reasonable request from the authors.

Acknowledgments

This research was funded by the Slovenian Research Agency, Grant Nos. P2-0082 and L2-4487.

ORCID iDs

Domen Paul https://orcid.org/0000-0002-5450-7101
Miran Mozetič https://orcid.org/0000-0003-3782-6001
Rok Zaplotnik https://orcid.org/0000-0002-1366-9147
Jernej Ekar https://orcid.org/0000-0001-8895-4746
Gregor Primc https://orcid.org/0000-0002-3959-776X

References

[1] Annušova A, Marinov D, Booth J-P, Sirse N, da Silva M L, Lopez B and Guerra V 2018 Kinetics of highly vibrationally excited O2(X) molecules in inductively-coupled oxygen plasmas *Plasma Sources Sci. Technol.* **27** 045006
[2] Baranov O, Bazaka K, Kersten H, Keidar M, Cvelbar U, Xu S and Levchenko I 2017 Plasma under control: advanced solutions and perspectives for plasma flux management in material treatment and nanosynthesis *Appl. Phys. Rev.* **4** 041302
[3] Booth J-P and Sadeghi N 1991 Oxygen and fluorine atom kinetics in electron cyclotron resonance plasma by time-resolved actinometry *J. Appl. Phys.* **70** 611–20
[4] Guerra V, Silva T, Ogloblina P, Grofulović M, Terraz L, da Silva M L, Pintassilgo C D, Alves L L and Guaitella O 2017 The case forn *in-situ* resource utilisation for oxygen production on Mars by non-equilibrium plasmas *Plasma Sources Sci. Technol.* **26** 11LT01
[5] Kersten H, Deutsch H, Steffen H, Kroesen G M W and Hippler R 2001 The energy balance at substrate surfaces during plasma processing *Vacuum* **63** 385–431
[6] Kutasi K, Bencs L, Tóth Z and Milošević S 2023 The role of metals in the deposition of long-lived reactive oxygen and nitrogen species into the plasma-activated liquids *Plasma Process. Polym.* **20** 2200143
[7] Vesel A, Kolar M, Recek N, Kutasi K, Stana-Kleinschek K and Mozetič M 2014 Etching of blood proteins in the early and late flowing afterglow of oxygen plasma *Plasma Process. Polym.* **11** 12–23
[8] Paul D, Mozetič M, Zaplotnik R, Primc G, Đonlagič D and Vesel A 2023 A review of recombination coefficients of neutral oxygen atoms for various materials *Materials* **16** 1774
[9] Dickens P G and Sutcliffe M B 1964 Recombination of oxygen atoms on oxide surfaces *Trans. Faraday Soc.* **60** 1272–85
[10] Greaves J C and Linnett J W 1958 The recombination of oxygen atoms at surfaces *Trans. Faraday Soc.* **54** 1323
[11] Mozetič M, Vesel A, Stoica S D, Vizireanu S, Dinescu G and Zaplotnik R 2015 Oxygen atom loss coefficient of carbon nanowalls *Appl. Surf. Sci.* **333** 207–13
[12] Primc G, Lojen D, Vesel A, Mozetič M and Zaplotnik R 2022 Oxygen atom density in a large reactor powered by four inductively coupled plasma sources *Vacuum* **199** 110964
[13] Lymberopoulos D P, Kolobov V I and Economou D J 1998 Fluid simulation of a pulsed-power inductively coupled argon plasma *J. Vac. Sci. Technol.* A **16** 564–71
[14] Myerson A L 1969 Exposure-dependent surface recombination efficiencies of atomic oxygen *J. Chem. Phys.* **50** 1228–34
[15] Mozetič M, Vesel A, Kovač J, Zaplotnik R, Modic M and Balat-Pichelin M 2015 Formation and reduction of thin oxide films on a stainless steel surface upon subsequent

treatments with oxygen and hydrogen plasma *Thin Solid Films* **591** 186–93

[16] Melin G E and Madix R J 1971 Energy accommodation during oxygen atom recombination on metal surfaces *Trans. Faraday Soc.* **67** P001–2

[17] Šorli I and Ročak R 2000 Determination of atomic oxygen density with a nickel catalytic probe *J. Vac. Sci. Technol.* A **18** 338–42

[18] Mozetič M and Cvelbar U 2007 Heterogeneous recombination of O atoms on metal surfaces *Int. J. Nanosci.* **6** 121–4

[19] Cvelbar U, Mozetič M and Ricard A 2005 Characterization of oxygen plasma with a fiber optic catalytic probe and determination of recombination coefficients *IEEE Trans. Plasma Sci.* **33** 834–7

[20] Poberaj I, Mozetič M and Babič D 2002 Comparison of fiber optics and standard nickel catalytic probes for determination of neutral oxygen atoms concentration *J. Vac. Sci. Technol.* A **20** 189–93

[21] Kutasi K, Saoudi B, Pintassilgo C D, Loureiro J and Moisan M 2008 Modelling the low-pressure N_2–O_2 plasma afterglow to determine the kinetic mechanisms controlling the UV emission intensity and its spatial distribution for achieving an efficient sterilization process *Plasma Process. Polym.* **5** 840–52

[22] Kutasi K, Zaplotnik R, Primc G and Mozetič M 2014 Controlling the oxygen species density distributions in the flowing afterglow of O_2/Ar–O_2 surface-wave microwave discharges *J. Phys. D: Appl. Phys.* **47** 025203

[23] Primc G, Zaplotnik R, Vesel A and Mozetič M 2011 Microwave discharge as a remote source of neutral oxygen atoms *AIP Adv.* **1** 022129

[24] Marschall J 2007 Laboratory determination of thermal protection system materials surface catalytic properties RTO-EN-AVT-142

[25] Kim Y C and Boudart M 1991 Recombination of O, N and H atoms on Silica *Langmuir* **7** 2999–3005

[26] Cartry G, Duten X and Rousseau A 2006 Atomic oxygen surface loss probability on silica in microwave plasmas studied by a pulsed induced fluorescence technique *Plasma Sources Sci. Technol.* **15** 479–88

[27] Lopaev D V, Malykhin E M and Zyryanow S M 2010 Surface recombination of oxygen atoms in O2 plasma at increased pressure: 1. The recombination probability and phenomenological model of surfae processes *J. Phys. D: Appl. Phys.* **44** 015201

[28] Ekar J, Panjan P, Drev S and Kovač J 2022 ToF-SIMS depth profiling of metal, metal oxide, and alloy multilayers in atmospheres of H_2,C_2H_2,CO, and O_2 *J. Am. Soc. Mass Spectrom.* **33** 31–44

[29] Booth J-P, Guaitella O, Chatterjee A, Drag C, Guerra V, Lopaev D, Zyryanov S, Rakhimova T, Voloshin D and Mankelevich Y 2019 Oxygen (3P) atom recombination on a pyrex surface in an O_2 plasma *Plasma Sources Sci. Technol.* **28** 055005

[30] Gudmundsson J T and Thorsteinsson E G 2007 Oxygen discharges diluted with argon: dissociation processes *Plasma Sources Sci. Technol.* **16** 399–412

[31] Arts K, Deijkers S, Puurunen R L, Kessels W M M and Knoops H C M 2021 Oxygen recombination probability data for plasma-assisted atomic layer deposition of SiO_2 and TiO_2 *J. Phys. Chem.* C **125** 8244–52

[32] Balat-Pichelin M 2007 Interactions of reactivegas flows and ceramics at high temperature—experimental methods for the measurements of species recombination during planetary entry RTO-EN-AVT-142

[33] Balat-Pichelin M and Beche E 2010 Atomic oxygen recombination on the ODS PM 1000 at high temperature under air plasma *Appl. Surf. Sci.* **256** 4906–14

[34] Balat-Pichelin M, Pascarelli M, Scatteia L and Alfano D 2009 Catalycity of zirconia nad of ZrBr2-based ultra-high temperature ceramics *Proc. Ot the 6th European Symp. on Aerothermodynamics for Space Vehicles* (*Noordwijk, Netherlands*)

[35] Guyon C, Cavadias S and Amouroux J 2001 Heat and mass transfer phenomenon from an oxygen plasma to a semiconductor surface *Surf. Coat. Technol.* **142–144** 959–63

[36] Guyon C, Cavadias S, Mabille I, Moscosa-Santillan M and Amouroux J 2004 Recombination of oxygen atomic excited states produced by non-equilibrium RF plasma on different semiconductor materials: catalytic phenomena and modelling *Catal. Today* **89** 159–67

[37] Kolodziej P and Stewart D A 1987 Nitrogen recombination on high-temperature reusable surface insulation and the analysis of its effect on surface catalysis AIAA-87-1637

[38] May J W and Linnett J W 1967 Recombination of atoms at surfaces *J. Catal.* **7**

[39] Pagnon D, Amorim J, Nahorny J, Touzeau M and Vialle M 1995 On the use of actinometry to measure the dissociation in O_2 DC glow discharges: determination of the wall recombination probability *J. Phys. D: Appl. Phys.* **28** 1856–68

[40] Stewart D A 1996 Determination of surface catalytic efficiency for thermal protection materials—room temperature to their upper use limit *31st Thermophysics Conf.* (*New Orelans, USA*)

[41] Stewart D A 1996 Surface catalytic efficiency of advanced carbon carbon candidate thermal protection materials for SSTO vehicles *NASA Tech. Memo.* **15** 110383

[42] Stewart D A 1999 Surface characterization of candidate metallic TPS for RLV *AIAA* pp 99–3458

[43] Babcock H D 1937 Internuclear distance in oxygen molecules *Proc. Natl Acad. Sci.* **23** 301–4

[44] Kim J S, Reibenspies J H and Darensbourg M Y 1996 Characteristics of nickel(0), nickel(I), and nickel(II) in phosphino thioether complexes: molecular structure and S-dealkylation of $(Ph_2P(o\text{-}C_6H_4)SCH_3)_2Ni_0$ *J. Am. Chem. Soc.* **118** 4115–23

[45] Booth J-P, Mozetič M, Nikiforov A and Oehr C 2022 Foundations of plasma surface functionalization of polymers for industrial and biological applications *Plasma Sources Sci. Technol.* **31** 103001

2.2 Loss of Oxygen Atoms on Well-Oxidized Cobalt by Heterogeneous Surface Recombination

Similarly to the previous chapter, the recombination coefficient of an oxidized metallic sample was determined, this time using well-oxidized cobalt as the tip of the catalytic probe. Again, the Šorli-Ročak method was used to determine the neutral atom densities across a wide range of conditions to enable systematic measurements.

The results of measurements by previous authors indicate a complex behavior of the recombination coefficient for oxygen atoms on a cobalt surface [89], [66], [67], [78], [70]. The effects of pressure inside the experimental systems and the temperature of the cobalt samples were observed but there were some discrepancies between the results of the authors which the proceeding article aims to clear up.

The same experimental system (Figure 10) is used in the measurements, with the addition of another pressure gauge measuring pressure in the glow chamber. The difference in pressures between the glow and afterglow chamber are measured, supporting the notion of a linear increase in gas drift velocity as the gas drifts through the experimental system.

The pressure and temperature dependence of the recombination coefficient of oxidized cobalt is seemingly the same as measured for nickel, with a few caveats. While the recombination coefficient does increase with increasing temperature, the Arrhenius plot is interrupted at higher temperatures (650 K and above) where the recombination coefficient seems to stabilize and remain at a constant value with increasing temperature. The recombination coefficient of oxidized cobalt also decreases with increasing pressure similarly to the recombination coefficient of oxidized nickel.

An AFM image of the oxidized cobalt sample used as the tip of the catalytic probe is shown, with some interesting differences when compared to the oxidized nickel sample. The surface morphology is much richer, with the estimated RMS surface roughness around ten times greater than for the oxidized nickel surface. Even more interesting is the ToF-SIMS depth profile, which indicates that the oxide layer present in the cobalt sample extends throughout the entire volume of the cobalt sample – in essence, the entire 50 µm thick sample is oxidized.

The richer surface morphology factors into the larger measured recombination coefficient of oxidized cobalt when compared to oxidized nickel. Additionally, the absence of any layers in the depth profile of the cobalt samples emphasizes the oxidation potential of cobalt.

Lastly, the results of the proceeding article are compared to the results of previous authors and seem to be mostly in agreement. For ease of comparison, a 3D plot of the results is provided along with dots representing the results of previous authors in a graph with surface temperature, pressure in the experimental system, and the recombination coefficient as the x, y, and z-axis, respectively.

The increase of the recombination coefficient with the increasing temperature of the oxidized cobalt sample is explained by the increasing mobility of adsorbed oxygen atoms on the sample surface, which increases the probability of surface recombination via the Langmuir-Hinshelwood mechanism. The decrease of the recombination coefficient with increasing pressure is explained as the effect of the abundance of oxygen molecules screening the sample surface from oxygen atoms.

materials MDPI

Article

Loss of Oxygen Atoms on Well-Oxidized Cobalt by Heterogeneous Surface Recombination

Domen Paul [1,2,*], Miran Mozetič [1], Rok Zaplotnik [1], Jernej Ekar [1,2], Alenka Vesel [1], Gregor Primc [1] and Denis Đonlagić [3]

[1] Jozef Stefan Institute, Jamova Cesta 39, 1000 Ljubljana, Slovenia
[2] Jozef Stefan International Postgraduate School, Jamova Cesta 39, 1000 Ljubljana, Slovenia
[3] Faculty of Electrical Engineering and Computer Science, University of Maribor, Koroska Cesta 46, 2000 Maribor, Slovenia
* Correspondence: domen.paul@ijs.si

Abstract: Calorimetry is a commonly used method in plasma characterization, but the accuracy of the method is tied to the accuracy of the recombination coefficient, which in turn depends on a number of surface effects. Surface effects also govern the kinetics in advanced methods such as atomic layer oxidation of inorganic materials and functionalization of organic materials. The flux of the reactive oxygen atoms for the controlled oxidation of such materials depends on the recombination coefficient of materials placed into the reaction chamber, which in turn depends on the surface morphology, temperature, and pressure in the processing chamber. The recombination coefficient of a well-oxidized cobalt surface was studied systematically in a range of temperatures from 300 to 800 K and pressures from 40 to 200 Pa. The coefficient increased monotonously with decreasing pressure and increasing temperature. The lowest value was about 0.05, and the highest was about 0.30. These values were measured for cobalt foils previously oxidized with oxygen plasma at the temperature of 1300 K. The oxidation caused a rich morphology with an average roughness as deduced from atomic force images of 0.9 µm. The results were compared with literature data, and the discrepancy between results reported by different authors was explained by taking into account the peculiarities of their experimental conditions.

Keywords: heterogeneous surface recombination; recombination coefficient; cobalt; cobalt oxide; temperature dependence; pressure dependence; plasma; oxygen

check for updates

Citation: Paul, D.; Mozetič, M.; Zaplotnik, R.; Ekar, J.; Vesel, A.; Primc, G.; Đonlagić, D. Loss of Oxygen Atoms on Well-Oxidized Cobalt by Heterogeneous Surface Recombination. *Materials* **2023**, *16*, 5806. https://doi.org/10.3390/ma16175806

Academic Editor: Andrés Nistal

Received: 3 August 2023
Revised: 18 August 2023
Accepted: 23 August 2023
Published: 24 August 2023

1. Introduction

Precise oxidation of various materials has attracted the attention of numerous authors involved across multiple research fields, from atomic layer oxidation [1,2] to polymer activation [3–5], sterilization [6,7], and degreasing of inorganic materials [8,9]. Oxygen under ambient conditions is composed of two-atom molecules, which are not very chemically reactive at room temperature [10,11]. Faster and more controlled oxidation is obtained by reactive oxygen, such as that of ozone, superoxide, and neutral oxygen atoms in the ground state [12,13]. All of these reactive oxygen species interact with solid materials at various rates, depending on the material type and temperature [14]. While both ozone and superoxide are challenging to produce and sustain at large concentrations, neutral oxygen atoms in the ground state are rather easily produced by electron-impact dissociation upon plasma conditions, because the dissociation energy of an oxygen molecule is only 5.2 eV [15].

The recombination in the gas phase cannot occur via collision between two atoms due to the conservation of energy and momentum. The conservation of energy and momentum can be satisfied only by three-body collisions. The probability of three-body collisions increases as a square of the density of atoms in the gas phase. It is as large as about 1 MHz at atmospheric pressure and only about 1 Hz at 1 mbar [16]. Neutral oxygen atoms are very stable at low pressures as long as the loss is due to the gas phase reactions. The major mechanism of association between atoms and stable molecules at low pressure is heterogeneous surface recombination. This reaction requires at least a moderate lifetime of atoms adsorbed on the material surface. Different materials provide various lifetimes for O atoms, depending on the chemical interaction between oxygen atoms and the substrate.

Inert materials will exhibit short lifetimes and, thus, a low recombination coefficient. On the other hand, reactive materials, which tend to form oxides of moderate binding energy, will exhibit large recombination coefficients. The recombination coefficient depends not only on the type of material but also on its roughness, temperature, or pressure [17]. Of particular interest are materials whose recombination coefficient does not depend so much on the temperature or pressure in the range, which is useful for the processing of materials by oxygen atoms, for example, atomic layer oxidation of metals [18] and functionalization of polymers with polar functional groups [19].

Transition metal oxides are candidates for materials with high recombination coefficients because they form various oxides whose binding energy is just a small amount of eV [20]. These have attracted the attention of numerous authors, who have reported various values. A material of particular interest is cobalt because it forms only one type of oxide, which is stable in a range of temperatures up to about 900 K [20]. The stable form of cobalt oxide is CoO, often referred to as Co (II) oxide. This oxide transforms to Co_3O_4 at elevated temperatures but decomposes back to Co (II) oxide at about 1200 K [21].

Additionally, cobalt is a highly sought-after catalytic material in various industrial applications [22]. Along with applications in renewable energy conversion, and oil purification, cobalt is a low-cost alternative to other catalytic materials, such as precious metals. In all of the above-mentioned processes, the presence of oxygen, especially the more reactive neutral oxygen atoms can alter the surface of the catalyst.

Probably the first report about the recombination of neutral oxygen atoms on the surface of cobalt oxide was published in 1959 in a classical paper by Greaves and Linnett [23]. The authors used the Wrede–Harteck gauge to estimate the recombination coefficient. The reported value was approximately 5×10^{-3}. This value was measured at room temperature and at an oxygen pressure of 650 Pa.

A few years later, Dickens and Sutcliffe measured the recombination coefficients of selected metal oxides versus material temperatures [24]. At room temperature, the recombination coefficient for Co_3O_4 was approximately 2.5×10^{-3}. The authors also reported a rise in the conductivity of cobalt oxide due to exposure to oxygen atoms. They performed measurements at a pressure as high as 13,333 Pa. They found an exponential increase in the recombination coefficient versus the temperature for many transition metal oxides, but not for Co_3O_4. Nevertheless, the recombination coefficient increased monotonously with increasing temperature and then reached a value of approximately 0.25 at the maximum temperature probed by [24], i.e., 625 K.

Melin and Madix [25] performed experiments in a sophisticated version of the reactor used originally by Greaves and Linnett [23]. Surprisingly enough, they reported an order of magnitude larger coefficient, i.e., 7.5×10^{-2}, at room temperature. They did not report the type of oxide formed on the metallic surface upon exposure to neutral oxygen atoms. More recently, Guyon et al. [26] used actinometry to estimate the recombination coefficients of selected metal oxides. They reported the coefficient for CoO of 2.9×10^{-2} at 300 K and 3.4×10^{-2} at 473 K. Unlike Dickens and Sutcliffe [24], they found a temperature (T) dependence of the recombination coefficient (γ) to be:

$$\gamma = \frac{T_0}{T} e^{-\frac{E_a}{RT}}, \tag{1}$$

where T_0 was a characteristic temperature, E_a was the activation energy of the surface reaction, and R was the gas constant. However, they performed measurements at only three different temperatures (i.e., 300, 385, and 473 K). Cvelbar et al. [27] compared several catalytic materials by exposing them to the oxygen with a dissociation fraction of the order of 10% in a broad range of pressures between 5 and 400 Pa. While the coefficient for copper was found to be independent of pressure, complex behavior was observed for cobalt. Namely, a maximum coefficient of 14×10^{-2} was observed at around 30 Pa, and the coefficient decreased almost exponentially at higher pressures and stabilized at the value of about 8.5×10^{-2} in the range of pressure between 200 and 400 Pa. At pressures lower than 30 Pa, however, the recombination coefficient decreased with decreasing pressure.

This brief literature survey indicates the inadequate knowledge of the recombination probability for oxygen atoms on the CoO surface. The discrepancy between the reported results may be due to several reasons, such as the different experimental methodologies used by authors and the different surface conditions of the material, i.e., the different morphology of samples. It is known that the measured recombination coefficient increases with increasing roughness [28,29], mainly because of the larger available surface area as compared with the geometrical area. The largest recombination coefficient reported in reliable literature is that of carbon nanowalls [30], with the very large coefficient explained by trapping oxygen atoms into the gaps between neighboring walls, thus causing numerous collisions of atoms on the material surface.

We performed experiments using samples of equal morphology and structure to clarify the temperature and pressure dependencies of the recombination coefficient for oxygen atoms on the surface of well-oxidized cobalt. A stable oxide film was prepared by exposing the high-purity cobalt disk to a mixture of molecular and atomic oxygen at a large atom flux and temperatures as high as 800 K. According to the knowledge of the stability of cobalt oxides [21], the surface composition should be independent of the flux of reactive oxygen species in a temperature range from room temperature to about 900 K. The purpose of this study was to determine the interaction of neutral oxygen atoms with oxidized cobalt under experimental conditions commonly used in plasma laboratories around the world, as both oxygen plasma and cobalt are often used without sufficient understanding of their interactions.

2. Experimental

The pressure and temperature evolution of the recombination coefficient for cobalt oxide was measured in the experimental setup shown schematically in Figure 1. First, molecular oxygen, supplied via the mass flow controller (MFC), entered a quartz tube, where it was partially dissociated in gaseous plasma, resulting in a mixture of O_2 and O. The plasma was sustained by a microwave discharge operating in the surfatron mode [31]. Such sources of neutral oxygen atoms are widely used in laboratories worldwide because of their robustness, stability, and ease of operation. The exact kinetics of plasma radicals was later reported by several authors, including Kutasi et al. [31], Ricard et al. [32], and Guerra et al. [33].

The source of oxygen atoms was connected to a measuring chamber, where a cobalt disk was positioned. There was a drift of gas from the oxygen flask through the discharge tube and the measuring chamber due to the continuous pumping of the experimental system. Our system was pumped with an Edwards E2M80 two-stage rotary pump with a nominal pumping speed of 80 m^3/h and ultimate pressure below 1 Pa. Molecular oxygen was introduced into the experimental system through a calibrated flow controller. As there was no detectable leakage of the vacuum system, the mass flow remained constant through all the vacuum elements between the flow meter and the pump, but the volume flow increased towards the pump. A pressure gradient was established along the narrowest vacuum elements. Because all components except the discharge tube have an inner diameter of 3.6 cm or more, practically the entire pressure gradient was established in the discharge tube. The discharge tube had an inner diameter of 6 mm and a length of 41.5 cm. Two absolute vacuum gauges were mounted on either side of the discharge tube, as shown in Figure 1. The discharge was powered with a microwave generator (Sairem GMS200WSM, Décines-Charpieu, France) with a maximum output power of 200 W. The reflected power was also measured, so all results presented in this paper are versus the difference between forward and reflected power.

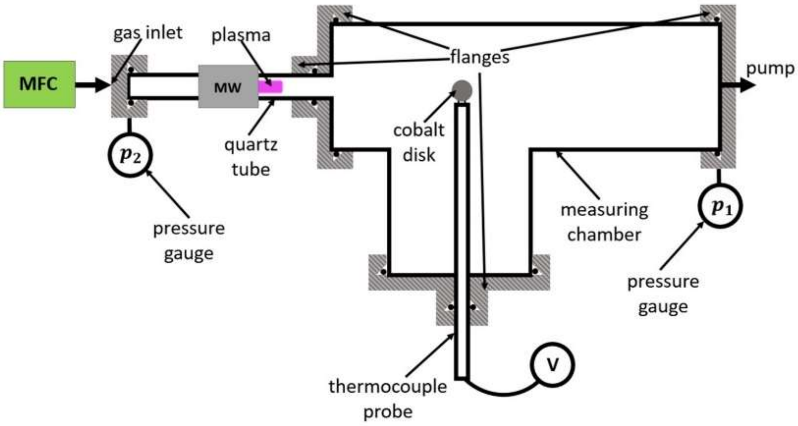

Figure 1. Schematic of the experimental setup that enabled exposure of a cobalt disk to a constant flux of O_2 and O.

The oxygen atom density in the measuring chamber was determined by the Šorli–Ročak method [34]. Briefly, this is a reliable method for the determination of the absolute density of neutral atoms in low-pressure systems. The accuracy of the method is about 20%. Details regarding this method are disclosed in our recent paper [35].

High-purity (99.99%) cobalt foil of a thickness of 0.05 mm was purchased from Goodfellow (Huntingdon, UK). Small disks of a diameter of 3 mm were cut from the foil and spot-welded to chromel–alumel thermocouple wires of a diameter of 0.25 mm. Each wire was placed into a very narrow glass tube to prevent extensive loss of O atoms on the wires themselves. Wires were connected to a voltmeter through a vacuum-tight feedthrough. The dimensions of the cobalt disk and the supporting wires and tubes are shown in Figure 2.

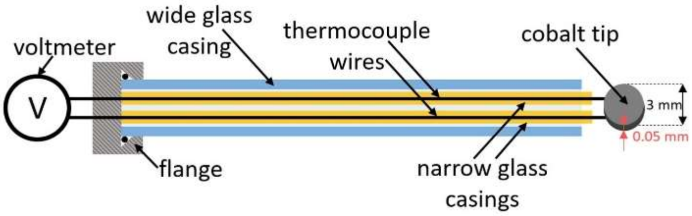

Figure 2. Schematic of the disk installation.

The disk shown in Figure 2 was thoroughly oxidized before measuring the recombination coefficient. The oxidation was performed by placing the disc into a rather dense oxygen plasma sustained by inductively coupled radiofrequency discharge in the H-mode. Details about this type of plasma are described elsewhere [36]. The disk heated up to about 1300 K in radiofrequency plasma. The disk was kept in plasma for about 10 min to form a stable oxide film. All experiments for measuring the recombination coefficients were performed at much smaller temperatures, i.e., up to 800 K, so it is believed that the surface structure, composition, and morphology did not change during these measurements.

3. Results and Discussion

3.1. Characterisation of the Discharge System

Determination of the loss of oxygen atoms on the cobalt disk requires detailed characterization of oxygen flow rates and fluxes of oxygen atoms to the cobalt surface as well as any gradients in the system. After evacuating the system down to the ultimate pressure, oxygen was leaked through the mass flow controller during continuous pumping, establishing pressure gradient along the discharge tube. The pressures at both sides of the discharge tube were measured versus the gas flow and the results are shown in Figure 3a. Figure 3b shows the ratio of pressures at each end of the discharge tube versus the gas flow. One can observe that the pressure ratio slowly decreases with increasing flow rate. This observation is explained by the way in which the conductivity of the tube increases with increasing gas pressure.

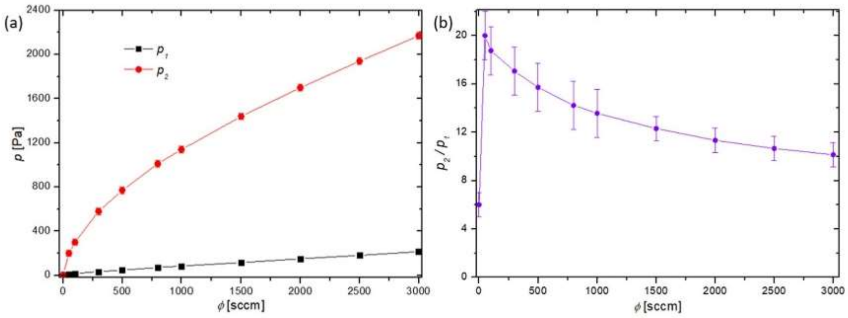

Figure 3. (**a**) The oxygen pressure on the high-pressure side (p_2) and low-pressure side (p_1) vs. the gas flow. (**b**) The ratio of pressures from each side of the discharge tube (p_2/p_1) vs. the gas flow.

This pressure gradient caused a drift of gas through the discharge tube. The gas velocity could be estimated, taking into account the results of Figure 3, and the gas flow rate determined by the flow controller, using the standard formula where the gas flow (in standard cubic centimeters (sccm)) is a constant at any given point in the system:

$$v_{drift} = \frac{\phi_{sccm} 10^{-2}}{1.425 \cdot 6\ p\ S_{quartz}}, \tag{2}$$

where ϕ_{sccm} is the gas flow rate (in sccm units), p is the pressure at a given position in the system, and S_{quartz} is the discharge tube cross-section. While the drift velocity is moderate at the entrance to the discharge tube, it is over 100 m/s at the exhaust of the measuring chamber. The sound velocity in gas limits the maximum drift velocity. Such a rapid transport of gas is essential to ensure a rather large density of atoms in the measuring chamber because the gas residence time in the discharge tube (marked as "quartz tube" in Figure 1) depends on the gas velocity. If the drift velocity were approaching zero, the transport of atoms from the plasma in the discharge tube to the position of the cobalt catalyst would have been by diffusion, so the atoms would have been lost during their collisions with the quartz tube surface.

The density of oxygen atoms in the measuring chamber at the position of the cobalt catalyst was measured using the Šorli–Ročak method [34] and is plotted versus the oxygen flow and pressure in Figure 4. There are several curves corresponding to different discharge powers. As expected, the lowest oxygen atom density is at the lowest discharge power of 50 W. The oxygen atom density does not depend much on the discharge power at low flow rates, but it increases with increasing power at elevated flow rates, i.e., above 500 sccm. This is explained by the fact that both the length of the plasma column in the discharge tube and the density and/or temperature of the electrons increase with increasing discharge power [31,37,38]. It is important to stress that the densities provided in Figure 4 are at the position of the catalytic disk (Figure 1). As there is a pressure gradient along the discharge tube (Figure 3a), and the dissociation fraction inside plasma is at least as large as in the measuring chamber, the oxygen atom density in plasma is several times larger than in the measuring chamber. It is reasonable to assume a constant gradient of gas pressure inside the discharge tube, so the actual pressure at the position where glowing plasma is sustained can be estimated from Figure 3.

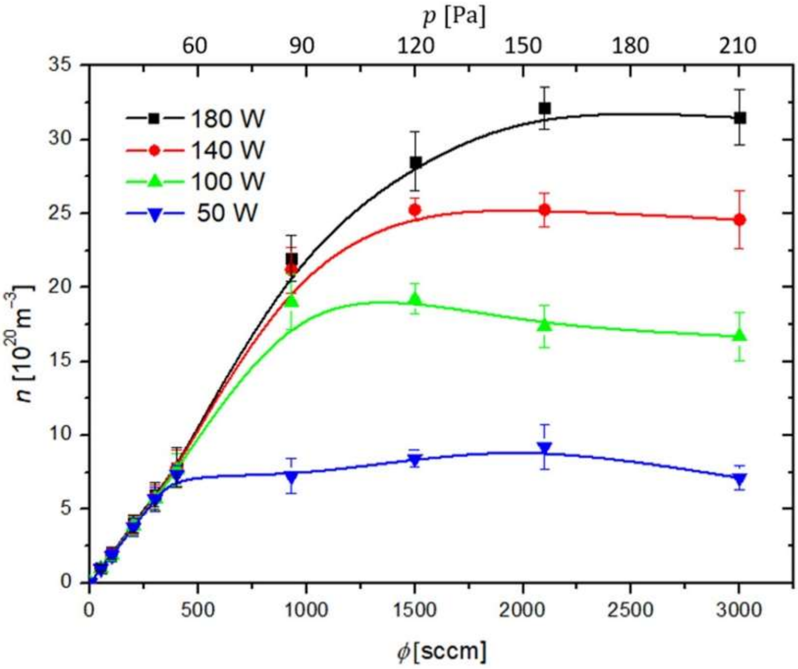

Figure 4. Oxygen atom density is measured at the position of the cobalt catalyst versus gas flow rate (ϕ) and pressure (p) inside the system at different discharge powers.

3.2. Determination of the Loss of Atoms on a Catalyst Material

Once the O-atom density in the measuring chamber is known, it is possible to determine the loss of atoms on a surface of any material mounted at the position marked as "cobalt disk" in Figure 1. A cobalt disk was connected to thermocouple wires as shown in Figure 2 and heated up to the temperature of about 1300 K in radiofrequency plasma for about 10 min to form a stable oxide film, as explained above. Such a well-oxidized disk was then mounted in the experimental system shown in Figure 1.

The recombination coefficient of the oxidized cobalt was determined as follows: the oxidized cobalt disk was at room temperature (about 300 K), before igniting the discharge. Despite the adiabatic expansion due to the pressure gradients (Figure 3), the gas temperature at the position of the cobalt disk was not much different from the ambient temperature. Once the discharge was ignited, the catalyst started heating due to the heterogeneous surface recombination of oxygen atoms into oxygen molecules. This reaction is highly exothermic, because the potential energy of an oxygen atom in the ground state is 2.6 eV, while the potential energy of O_2 molecules in the ground electronic state and room temperature is practically 0 [39]. Because the supply of oxygen atoms into the measuring chamber is constant at a given flow rate and discharge power, the power dissipated on the catalyst surface due to the surface association is also constant. Within several seconds, the cobalt disk assumes a constant temperature, where the heating by heterogeneous surface recombination is equal to the cooling by any process, including the processes of grey body radiation, the thermal conduction of the thermocouple wires and the surrounding gas, and cooling by gas drift. The constant temperature after prolonged exposure of the disc to O atoms depends on the flux of oxygen atoms on the surface and the recombination coefficient. When the discharge is turned off, the disc temperature starts decreasing because of the absence of heating. The recombination coefficient (γ) is calculated from the measured absolute value of the time-derivative of the temperature of the disk (dT/dt) as:

$$\gamma = \frac{8\, m\, c_p}{v\, W_D\, A\, n} \frac{dT}{dt}\,, \tag{3}$$

where m is the mass of the cobalt disk, c_p is the specific heat of cobalt, v is the average value of the gas random velocity, W_D is the dissociation energy of an oxygen molecule, A is the geometric surface area of the cobalt disk, and n is the density of neutral oxygen atoms at the position of the cobalt disk. The recombination coefficient versus the oxygen flow rate is shown in Figure 5. The discharge power is the parameter. Figure 5 indicates some dependencies, particularly the pressure dependence of the recombination coefficient (Figure 3), but according to previous authors, the coefficient should also depend on the temperature of the cobalt catalyst. Furthermore, the equilibrium temperature of the cobalt disc upon heating by the surface recombination of O atoms depends on the pressure, so Figure 5 is not valid for the determination of the pressure and temperature dependencies.

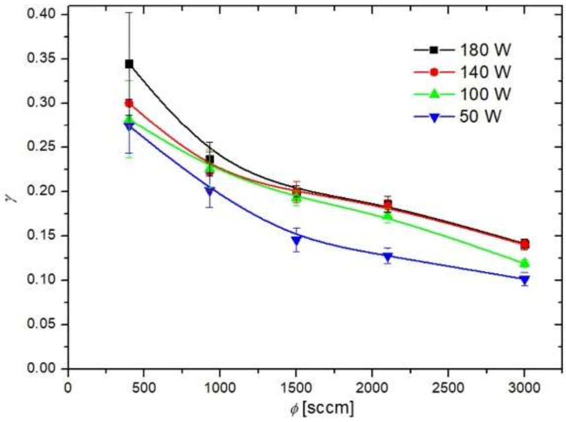

Figure 5. Recombination coefficient (γ) versus gas flow rate (ϕ) at various discharge powers. The error bars represent the statistical error only, as the measurements were repeated several times at identical conditions.

To determine the temperature dependence, the recombination coefficient is plotted in Figure 6 versus the maximum temperature of the catalytic disk, where the discharge pressure in the measuring chamber is the parameter. The results of Figure 5 were also used to determine the variation of the recombination coefficient versus the pressure in the measuring chamber. Figure 7 shows the values with the catalyst temperatures as the parameter. Figure 6 indicates a monotonous increase of the recombination coefficient with the increasing temperature of the cobalt disc. This observation is found with Dickens et al. [24] as well as Guyon et al. [26]. As mentioned earlier, Guyon et al., found a logarithmic increase in the recombination coefficient, but their results are based on only three measured points. In contrast, Dickens et al. found a complex behavior; in particular, a rather large increase of the recombination coefficient with increasing temperature from room temperature up to 500 K, but a marginal increase at temperatures above 500 K. By considering the results of Figure 6, the observations of Dickens et al., are closer to the measured temperature dependence of the recombination coefficient, as Figure 6 indicates stabilization of the recombination coefficient at temperatures above, e.g., 700 K.

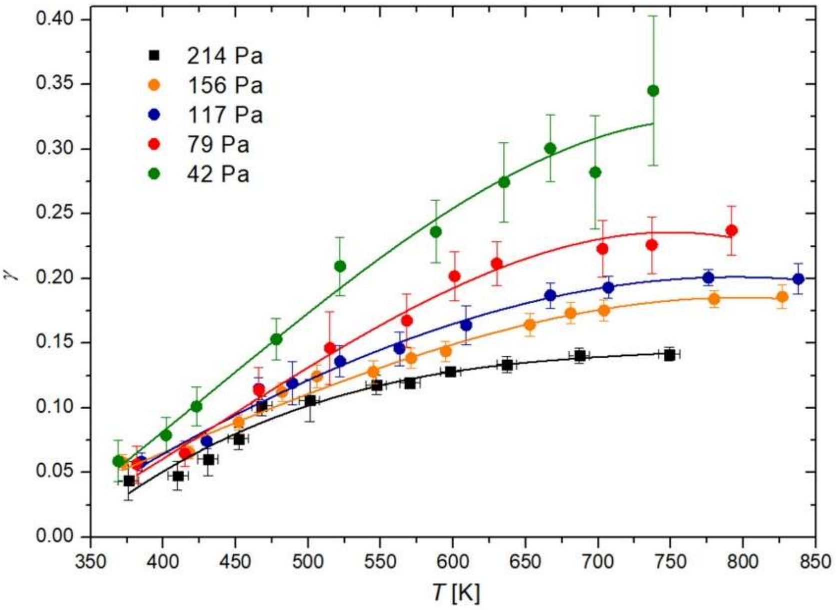

Figure 6. Recombination coefficient (γ) of the cobalt disk with respect to the temperature (T) of the cobalt disk at various pressures inside the system.

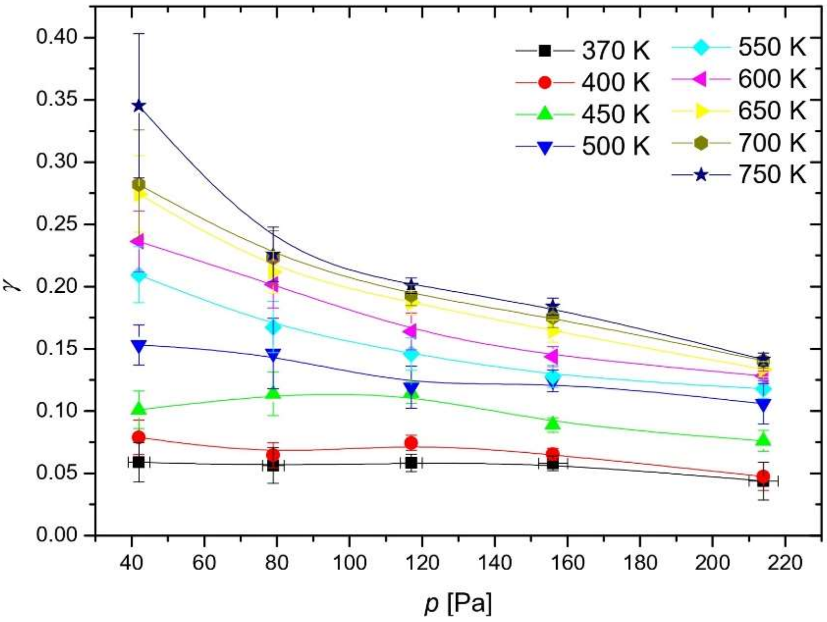

Figure 7. Recombination coefficient (γ) of the cobalt disk versus pressure (p) inside the system at various temperatures of the cobalt disk.

The rather limited range of temperatures of the cobalt catalyst is the result of practical limitations—the upper limit, at around 850 K, was the highest achievable temperature of the cobalt catalyst in our experimental setup. On the other hand, the lower limit was room temperature as our experimental system does not allow us to use any advanced cooling method on the cobalt catalyst. As a result of this, we did not reach temperatures where the cobalt oxide layer becomes unstable [20,21], thus achieving reliable and repeatable results. Furthermore, the industrial use of cobalt as a catalyst for different reactions usually occurs at elevated temperatures [40,41], which are encompassed in this study.

Figure 7 clearly shows that the recombination coefficient does not depend much on the pressure at low catalyst temperatures, up to approximately 500 K, but at higher temperatures, the recombination coefficient decreases with increasing pressure. This observation may explain the fact that Dickens et al., reported a very low recombination coefficient because they worked at a pressure as large as 13,333 Pa. In contrast, Cvelbar et al. [27] reported a coefficient about 30 times larger than Dickens et al., at a pressure of approximately 40 Pa. At higher pressures, Cvelbar et al., reported a decreasing recombination coefficient and stabilization at a value of approximately 0.085. Unfortunately, Cvelbar et al., did not report on the disk temperature upon measuring the recombination coefficients. The results shown in Figure 7 clearly show that the coefficient at an elevated pressure of approximately 200 Pa may assume any value between 0.05 and 0.15. The exact values depend significantly on the temperature of the catalytic disk.

The pressure range was chosen due to a few constraining factors. The first was the mass flow controller, which had a maximum flow rate of 3000 sccm. This resulted in a pressure in the measuring chamber of 214 Pa. While higher pressures could be achieved by limiting the pumping speed of the pump, the resulting pressures were highly inconsistent and were thus exempt from this study. At pressures lower than 42 Pa, the range of temperatures achievable by the cobalt probe was severely limited, and thus we limited ourselves to the specified pressure range. While the pressures chosen are not typical in industrial plasma applications [42,43], they still provide some useful data on the behavior of oxidized cobalt.

As mentioned earlier, the recombination coefficient is likely to depend on the surface morphology and composition. We processed our material at extreme conditions (at 1300 K in oxygen plasma) to obtain a stable film of cobalt oxide. The morphology as examined by atomic force microscopy (AFM) is shown in Figure 8. The AFM imaging was performed for the as-oxidized sample and oxidized sample treated with O atoms at several pressures and temperatures. No deviation from the as-oxidized sample was observed, thus confirming the stability of the oxide film throughout the experiments with O atoms. In Figure 8, one can observe a very rough surface with cobalt oxide structures of a vertical dimension exceeding 1 μm. The actual area of the well-oxidized cobalt surface is thus several times larger than the geometrical area. The roughness of the sample probed for the recombination coefficient probably explains the discrepancies in the absolute values as compared with some other reports [23–27]. As mentioned in the introduction, earlier authors reported various values ranging between 0.0025 and 0.25. Our measurements fall into the range between approximately 0.05 and 0.30 (Figures 5–7). The lack of low values is explained by the high roughness of our samples because the recombination coefficient depends on the real, not geometric surface area.

The systematic measurements reported in this paper enable an insight into the mechanisms involved in the association of neutral oxygen atoms in the ground state on the surface of oxidized cobalt samples. Somewhat larger values than those reported by other authors are explained by rather large surface roughness, which develops upon oxidation at elevated temperatures. We performed the oxidation at the temperature of 1300 K for about 10 min to assure an approximately stable oxide film. All measurements of the recombination coefficient reported in this paper were performed in a temperature range between 300 and 850 K, which is well below the temperature used for the formation of the stable oxide film. The stability of the oxide film is crucial for the appropriate determination of the recombination coefficient because a rich morphology will develop on smooth metallic foil upon gradual oxidation at elevated temperatures.

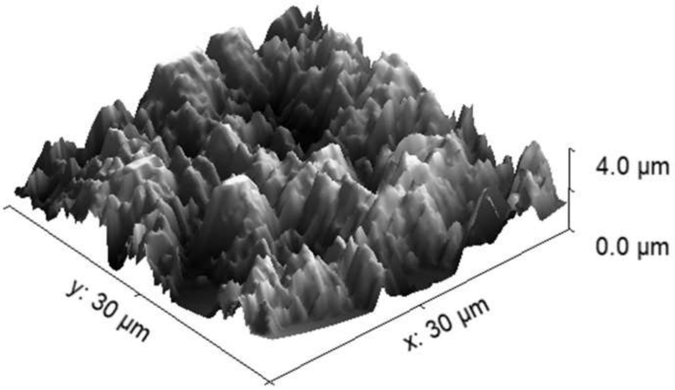

Figure 8. AFM image of a 30 × 30 μm^2 surface area of the oxidized cobalt disk. The RMS surface roughness was estimated to be $S_q = 895$ nm.

It is well known that the surface association of oxygen atoms on solid materials follows two distinguished mechanisms, explained by the Eley–Rideal (ER) and Langmuir–Hinshelwood (LH) models. The ER model predicts an association of oxygen atoms impinging the surface with already adsorbed O atoms [44]. The association is instant, so there is no time for the accommodation of the impinging atoms on the surface. On the other hand, the LH model predicts the accommodation of atoms in the potential well of chemisorption on the surface, and the association of two adsorbed atoms [45]. The molecule formed on the surface, according to the LH model, then leaves the surface. The LH model requires the proximity of two adatoms to enable the formation of an oxygen molecule. The proximity is assured by oscillating the chemisorbed O atoms in the potential well of chemisorption. Because the amplitude of surface oscillations increases with increasing temperature, the recombination coefficient, according to the LH model, also increases with increasing temperature. Figure 6 reveals increasing γ with increasing temperature in the range from 300 to approximately 700 K, but the coefficient stabilizes at high temperatures. This stabilization can be explained by the saturation of the coefficient according to the LH model, i.e., almost all O atoms trapped in the chemisorption well are recombined at high temperatures. The concentration of adsorption sites on the solid material is limited, so the coefficient is well below 1 even for the surface with a very rich morphology (Figure 8). The coefficient should be lower for smooth surfaces, but well-oxidized metals are usually rough, so the values for polished samples would be misleading in practical cases.

A graphical presentation of the recombination coefficient is shown in Figure 9. The measured points reported by previous authors who mentioned the gas pressure and the sample temperature in their reports are also shown in Figure 9. There are not many of these, because most authors either failed to report both parameters or because they chose the pressures well above the range probed in this work. We performed systematic measurements in the range of 40–220 Pa because the O-atom density in reactors for the treatment of solid materials peaks in this range as long as the treatment is performed at highly non-equilibrium conditions in which the gas is close to room temperature and free from charged particles [46]. Additionally, in Table 1, the measured recombination coefficient of cobalt for oxygen atoms is compared with results from the literature.

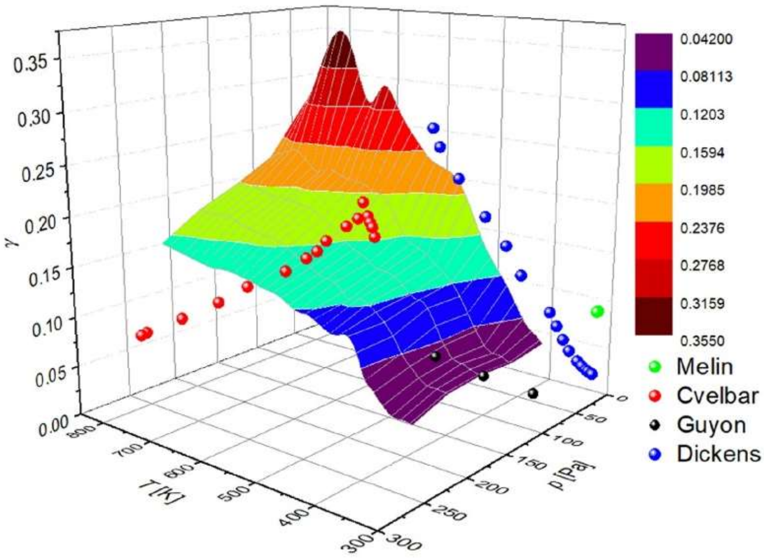

Figure 9. The recombination coefficient (γ) of the oxidized cobalt disk versus the temperature (T) of the cobalt disk and the pressure (p) inside the system.

Table 1. Comparison of measurements with various literature for the recombination coefficient (γ) of a cobalt surface for neutral oxygen atoms at various pressure (p) and temperature (T) ranges.

p[**Pa**]	T[**K**]	γ	**Reference**
42–214	370–850	0.04–0.35	this article
650	300	0.00049	[23]
4	300–625	0.0018–0.25	[24]
1–4	300	0.075	[25]
110	300–473	0.029–0.034	[26]
10–400	750	0.08–0.14	[27]

Finally, it should be stressed that we chose the range of experimental conditions (in particular, pressure) in order to perform reliable measurements and interpret them spotlessly. Namely, in the range of pressures up to about 2 mbar, the gas-phase association of O atoms to oxygen molecules is negligible because such a reaction requires a three-body collision in order to satisfy the conservation of energy and momentum. Any attempt to perform measurements at an elevated pressure would require taking into account the gas-phase reactions, which would complicate the mathematical formalism, in particular Equation (3).

The systems employing cobalt oxide catalysis often operate at atmospheric pressure and above to take advantage of the large gas throughput. We limited our study to the heterogeneous surface association of O atoms to oxygen molecules. Practically important catalysts include other gases, and perhaps the most studied is the relatively low-temperature oxidation of carbon monoxide [47–49]. Numerous authors have reported high oxidation rates, but the coefficients in terms of the probability for an impinging radical (e.g., a CO molecule) to interact on the surface have rarely been reported since the atmospheric pressure gas dynamics include the concentration gradients, diffusion, and adsorption on available surface sites. The modeling of the gas kinetics at atmospheric pressure is complex as compared with the low-pressure systems. The results provided in this article thus illustrate the surface recombination efficiency in the limitation of low-pressure systems, such as diffusion-governed motion. Any extrapolation of the measured values is not scientifically justified but could be useful for the estimation of the reaction probabilities at elevated pressure. Figure 7 indicates a rather stable coefficient in the range of pressures between 100 and 200 Pa and temperatures between 450 and 550 K. The large deviation for the values obtained in this range of experimental conditions was observed at lower pressures and, especially, higher temperatures, which are not relevant for surface reactions such as the heterogeneous oxidation of carbon monoxide.

4. Conclusions

The paradox of large discrepancies between the measured values of the coefficient for the heterogeneous recombination of oxygen atoms on cobalt surfaces has been resolved. The coefficient depends on the roughness and thus the real surface area, as well as the temperature of the oxidized cobalt foil and the pressure in the experimental chamber. We oxidized the foil during exposure to oxygen plasma at a temperature of 1300 K for about 10 min in order to assure a stable oxide film during the measurements of the recombination coefficient. The recombination coefficient increases monotonously with increasing surface temperature, which has been explained by increasing the mobility of adsorbed O atoms and thus increasing the probability for surface association due to the Langmuir–Hinshelwood model. The recombination coefficient somehow decreases with increasing pressure in the range of pressures between 40 and 200 Pa, which might be explained by the screening effect of physisorbed O_2 molecules and thus suppressing the direct association of O atoms impinging the surface covered by the chemisorbed O atoms, i.e., the Eley–Rideal model. Knowledge of the variation in the recombination coefficient is necessary to understand the surface kinetics involved in atomic layer oxidation of both inorganic and organic materials.

Author Contributions: Conceptualization, M.M., R.Z. and D.P.; methodology, D.P., J.E. and R.Z.; validation, A.V. and G.P.; formal analysis, A.V. and D.Đ.; investigation, M.M. and G.P.; resources, A.V., data curation, M.M. and D.P.; writing—original draft preparation, M.M. and D.P.; writing—review and editing, R.Z., A.V. and G.P.; visualization, J.E. and D.Đ.; supervision, R.Z. and M.M.; project administration, A.V. and G.P.; funding acquisition, M.M. and D.Đ. All authors have read and agreed to the published version of the manuscript.

Funding: This research was funded by the Slovenian Research Agency, grant numbers P2-0082 and L2-4487.

Institutional Review Board Statement: Not applicable.

Informed Consent Statement: Not applicable.

Data Availability Statement: The data that support the findings of this study are available upon reasonable request from the authors.

Conflicts of Interest: The authors declare no conflict of interest. The funders had no role in the design of the study; in the collection, analyses, or interpretation of data; in the writing of the manuscript; or in the decision to publish the results.

References

1. Di Palma, V.; Pianalto, A.; Perego, M.; Tallarida, G.; Codegoni, D.; Fanciulli, M. Plasma-Assisted Atomic Layer Deposition of IrO_2 for Neuroelectronics. *Nanomaterials* **2023**, *13*, 976. [CrossRef]
2. Fan, Z.-Y.; Yang, M.-J.; Fan, B.-Y.; Mavrič, A.; Pastukhova, N.; Valant, M.; Li, B.-L.; Feng, K.; Liu, D.-L.; Deng, G.-W.; et al. Plasma-enhanced atomic layer deposition of amorphous Ga_2O_3 for solar-blind photodetection. *J. Electron. Sci. Technol.* **2022**, *20*, 100176. [CrossRef]
3. Baranov, O.; Bazaka, K.; Kersten, H.; Keidar, M.; Cvelbar, U.; Xu, S.; Levchenko, I. Plasma under control: Advanced solutions and perspectives for plasma flux management in material treatment and nanosynthesis. *Appl. Phys. Rev.* **2017**, *4*, 041302. [CrossRef]
4. Wieland, F.; Bruch, R.; Bergmann, M.; Partel, S.; Urban, G.A.; Dincer, C. Enhanced Protein Immobilization on Polymers—A Plasma Surface Activation Study. *Polymers* **2020**, *12*, 104. [CrossRef] [PubMed]
5. Levchenko, I.; Xu, S.; Baranov, O.; Bazaka, O.; Ivanova, E.P.; Bazaka, K. Plasma and Polymers: Recent Progress and Trends. *Molecules* **2021**, *26*, 4091. [CrossRef]

6. Moreira, A.J.; Mansano, R.D.; Pinto, T.d.J.A.; Ruas, R.; Zambon, L.d.S.; da Silva, M.V.; Verdonck, P.B. Sterilization by oxygen plasma. *Appl. Surf. Sci.* **2004**, *235*, 151–155. [CrossRef]
7. Senthilkumar, P.; Arun, N.; Vigneswaran, C. Plasma Sterilization: New Epoch in Medical Textiles. *J. Inst. Eng. Ser. E* **2015**, *96*, 75–84. [CrossRef]
8. Petasch, W.; Kegel, B.; Schmid, H.; Lendenmann, K.; Keller, H. Low-pressure plasma cleaning: A process for precision cleaning applications. *Surf. Coat. Technol.* **1997**, *97*, 176–181. [CrossRef]
9. Izdebska-Podsiadły, J. Study of Argon and Oxygen Mixtures in Low Temperature Plasma for Improving PLA Film Wettability. *Coatings* **2023**, *13*, 279. [CrossRef]
10. Stuhr, R.; Bayer, P.; von Wangelin, A.J. The Diverse Modes of Oxygen Reactivity in Life & Chemistry. *ChemSusChem* **2022**, *15*, e202201323.
11. Ho, R.Y.N.; Liebman, J.F.; Valentine, J.S. Overview of the Energetics and Reactivity of Oxygen. In *Active Oxygen in Chemistry*; Springer: Dordrecht, The Netherlands, 1995. [CrossRef]
12. Annušová, A.; Marinov, D.; Booth, J.-P.; Sirse, N.; da Silva, M.L.; Lopez, B.; Guerra, V. Kinetics of highly vibrationally excited $O_2(X)$ molecules in inductively-coupled oxygen plasmas. *Plasma Sources Sci. Technol.* **2018**, *27*, 045006. [CrossRef]
13. Zhang, K.; Shafer, B.M.; Demars, M.D.; Stern, H.A.; Fasan, R. Controlled Oxidation of Remote sp^3 C–H Bonds in Artemisinin via P450 Catalysts with Fine-Tuned Regio- and Stereoselectivity. *J. Am. Chem. Soc.* **2012**, *134*, 18695–18704. [CrossRef] [PubMed]
14. Balat-Pichelin, M.; Badie, J.; Berjoan, R.; Boubert, P. Recombination coefficient of atomic oxygen on ceramic materials under earth re-entry conditions by optical emission spectroscopy. *Chem. Phys.* **2003**, *291*, 181–194. [CrossRef]
15. Brix, P.; Herzberg, G. The Dissociation Energy of Oxygen. *J. Chem. Phys.* **1953**, *21*, 2240. [CrossRef]
16. Zaplotnik, R.; Primc, G.; Paul, D.; Mozetič, M.; Kovač, J.; Vesel, A. Atomic species generation by plasmas. In *Plasma Applications for Material Modification: From Microelectronics to Biological Materials*; Jenny Stanford Publishing: Singapore, 2021; pp. 107–177.
17. Paul, D.; Mozetic, M.; Zaplotnik, R.; Primc, G.; Đonlagić, D.; Vesel, A. A Review of Recombination Coefficients of Neutral Oxygen Atoms for Various Materials. *Materials* **2023**, *16*, 1774. [CrossRef]
18. Zhang, X.; Zheng, P.; Ma, Y.; Jiang, Y.; Li, H. Atomic-scale understanding of oxidation mechanisms of materials by computa-tional approaches: A review. *Mater. Des.* **2022**, *217*, 110605. [CrossRef]
19. Saka, C. Overview on the Surface Functionalization Mechanism and Determination of Surface Functional Groups of Plasma Treated Carbon Nanotubes. *Crit. Rev. Anal. Chem.* **2018**, *48*, 1–14. [CrossRef]
20. Greenwood, N.N.; Earnshaw, A. *Chemistry of the Elements*; Butterworth-Heinemann: Oxford, UK, 1997.
21. Linde, D.R. *CRC Handbook of Chemistry and Physics*; CRC Press: Boca Raton, FL, USA, 2006.
22. Gupta, S.; Fernandes, R.; Patel, R.; Spreitzer, M.; Patel, N. A review of cobalt-based catalysts for sustainable energy and en-viromental applications. *Appl. Catal. A Gen.* **2023**, *661*, 119254. [CrossRef]
23. Greaves, J.C.; Linnett, J.W. Recombination of atoms at surfaces. Part—Oxygen atoms at oxide surfaces. *Trans. Faraday. Soc.* **1959**, *55*, 1346–1354. [CrossRef]
24. Dickens, P.G.; Sutcliffe, M.B. Recombination of oxygen atoms on oxide surfaces. *Trans. Faraday Soc.* **1964**, *60*, 1272–1285. [CrossRef]
25. Melin, G.A.; Madix, R.J. Energy accommodation during oxygen atom recombination on metal surfaces. *Trans. Faraday Soc.* **1971**, *67*, 198–211. [CrossRef]
26. Guyon, C.; Cavadias, S.; Amouroux, J. Heat and mass transfer phenomenon from an oxygen plasma to a semiconductor surface. *Surf. Coat. Technol.* **2001**, *142–144*, 959–963. [CrossRef]
27. Cvelbar, U.; Mozetic, M.; Ricard, A. Characterization of oxygen plasma with a fiber optic catalytic probe and determination of recombination coefficients. *IEEE Trans. Plasma Sci.* **2005**, *33*, 834–837. [CrossRef]
28. Kim, I.; Park, G.; Na, J.J. Experimental study of surface roughness effect on oxygen catalytic recombination. *Int. J. Heat Mass Transf.* **2019**, *138*, 916–922. [CrossRef]
29. Kim, I.; Yang, Y.; Park, G. Effect of titanium surface roughness on oxygen catalytic recombination in a shock tube. *Acta Astronaut.* **2020**, *166*, 260–269. [CrossRef]
30. Mozetic, M.; Vesel, A.; Stoica, S.D.; Vizireanu, S.; Dinescu, G.; Zaplotnik, R. Oxygen atom loss coefficient of carbon nanowalls. *Appl. Surf. Sci.* **2015**, *333*, 207–213. [CrossRef]
31. Kutasi, K.; Saoudi, B.; Pintassilgo, C.D.; Loureiro, J.; Moisan, M. Modelling the Low-Pressure N_2-O_2Plasma Afterglow to Determine the Kinetic Mechanisms Controlling the UV Emission Intensity and Its Spatial Distribution for Achieving an Efficient Sterilization Process. *Plasma Process. Polym.* **2008**, *5*, 840–852. [CrossRef]
32. Ricard, A.; Henriques, J.; Cousty, S.; Villeger, S.; Amorim, J. Determination of N-, H- and O-Atom Densitiesin N_2–H_2 and in N_2–O_2 Gas Mixtures by Optical Actinometry in Flowing Microwave Discharges and by NO Titration in Post-Discharges. *Plasma Process. Polym.* **2007**, *4*, S965–S968. [CrossRef]
33. Guerra, V.; Tejero-del-Caz, A.; Pintassilgo, C.D.; Alves, L.L. Modelling N_2–O_2 plasmas: Volume and surface kinetics. *Plasma Sources Sci. Technol.* **2019**, *28*, 073001. [CrossRef]
34. Šorli, I.; Ročak, R. Determination of atomic oxygen density with a nickel catalytic probe. *J. Vac. Sci. Technol. A* **2000**, *18*, 338–342. [CrossRef]
35. Paul, D.; Mozetič, M.; Zaplotnik, R.; Ekar, J.; Vesel, A.; Primc, G.; Đonlagič, D. Recombination of oxygen atoms on the surface of oxidized polycrystalline nickel—Temperature and pressure dependences. *Plasma Sources Sci. Technol.* **2023**, *32*, 7. [CrossRef]

36. Zaplotnik, R.; Vesel, A.; Mozetič, M. Transition from E to H mode in inductively coupled oxygen plasma: Hysteresis and the behavior of oxygen atom density. *Europhys. Lett.* **2011**, *95*, 55001. [CrossRef]
37. Nowakowska, H.; Czylkowski, D.; Zakrzewski, Z. Surface wave sustained discharge in Argon: Two-temperature collision-al-radiative model and experimental verification. *J. Optoelectron. Adv. Mater.* **2005**, *7*, 2427–2434.
38. Umetsu, J.; Koga, K.; Inoue, K.; Matsuzaki, H.; Takenaka, K.; Shiratani, M. Discharge power dependence of Hα intensity and electron density of Ar+H_2 discharges in H-assisted plasma CVD reactor. *Surf. Coatings Technol.* **2008**, *202*, 5659–5662. [CrossRef]
39. Ionin, A.A.; Kochetov, I.V.; Napartovich, A.P.; Yuryshev, N.N. Physics and engineering of singlet delta oxygen production in low-temperature plasma. *J. Phys. D Appl. Phys.* **2007**, *40*, R25–R61. [CrossRef]
40. Dou, L.; Liu, Y.; Gao, Y.; Li, J.; Hu, X.; Zhang, S.; Ostrikov, K.; Shao, T. Disentangling metallic cobalt sites and oxygen vacancy effects in synergistic plasma-catalytic CO_2/CH_4 conversion into oxygenates. *Appl. Catal. B Environ.* **2022**, *318*, 121830. [CrossRef]
41. Fan, R.-Y.; Xie, J.-Y.; Yu, N.; Chai, Y.-M.; Dong, B. Interface design and composition regulation of cobalt-based electrocatalysts for oxygen evolution reaction. *Int. J. Hydrog. Energy* **2022**, *47*, 10547–10572. [CrossRef]
42. Chun, S.M.; Park, S.M.; Yang, G.W.; Shin, D.H.; Moon, H.S.; Hong, Y.C.; Moon, S.Y. Improvement of the flowability of fine yttrium oxide powders by microwave oxygen plasma and evaluation of the dense coating layer. *Ceram. Int.* **2021**, *47*, 17476–17486. [CrossRef]
43. Hou, M.; Guo, S.; Yang, L.; Gao, J.; Hu, T.; Wang, X.; Li, Y. Improvement of gas sensing property for two-dimensional Ti_3C_2Tx treated with oxygen plasma by microwave energy excitation. *Ceram. Int.* **2020**, *47*, 7728–7737. [CrossRef]
44. Shi, H.; Huang, M.; Huang, Y.; Cui, L.; Zheng, L.; Cui, M.; Jiang, L.; Ibrahim, H.; Tontiwachwuthikul, P. Eley–Rideal model of heterogeneous catalytic carbamate formation based on CO_2–MEA absorptions with $CaCO_3$, $MgCO_3$ and $BaCO_3$. *R. Soc. Open Sci.* **2019**, *6*, 190311. [CrossRef]
45. Baxter, R.J.; Hu, P. Insight into why the Langmuir–Hinshelwood mechanism is generally preferred. *J. Chem. Phys.* **2002**, *116*, 4379–4381. [CrossRef]
46. Booth, J.-P.; Mozetič, M.; Nikiforov, A.; Oehr, C. Foundations of plasma surface functionalization of polymers for industrial and biological applications. *Plasma Sources Sci. Technol.* **2022**, *31*, 103001. [CrossRef]
47. Kang, M.; Song, M.W.; Kim, K.L. Catalytic oxidation of carbon monoxide over CoOX/CeO_2 catalysts. *React. Kinet. Catal. Lett.* **2003**, *79*, 3–10. [CrossRef]
48. Dey, S.; Dhal, G. The catalytic activity of cobalt nanoparticles for low-temperature oxidation of carbon monoxide. *Mater. Today Chem.* **2019**, *14*, 100198. [CrossRef]
49. Molavi, R.; Safaiee, R.; Sheikhi, M.; Hassani, N. Theoretical perspective on CO oxidation over small cobalt oxide clusters. *Chem. Phys. Lett.* **2021**, *767*, 138361. [CrossRef]

2.3 The Penetration Depth of Atomic Radicals in Tubes with Catalytic Surface Properties

Now that we have a well-defined description of the recombination coefficient of nickel and cobalt for oxygen atoms, we can use catalytic probes with nickel and cobalt probe tips to reliably measure the neutral oxygen atom density. In the proceeding article, a catalytic probe with a cobalt tip is used to measure the penetration depth of oxygen atoms inside metallic tubes with catalytic surface properties. While noble metals are best suited for catalysis, they are quite expensive, hence the popularity of cheaper alternatives, among them nickel [90], cobalt [91], and copper [92]. Another important aspect of catalysis is the geometry of the catalytic material. Nanostructured catalysts are effective [93] but the fabrication is more complex. On the other hand, due to their simpler fabrication, tubular catalysts are an attractive alternative [94].

In the proceeding article, three 10 cm long tubes with a diameter of 8 mm are used, made of nickel, cobalt, and copper. All three materials are considered catalytic for the recombination of neutral oxygen atoms [56]. A catalytic probe is placed inside a metallic tube and the neutral oxygen atom density profile is measured along the length of the tube. This process is repeated for each of the metallic tubes at different gas flow rates and pressures inside the experimental system. Along with neutral atom density, another property is measured: the dissociation fraction of oxygen molecules (η) which is defined as the ratio of the densities of neutral oxygen atoms (n) and oxygen molecules (n_m):

$$\eta = \frac{n}{2n_m}, \tag{2.5}$$

with the factor 2 in equation (2.5) used for diatomic molecules, reflecting the fact that it takes two oxygen atoms to form a single oxygen molecule. In the proceeding article, the profile of the dissociation fraction of oxygen atoms is studied along the length of the metallic tubes, with the experimental results hinting at an exponential decrease of the dissociation fraction of oxygen molecules along the length of the metallic tubes. The results are fitted with an exponential function. Evidently, both cobalt and copper are better catalysts for the recombination of neutral oxygen atoms into oxygen molecules than nickel, which performs slightly worse.

The penetration depth of oxygen atoms for each metallic tube is calculated and found to increase with increasing gas flow rate. Evidently, most of the neutral atoms successfully recombine along the first few centimeters of the metallic tubes, which further supports the use of shorter catalytic tubes in the previous chapters when determining the absolute neutral atom density with the Šorli-Ročak method [20], [95].

The penetration depth of atomic radicals in tubes with catalytic surface properties

Domen Paul 1,2,*, Miran Mozetič 1, Rok Zaplotnik 1, Alenka Vesel 1, Gregor Primc 1 and Denis Đonlagič 3
1 Jozef Stefan Institute, Jamova Cesta 39, 1000 Ljubljana, Slovenia
2 Jozef Stefan International Postgraduate School, Jamova Cesta 39, 1000 Ljubljana, Slovenia
3 Faculty of Electrical Engineering and Computer Science, University of Maribor, Koroska Cesta 46, 2000 Maribor, Slovenia
* Correspondence: domen.paul@ijs.si

Abstract:

Catalysis of molecular radicals is often performed in tubular geometry. The radicals are introduced into the tubes on one side, and stable molecules are exhausted on the other side. The penetration depth of radicals depends on numerous parameters, so it is not always feasible to calculate it. This article presents systematic measurements of the penetration depth of oxygen atoms along tubes made from nickel, cobalt, and copper. The source of O atoms was a surfatron-type microwave plasma. The initial density of O atoms depended on the gas flow and was 0.7, 2.4, and $4.2 \cdot 10^{21} \mathrm{m}^{-3}$ at the flow rates of 50, 300, and 600 sccm, respectively. The dissociation fraction decreased exponentially along the length of the tubes in all cases. The penetration depths for well-oxidized nickel were 1.2, 1.7, and 2.4 cm, respectively. For cobalt, they were slightly lower at 1.0, 1.3, and 1.6 cm, respectively, while for copper, they were 1.1, 1.3, and 1.7 cm, respectively. The results were explained by gas dynamics and heterogeneous surface association. These data are useful in any attempt to estimate the loss of molecular fragments along tubes, which serve as catalysts for the association of various radicals to stable molecules.

Keywords: oxygen atoms, atomic radicals, oxygen plasma, penetration depth, metallic tubes, nickel, cobalt, copper, catalysis, heterogeneous surface recombination, atom loss.

1. Introduction

Surface catalysis has attracted significant attention from both the scientific community and the users. Surface catalysis often occurs at elevated temperatures. The temperatures are needed to facilitate surface adhesion and dissociation of different molecules [1]. The surface reactions at low temperatures may be accelerated by pre-dissociation of stable molecules. Molecular fragments such as radicals exhibit a much larger surface adsorption rate than stable molecules [2]. For example, methane will not dissociate on many materials at ambient conditions, but the methane radicals $\mathrm{CH_x}$ will readily adsorb on the various solid materials [3]. The formation of molecular radicals in the gas phase could be performed by heating the gas to high temperatures, but such a procedure is energetically unfavorable. Instead, non-equilibrium gaseous plasma is often used for pre-dissociation of stable molecules [4], [5].

The best catalysts are noble metals such as platinum [6]. The high cost of such materials, however, suppresses a broad application, so scientists are involved in research on the surface catalysis of cheaper materials, such as nickel [7], cobalt [8], and copper [9].

The intensity of surface catalysis depends on the actual surface area of the catalysts. From this point of view, nanostructured catalysts are preferred [10]. Another preferred option is using arrays of numerous tubes [11]. The gaseous molecules enter the tube on one side and are transferred through the tube by a pressure gradient. Upon passing the tube, the molecules also move by diffusion, so they reach the tube wall, where they can be adsorbed, interact with other adsorbed species, and convert into the desired products, which desorb from the surface and continue their drifting towards the exhaust of the tubes. The molecular radicals will never stick to the surface of the tube at 100% probability, so the penetration depth of such radicals in the tube depends on the sticking probability and probability for chemical reactions [12]. The effectiveness of the gas transformation depends on the diameter of the tube, the probability of surface reactions, the length of the tube, and the gas drift velocity. The sound velocity in the gas limits the latter, which is about 340 m/s. In practical cases, the drift velocities are lower but significant to assure a reasonable throughput.

The optimization of the tubular catalysts should take into account all these effects. Theoretically, the efficiency of the gas conversion upon passing a tube could be calculated by taking into account the gas kinetics, including the diffusion and the surface loss probabilities. Unfortunately, the loss probabilities are often unknown or there is a large scattering of the results reported by different authors [13], [14]. From this point of view, it is more straightforward to measure the gradients of the molecular fragments along the metallic tube to determine the appropriate geometrical dimensions of the tubes. Radicals of high oxidation potential, such as O, OH, F, etc., are of particular interest. Oxidation of hazardous molecules such as CO with atomic oxygen is particularly effective [15]. The oxygen atoms will adhere to the surface of the tube and interact with other molecules arriving from the gas phase by the Eley-Rideal model [16]. The oxygen atoms adsorbed on the catalyst surface, however, do not only interact with radicals such as CO but also with atoms arriving from the gas phase to form O_2 molecules. Any optimization of the efficiency requires the knowledge of the penetration depth of O atoms in tubes, which are fed on one side and pumped on the opposite side. The penetration depth depends on the atom loss probability, which has been described by many authors with the atom loss coefficient (sometimes equated to the recombination coefficient). The lists of coefficients for nickel, cobalt, and copper are presented in Table 1, Table 2, and Table 3, respectively. One can observe a large scattering of the results, indicating that the coefficients probably depend on other parameters, not only the type of catalyst. In the present paper, we report the penetration depth of O atoms in the tubes made from these materials.

Table 1. List of atom loss coefficients (γ) for nickel determined using various measurement methods at different pressures (p) and material temperatures (T) from the literature.

Author	**Method**	***p* [Pa]**	***T* [K]**	**γ**	**Ref.**
Greaves	calorimetry	10	300	0.028	[17]
Šorli	calorimetry	10–100	500–1100	0.27	[18]
Myerson	calorimetry, NO titration	750	/	0.0085	[19]
Melin	Wrede–Harteck, NO titration	1–4	300	0.017	[20]
Cvelbar	calorimetry	10–400	800	0.27	[21]
Mozetič	calorimetry, NO titration	100	550	0.27	[22]

Drenik	calorimetry	30–280	300	0.28	[23]
Greaves	thermocouple probe	10	300	0.0077	[17]
Hartunian	calorimetry	7–15	300	0.04	[24]
Dickens	calorimetry	4	295–620	0.0008–0.056	[25]
Rosner	NO titration	4	300	0.1	[26]
Greaves	Wrede–Harteck	650	300	0.00089	[27]

Table 2. List of atom loss coefficients (γ) for cobalt determined using various measurement methods at different pressures (p) and material temperatures (T) from the literature.

Author	**Method**	p **[Pa]**	T **[K]**	γ	**Ref.**
Melin	Wrede–Harteck, NO titration	1–4	300	0.075	[20]
Cvelbar	calorimetry	10–400	750	0.14–0.08	[21]
Guyon	actinometry	110	300–473	0.029–0.034	[28]
Dickens	calorimetry	4	300–625	0.0018–0.25	[25]
Greaves	Wrede–Harteck	650	300	0.00049	[27]

Table 3. List of atom loss coefficients (γ) for copper determined using various measurement methods at different pressures (p) and material temperatures (T) from the literature.

Author	**Method**	p **[Pa]**	T **[K]**	γ	**Ref.**
Greaves	calorimetry	10	300	0.17	[17]
Donnelly	mass spectrometry	0.02	300	0.07	[29]
Herdrich	calorimetry	25620	300	0.00217	[30]
Herdrich	calorimetry	18400	300	0.00899	[30]
Herdrich	calorimetry	13410	300	0.0213	[30]
Park	calorimetry	1400	300	0.016	[31]
Goulard	calorimetry	1400	300	0.4	[32]
Myerson	calorimetry, NO titration	760	/	0.031	[19]
Melin	Wrede–Harteck, NO titration	1–4	300–370	0.015–0.024	[20]
Cvelbar	calorimetry	10–400	800	0.225	[21]
May	calorimetry, effusion	1–2	298–375	0.070–0.11	[33]
Cauquot	calorimetry, NO-titration	300	313	0.025	[34]
Wickramanayaka	NO-titration	93	300	0.019, 0.026	[35]
Mozetič	calorimetry, NO titration	100	550	0.23	[22]
Park	calorimetry	14000	300	0.0026–0.0032	[31]
Dickens	calorimetry	4	295–485	0.034–0.18	[25]
Greaves	Wrede–Harteck	650	300	0.043	[27]
Greaves	calorimetry	10	300	0.02	[17]
Dickens	calorimetry	4	300–540	0.1–0.34	[25]

2. Experimental

The penetration depth of oxygen atoms in nickel, cobalt, and copper tubes was determined using appropriately designed metallic tubes with a diameter of 8 mm, which were connected to a source of oxygen atoms. A movable probe for oxygen atoms was mounted into the metallic tubes, and the O-atom density was measured versus the position of the probe. Figure 1 shows the dimensions of the metallic tubes and the position of the probe. The position l = 0 cm corresponds to the entrance of the metallic tube, and l =10 cm to the exhaust.

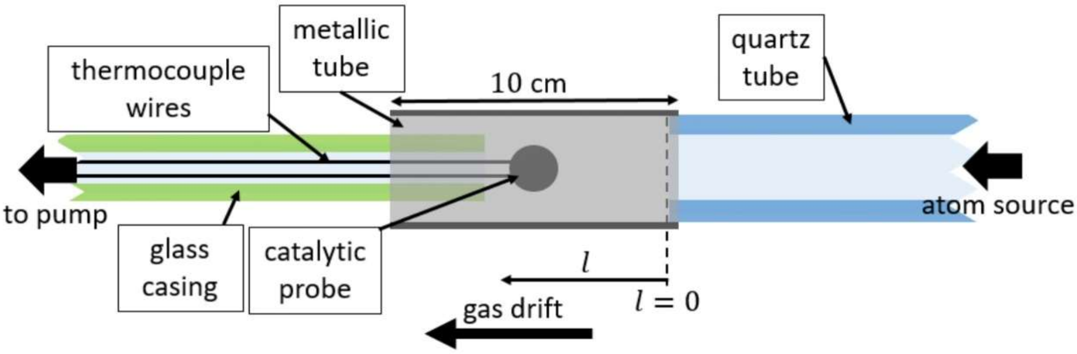

Figure 1. Schematic of the catalytic probe inside the metallic tube, with a marked position (l) of the catalytic probe. The catalytic probe was connected to a voltmeter with thermocouple wires enveloped in a glass casing.

The source of oxygen atoms was weakly ionized oxygen plasma sustained by a microwave discharge in the surfatron mode. A quartz tube was immersed into a microwave cavity, which was powered with a microwave generator operating at the standard frequency of 2.45 GHz and a power of 180 W (GMS200WSM by Sairem, Décines-Charpieu, France). Details about such sources were disclosed in earlier papers [36], [37], [38], [39]. A high electric field causes gas breakdown and formation of gaseous plasma, whose critical electron density is $3 \cdot 10^{17} m^{-3}$ [40]. Gaseous plasma is moderately conductive, so the electromagnetic fields cannot penetrate deep into the plasma due to the skin effect. Instead, the microwaves propagate within a sheath between the plasma and the quartz tube, where the electric conductivity is optimal for the absorption of the microwaves by plasma electrons. The electrons accelerate in the sheath and then transfer their energy to slower plasma electrons at elastic collisions, so the plasma is sustained at the electron temperature of a few eV [41]. The dissociation fraction of oxygen molecules passing through the quartz tube is several percent, depending on the discharge power, the pressure, and the gas speed [15]. Gaseous plasma only propagates along the quartz tube as long as the critical electron density is ensured. Further, along the quartz tube, the concentration of charged particles becomes negligible, but the dissociation fraction remains practically the same because of the very low probability of loss of oxygen atoms on the quartz surface, which is roughly 10^{-4} [25], [42], [43]. Therefore, the gas entering the metal tube is practically free from charged particles but rich in neutral radicals.

The probability for surface loss of oxygen atoms on metals such as nickel, cobalt, and copper is much larger, as shown in Tables 1-3. The O-atom density along the metallic tube will likely decrease with increasing distance from the quartz tube. The density was measured with a calibrated catalytic probe, which is explained in detail elsewhere [44]. The probe tip is very small so that the probe itself does not influence the kinetics of the gas inside the metallic tube. The exhaust of the metallic tube was connected to a vacuum system, and pumped with a two-stage rotary pump with a nominal pumping speed of 80 m^3/h (E2M80 by Edwards Vacuum, Burgess Hill, UK). The schematic of the entire experimental setup is shown in Figure 2. All tubes were made from 0.05 mm thin foils of 99.99% purity nickel, cobalt, and copper (purchased from Goodfellow, Huntingdon, UK). Before conducting the experiments, all tubes were immersed in oxygen plasma for an hour to stabilize the oxide layer.

The density of neutral oxygen atoms along the tubes made from nickel, cobalt, and copper was measured systematically at a fixed discharge power of 180 W and 3 different flow rates: 50, 300, and 600 sccm, which equated to pressures of 10, 35, and 60 Pa. At those conditions, the metallic tubes were heated to 360, 390, and 450 K at the flow rates of 50, 300, and 600 sccm, respectively. The pressure gradient along the tubes appeared because of the constant introduction of oxygen on one side of the experimental system, and pumping on the other side (Figure 3). By measuring the pressures at both sides of the experimental system, the following gradients were obtained by taking into account a linear decrease 17, 54, and 80 Pa/cm for the flow rates of 50, 300, and 600 sccm, respectively.

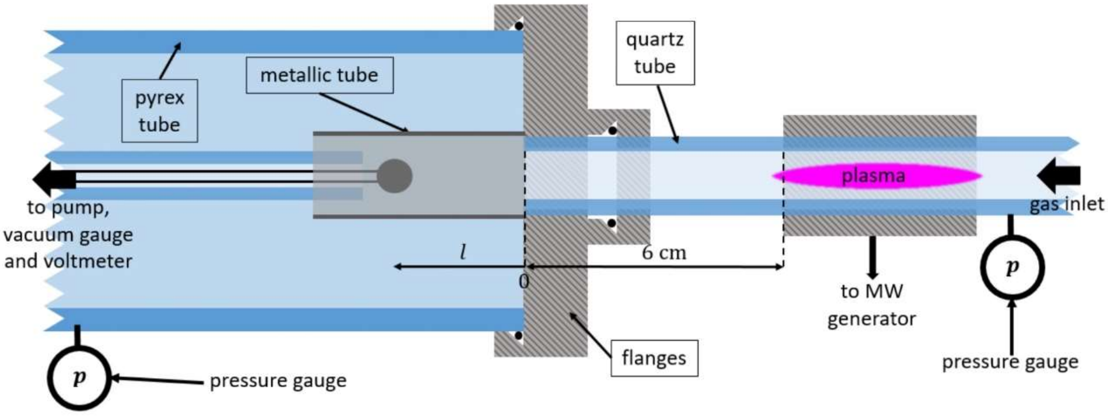

Figure 2. Schematic of the microwave plasma reactor, with gaseous oxygen entering the system on the right-hand side and exiting on the left-hand side. Two pressure gauges (p) were installed at each end of the experimental setup.

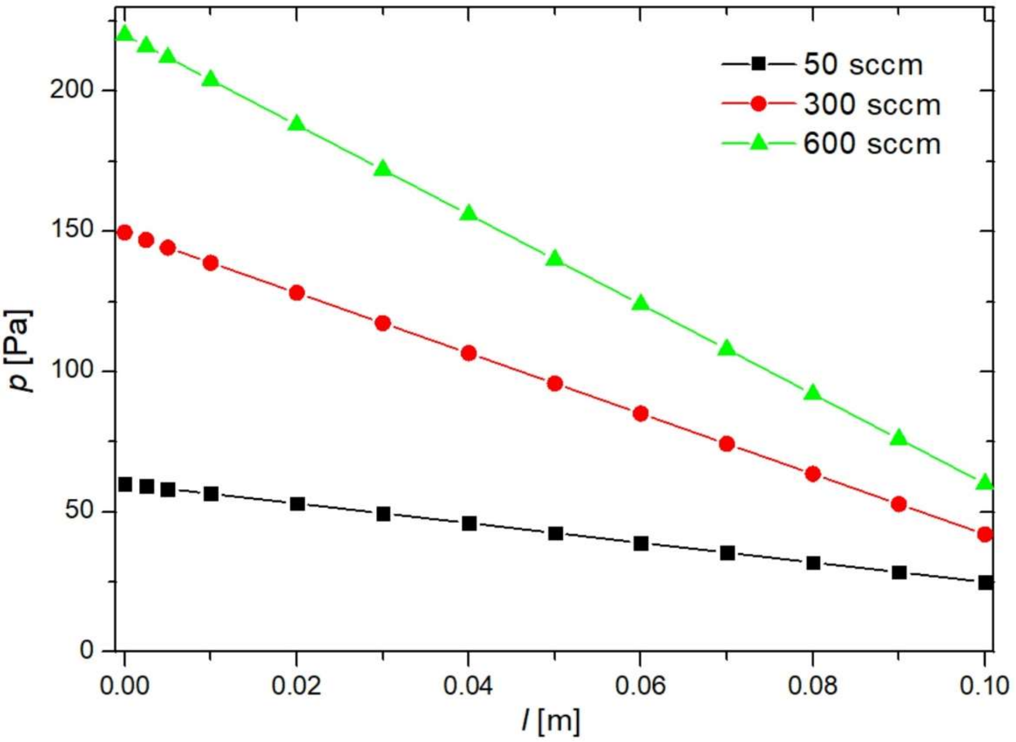

Figure 3. Pressure (p) profile along the length (l) of the metallic tubes at the given gas flow rates.

3. Results and discussion

The behavior of the O-atom density versus the length of the tube is shown in Figures 4, 5 and 6 for nickel, cobalt, and copper respectively, with position 0 marked in Figures 1 and 2. The curves exhibit a gradual decrease in the O-atom density. Two effects explain the decreasing atom density: i - loss of atoms on the surface by heterogeneous association to parent molecules, and ii - the pressure gradient along the tube. The error bars represent the statistic error of repeated measurements.

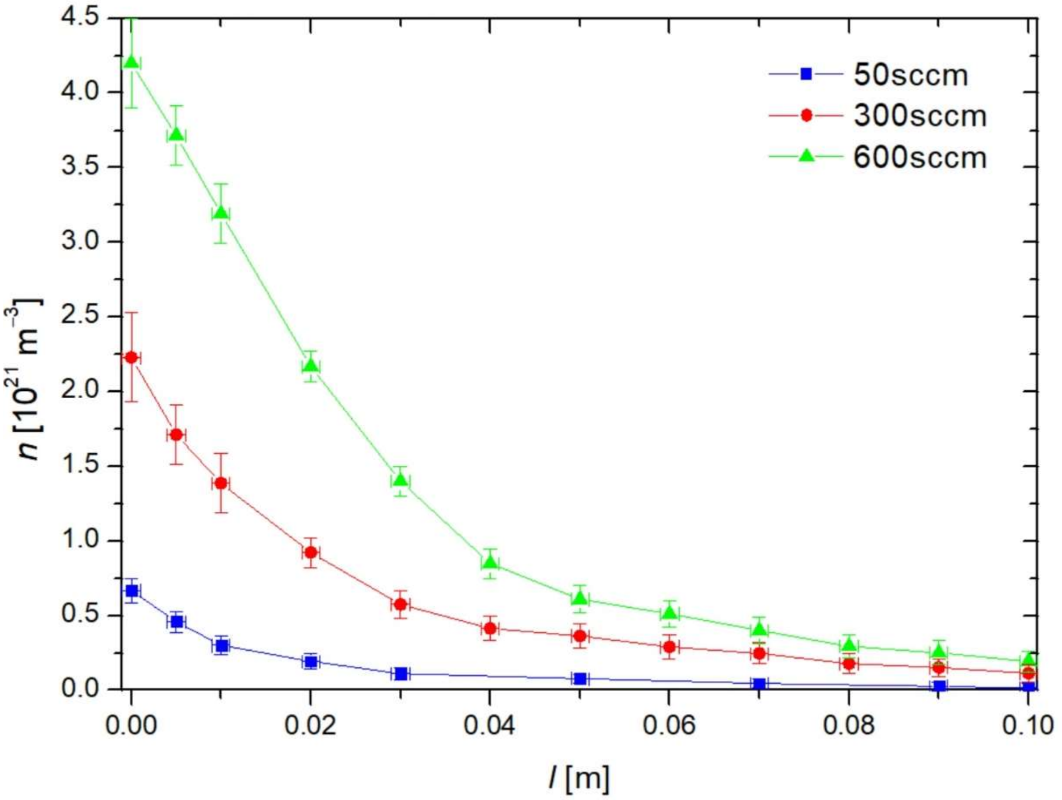

Figure 4. Neutral oxygen atom density (n) along the length (l) of the nickel tube.

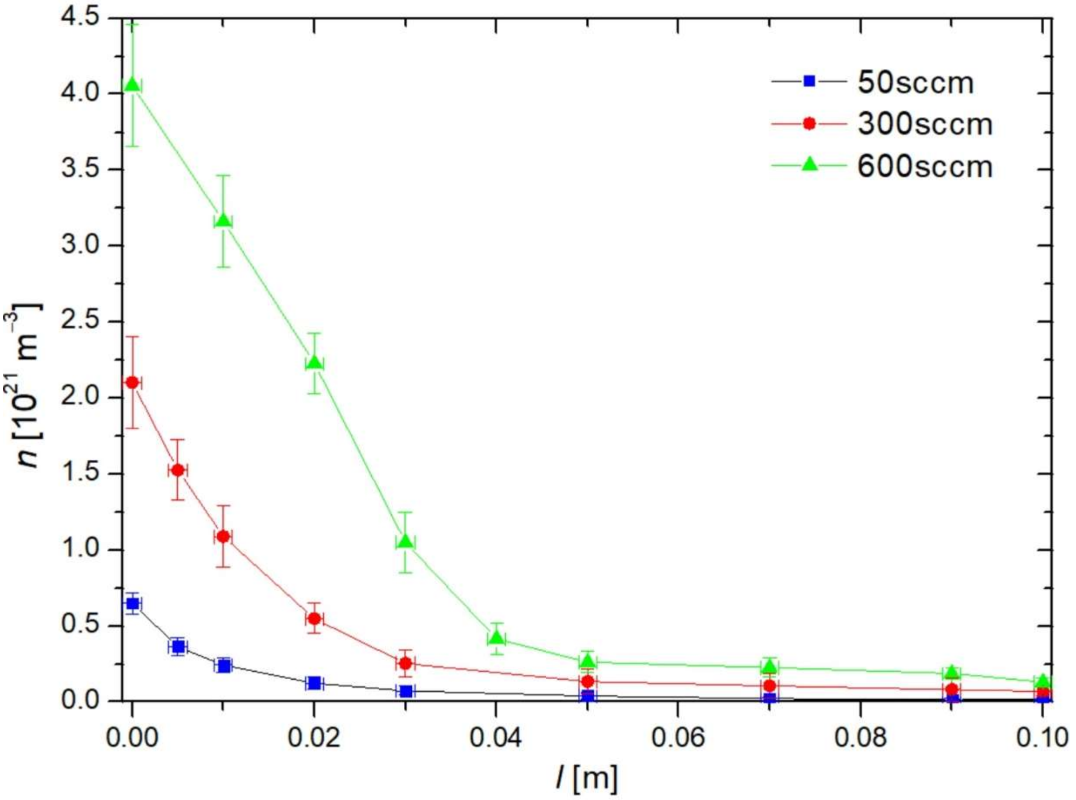

Figure 5. Neutral oxygen atom density (n) along the length (l) of the cobalt tube.

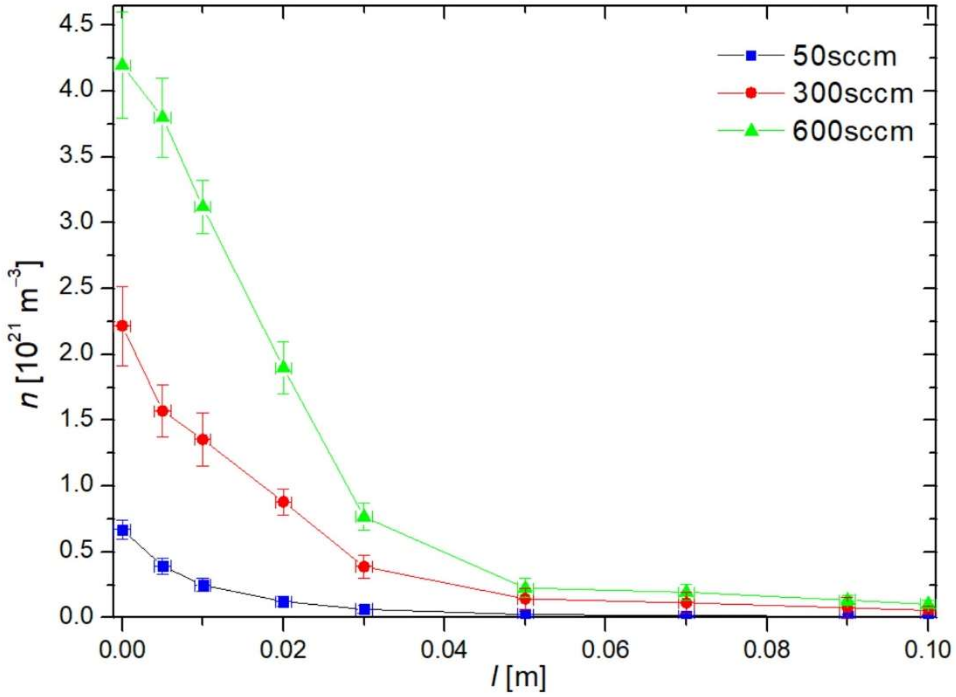

Figure 6. Neutral oxygen atom density (n) along the length (l) of the copper tube.

The pressure gradient in the metallic tube was determined from measured pressures on both sides of the experimental setup shown in Figure 2 as explained above. By considering the linear dependence of the pressure gradient, the decrease of O-atom density should be also linear in the absence of the surface effects. The curves in Figures 4 – 6, however, are not linear, indicating that the surface effects are the major cause of the decreasing O-atom density. The O-atom density at the exhaust from all three metallic tubes is at the detection limit of our probe (approximately 10^{19} m^{-3}), taking into account the probe accuracy, which is about $\pm 10\%$. Still, the densities as revealed in Figures 4 – 6 do not drop to zero. This effect will be explained later.

As mentioned earlier, the decreasing density is also a consequence of the pressure gradient. To clarify this, we used the measured O-atom densities from Figures 4-6 to calculate the dissociation fractions (η) of oxygen molecules, which are defined as:

$$\eta = \frac{nkT}{2p} , \tag{1}$$

where n is the oxygen atom number density, k is the Maxwell-Boltzmann constant, T is the gas temperature, and p is the gas pressure. The dissociation fractions along the metallic tubes are shown in Figures 7 – 9. The dissociation fractions first decrease almost exponentially with increasing depth, but then stabilize at a finite value. The curves in Figures 7 – 9 were fitted with an exponential curve in the form of:

$$\eta(l) = \eta_0 + Ae^{-\frac{l}{l_0}} , \tag{2}$$

where η_0 and A are the fitting parameters and l_0 is the penetration depth.

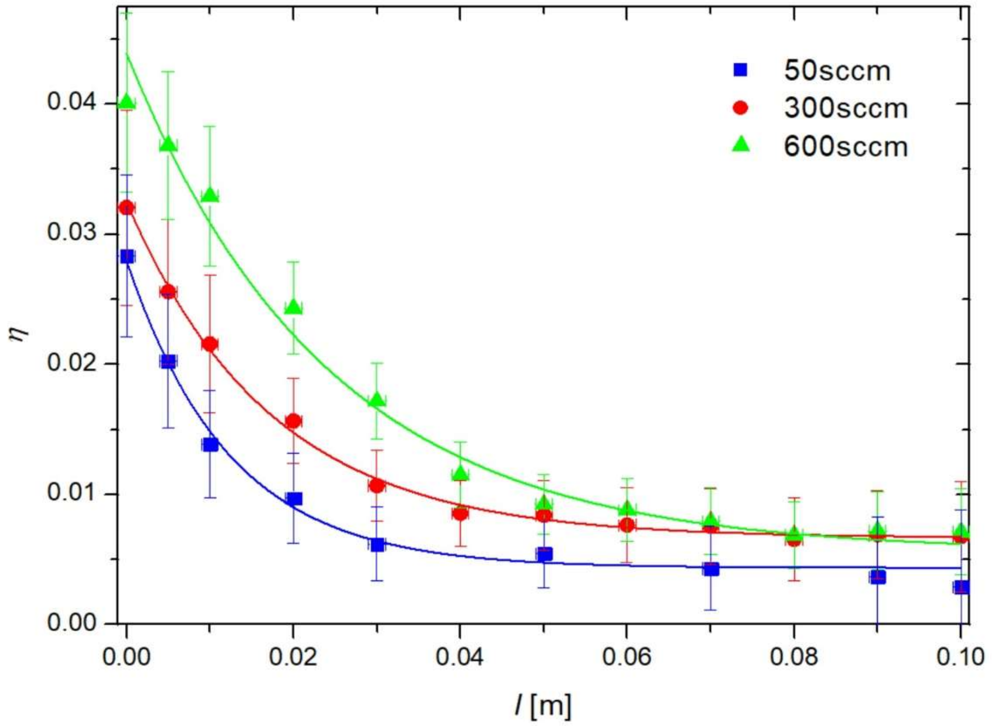

Figure 7. The dissociation fraction (η) of oxygen molecules along the length (l) of the nickel tube.

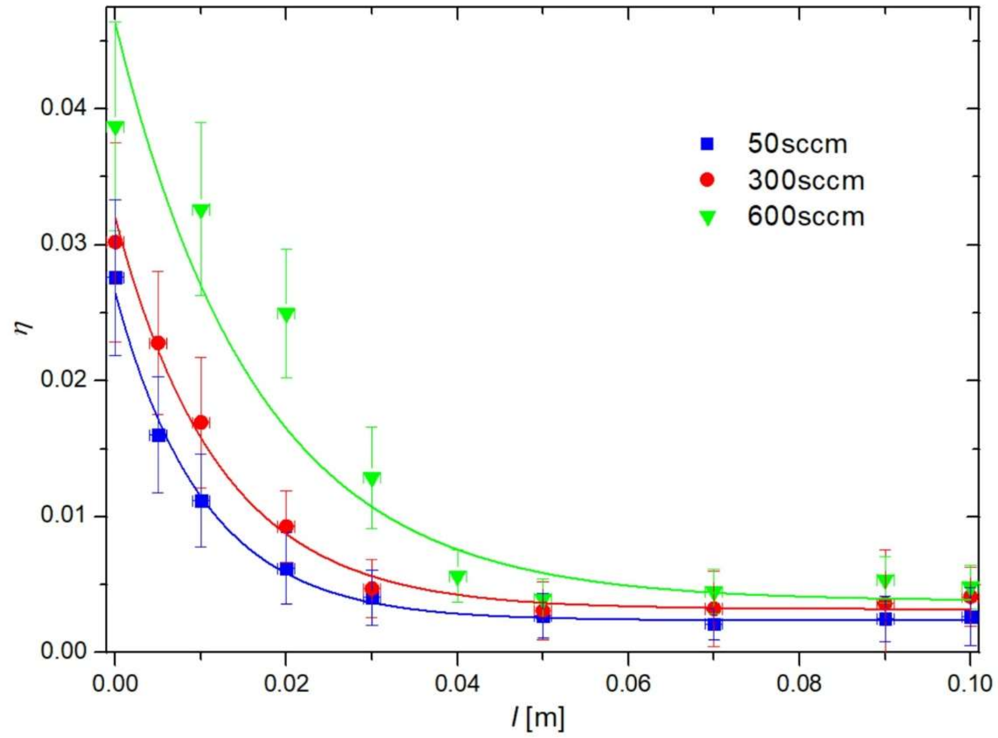

Figure 8. The dissociation fraction (η) of oxygen molecules along the length (l) of the cobalt tube.

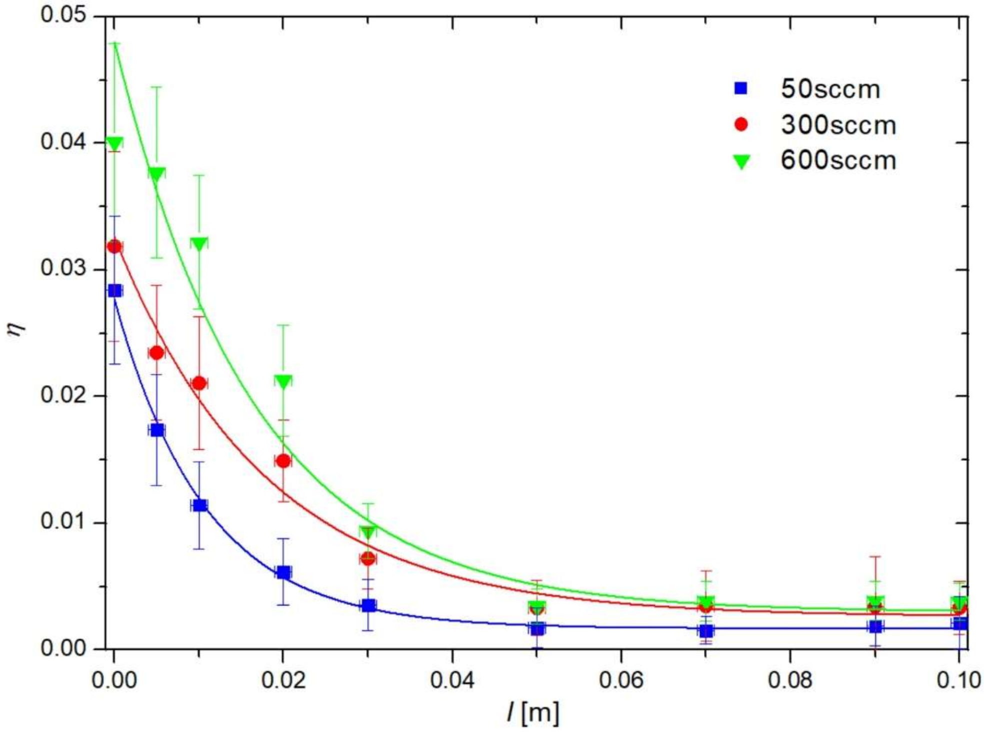

Figure 9. The dissociation fraction (η) of oxygen molecules along the length (l) of the copper tube.

The exponential curves fit the measured data very well, taking into account the accuracy of our probe. The fitting curves plotted in Figure 7 – 9 enable the calculation of the penetration depth, i.e. the depth at which the dissociation fraction of oxygen molecules drops to 1/e of the initial value at the entrance to the metallic tube. The penetration depths are summarized in Table 4. The penetration depths depend on the gas flow and increase monotonously with the flow. This effect is explained by the decreasing flux of O atoms on the catalyst surface, which is due to the decreasing mean free path of O atoms with increasing pressure. Namely, the mean free path decreases linearly with increasing pressure. Another explanation would be the pressure dependence of the atom loss probability. The results in Tables 1 – 3 do not allow for drawing the pressure dependence, because different authors used different experimental setups and different methods for the determination of the atom loss coefficient. Still, some recent studies reported that the atom loss coefficient for some materials decreases with increasing pressure [45], [46], [47]. The pressure dependence of the atom loss coefficient for oxygen atoms on nickel and cobalt was studied systematically previously, and the results were published recently [48], [49]. Still, any distinguishing between the effects of the mean free path and the pressure dependence of the atom loss coefficient is impossible from the results summarized in Table 4.

Table 4. The penetration depth of oxygen atoms in metallic tubes with a diameter of 8 mm made from nickel, cobalt, and copper at three different gas flows.

	Nickel	**Cobalt**	**Copper**
50 scmm	1.2 cm	1.0 cm	1.1 cm
300 sccm	1.7 cm	1.3 cm	1.3 cm
600 sccm	2.4 cm	1.7 cm	1.6 cm

Table 4 gives guidelines about the penetration depth of radicals, which associate to stable molecules by heterogeneous surface recombination. Knowing the penetration depth, one can calculate the depth at which the degree of dissociation drops to any value using equation (2). If the goal is total consumption of radicals, the metallic tubes would be long. If the diameter is 8 mm, as in our case, 90% consumption of the radicals is achieved at a depth of a couple of centimeters, depending on the gas flow and tube material. If the goal is efficiency in terms of the length of the tubes, the tubes should be much shorter than in our case. The conductance of the tubes decreases with increasing length, so it is obsolete to use long metallic tubes, because they suppress the gas throughput.

The constant value of the dissociation fraction along the tube from about 5 – 10 cm is highly unexpected and cannot be explained by surface effects. A feasible explanation of the finite O-atom density in the range between about 5 and 10 cm is the accuracy of our probes. As explained in the classical paper [44], the probe calculates the O-atom density from the power dissipated on the catalytic tip due to the heterogeneous surface recombination. While this power is by far the most important contribution to the catalyst heating, other channels will also contribute to the probe heating. Among them is the accommodation of gaseous molecules. The gas kinetic temperature in gaseous plasma exceeds the ambient temperature due to the abundance of super elastic collisions in the ionized gas. Another explanation is offered up by examining equation (1): since pressure decreases along the length of the metallic tubes, this seemingly increases the dissociation fraction towards the exhaust of the metallic tubes. Instead of a slow decline, we therefore get a constant value of the dissociation fraction near the exhaust of the metallic tubes.

Other authors have measured the kinetic temperature of gaseous molecules in plasmas sustained by microwave discharge in the surfatron mode [50]. The measurements are not feasible for oxygen because of the peculiarities of rovibrational states, but it was determined rather precisely for nitrogen [51]. The gas kinetic temperature in such plasma depends on the discharge power and the gas pressure and is roughly between 700 and 1000 K [52]. The gas cools down on its way from gaseous plasma to the metallic tubes by adiabatic expansion and accommodation on the surfaces of both quartz and metallic tubes. The gas speed, however, is large, so the accommodation is not complete. The artefact of the method used for measuring the O-atom density therefore explains the finite dissociation fraction along the metallic tubes between 5 and 10 cm. The actual dissociation fraction is probably very low at the exhaust from the metallic tube.

The metals always oxidize upon exposure to the air, so that a native layer of oxide is formed. In our case, however, the catalytic metals are not exposed only to molecular oxygen, but also to oxygen atoms. The oxidation of copper upon treatment with oxygen plasma was studied by several authors, including Ooi and Goh [53], and Tang et al. [9]. In a recent paper, Xia and Sautet [54] reported a systematic study of copper oxidation upon treatment with atomic oxygen and found that a few nanometer-thick oxide film forms even at room temperature. A recent experimental report by Kuo and Su [55] showed that the oxide films could be much thicker and it includes the penetration of the native oxide film, and transportation of precursors through the oxide film, leading to much thicker films than forecasted from theoretical works [54]. Various oxides are formed on the copper surface, which further complicates the oxidation kinetics and thus the mechanisms of the oxygen atom loss on copper tubes. The same applies to cobalt. Different authors reported various methods for cobalt oxidation and agreed that at least two oxides are formed upon exposure to atomic oxygen, i.e. CoO and $\mathrm{Co_3O_4}$ [56], [57], [58]. Nickel oxide behaves similarly, but only has one known form of oxide: NiO [59], [60]. This oxide tends to be structured in a simple cubic crystal lattice [61].

In any case, the treatment of nickel, cobalt, or copper tubes with oxygen atoms causes oxidation and the oxides are rarely in the form of a smooth film of uniform thickness. Many authors reported very rich morphology after treating metallic samples with oxygen plasma [62], [63], [64]. The evolution of surface morphology depends on numerous parameters, but it is clear that the morphology evolves with increasing treatment times. To avoid the effect of unpredictable evolution of surface morphology and thus increase the actual surface area, we pre-treated all three metallic tubes in oxygen plasma at elevated temperatures. The metallic tubes were mounted in a radiofrequency plasma reactor and exposed to oxygen plasma at the temperature of about 700 K for 20 minutes. This treatment caused the formation of a rather thick oxide film, which was not supposed to change during our experiments because the experiments disclosed in this article were performed at much lower temperatures of the metallic tubes. The metallic tubes did not heat over 100°C during our experiments. The heating is, of course, predominantly due to the exothermic surface association of oxygen atoms to O_2 molecules. The pre-treatment of the metallic tubes in oxygen plasma therefore assured for formation of a stable oxide film before conducting our experiments, and thus reliability of our results.

4. Conclusions

Systematic measurements of the O-atom density inside metallic tubes, which were connected to a source of O atoms on one side and pumped on the other side, enabled the determination of the penetration depths for O atoms. The O-atom density decreased monotonously along the metallic tubes, which was an effect of both the pressure gradient and the loss of atoms by heterogeneous surface recombination. The dissociation fraction of oxygen molecules along the metallic tubes was calculated from measured O-atom density and measured pressure drop along the narrow tubes. The dissociation fraction decreased exponentially along the length of the tubes. The penetration depth in 8 mm wide metallic tubes depended on the type of metal and the gas flow. At the lowest flow probed in our experiments, i.e. 50 sccm, the penetration depth was about 1 cm. At the highest flow of 600 sccm, the penetration depth was about 2 cm. These data are useful in any attempt to estimate the loss of molecular fragments along tubes, which serve as catalysts for the association of various radicals to stable molecules.

Acknowledgments: This research was funded by the Slovenian Research Agency, core funding P2-0082 and project L2-4487.

Conflicts of interest: The authors declare no conflict of interest. The funders had no role in the design of the study; in the collection, analyses, or interpretation of data; in the writing of the manuscript; or in the decision to publish the results.

Data Availability Statement: The data that support the findings of this study are available upon reasonable request from the authors.

Author Contributions: Conceptualization, M.M., R.Z. and D.P.; methodology, D.P. and R.Z.; validation, A.V. and G.P.; formal analysis, A.V. and D.Đ.; investigation, M.M. and G.P.; resources, A.V., data curation, M.M. and D.P.; writing-original draft preparation, M.M. and D.P.; writing-review and editing, R.Z., A.V. and G.P.; visualization, R.Z. and D.Đ.; supervision, R.Z. and M.M.; project administration, A.V. and G.P.; funding acquisition, M.M. and D.Đ. All authors have read and agreed to the published version of the manuscript.

References

[1] Z. Xu, N. Gao, Y. Ma, W. Wang, C. Quan, X. Tu and N. Miskolczi, "Biomass volatiles reforming by integrated pyrolysis and plasma-catalysis system for H2 production: Understanding roles of temperature and catalyst," *Energy Conversion and Management,* vol. 288, 2023.

[2] D. Marinov, "Reactive adsorption of molecules and radicals on surfaces under plasma exposure. Ph.D. Thesis," Ecole Polytechnique, Paris, 2012.

[3] J.-Y. Zhang, N. Sun, L.-X. Ling, R.-G. Zhang, L.-T. Jia, D.-B. Li and B.-J. Wang, "Effect of different valence metals doping on methane activation over La2O3(001) surface," *J. Fuel Chem. Technol.,* vol. 51, 2023.

[4] P. Navascues, J. Cotrino, A. R. Gonzalez-Elipe and A. Gomez-Ramirez, "Plasma assisted CO2 dissociation in pure and gas mixture streams with a ferroelectric packed-bed reactor in ambient conditions," *Chemical Engineering Journal,* vol. 430, 2022.

[5] Y. T. Shah, J. Verma and S. S. Katti, "Plasma activated catalysis for carbon dioxide dissociation: A review," *Journal of the Indian Chemical Society,* vol. 98, 2021.

[6] S. Kolbadinejad and A. Ghaemi, "Recovery and extraction of platinum from spent catalysts: A review," *Case Studies in Chemical and Environmental Engineering,* vol. 7, 2023.

[7] H. M. Bui, T. Kratky, I. Lee, R. Khare, M. Hiller, S. Wedig, S. Günther and O. Hinrichsen, "In situ impregnated Ni/Al2O3 catalysts prepared by binder jet 3D printing using nickel nitrate-containing ink," *Catalysis Communications,* vol. 182, 2023.

[8] M. M. Tohidi, B. Paymard, S. R. Vasquez-Garcia and D. Fernandez-Quiroz, "Recent progress in applications of cobalt catalysts in organic reactions," *Tetrahedron,* vol. 136, 2023.

[9] Y. Tang, Y. Cui, G. Ren, K. Ma, X. Ma, C. Dai and C. Song, "One-step synthesis of methanol and hydrogen from methane and water using non-thermal plasma and Cu-Modernite catalyst," *Fuel Processing Technology,* vol. 244, 2023.

[10] D. Wang, Y. Li, Y. Jiang, X. Cai and X. Yao, "Perspectives on surface chemistry of nanostructured catalysts for heterogeneous advanced oxidation processes," *Enviromental Functional Materials,* vol. 1, 2022.

[11] Y. Shi, W. Su, X. Wei, X. Song, Y. Bai, J. Wang, P. Lv and G. Yu, "Highly active MIL-68(In)-derived In2O3 hollow tubes catalysts to boost CO2 hydrogenation to methanol," *Fuel,* vol. 334, 2023.

[12] M. Michliček, L. Blahova, E. Dvorakova, D. Nečas and L. Zajičkova, "Deposition penetration depth and sticking probability in plasma polymerization of cyclopropylamine," *Applied Surface Science,* vol. 540, 2021.

[13] J.-P. Booth and N. Sadeghi, "Oxygen and fluorine atom kinetics in electron cyclotron resonance plasma by time-resolved actinometry," *J. Appl. Phys.,* vol. 70, 1991.

[14] A. Bousquet, G. Cartry and A. Granier, "Investigation of O-atom kinetics in O2, CO2, H2O and O2/HMDSO low pressure radiofrequency pulsed plasmas by time-resolved optical emission spectroscopy," *Plasma Sources Sci. Technol.,* vol. 16, 2007.

[15] A. Vesel, M. Mozetič, A. Drenik and M. Balat-Pichelin, "Dissociation of CO 2 molecules in microwave plasma," *Chemical Physics,* vol. 382, 2011.

[16] M. Cacciatore, M. Rutigliano and G. D. Billing, "Eley-Rideal and Langmuir-Hinshelwood recombination coefficients for oxygen on silica surfaces," *J. Thermophys. Heat Trans.,* vol. 13, 1999.

[17] J. C. Greaves and J. W. Linnett, "The recombination of oxygen atoms at surfaces," *Trans. Faraday Soc.,* vol. 54, 1958.

[18] I. Šorli and R. Ročak, "Determination of atomic oxygen density with a nickel catalytic probe," *Journal of Vacuum Science & Technology A,* vol. 18, 2000.

[19] A. L. Myerson, "Exposure-dependent surface recombination efficiencies of atomic oxygen," *J. Chem. Phys.,* vol. 50, 1969.

[20] G. E. Melin and R. J. Madix, "Energy accommodation during oxygen atom recombination on metal surfaces," *Trans. Faraday Soc.,* vol. 67, 1971.

[21] U. Cvelbar, M. Mozetič and A. Ricard, "Characterization of oxygen plasma with a fiber optic catalytic probe and determination of recombination coefficients," *IEEE Transactions on Plasma Science,* vol. 33, 2005.

[22] M. Mozetič and U. Cvelbar, "Heterogeneous recombination of O atoms on metal surfaces," *Int. J. Nanosci.,* vol. 6, 2007.

[23] A. Drenik, "The probability of heterogeneous recombination of hydrogen and oxygen atoms on the surfaces of fusion-relevant materials," Jožef Stefan International Postgraduate School, 2009.

[24] R. A. Hartunian, W. P. Thompson and S. Safron, "Measurements of catalytic efficiency of silver for oxygen atoms and the O-O2 diffusion coefficient," *J. Chem. Phys.,* vol. 43, 1965.

[25] P. G. Dickens and M. B. Sutcliffe, "Recombination of oxygen atoms on oxide surfaces," *Trans. Faraday Soc.,* vol. 60, 1964.

[26] D. E. Rosner, J. Breen, W. N. Delgass, N. G. Krichnan, P. C. Nordine and R. Cibrian, "Catalysis study for space shuttle vehicle thermal protection systems," NASA CR-134124, 1973.

[27] J. C. Greaves and J. W. Linnett, "Recombination of atoms at surfaces. Part 5. - Oxygen atoms at oxide surfaces," *Trans. Faraday. Soc.,* vol. 55, 1959.

[28] C. Guyon, S. Cavadias and J. Amouroux, "Heat and mass transfer phenomenon from an oxygen plasma to a semiconductor surface," *Surface and Coatings Technology,* Vols. 142-144, 2001.

[29] V. M. Donnelly, J. Guha and L. Stafford, "Critical review: plasma - surface reactions and the spinning wall method," *J. Vac. Sci. Technol. A,* vol. 29, 2011.

[30] G. Herdrich, M. Fertig, D. Petkow, A. Steinbeck and S. Fasoulas, "Experimental and numerical techniques to assess catalysis," *Progress in Aerospace Sciences,* Vols. 48-49, 2012.

[31] G. Park, "Oxygen catalytic recombination on copper oxide in tertiary gas mixtures," *J. Spacecraft and Rockets,* vol. 50, 2013.

[32] R. Goulard, "On catalytic recombination rates in hypersonic stagnation heat transfer," *Jet Propulsion,* vol. 28, 1958.

[33] J. W. May and J. W. Linnett, "Recombination of atoms at surfaces," *Journal of Catalysis,* vol. 7, 1967.

[34] P. Cauquot, S. Cavadias and J. Amouroux, "Thermal energy accommodation from oxygen atoms recombination on metallic surfaces," *J. Thermophysics and Heat Transfer,* vol. 12, 1998.

[35] S. Wickramanayaka, S. Meikle, T. Kobayashi, N. Hosokawa and Y. Hatanaka, "Measurements of catalytic efficiency of surfaces for the removal of atomic oxygen using NO2* continuum," *J. Vac. Sci. Technol. A,* vol. 9, 1991.

[36] K. Kutasi, B. Saoudi, C. D. Pintassilgo, J. Loureiro and M. Moisan, "Modelling the Low-Pressure N 2 – O 2 Plasma Afterglow to Determine the Kinetic Mechanisms Controlling the UV Emission Intensity and Its Spatial Distribution for Achieving an Efficient Sterilization Process," *Plasma Process. Polym.,* vol. 5, 2008.

[37] T. Czerwiec, J. Gavillet, T. Belmonte, H. Michel and A. Ricard, "Determination of 0 atom density in Ar-0 2 and Ar-0 2-H 2 flowing microwave discharges," *Surface and Coatings Technology,* vol. 98, 1998.

[38] T. Belmonte, C. Jaoul and J. N. Borges, "Modelling nitrogen atom flux in post-discharge nitriding processes," *Surface & Coatings Technology,* Vols. 188-189, 2004.

[39] M. Moisan and M. R. Wertheimer, "Comparison of microwave and r.f. plasmas: fundamentals and applications," *Surface & Coatings Technology,* vol. 59, 1993.

[40] Y. A. Lebedev and M. V. Mokeev, "Determination of the Electron Density and Electric Field in the Plasma of a Low-Pressure Microwave Electrode Discharge in Hydrogen from the Measured Spectral Line Intensities," *Plasma Physics Reports,* vol. 11, 2003.

[41] U. Kortshagen, A. Shivarova, E. Tatarova and D. Zamfirov, "Electron energy distribution function in a microwave discharge created by propagating surface waves," *J. Phys. D: Appl. Phys.,* vol. 27, 1994.

[42] G. Cartry, L. Magne and G. Cernogora, "Atomic oxygen recombination on fused silica: modelling and comparison to low-temperature experiments (300K)," *J. Phys. D: Appl. Phys.,* vol. 33, 2000.

[43] Y. C. Kim and M. Boudart, "Recombination of O, N and H atoms on Silica," *Langmuir,* vol. 7, 1991.

[44] M. Mozetič, "Characterization of reactive plasmas with catalytic probes," *Surface & Coatings Technology,* vol. 201, 2007.

[45] J.-P. Booth, O. Guaitella, A. Chatterjee, C. Drag, V. Guerra, D. Lopaev, S. Zyryanov, T. Rakhimova, D. Voloshin and Y. Mankelevich, "Oxygen (3P) atom recombination on a pyrex surface in an O2 plasma," *Plasma Sources Sci. Technol.,* vol. 28, 2019.

[46] K. Arts, S. Deijkers, R. L. Puurunen, W. M. M. Kessels and H. C. M. Knoops, "Oxygen Recombination Probability Data for Plasma-Assisted Atomic Layer Deposition of SiO2 and TiO2," *J. Phys. Chem. C,* vol. 125, 2021.

[47] J. T. Gudmundsson and E. G. Thorsteinsson, "Oxygen discharges diluted with argon: dissociation process," *Plasma Sources Sci. Technol.,* vol. 16, 2007.

[48] D. Paul, M. Mozetič, R. Zaplotnik, J. Ekar, A. Vesel, G. Primc and D. Đonlagič, "Loss of Oxygen Atoms on Well-Oxidized Cobalt by Heterogeneous Surface Recombination," *Materials,* vol. 16, 2023.

[49] D. Paul, M. Mozetič, R. Zaplotnik, J. Ekar, A. Vesel, G. Primc and D. Đonlagič, "Recombination of oxygen atoms on the surface of oxidized polycrystalline nickel - temperature and pressure dependences," *Plasma Sources Sci. Technol.,* vol. 32, 2023.

[50] L. Vialetto, A. W. van de Steeg, P. Viegas, S. Longo, G. J. van Rooij, M. C. M. van de Sanden, J. van Dijk and P. Diomede, "Charged particle kinetics and gas heating in CO2 microwave plasma contraction: comparisons of simulations and experiments," *Plasma Sources Sci. Technol.,* vol. 31, 2022.

[51] S. Kelly and A. Bogaerts, "Nitrogen fixation in an electrode-free microwave plasma," *Joule,* vol. 5, 2021.

[52] J. Levaton, A. Ricard, J. Henriques, H. R. T. Silva and J. Amorim, "Measurements of N(4 S) absolute density in a 2.45 GHz surface wave discharge by optical emission spectroscopy," *J. Phys. D: Appl. Phys.,* vol. 39, 2006.

[53] C. Ooi and G. K. L. Goh, "Formation of cuprous oxide films via oxygen plasma," *Thin Solid Films,* vol. 518, 2010.

[54] Y. Xia and P. Sautet, "Plasma oxidation of copper: Molecular dynamics study with neural network potentials," *ACS Nano,* vol. 16, 2022.

[55] Y. Kuo and J. Q. Su, "Plasma oxidation as an effective method in etching copper interoconnect lines at room-temperature," *Jpn. J. Appl. Phys.,* vol. 61, 2022.

[56] H. G. Tompkins and J. A. Augis, "The oxidation of cobalt in air from room temperature to 467°C," *Oxidation of Metals,* vol. 16, 1981.

[57] E. A. Gulbransen and K. F. Andrew, "The kinetics of the oxidation of cobalt," *Journal of the Electrochemical Society,* vol. 98, 1951.

[58] I. Saric, R. Peter and M. Petravic, "Oxidation of cobalt by oxygen bombardment at room temperature," *J. Phys. Chem. C,* vol. 120, 2016.

[59] Y. Unutulmazsoy, R. Merkle, D. Fischer, J. Mannhart and J. Maier, "The oxidation kinetics of thin nickel films between 250 and 500 °C," *Phys. Chem. Chem. Phys.,* vol. 19, 2017.

[60] S. Mrowec and Z. Grzesik, "Oxidation of nickel and transport properties of nickel oxide," *Journal of Physics and Chemistry of Solids,* vol. 65, 2004.

[61] X. Cai, T. Hu, H. Hou, P. Zhu, R. Liu, J. Peng, W. Luo and H. Yu, "A review for nickel oxide hole transport layer and its application in halide perovskite solar cells," *Materials Today Sustainability,* vol. 23, 2023.

[62] L. Qin, A. Majumder, J. A. Fan, D. Kopechek and L.-S. Fan, "Evolution of nanoscale morphology in single and binary metal oxide microparticles during reduction and oxidation processes," *J. Mater. Chem. A,* vol. 2, 2014.

[63] A. E. Nyong, G. Udoh, J. J. Awaka-Ama, E. W. Nsi and P. K. Rohatgi, "A Study of the Morphological Changes and the Growth Kinetics of the Oxides Formed by the High Temperature Oxidation of Cu-32.02% Zn-2.30% Pb Brass," *Materials Research,* vol. 25, 2022.

[64] D. Serafin, W. J. Nowak and B. Wierzba, "Differences in oxides morphology as a result of surface preparation of NiFe alloy," *Surface & Coatings Technology,* vol. 385, 2020.

Chapter 3

Recombination of Atoms on Nanostructured Materials

One of our hypotheses pertains to the surface morphology of materials impacting the recombination coefficient. To confirm the hypothesis, materials with complex surface morphologies are studied. One such group of materials is nanomaterials. One of the most commonly used and widely applicable is carbon nanomaterials which can come in many different forms, such as nanowires, nanotubes, graphene, fullerenes, etc. Carbon nanomaterials have been a popular scientific venue for many years due to their interesting properties, such as their mechanical properties, chemical inertness, good electrical conductivity, and especially their large surface-to-mass ratio.

Carbon nanomaterials are often used in different applications. Starting with their electrochemical applications, carbon nanomaterials have been successfully used in supercapacitors [96], batteries [97], fuel cells [98], gas sensors [99], memory devices [100], emission devices [101], photo-catalyzers [102], and photovoltaic devices [103]. The mechanical properties of carbon nanomaterials lend themselves well to the use of carbon nanomaterials in compressive strain sensors [104], various biomedical applications [105], [106], [107], and so on.

One of the more promising carbon nanomaterials is carbon nanowalls (CNW), with the first successful synthesis happening by accident [108]. CNW can be described as thin sheets of carbon, such as flakes of graphene, which grow in a dense array perpendicular to the surface of a substrate (Figure 12). This morphology leads to an extremely high specific surface area when compared with smooth and amorphous materials. Carbon is the main building block of CNW but other elements, such as hydrogen, oxygen, nitrogen, halogen elements, and metals can also be present. The average thickness of CNW can be anywhere between a few nanometers up to 100 nm, and the average height of CNW can be anything between 100 nm and 100 μm [109]. Usually, the synthesis of CNW produces other carbon nanoparticles, and CNW can be a by-product when growing other carbon nanomaterials. Interestingly, the highest measured recombination coefficient in the literature is attributed to CNW [110].

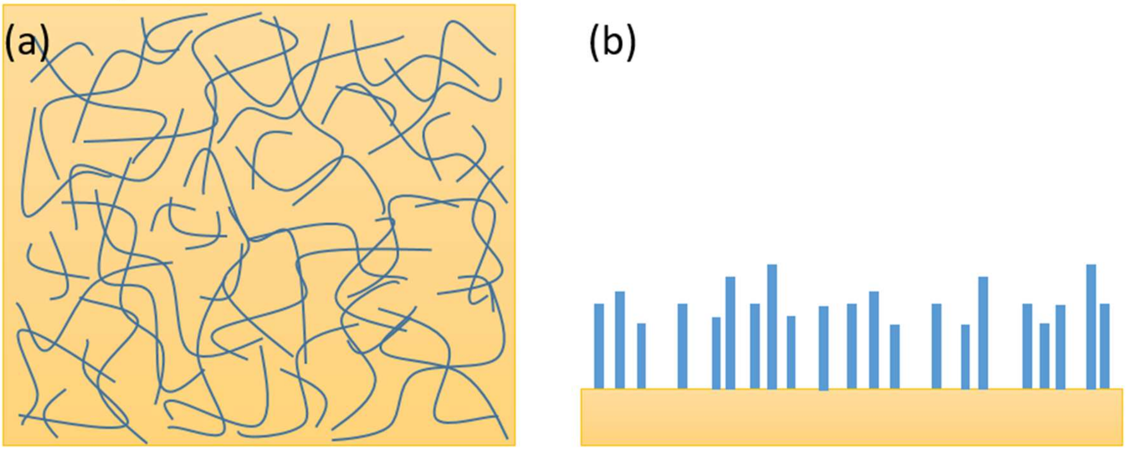

Figure 12: A simple schematic of carbon nanowalls (blue) on a substrate (yellow) from the (a) top-down view and (b) from the side-view.

3.1 Comparison of Plasma Decomposition of Carbon Nanomaterials Using Various Polymer Materials as a Carbon Atom Source

Synthesis of carbon nanowalls, as well as other carbon nanoparticles, is the main topic of the proceeding article. There are many different methods with which we can grow carbon nanomaterials but they mostly involve some form of chemical vapor deposition (CVD). Our focus is on plasma-enhanced chemical vapor deposition (PE-CVD). This method utilizes plasma to create gaseous carbon atoms which are then deposited on the surface of a chosen substrate. The creation of gaseous carbon atoms requires some form of carbon precursor material, be it in solid or gaseous form.

In our experiments [111], we use two types of carbon precursors: gaseous and solid. For gaseous precursors, we used propane gas (C_3H_8, excluded in the proceeding article) and carbon dioxide (CO_2) whereas for solid carbon precursors, we used different polymers which include polystyrene (PS), polyethylene (both the low-density polyethylene – LDPE and high-density polyethylene – HDPE), polypropylene (PP), polyamide (PA6), polyethylene terephthalate (PET), and acrylonitrile butadiene styrene (ABS). The amounts of polymer used in the synthesis processes varied but did not influence the growth of carbon nanomaterials, as long as there were enough carbon precursors in the plasma system.

For carbon nanoparticle synthesis, we use an inductively coupled low-pressure radiofrequency plasma, as shown in the proceeding article. Along with polymers, gaseous nitrogen, oxygen, hydrogen, and carbon dioxide are introduced into the experimental system, acting as carrier gases for carbon atoms.

The substrates we use are thin square ribbons of titanium foil. This synthesis also proved to be successful on nickel and cobalt, as well as different types of stainless steel samples. To characterize the samples, different techniques are used. During carbon nanomaterial synthesis, optical emission spectroscopy (OES) is used to monitor the optical emission of the plasma in the visual spectrum. After synthesis, samples are examined with two techniques. Secondary electron microscopy (SEM) is used to map the surface morphology of samples, and X-ray photoelectron spectroscopy (XPS) is used to study the chemical composition of samples.

CNW is successfully grown on titanium samples, with the thickness of the CNW layer varying from 0.5 to 8 μm, depending on the deposition time. Interestingly, the thickness of the CNW layer stops increasing with longer times at around 40 seconds when using polymers as carbon precursors. In all cases, the carbon nanomaterial compositions consist of over 90% carbon, with varying amounts of nitrogen and oxygen (a few %), and trace amounts of other elements. More importantly, it is discovered that aromatic polymers (presence of aromatic benzene rings), such as PS, PET, and ABS, are not as effective for CNW growth when compared to aliphatic polymers (chain-like structure), which can decompose to lightweight C_xH_y species. Another important finding is that all gases behaved similarly during CNW synthesis, downplaying the importance of choosing a proper carrier gas.

nanomaterials MDPI

Article

Comparison of Plasma Deposition of Carbon Nanomaterials Using Various Polymer Materials as a Carbon Atom Source

Alenka Vesel [1,*], Rok Zaplotnik [1], Gregor Primc [1], Domen Paul [1,2] and Miran Mozetič [1]

[1] Department of Surface Engineering, Jozef Stefan Institute, Jamova cesta 39, 1000 Ljubljana, Slovenia; rok.zaplotnik@ijs.si (R.Z.); gregor.primc@ijs.si (G.P.); domen.paul@ijs.si (D.P.); miran.mozetic@ijs.si (M.M.)
[2] Jozef Stefan International Postgraduate School, Jamova cesta 39, 1000 Ljubljana, Slovenia
* Correspondence: alenka.vesel@guest.arnes.si

Abstract: Carbon nanowalls are promising materials for various electrochemical devices due to their chemical inertness, desirable electrical conductivity, and excellent surface-to-mass ratio. Standard techniques, often based on plasma-assisted deposition using gaseous precursors, enable the synthesis of top-quality carbon nanowalls, but require long deposition times which represents a serious obstacle for mass applications. Here, an alternative deposition technique is presented. The carbon nanowalls were synthesized on titanium substrates using various polymers as solid precursors. A solid precursor and the substrate were mounted into a low-pressure plasma reactor. Plasma was sustained by an inductively coupled radiofrequency discharge in the H-mode at the power of 500 W. Spontaneous growth of carbon nanomaterials was observed for a variety of polymer precursors. The best quality of carbon nanowalls was obtained using aliphatic polyolefins. The highest growth rate of a thin film of carbon nanowalls of about 200 nm/s was observed. The results were explained by different degradation mechanisms of polymers upon plasma treatment and the surface kinetics.

Keywords: carbon nanowalls; plasma deposition; fast synthesis; one-step procedure; polymer source

check for updates

Citation: Vesel, A.; Zaplotnik, R.; Primc, G.; Paul, D.; Mozetič, M. Comparison of Plasma Deposition of Carbon Nanomaterials Using Various Polymer Materials as a Carbon Atom Source. *Nanomaterials* **2022**, *12*, 246. https://doi.org/10.3390/nano12020246

Academic Editor: Orietta Monticelli

Received: 7 December 2021
Accepted: 12 January 2022
Published: 13 January 2022

1. Introduction

For decades, the synthesis of carbon nanomaterials has been a hot topic of interdisciplinary research because of the numerous possible applications. The materials exhibit good chemical inertness, reasonable electrical conductivity, and a large surface-to-mass ratio. A variety of carbon nanomaterials have been invented, including fullerenes, nanotubes, nanowires, graphene and its derivatives, and less-oriented materials such as soot. Of particular importance are carbon nanomaterials in the form of evenly distributed flakes stretching from a substrate surface. Such materials are promising for application in electrochemical and photoelectrical devices such as supercapacitors, super-batteries, fuel cells, and photo-catalyzers [1–6]. A sophisticated version of such materials is carbon nanowalls (CNWs). Carbon nanowalls are flakes of multilayer graphene sheets vertically oriented on a suitable substrate. The typical thickness of the CNWs is several nm, and the area of a flake is of the order of μm^2. The distance between neighboring flakes in carbon nanowalls is several 10 μm, thus making this material superior in terms of the surface-to-mass ratio.

Several methods were proposed for the synthesis of carbon nanowalls. They are usually based on classical chemical vapor deposition (CVD) or plasma-enhanced chemical vapor deposition (PECVD). These techniques usually require a long deposition time of minutes or even hours. The current progress in the synthesis of carbon nanowalls has been reviewed in the papers [7,8]. Recently, we have shown that nitrogen-containing carbon nanomesh can be deposited in nitrogen plasma using polymer polyethylene terephthalate as the source of a carbon precursor [9]. The aim of this paper was to investigate the influence of the type of polymer material used as a carbon precursor on the growth of carbon nanostructures. Therefore, several different polymers were used in the study presented in this paper. Additionally, besides the effect of the source of the carbon precursor on the CNWs' growth, the effect of the type of processing plasma gas was also investigated.

2. Materials and Methods

2.1. Plasma Synthesis of Carbon Nanomaterials

The deposition of carbon nanomaterials was performed in an inductively coupled radiofrequency plasma (ICP-RF) system shown in Figure 1. The system consisted of the discharge tube with a coil of six turns that was positioned in the middle of the tube. The tube was made of borosilicate glass with dimensions 80 cm in length and 4 cm in diameter. The system was first pumped with a Hi-Cube 300 Classic pumping station (Pfeiffer Vacuum, Asslar, Germany), consisting of a turbomolecular pump of a nominal pumping speed of 260 L/s backed with a rotary pump with a nominal pumping speed of 5 m^3/h. This pumping station was used to get the base pressure of 10^{-2} Pa and to achieve low levels of the residual atmosphere. After achieving the base pressure, we continued pumping only with a rotary pump with a nominal pumping speed of 80 m^3/h. A gas of commercial purity was released into the discharge system using a mass flow controller Aera FC7700 (Advanced Energy, Denver, CO, USA). Various gasses were used to manipulate the morphology and chemical composition of deposited carbon nanostructures. The deposition was thus performed using N_2 (43 sccm), O_2 (35 sccm), H_2 (82 sccm), and CO_2 (58 sccm), keeping the gas pressure constant at 16 Pa. This was the pressure obtained using the smallest flow rate that was possible to set on our flow controller. If the flow rate was higher, it was not good for the synthesis because the polymer degradation products were too quickly pumped away. Here we should mention that CNWs could also be synthesized in a closed system without pumping, but this was not practical because it was more difficult to control the constant experimental conditions and the repeatability.

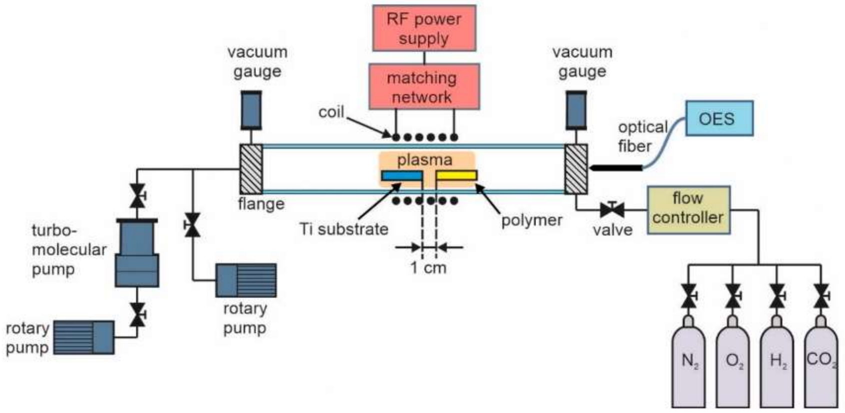

Figure 1. Experimental set-up.

Deposition of carbon nanomaterials was performed on the substrates made from titanium foil which were placed in the middle of the coil (i.e., in the glowing discharge). Ti substrates were in the form of a square with a size of 8 × 8 mm^2. At the same time, a piece of a polymer material was also placed into the discharge tube, as shown in Figure 1.

The polymer was placed 1 cm before the Ti substrate. The polymer material served as a source of carbon precursors. Different polymer materials (from Goodfellow Ltd., Huntingdon, UK) were used to study the influence of the source material on the properties of the nanocarbon deposit. The following polymer materials were selected: low-density polyethylene (LDPE), high-density polyethylene (HDPE), polypropylene (PP), polyamide (PA6), polyethylene terephthalate (PET), polystyrene (PS), and acrylonitrile butadiene styrene (ABS). For all polymers, equal masses (200 mg) were used. The amount of a polymer does not affect the synthesis of CNWs as long as it is large enough to provide a sufficient flux of carbon precursors to the polymer surface. We found that 200 mg of a polymer is more than enough, so we always chose this mass of a polymer. If the amount of a polymer was too small compared to the size of the substrate surface, the surface would be poorly covered with CNWs because of the insufficient flux of carbon precursors.

The deposition time was varied using PP polymer to find the most optimal time for the deposition of CNWs—which was 60 s. Then, the deposits were formed using all the above-mentioned polymers at a constant treatment time of 60 s.

The plasma was ignited and sustained at the forward power of the RF generator of 500 W (Advanced Energy, Denver, CO, USA). The RF generator operated at the standard industrial frequency of 13.56 MHz. Inductively coupled plasma was sustained in the H-mode, where the absorbed power was high (reflected power only 20 W). At these conditions, a Ti substrate was heated in the plasma because of exothermic heterogeneous surface reactions and reached a temperature of approximately 800 °C after several seconds. At the same time, the polymer material was also heated and melted. Degradation products of polymer evaporated from the solid precursors and deposited on the Ti substrate forming a layer of nanowalls.

To understand deposition mechanisms occurring in plasma when using various gases and polymer materials, we characterized the plasma by optical emission spectroscopy (OES) using AvaSpec-3648 Fiber Optic Spectrometer (Avantes, Apeldoorn, The Netherlands). The spectrometer resolution was 0.5 nm in the range of wavelengths between 200 to 1100 nm. The integration time was 1 ms. The spectrometer was placed at the end of the tube on its axis because the sidewalls of the tube quickly became opaque due to the formation of a deposit.

2.2. Characterization of the Samples

The surface morphology of the deposits was analyzed by secondary electron microscopy (SEM). Microscopic images were acquired in immersion mode using Schottky field emission scanning electron microscope with a monochromator (Thermo Fisher Verios 4G HP, Waltham, MA, USA).

The chemical composition of the samples was analyzed by X-ray photoelectron spectroscopy (XPS). The characterization was performed by using an XPS (TFA XPS Physical Electronics, Münich, Germany). The samples were excited with monochromatic Al K$\alpha_{1,2}$ radiation at 1486.6 eV over an area with a diameter of 400 μm. Photoelectrons were detected with a hemispherical analyzer positioned at an angle of 45° with respect to the normal of the sample surface. Survey spectra were measured to determine the surface composition—i.e., the presence of any other elements except carbon. The survey spectra were measured at a pass energy of 187 eV with an energy step of 0.4 eV. The measured spectra were analyzed using MultiPak v8.1c software (Ulvac-Phi Inc., Kanagawa, Japan, 2006) from Physical Electronics, which was supplied with the spectrometer. Standard sensitivity factors were used for the calculation of the surface composition.

3. Results and Discussion

3.1. Influence of the Deposition Time

Various deposition times were used to find the most optimal conditions for the synthesis of a thin film of carbon nanowalls. In Figure 2, examples of SEM images of CNW deposits when using the PP polymer as a source of carbon atoms are shown. One can observe that at the shortest deposition time of 10 s, CNWs are small and dense on the substrate surface (Figure 2a). When the deposition time is increased, the size of the vertical flakes increases, as well as the distance between them (Figure 2a–c), reaching the maximum size of the nanowalls and a maximum distance between them at 60 s of treatment (Figure 2d). At longer deposition times (Figure 2e,f), CNWs become slightly smaller and denser again. Furthermore, the edges of CNWs are less sharp, indicating that etching and their destruction had already occurred.

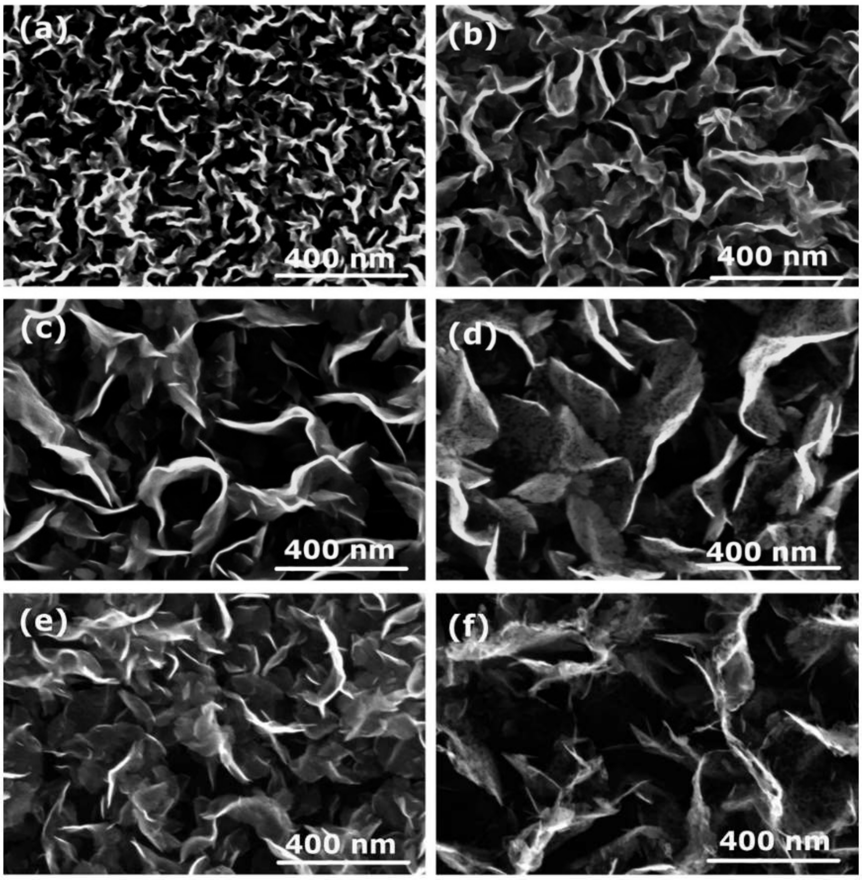

Figure 2. SEM images of CNWs for various deposition times in N_2 plasma when using PP polymer: (**a**) 10 s, (**b**) 20 s, (**c**) 30 s, (**d**) 60 s, (**e**) 90 s, and (**f**) 120 s.

The results presented in Figure 2 are further evidenced in Figure 3, which represents the thickness of the CNW film versus the deposition time. The deposition time does not affect just the morphology of CNWs but also the thickness of the deposited layer. One can observe a maximum thickness at the treatment times between 30 and 60 s. A decrease in the film thickness at a longer treatment time is a consequence of plasma etching and simultaneous removal of the deposit during its growth.

The results presented in Figures 2 and 3 are in agreement with our previous investigation, where we deposited CNWs in nitrogen plasma with the same experimental conditions but using PET polymer as the solid precursor and found the most optimal deposition time was 60 s [9]—i.e., the same as in this study. Therefore, in all further experiments, the deposition time was fixed to 60 s.

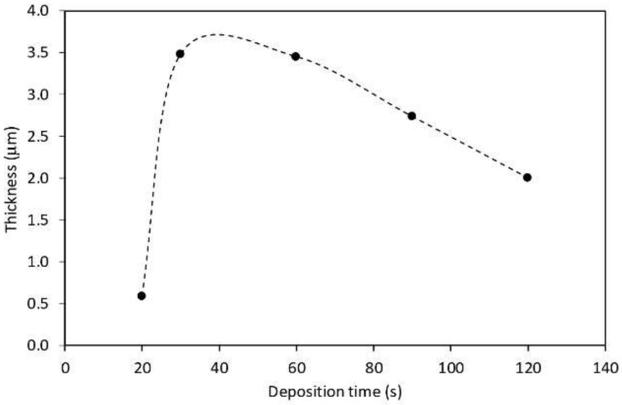

Figure 3. The thickness of CNWs, shown in Figure 2, versus deposition time.

3.2. *Influence of the Polymer Material as a Carbon Atom Source*

In the next set of experiments, different polymer materials were used to study the influence of the carbon source material on the characteristics of the deposits. Therefore, examples of aromatic (PET, PS, ABS) and aliphatic (LDPE, HDPE, PP, PA6) polymers were used to produce different plasma radicals acting as building blocks for the growth of CNWs. Some of these polymers were olefins (PS, LDPE, HDPE, PP), whereas the others contained heteroatoms O and/or N (PET, ABS, PA6). The structure of these polymers is shown in Table 1.

Table 1. Chemical structure of the polymers used as a carbon precursor.

Polymer	Structure
PS	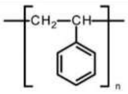
LDPE/HDPE	–CH$_2$–CH$_2$–
PP	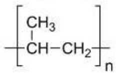
PET	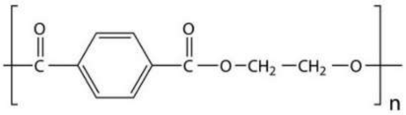
PA6	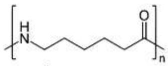
ABS	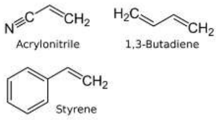

SEM images of the deposits synthesized from the above-mentioned polymers are shown in Figure 4. Figure 4a–d show the deposits formed on the titanium substrate when using polymers PP, PA6, LDPE, and HDPE. In all four cases of polymers, we can clearly observe the formation of CNWs. However, the next three images shown in Figure 4e–g significantly differ from Figure 4a–d. Instead of CNWs, a dense mesh of small nanocarbon was formed, resembling cauliflower-like structures. These samples with the cauliflower-like structures were synthesized from polymers PS, PET, and ABS, all examples of aromatic polymers. In contrast, images with CNWs (Figure 4a–d) were all obtained when using aliphatic polymers as a source of the carbon precursor. The results shown in Figure 4 indicate that there must be a significant difference in the thermal degradation of aromatic and aliphatic polymers upon plasma conditions leading to different carbon radicals acting as building blocks for CNWs. Aromatic polymers are in general more thermally stable than aliphatic, and it seems that aromatic rings, which are in the first approximation similar to a graphite structure (except that the rings are terminated with hydrogen), are not key building blocks for the growth of CNWs, or they have a different influence on the formation of the nucleation sites and growth process [10]. In addition, the dynamics of the migration and reorientation of these species as well as the time scale of their growth may be different, thus affecting the growth of the deposit.

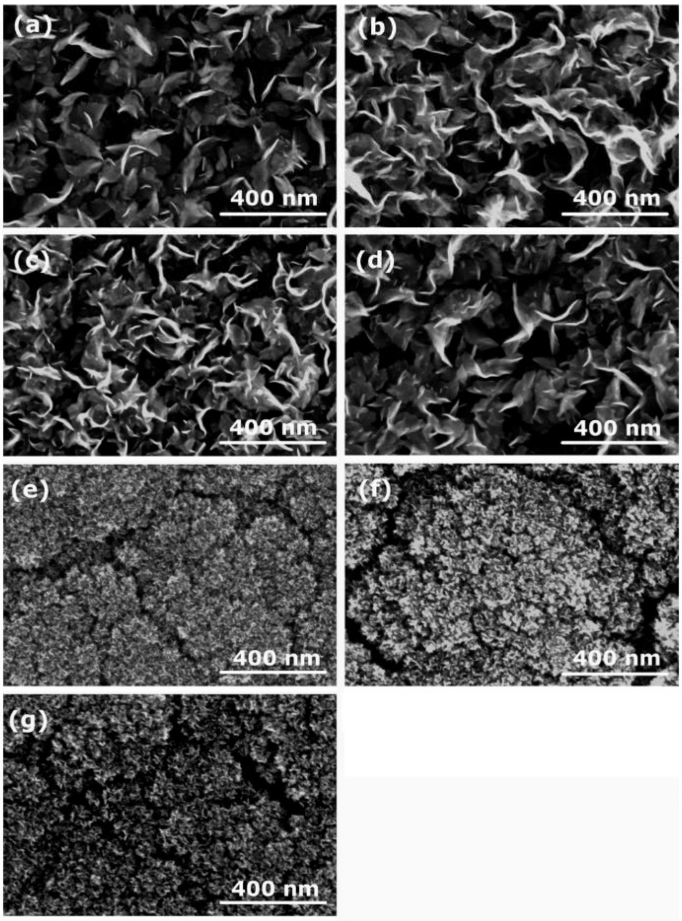

Figure 4. SEM images of carbon nanostructures synthesized from various polymers: (**a**) PP, (**b**) PA6, (**c**) LDPE, (**d**) HDPE, (**e**) PET, (**f**) PS, and (**g**) ABS. Deposition time in nitrogen plasma was 60 s.

To get a further insight into the degradation mechanisms of various polymers and the consequent formation of their degradation products, we studied the literature. The explanation is far from being simple because of the presence of various factors in plasma (i.e., heat load, irradiation, reactive (oxidizing) plasma species) that may all influence the degradation kinetics of polymers in plasma. Depending on the environmental conditions, polymers can undergo different degradation mechanisms [11]: (i) thermal degradation, (ii) photochemical degradation, and (iii) oxidative degradation. Thermal degradation is caused by a temperature increase leading to conformational changes, bond dissociation, and radical formation. Photochemical degradation is triggered by photon irradiation (visible, UV, VUV), causing bond dissociation and cross-linking. If the treatment is performed in an oxidizing atmosphere such as air, the bond-scission is followed by oxidation (photooxidative degradation). Oxidative degradation is caused by the presence of oxygen. This process is particularly effective in gaseous discharges (i.e., oxygen plasmas) that are a rich source of various reactive oxygen species—the most important are neutral oxygen atoms. Even when using discharges sustained in other gasses, some oxygen is present in vacuum systems as water vapor. In the presence of reactive oxygen species, the process of polymer degradation is often initiated by hydrogen subtraction from polymer, followed by various reactions [12]. However, plasmas are not only a rich source of oxygen atoms but also a source of radiation by photons (UV/VUV). Furthermore, because of exothermic heterogeneous surface recombination and chemical reactions of oxygen radicals on the polymer surface, the polymer can be heated well above the melting temperature. All the above-mentioned processes occur on the polymer surface upon plasma conditions simultaneously, making the plasma–polymer interaction very complex. In extreme cases of polymer oxidation, polymer burning occurs [11]. The interior of the polymer is subjected to thermal degradation, causing the formation of molecular fragments, which migrate towards the polymer surface, where they mix with oxygen and burn [11]. When using plasma afterglows for surface functionalization of polymers, the polymer is kept at room temperature. Therefore, only prolonged treatment with oxygen radicals can cause etching and degradation. In our case, the polymer was placed in the intense glowing region; therefore, it was heated above its melting temperature in a short time. Furthermore, experiments were performed in nitrogen plasma with a low base pressure; therefore, the contribution of oxidizing species to polymer degradation is negligible in our case. For this reason, we can assume that thermal degradation is the most important mechanism in our conditions. For all polymers probed in this study, the final degradation product after prolonged plasma treatment was black carbon residues, although some visual differences were observed during the plasma treatment. ABS polymer immediately carbonized. PS and PET polymers shrank into a ball, started boiling, and finally carbonized. LDPE and HDPE twisted, intensely boiled, and then carbonized. PA6 was also intensively boiling, but it neither shrank nor twisted. For PP polymer, no special visible changes were observed in terms of twisting, shrinkage, or bubble formation, and it looked as if only evaporation was occurring on the surface before the carbonization. From these observations, it seems that intensive boiling or evaporation is the most important process for providing appropriate volatile low-mass species, which served as building blocks of nanocarbon on the titanium substrate.

To further check whether just high temperature causing thermal degradation is sufficient for CNW synthesis or whether plasma is needed at all, we performed an additional experiment in the same vacuum system without igniting the plasma. An additional heater was used to heat the polymer and the Ti substrate; however, CNWs did not form. In yet another modification of this experiment, the Ti substrate was placed in the glowing plasma, whereas the polymer was placed far away from plasma and heated by an additional heater. In these conditions, CNWs were formed on the Ti-substrate, thus proving that plasma has an important role in the growth of CNWs on the substrate or in the modification of polymer-degradation products reaching the plasma. However, for polymer degradation itself, the plasma is not essential for the deposition of nanocarbon on the titanium surface; therefore, a simple thermal degradation can also be applied.

Polymers may have different weight-loss rates during their thermal degradation [13]. Furthermore, different degradation products may also be formed. As found in the literature review, the most important thermal and photodegradation products of the polymers used in our study are summarized in Table 2 [14–19]. We can notice that in the case of aromatic polymers, degradation products contain aromatic rings (e.g., styrene monomer), whereas in the case of aliphatic polymers, various low-molecular unsaturated and saturated aliphatic compounds are formed. As already mentioned before, despite some similarities of aromatic rings to graphite structure, it is apparent that aromatic rings are not important building blocks in the formation of CNWs. It is much more likely that low-molecular aliphatic compounds that can be further dissociated in plasma are the most important building blocks. This is also in agreement with the classical PECVD techniques that apply CH_4, C_2H_2, or even ethanol and hexane vapor or fluorinated compounds CF_4, CHF_3, and C_2F_6 for the deposition of CNWs [20–22]. Currently, it is supposed that C_2 dimers are the most important building units for CNWs growth [23]. From C_2 dimers, higher mass-carbon clusters $C_nH_x^+$ may be formed, initiating the growth process [23,24].

In fact, we have found only one publication, published by Lehman et al. [24], where authors used aromatic precursor p-xylene for the synthesis of CNWs. They also used ICP-RF plasma but with a very low discharge power of just 150 W. Very low power was responsible for breaking the C–H bond in the methyl group attached to the aromatic ring, leaving the aromatic ring (which exhibits higher stability) rather intact. The growth of CNWs was explained by the condensation of p-xylyl radicals and the formation of polycyclic aromatic 2,6-dimethylanthracene. In another publication by Hsu et al. [25], the authors also reported the synthesis of CNWs using a low-power plasma (60 W) and 1,2-dichlorobenzene as the precursor; however, methane was also introduced into the plasma to enhance the growth process. Since methane is a commonly used precursor, it is questionable if 1,2-dichlorobenzene was needed for the successful deposition of CNWs at all. In RGA spectra, the authors found substantial amounts of C_2 together with smaller amounts of C_6 and C_6H_6.

The formation of C_2 was also monitored in our experiment using OES. The evolution of C_2 species during the plasma treatment of various polymers is shown in Figure 5. No correlation was found between the intensity of C_2 species and the morphology of the deposits. Nevertheless, the final growth of nanostructures obviously depends on many factors: supply of appropriate building units, their consumption by the growth process, the time scale needed for transport and reorganization, etc. These processes do not depend just on the type of precursor used but also on the surface temperature, which in turn depends on the discharge power [26]. Building units are not produced only as a consequence of the thermal decomposition of polymers, but they can also be produced in plasma as well as within the sheath, where fluxes of ions may be important, especially at the initial stages of the formation of nucleation sites [26].

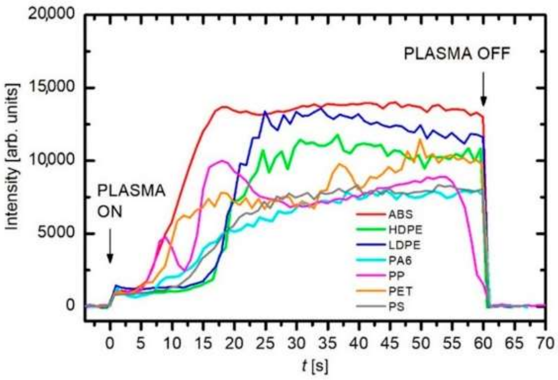

Figure 5. Variation of the OES intensity of C_2 species formed during burning of different polymer materials in nitrogen plasma.

Table 2. Thermal and photooxidative degradation products. Information for melting and deposition temperature was obtained from [16].

Polymer	Melting T	Decomposition T	Thermal Degradation Products	Refs.
PS	503 K	549 K	monomer styrene (40%), dimer, trimer, tetramer, pentamer, benzene, ethylbenzene, α-methylstyrene; in the presence of oxygen: phenol, ketones, benzoic acid, benzyl alcohol, benzaldehyde	[14–16]
PE	378–408 K	650 K	propene (up to 25%), propane, ethene, ethane, butene, hexene (formation of the transition state six-membered ring)	[14–16]
PP	443 K	624 K	pentane (24%), 2-methyl-1-pentene, 2,4-dimethyl-1-heptene, propane	[14–16]
PET	523–533 K	698 K	cleavage of ester groups and formation of carboxylic acids and vinyl esters (benzoic acid (43%), acetaldehyde (16%), CO_2, vinyl esters of benzoic acid), anhydride containing oligomers, cyclic oligomers; also scission through a six-membered ring transition state; formation of non-volative residues of interconnected aromatic rings was also reported.	[15–18]
PA6	498–508 K	708 K	cyclic oligomers, caprolactam (73%), CO_2	[19]
ABS	383–398 K	693 K	degradation to its constituents, depending on temperature: butadiene, sytrene, ethylbenzene, N-containing products	[27,28]

Here we should also note that the different morphology of the deposited carbon nanostructures when using aromatic or aliphatic polymer precursors is not the only outcome of this study. We have also noticed significant variations in the thickness of the deposited layers. In Figure 6a–g cross-sections of the deposits and their thicknesses are shown. In general, we can observe that, when using aromatic polymers (Figure 6e–g), the layers are thicker than for aliphatic polymers (Figure 6a,c,d). It was reported that etching and removal of amorphous carbon from the deposit was an important step in the formation of CNWs [29]. In addition, hydrogen was found to play a significant role in the growth of CNWs [30–32]. A generally accepted mechanism of CNW growth includes: (i) adsorption of CH_x radicals and formation of an amorphous layer, (ii) formation of defects acting as nucleation sites, and (iii) migration and nucleation of carbon species leading to the growth of graphene sheets [29,33]. Therefore, etching is essential for helping the formation of appropriate nucleation sites and removal of small randomly oriented structures, including amorphous fractions, thus enabling the growth of relatively large vertical graphene sheets. Moreover, etching also prevents the formation of additional graphene layers by the removal of weakly bonded carbon atoms, and it enhances the migration of carbon precursors [33]. All these facts can explain the formation of thicker layers when using aromatic polymers. It seems that there was no simultaneous etching of amorphous parts during the growth to allow the migration, nucleation, and formation of highly ordered structures. Furthermore, simple low-weight polymer degradation products in the case of aliphatic compounds probably have a higher ability for migration and appropriate orientation during CNW growth than larger aromatic fractions.

3.3. *Influence of the Processing Gas*

As mentioned in the previous subsection, the presence of oxidative species and radiation may influence the thermal degradation mechanisms of polymers. However, it was also reported that the addition of hydrogen, argon, and even oxygen in classical PECVD techniques using a CH_4 precursor could greatly improve the quality of CNWs [7]. The quality of carbon nanowalls is often attributed to the quantity of inadequately bonded carbon. The best quality is attributed to graphene sheets free from the amorphous hydrogenated carbon phase. The amorphous phase will deposit, especially at elevated pressures, but will be effectively removed by weak bombardment with positive ions and chemical interaction with reactive neutral species such as H and/or O atoms. Some authors also performed the synthesis of CNWs in nitrogen or ammonia plasma to allow for the doping of CNWs with nitrogen atoms and thus affecting their electronic properties [8]. This was also one of the reasons for choosing polymers such as PA6 and ABS in this investigation, because they contain nitrogen. We wanted to check if this can help obtain CNWs with more N-doped atoms. Table 3 shows the surface composition of the deposits as revealed from XPS survey spectra acquired on samples whose SEM images are shown in Figure 4. We have to stress again that the deposits were formed using nitrogen plasma. The measured concentration of nitrogen for all polymers is rather small. The highest amounts were found when using PS, PET, and PA6 with no significant difference between them. For ABS polymer, the nitrogen content was at the detection limit of XPS. Therefore, using N-containing polymer as a carbon as well as a nitrogen precursor does not allow a higher content of nitrogen to be obtained within the surface film as probed by XPS.

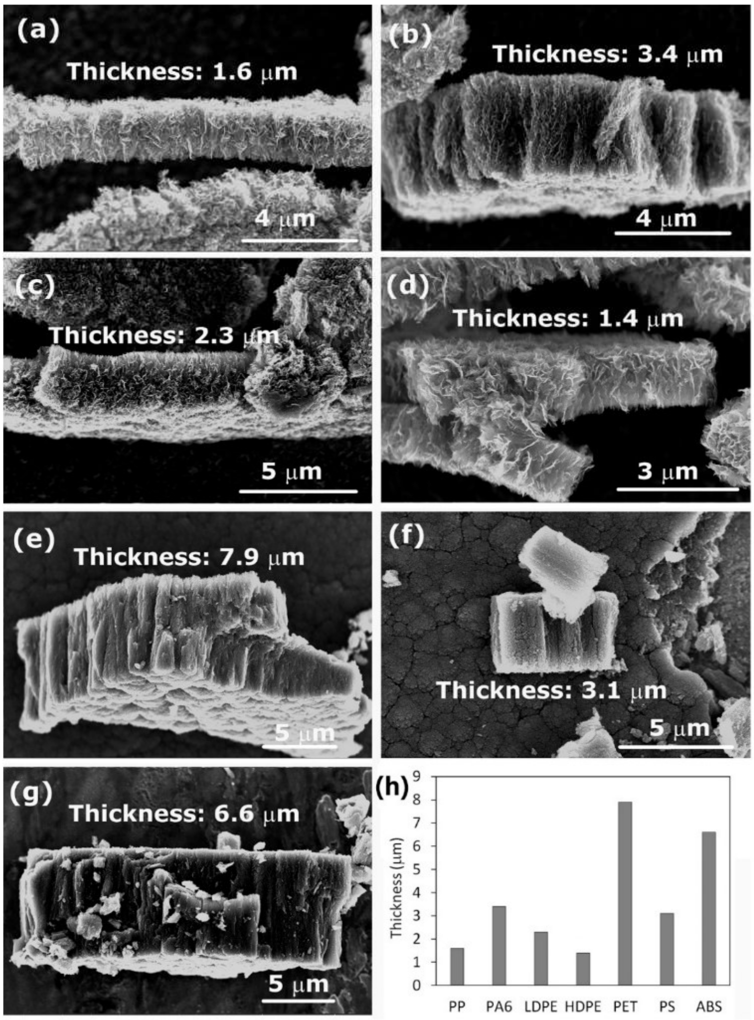

Figure 6. Cross-section of the deposited carbon nanostructures: (**a**) PP, (**b**) PA6, (**c**) LDPE, (**d**) HDPE, (**e**) PET, (**f**) PS, (**g**) ABS, and (**h**) a thickness of the deposited layer. Deposition time was 60 s.

Table 3. XPS surface composition of the deposits synthesized in nitrogen plasma using various polymer sources.

Polymer	Gas	C (atom. %)	N (atom. %)	O (atom. %)	N/C
PS	N_2	93.8	3.7	2.6	0.04
PET	N_2	94.4	2.6	3.0	0.03
ABS	N_2	98.0	0.7	1.3	0.03
PA6	N_2	94.4	2.8	2.8	0.003
LDPE	N_2	98.6	0.3	1.1	0.02
HDPE	N_2	95.6	1.7	2.8	0.01
PP	N_2	96.7	1.0	2.3	0.01

The influence of the processing gas on the growth and morphology of CNWs was studied using different gases instead of nitrogen to reveal the role of the presence of oxygen, hydrogen, or other species in the plasma. CNWs were synthesized from PP and PS polymers using plasmas created in H_2, O_2, N_2, and CO_2 gases. Figure 7a–h shows SEM images of the deposits (left column) and their cross-sections (right column) for the case of aliphatic PP polymer, whereas Table 4 shows the surface compositions as deduced from XPS survey spectra. An important conclusion from Figure 7 is that no matter what gas we use, the CNWs are always synthesized on the surface when using this aliphatic polymer as the solid precursor. This is another indication that, in our case, oxidative degradation of a polymer is not the most important mechanism that leads to the growth of CNWs, at least for this type of polymer. The CNWs only differ in the size of the graphene flakes. Furthermore, their chemical composition (Table 4) is similar—according to experimental error, the oxygen concentration is practically the same, regardless of the type of processing gas used.

Table 4. XPS surface composition of the deposits synthesized from PP polymer using various gaseous discharges.

Polymer	Gas	C (atom. %)	N (atom. %)	O (atom. %)
PP	N_2	96.7	1.0	2.3
PP	O_2	97.5		2.5
PP	H_2	98.3		1.7
PP	CO_2	98.5		1.5

In order to check if this is true also for aromatic polymers, we show in Figure 8a–h SEM images of CNWs synthesized from PS polymer using different gases. Opposite to aliphatic polymer used in Figure 7, we can now observe the best formation of CNWs in the case of O_2 plasma. It is known that O_2 plasma treatment of aromatic polymers causes destruction and opening of the aromatic rings and thus a loss of aromatic structure [34,35], which can explain why we can only get CNWs in the case of O_2 plasma treatment.

The method for synthesizing carbon nanowalls presented in this paper enables deposition rates as large as a few 100 nm/s. This is much larger compared to the classical technique using gaseous precursors. The deposition rates reported by various authors were presented in the review paper [7]. The achievable deposition rates were between about 0.1 and 100 nm/s, but most authors reported values between 1 and 10 nm/s. The highest deposition rate (300 nm/s), which deviates greatly from other reported data, was obtained by Zhang et al. [36], who used a mixture of argon, hydrogen, and methane at the pressure of 800 Pa, a discharge power of 18 kW, using a combination of inductively and capacitively coupled discharges. All other authors reported values below about 10 nm/s.

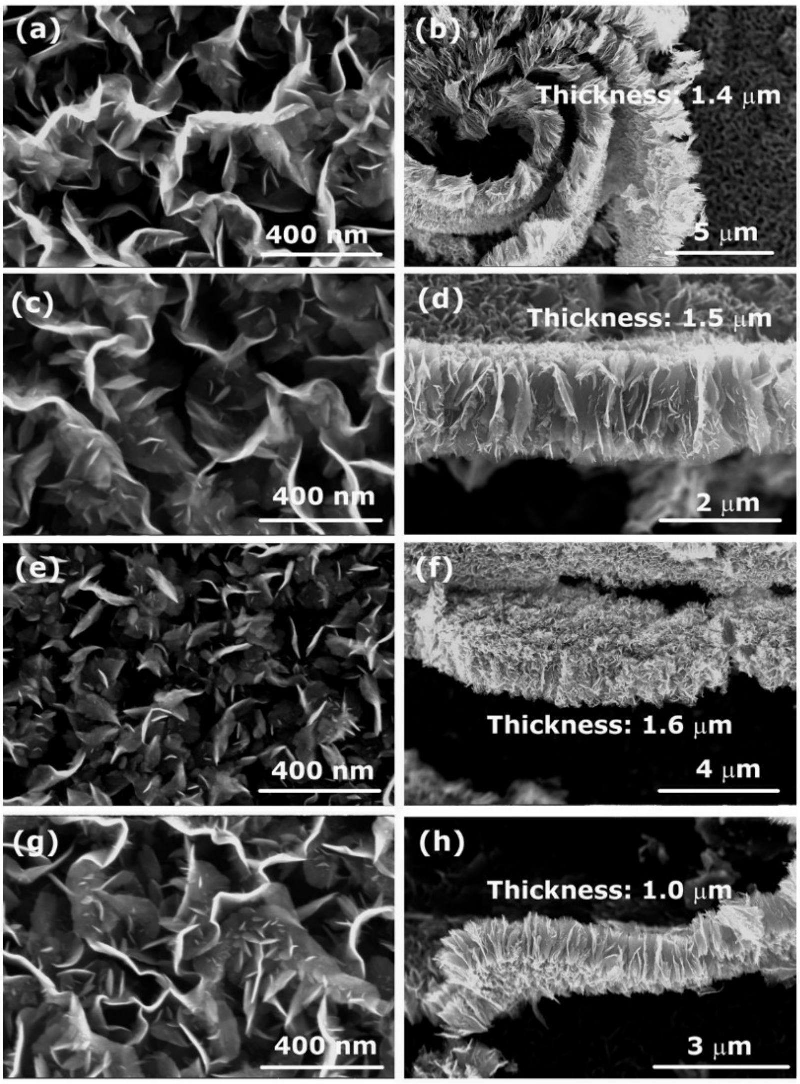

Figure 7. SEM images of CNWs (left) and their cross-section (right) synthesized from the aliphatic PP polymer in plasma created in: (**a**,**b**) O_2, (**c**,**d**) H_2, (**e**,**f**) N_2, and (**g**,**h**) CO_2 gas. Deposition time was 60 s.

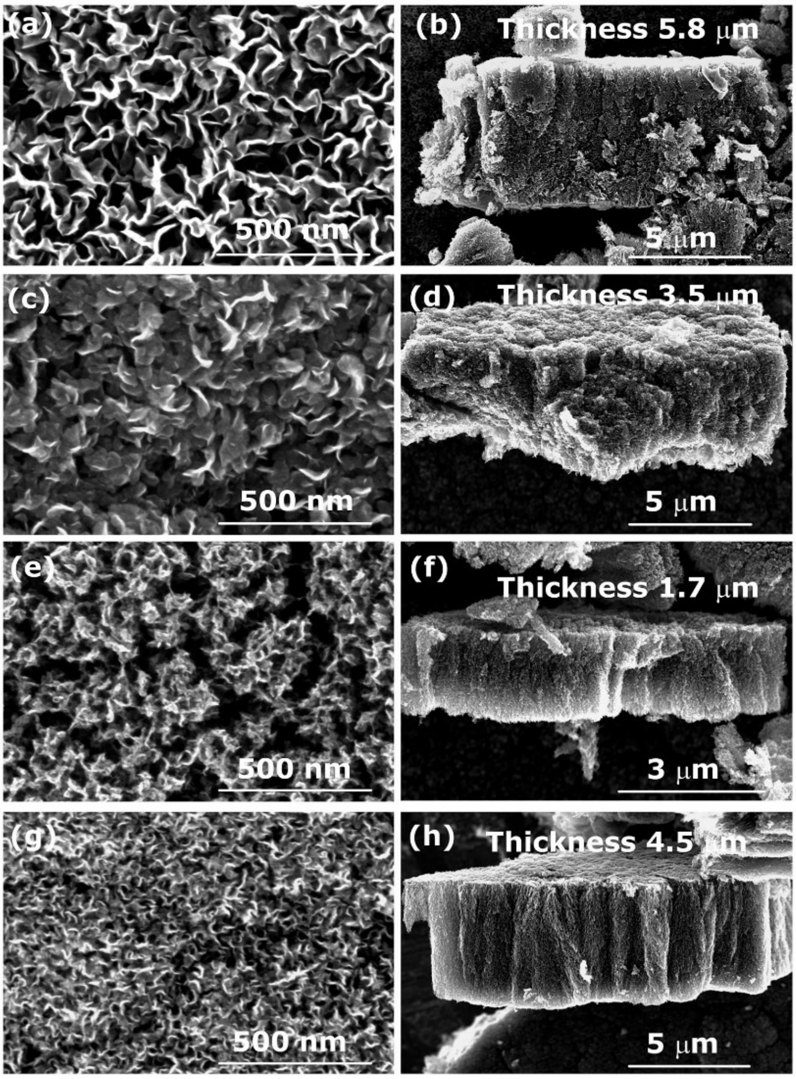

Figure 8. SEM images of carbon nanostructures (left) and their cross-section (right) synthesized from the aromatic PS polymer in plasma created in: (**a**,**b**) O_2, (**c**,**d**) H_2, (**e**,**f**) N_2, and (**g**,**h**) CO_2 gas. Deposition time was 60 s.

4. Conclusions

CNW growth in low-pressure plasma sustained by an inductively coupled RF discharge at the power of about 500 W was investigated using various polymers as solid precursors as well as various gases. The substrates were titanium mounted inside the RF coil and left at the floating potential. Important findings were derived from these investigations. We found that aromatic precursors were unsuitable for CNW growth, indicating that aromatic rings are not the most useful building blocks for CNWs. Aliphatic precursors which thermally degrade to simple low-weight C_xH_y species were found more relevant for CNW growth. These two findings are in agreement with the generally accepted theory that C_2 dimers are the most important building blocks involved in the formation of CNWs. In the presence of appropriate building blocks, CNWs will grow in plasma regardless of the gas type used for creating the discharge. The results indicate that the procedure elaborated in this paper may be applicable to mass production, as the optimal growth rate of a film consisting of good quality CNWs is over 100 nm/s.

Author Contributions: Conceptualization, R.Z. and D.P.; methodology, R.Z.; validation, R.Z., D.P., G.P. and A.V.; formal analysis, G.P., investigation, R.Z. and A.V.; data curation, R.Z., G.P., and A.V.; writing—original draft preparation, A.V.; writing—review and editing, M.M.; visualization, R.Z.; supervision, M.M.; project administration, A.V.; funding acquisition, A.V. All authors have read and agreed to the published version of the manuscript.

Funding: This research was funded by the Slovenian Research Agency—project No. L2-1834 (Carbon nanowalls for future supercapacitors), core fund P2-0082 (Thin-film structures and plasma surface engineering). The research was also supported by a bilateral project to co-fund international bilateral scientific cooperation with the USA (Project No. BI-US/18-20-023, Advanced catalysts based on multilayered vertically oriented graphene nanostructures).

Institutional Review Board Statement: Not applicable.

Informed Consent Statement: Not applicable.

Data Availability Statement: The data presented in this study are available on request from the corresponding author.

Conflicts of Interest: The authors declare no conflict of interest. The funders had no role in the design of the study; in the collection, analyses, or interpretation of data; in the writing of the manuscript; or in the decision to publish the results.

References

1. Li, J.H.; Zhu, M.J.; An, Z.L.; Wang, Z.Q.; Toda, M.; Ono, T. Constructing in-chip micro-supercapacitors of 3d graphene nanowall/ruthenium oxides electrode through silicon-based microfabrication technique. *J. Power Sources* **2018**, *401*, 204–212. [CrossRef]
2. Liu, L.L.; Guan, T.; Fang, L.; Wu, F.; Lu, Y.; Luo, H.J.; Song, X.F.; Zhou, M.; Hu, B.S.; Wei, D.P.; et al. Self-supported 3d nico-ldh/gr composite nanosheets array electrode for high-performance supercapacitor. *J. Alloys Compd.* **2018**, *763*, 926–934. [CrossRef]
3. Shin, S.C.; Yoshimura, A.; Matsuo, T.; Mori, M.; Tanimura, M.; Ishihara, A.; Ota, K.; Tachibana, M. Carbon nanowalls as platinum support for fuel cells. *J. Appl. Phys.* **2011**, *110*, 104308. [CrossRef]
4. Krivchenko, V.A.; Itkis, D.M.; Evlashin, S.A.; Semenenko, D.A.; Goodilin, E.A.; Rakhimov, A.T.; Stepanov, A.S.; Suetin, N.V.; Pilevsky, A.A.; Voronin, P.V. Carbon nanowalls decorated with silicon for lithium-ion batteries. *Carbon* **2012**, *50*, 1438–1442. [CrossRef]
5. Takeuchi, W.; Kondo, H.; Obayashi, T.; Hiramatsu, M.; Hori, M. Electron field emission enhancement of carbon nanowalls by plasma surface nitridation. *Appl. Phys. Lett.* **2011**, *98*, 123107. [CrossRef]
6. Wei, W.; Hu, Y.H. Highly conductive na-embedded carbon nanowalls for hole-transport-material-free perovskite solar cells without metal electrodes. *J. Mater. Chem. A* **2017**, *5*, 24126–24130. [CrossRef]
7. Vesel, A.; Zaplotnik, R.; Primc, G.; Mozetič, M. Synthesis of vertically oriented graphene sheets or carbon nanowalls—Review and challenges. *Materials* **2019**, *12*, 2968. [CrossRef]
8. Vesel, A.; Zaplotnik, R.; Primc, G.; Mozetič, M. A review of strategies for the synthesis of n-doped graphene-like materials. *Nanomaterials* **2020**, *10*, 2286. [CrossRef]
9. Vesel, A.; Zaplotnik, R.; Primc, G.; Pirker, L.; Mozetič, M. One-step plasma synthesis of nitrogen-doped carbon nanomesh. *Nanomaterials* **2021**, *11*, 837. [CrossRef]
10. Arnold, C., Jr. Stability of high-temperature polymers. *J. Polym. Sci. Macromol. Rev.* **1979**, *14*, 265–378. [CrossRef]
11. Vohlídal, J. Polymer degradation: A short review. *Chem. Teach. Int.* **2021**, *3*, 213–220. [CrossRef]
12. Dorai, R.; Kushner, M.J. A model for plasma modification of polypropylene using atmospheric pressure discharges. *J. Phys. D Appl. Phys.* **2003**, *36*, 666–685. [CrossRef]
13. Zhang, M.; Buekens, A.; Jiang, X.; Li, X. Dioxins and polyvinylchloride in combustion and fires. *Waste Manag. Res.* **2015**, *33*, 630–643. [CrossRef]
14. Peterson, J.D.; Vyazovkin, S.; Wight, C.A. Kinetics of the thermal and thermo-oxidative degradation of polystyrene, polyethylene and poly(propylene). *Macromol. Chem. Phys.* **2001**, *202*, 775–784. [CrossRef]
15. Gewert, B.; Plassmann, M.M.; MacLeod, M. Pathways for degradation of plastic polymers floating in the marine environment. *Environ. Sci. Process. Impacts.* **2015**, *17*, 1513–1521. [CrossRef]

16. Witkowski, A.; Stec, A.A.; Hull, T.R. Thermal decomposition of polymeric materials. In *Sfpe Handbook of Fire Protection Engineering*; Hurley, M.J., Gottuk, D., Hall, J.R., Harada, K., Kuligowski, E., Puchovsky, M., Torero, J., Watts, J.M., Wieczorek, C., Eds.; Springer: New York, NY, USA, 2016; pp. 167–254.
17. Samperi, F.; Puglisi, C.; Alicata, R.; Montaudo, G. Thermal degradation of poly(ethylene terephthalate) at the processing temperature. *Polym. Degrad. Stab.* **2004**, *83*, 3–10. [CrossRef]
18. Holland, B.J.; Hay, J.N. The thermal degradation of pet and analogous polyesters measured by thermal analysis–fourier transform infrared spectroscopy. *Polymer* **2002**, *43*, 1835–1847. [CrossRef]
19. Davis, R.D.; Gilman, J.W.; VanderHart, D.L. Processing degradation of polyamide 6/montmorillonite clay nanocomposites and clay organic modifier. *Polym. Degrad. Stab.* **2003**, *79*, 111–121. [CrossRef]
20. Teii, K.; Shimada, S.; Nakashima, M.; Chuang, A.T.H. Synthesis and electrical characterization of n-type carbon nanowalls. *J. Appl. Phys.* **2009**, *106*, 084303. [CrossRef]
21. Yu, K.H.; Wang, P.X.; Lu, G.H.; Chen, K.H.; Bo, Z.; Chen, J.H. Patterning vertically oriented graphene sheets for nanodevice applications. *J. Phys. Chem. Lett.* **2011**, *2*, 537–542. [CrossRef]
22. Meško, M.; Vretenár, V.; Kotrusz, P.; Hulman, M.; Šoltýs, J.; Skákalová, V. Carbon nanowalls synthesis by means of atmospheric dcpecvd method. *Phys. Status Solidi B* **2012**, *249*, 2625–2628. [CrossRef]
23. Teii, K.; Hori, M.; Goto, T. Negative bias dependence of sulfur and fluorine incorporation in diamond films etched by an sf_6 plasma. *J. Electrochem. Soc.* **2001**, *148*, G55. [CrossRef]
24. Lehmann, K.; Yurchenko, O.; Urban, G. Effect of the aromatic precursor flow rate on the morphology and properties of carbon nanostructures in plasma enhanced chemical vapor deposition. *RSC Adv.* **2016**, *6*, 32779–32788. [CrossRef]
25. Hsu, C.-C.; Bagley, J.D.; Teague, M.L.; Tseng, W.-S.; Yang, K.L.; Zhang, Y.; Li, Y.; Li, Y.; Tour, J.M.; Yeh, N.C. High-yield single-step catalytic growth of graphene nanostripes by plasma enhanced chemical vapor deposition. *Carbon* **2018**, *129*, 527–536. [CrossRef]
26. Ostrikov, K.; Neyts, E.C.; Meyyappan, M. Plasma nanoscience: From nano-solids in plasmas to nano-plasmas in solids. *Adv. Phys.* **2013**, *62*, 113–224. [CrossRef]
27. Suzuki, M.; Wilkie, C.A. The thermal degradation of acrylonitrile-butadiene-styrene terpolymei as studied by tga/ftir. *Polym. Degrad. Stab.* **1995**, *47*, 217–221. [CrossRef]
28. Lee, K.-H.; Shin, D.-H.; Seo, Y.-H. Thermal degradation of nitrogen-containing polymers, acrylonitrile-butadiene-styrene and styrene-acrylonitrile. *Korean J. Chem. Eng.* **2006**, *23*, 224–229. [CrossRef]
29. Hiramatsu, M.; Kondo, H.; Hori, M. Graphene nanowalls. In *New Progress on Graphene Research*; Gong, J.R., Ed.; IntechOpen: London, UK, 2013.
30. Cui, L.; Chen, J.; Yang, B.; Sun, D.; Jiao, T. Rf-pecvd synthesis of carbon nanowalls and their field emission properties. *Appl. Surf. Sci.* **2015**, *357*, 1–7. [CrossRef]
31. Jiang, L.; Yang, T.; Liu, F.; Dong, J.; Yao, Z.; Shen, C.; Deng, S.; Xu, N.; Liu, Y.; Gao, H.-J. Controlled synthesis of large-scale, uniform, vertically standing graphene for high-performance field emitters. *Adv. Mater.* **2013**, *25*, 250–255. [CrossRef] [PubMed]
32. Wang, J.; Zhu, M.; Outlaw, R.A.; Zhao, X.; Manos, D.M.; Holloway, B.C. Synthesis of carbon nanosheets by inductively coupled radio-frequency plasma enhanced chemical vapor deposition. *Carbon* **2004**, *42*, 2867–2872. [CrossRef]
33. Hiramatsu, M.; Hori, M. *Carbon Nanowalls: Synthesis and Emerging Applications*; Springer: Wien, Austria, 2010.
34. Gonzalez, E.; Barankin, M.D.; Guschl, P.C.; Hicks, R.F. Ring opening of aromatic polymers by remote atmospheric-pressure plasma. *IEEE Trans. Plasma Sci.* **2009**, *37*, 823–831. [CrossRef]
35. Liang, Y.; Li, J.; Xue, Y.; Tan, T.; Jiang, Z.; He, Y.; Shangguan, W.; Yang, J.; Pan, Y. Benzene decomposition by non-thermal plasma: A detailed mechanism study by synchrotron radiation photoionization mass spectrometry and theoretical calculations. *J. Hazard. Mater.* **2021**, *420*, 126584. [CrossRef] [PubMed]
36. Zhang, H.; Wu, S.; Lu, Z.; Chen, X.; Chen, Q.; Gao, P.; Yu, T.; Peng, Z.; Ye, J. Efficient and controllable growth of vertically oriented graphene nanosheets by mesoplasma chemical vapor deposition. *Carbon* **2019**, *147*, 341–347. [CrossRef]

3.2 Recombination Coefficient of Carbon Nanomaterials Deposited on a Cobalt Sample

As mentioned before, many different authors have tackled the synthesis of carbon nanomaterials, with chemical vapor deposition proving to be the most common method, further improved in the form of plasma-enhanced chemical vapor deposition. Guidelines based on the results of previous authors in the field of carbon nanomaterial synthesis can be summarized as follows: a continuous supply of carbon is required, be it a carbon-based gas, or a solid material containing large amounts of carbon, as long as carbon-based gas can be evaporated from the solid. Hydrogen gas must be present, and the ratio between carbon and hydrogen affects the growth of carbon nanomaterials. Other gases may be added to the carbon and hydrogen mixture and can also affect the growth process. Crucially, the temperature of the substrate affects the synthesis, with materials, such as CNW only growing at elevated temperatures (800 K and above) [109].

Taking the above guidelines into consideration, a method similar to the one previously mentioned in this chapter is used. The most notable difference is the use of propane gas as a source of carbon atoms, without any polymers added to the system. This results in the synthesis of CNW, as well as other carbon nanomaterials, on different substrates. Our focus is cobalt substrates, which proved to be the most interesting and easiest to handle. One problem with synthesized nanoparticles is their brittle nature, which makes handling the samples tricky. This is especially true for nickel substrates, and to a lesser extent stainless steel, titanium, and cobalt. Therefore, cobalt substrates were used. The synthesis process was adjusted to let us grow carbon nanomaterials on the tip (made of cobalt) of a catalytic probe (Figure 13). Propane was introduced into the system from a high-pressure container. This experimental setup allowed us to monitor the temperature of the substrate, use the probe in oxygen plasma, and finally calculate the recombination coefficient of the different carbon nanomaterials in reference to oxidized cobalt [95].

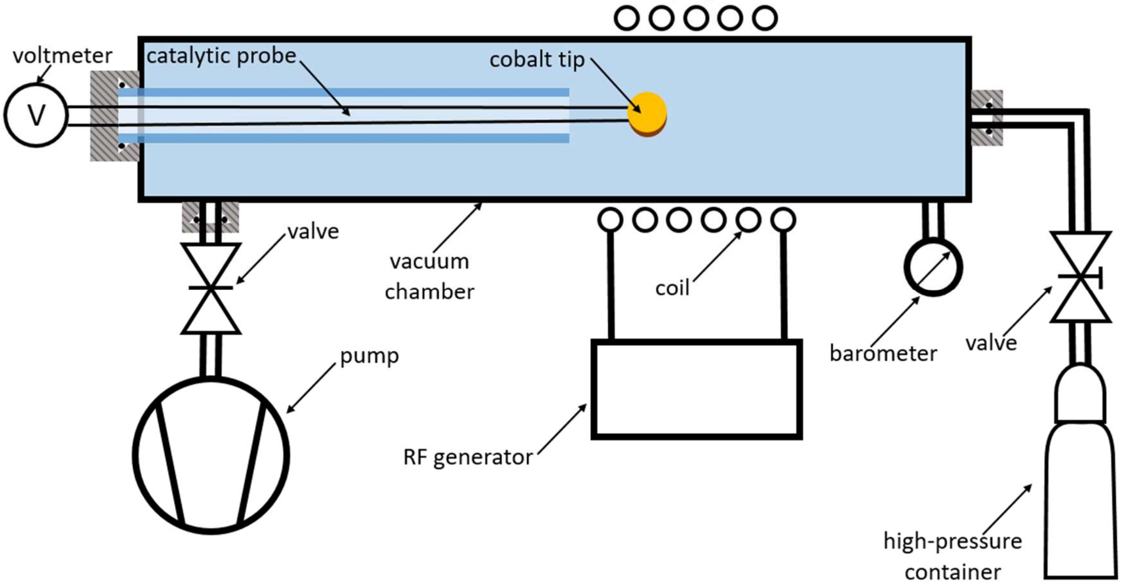

Figure 13: A simple schematic of the experimental setup used for the synthesis of carbon nanomaterials on the cobalt tip of a catalytic probe.

Before the synthesis of carbon nanomaterials, the catalytic probe with an oxidized cobalt tip was used to measure the neutral oxygen atom density in the RF plasma system. Afterward, the probe tip was placed inside the glow region of plasma (inside the coil, as in Figure 13), and exposed to propane plasma. The temperature of the probe was monitored during the deposition process (Figure 14). Compared to a discharge in oxygen (Figure 7), we observe an interesting behavior of the probe tip. At first, the probe heats up to a certain equilibrium temperature (region 1 in Figure 14) but shortly after, it heats up again to a second equilibrium temperature (region 2 in Figure 14). After reaching this second, higher equilibrium temperature, the probe tip cools to a slightly lower temperature more in line with the first equilibrium temperature (region 3 in Figure 14). Once the discharge is turned off, the probe tip cools to room temperature. This would suggest that at first, the probe tip is heated by processes, such as recombination and ion bombardment, followed by a brief period where another process heats the probe tip. It is safe to assume that this process is related to the creation of the first layer of carbon nanomaterials at the cobalt oxide and carbon deposit interface.

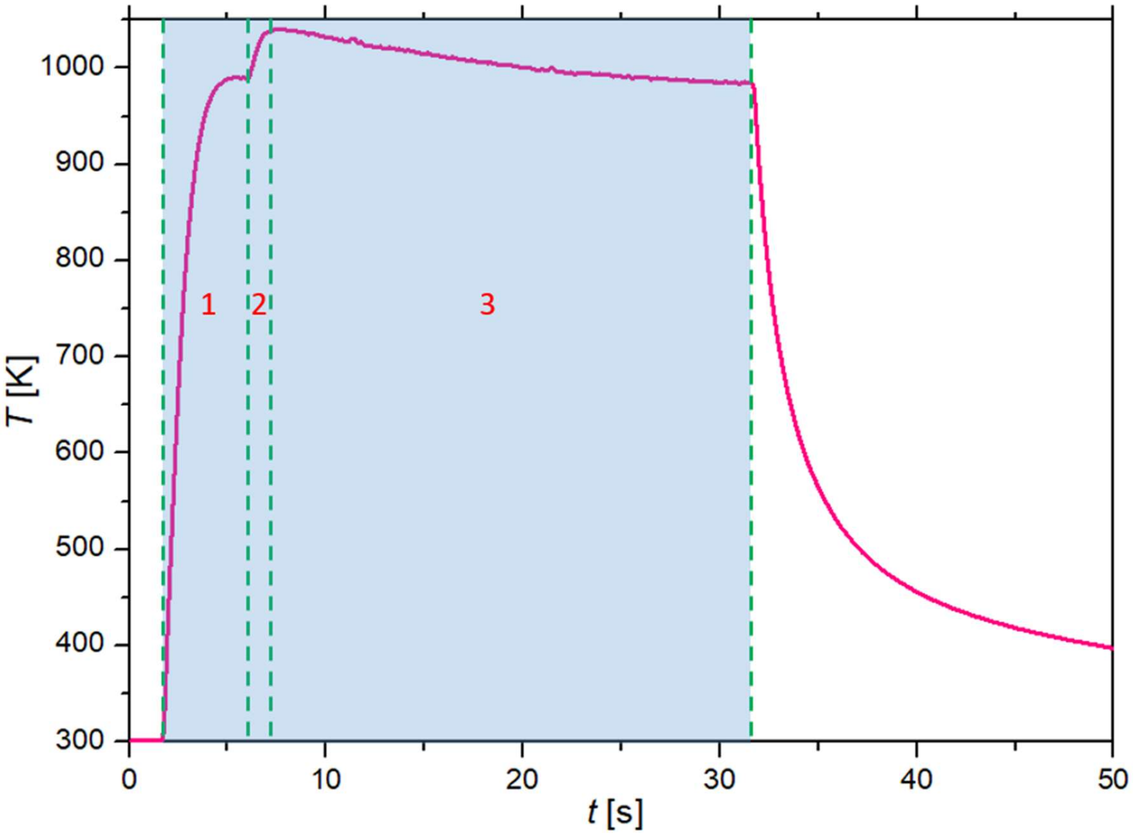

Figure 14: The temperature (T) of the cobalt tip of the catalytic probe versus time (t) during a typical 30-second deposition (blue section) of carbon nanomaterials using propane gas as a carbon atom source.

The different deposition times (30, 60, 120, and 300 s) resulted in different thicknesses of the carbon nanomaterial layer (Table 1) and different surface morphologies (Figure 15). After the successful synthesis of carbon nanomaterials at varying deposition times, the probe was used again to measure the neutral atom densities for the same conditions (5 different flows and 5 different powers of the generator, resulting in 25 different conditions). Table 1 clearly demonstrates the correlation between the average deposition time and the thickness of the carbon nanomaterial layer, with thicker layers being the result of longer deposition times.

Table 1: The average thickness of carbon nanomaterial layers ($\bar{d}$) for four different times of deposition (t_d), with a statistical error of ±10%.

t_d $[s]$	30	60	120	300
$\bar{d}$ [µm]	1.7	2.5	7.2	14.6

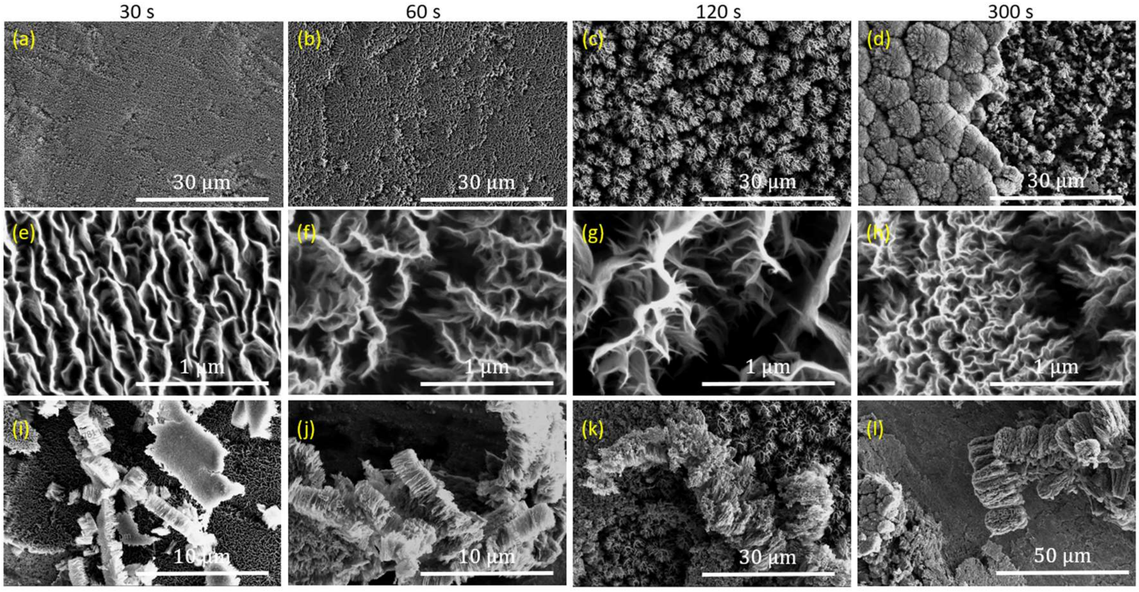

Figure 15: SEM images of the surface of the cobalt sample where carbon nanomaterials were grown. The first row shows a larger part of the surface, the second row is a close-up of finer details, and the third row shows the thickness of the carbon nanomaterial layer. Pictures were taken for deposition times of 30 s (first column: a, e, and i), 60 s (second column: b, f, and j), 120 s (third column: c, g, and k), and 300 s (last column: d, h, and l).

Comparing the results with those done with the catalytic probe with a “clean” oxidized cobalt tip allowed us to calculate the recombination coefficient of the deposited carbon nanomaterials at five different pressures: 42 (Figure 16), 79 (Figure 17), 117 (Figure 18), 156 (Figure 19), and 214 Pa (Figure 20). As with our previous findings in Chapter 2, the recombination coefficient increases with the temperature of the sample. It can also be observed that at higher pressures, the recombination coefficient is generally smaller, again in line with our previous findings in Chapter 2. It is evident that increasing the thickness of the carbon nanomaterial layer increases the recombination coefficient – the thickest layer of the carbon nanomaterial layer has the highest recombination coefficient. Since the layer of carbon nanomaterials has a large surface-to-mass ratio (as seen in Figure 15), thicker layers lead to an increased surface roughness, which leads to a larger effective surface area, which increases the recombination coefficient. This confirms one of our hypotheses. Additionally, the value of the recombination coefficient of the thickest layer of carbon nanomaterials is more than twice the value of the recombination coefficient of “clean” oxidized cobalt, hinting at the great potential of using carbon nanomaterials in calorimetry.

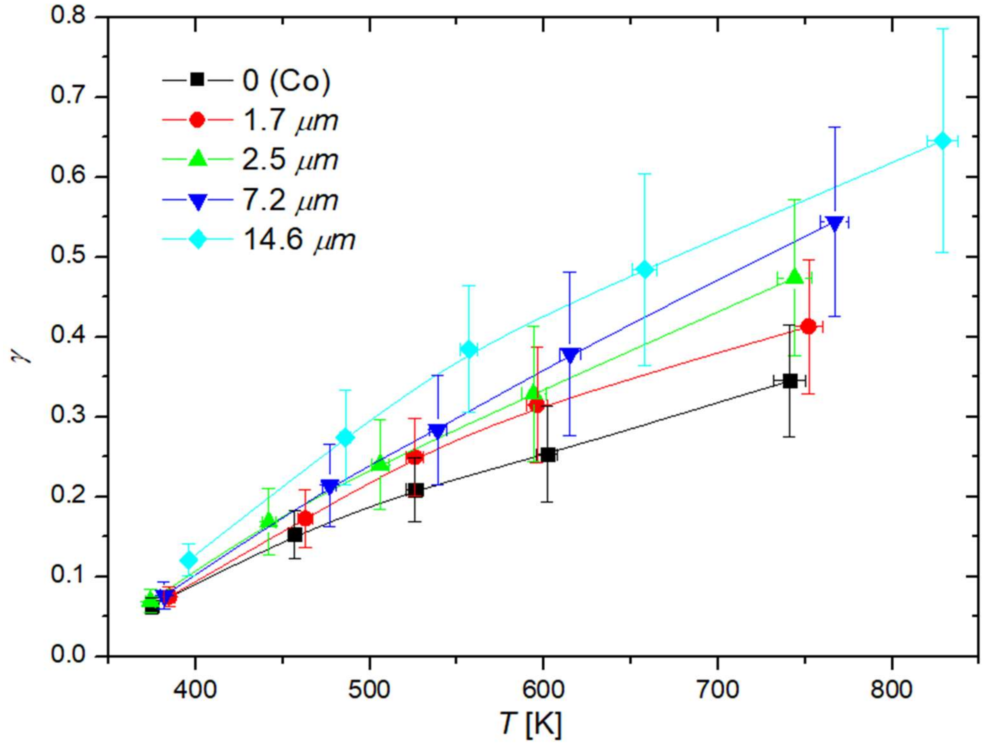

Figure 16: Recombination coefficient (γ) of oxidized cobalt with different thicknesses of the deposited carbon nanomaterial layer versus temperature (T) of the oxidized cobalt sample at 42 Pa.

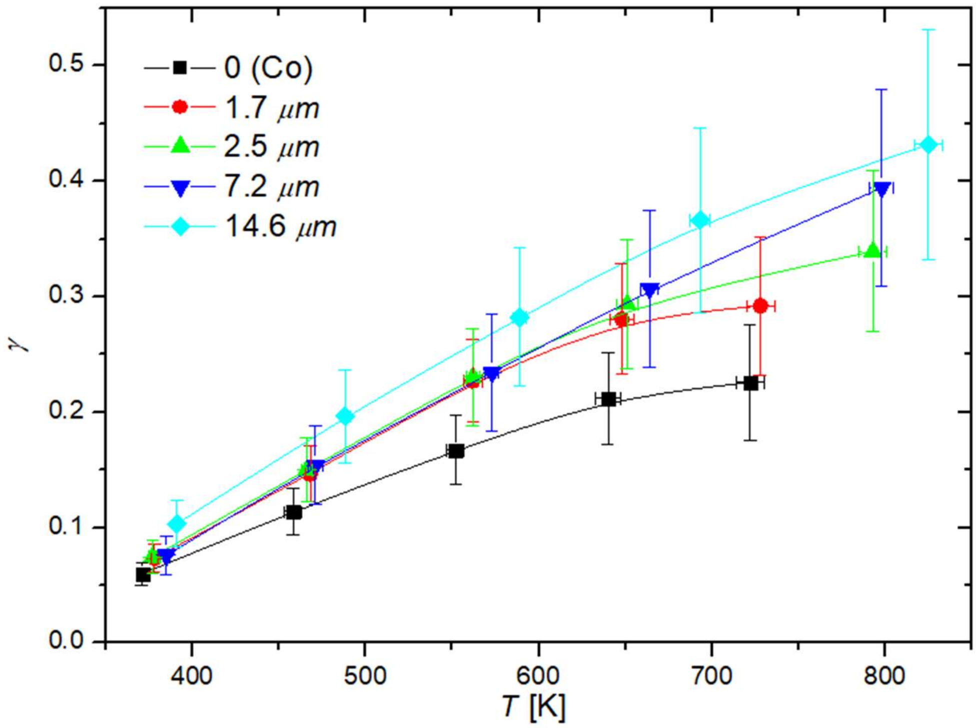

Figure 17: Recombination coefficient (γ) of oxidized cobalt with different thicknesses of the deposited carbon nanomaterial layer versus temperature (T) of the oxidized cobalt sample at 79 Pa.

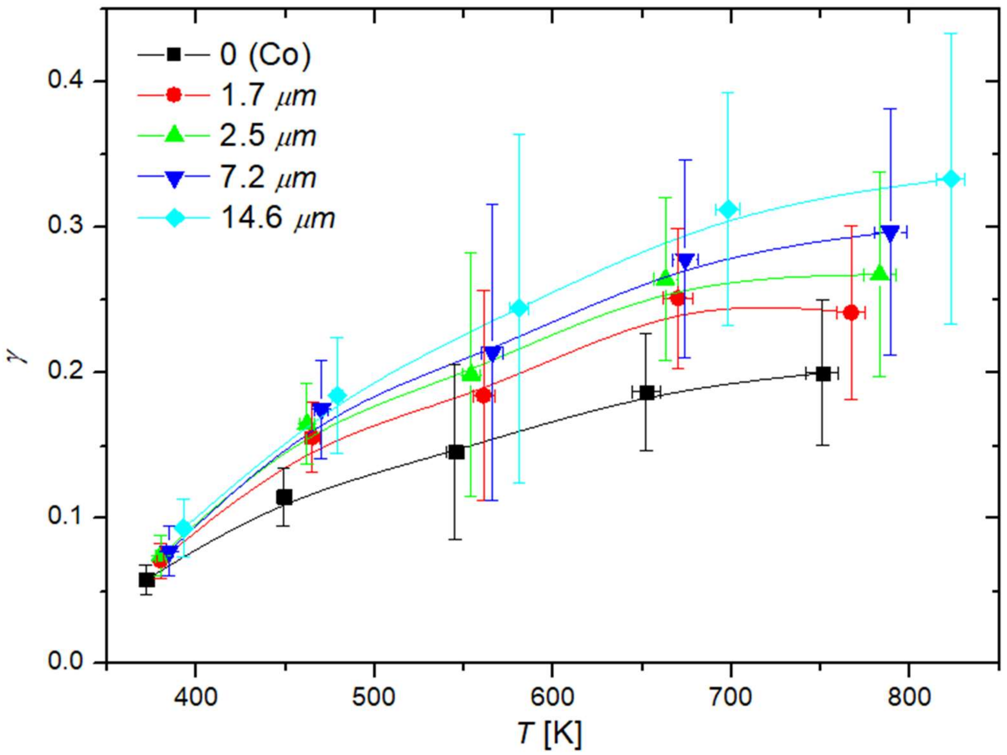

Figure 18: Recombination coefficient (γ) of oxidized cobalt with different thicknesses of the deposited carbon nanomaterial layer versus temperature (T) of the oxidized cobalt sample at 117 Pa.

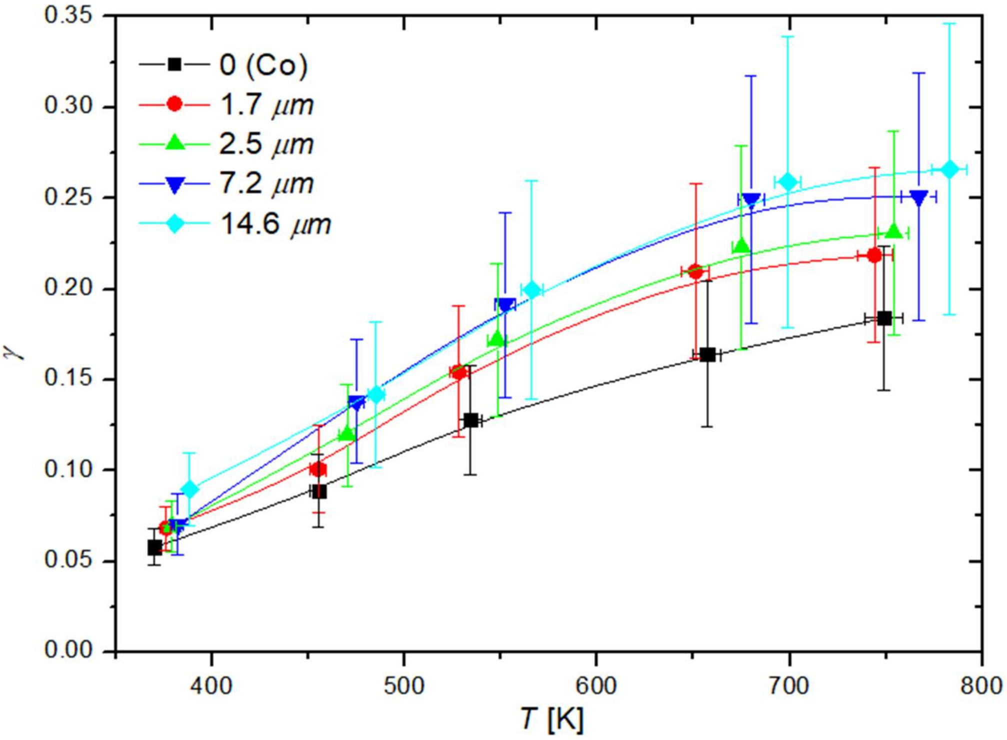

Figure 19: Recombination coefficient (γ) of oxidized cobalt with different thicknesses of the deposited carbon nanomaterial layer versus temperature (T) of the oxidized cobalt sample at 156 Pa.

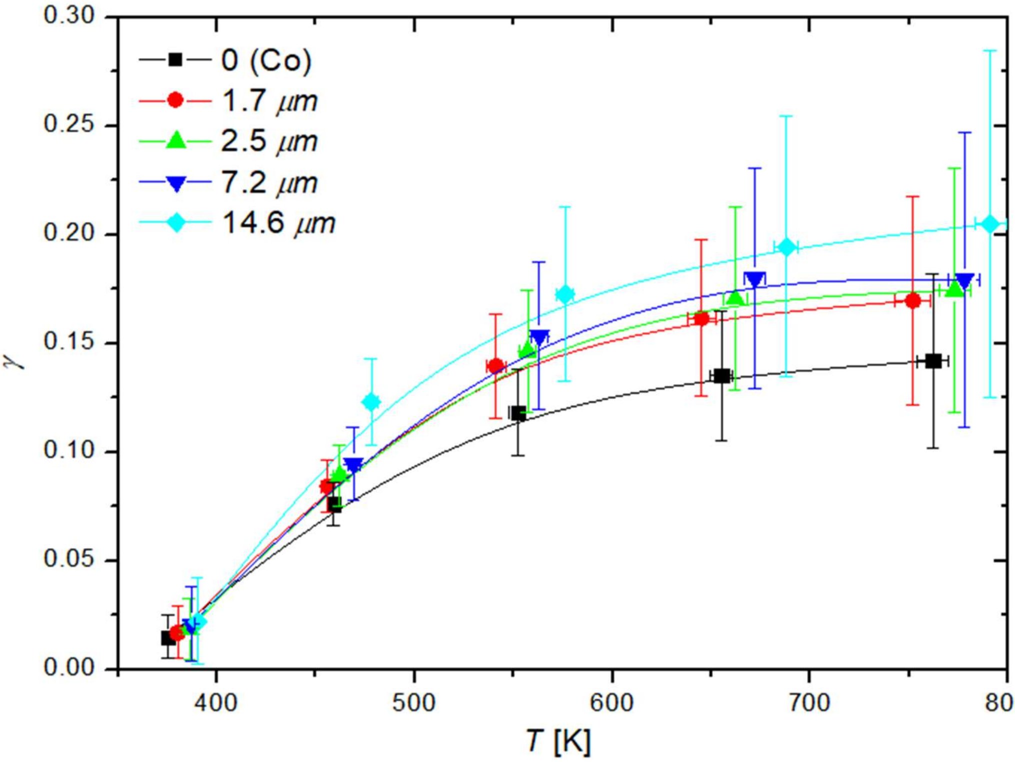

Figure 20: Recombination coefficient (γ) of oxidized cobalt with different thicknesses of the deposited carbon nanomaterial layer versus temperature (T) of the oxidized cobalt sample at 214 Pa.

Chapter 4

Conclusions

Heterogeneous surface recombination of neutral oxygen atoms was examined during the course of this dissertation. We started with a description of plasma, which can be utilized as a reliable source of neutral oxygen atoms. We pointed out two possible mechanisms for the heterogeneous surface recombination of neutral atoms: the Eley-Rideal and Langmuir-Hinshelwood mechanisms [14]. We pointed out the possible parameters that could affect the recombination coefficient: temperature of the surface, morphology of the surface, and pressure in the vicinity.

For the determination of neutral atom density, we chose calorimetry. Specifically, we described working with a catalytic probe and how one can also use it to determine the recombination coefficient of a given material. We examined RF discharges and the transition between E and H modes. We also studied the decrease of neutral atoms when moving away from the atom source (the discharge or glow area of plasma).

We also reviewed the literature about the recombination coefficients of different materials for oxygen atoms [56]. We wanted to find correlations between the recombination coefficient and different parameters, with an emphasis on surface temperature and pressure in the experimental system. We found that most authors agree that the recombination coefficient of a material increases with increasing material temperature but much less agreement was found when concerning pressure in the experimental system where only a few authors pointed to possibly some sort of inverse proportionality between the recombination coefficient and pressure. We also examined whether the type of discharge affected the recombination coefficient, with no discernable correlations. We did discover some discrepancies in the recombination coefficient when using different measurement methods. For example, actinometry gave slightly higher recombination coefficients, which was explained by the fact that opposed to other methods: actinometry can only be done in the glow region of the plasma where ions create new binding sites for neutral atoms,+ and thus the seemingly increased recombination coefficient was measured.

We established five hypotheses: the validity of the Šorli-Ročak method, the variable nature of the recombination coefficient, the increase in the recombination coefficient with increasing temperature, the decrease of the recombination coefficient with increasing pressure, and the increase of the recombination coefficient with surface roughness. All the hypotheses were tested.

We proceeded with a description of the Šorli-Ročak method, which we used to determine the absolute neutral oxygen atom density in a low-pressure microwave plasma system [20]. Three different materials were used as recombinators: nickel, cobalt, and iron, and they all yielded the same result, thereby confirming the first hypothesis. Replacing the recombinators with a catalytic probe with an oxidized nickel tip allowed us to determine the recombination coefficient of oxidized nickel, which was not constant, confirming the second hypothesis. We found that the recombination coefficient increased with increasing temperature of the probe tip and decreased with increasing pressure in the experimental system. This confirmed the third and fourth hypotheses. The relation between the recombination coefficient of oxidized nickel and the temperature and pressure was described with an empirical formula, which was partly based on the Arrhenius plot, commonly used by other authors when describing the temperature dependence of the recombination coefficient.

In an expansion of this study, we also determined the recombination coefficient of oxidized cobalt [95]. We obtained very similar results, with one caveat: the recombination coefficient of oxidized cobalt seemed to stop increasing and instead stabilize at elevated temperatures. This was in excellent agreement with studies done by previous authors and another confirmation of the second, third, and fourth hypotheses.

Later on, we performed systematic measurements of neutral oxygen atom densities inside metallic tubes made of nickel, cobalt, and copper. These measurements allowed us to calculate the dissociation fraction along the length of the metallic tubes, which in turn provided us with the penetration depth of oxygen atoms for each material. We confirmed that all three materials were effective recombinators, reaffirming the first hypothesis.

In the third chapter, an emphasis was placed on carbon nanomaterials which are interesting due to their high surface-to-mass ratio. We used plasma-enhanced chemical vapor deposition to synthesize different carbon nanomaterials, including carbon nanowalls [111]. The source of carbon atoms varied, with the use of different polymers yielding different carbon nanomaterials. Different techniques were used to examine the carbon nanomaterials, with secondary electron microscopy proving very useful when studying the surface morphology of carbon nanomaterials.

The method for the synthesis of carbon nanomaterials was later altered to allow us to grow carbon nanomaterials on the tip of a catalytic probe while monitoring the temperature of the probe tip. Four different deposition times were used to get carbon nanowall-like deposits on an oxidized cobalt surface, with the thickness of the carbon nanomaterial layer increasing with increasing deposition time. After the deposition of the carbon nanomaterials on the probe tip, the catalytic probe was used to determine the recombination coefficient of oxygen atoms on the carbon nanomaterials of varying thickness. We discovered that the thicker nanomaterials exhibited a higher recombination coefficient due to their higher surface-to-mass ratio, confirming the last hypothesis.

We successfully confirmed each of the five hypotheses and demonstrated the variability of the recombination coefficient for nickel, cobalt, and carbon nanomaterials. This outlines the importance of choosing the right material for contact with the plasma, especially when concerning different temperatures of the material, the pressure in the vicinity of the material, and the surface morphology of said material. This dissertation will hopefully guide authors to perform similar studies for different materials, and a more systematic determination of the recombination coefficient, especially concerning the aforementioned parameters.

References

[1] J. A. Bittencourt, Fundamentals of plasma physics, New York: Springer Verlag, 2004.

[2] A. A. Fridman and L. A. Kennedy, Plasma physics and engineering, Milton Park, Abingdon-on-Thames: Taylor & Francis Routledge, 2004.

[3] A. Annušova, D. Marinov, J.-P. Booth, N. Sirse, M. L. da Silva, B. Lopez and V. Guerra, "Kinetics of highly vibrationally excited O2(X) molecules in inductively-coupled oxygen plasmas," *Plasma Sources Sci. Technol.,* vol. 27, 2018.

[4] O. Baranov, K. Bazaka, H. Kersten, M. Keidar, U. Cvelbar, S. Xu and I. Levchenko, "Plasma under control: Advanced solutions and perspectives for plasma flux management in material treatment and nanosynthesis," *Appl. Phys. Rev.,* vol. 4, 2017.

[5] J.-P. Booth and N. Sadeghi, "Oxygen and fluorine atom kinetics in electron cyclotron resonance plasma by time-resolved actinometry," *J. Appl. Phys.,* vol. 70, 1991.

[6] V. Guerra, T. Silva, P. Ogloblina, M. Grofulović, L. Terraz, M. L. da Silva, C. D. Pintassilgo, L. L. Alves and O. Guaitella, "The case for in-situ resource utilization for oxygen production on Mars by non-equilibrium plasmas," *Plasma Sources Sci. Technol.,* vol. 26, 2017.

[7] H. Kersten, H. Deutsch, H. Steffen, G. M. W. Kroesen and R. Hippler, "The energy balance at substrate surfaces during plasma processing," *Vacuum,* vol. 63, 2001.

[8] K. Kutasi, L. Bencs, Z. Tóth and S. Milošević, "The role of metals in the deposition of long-lived reactive oxygen and nitrogen species into the plasma-activated liquids," *Plasma Process Polym.,* vol. 20, 2023.

[9] A. Vesel, M. Kolar, N. Recek, K. Kutasi, K. Stana-Kleinschek and M. Mozetič, "Etching of Blood Proteins in the Early and Late Flowing Afterglow of Oxygen Plasma," *PlasmaProcess.Polym.,* vol. 11, 2014.

[10] H. D. Babcock, "Internuclear distance in oxygen molecules," *Proc. N. A. S.,* vol. 23, 1937.

[11] J. S. Kim, J. H. Reibenspies and M. Y. Darensbourg, "Characteristics of Nickel(0), Nickel(I), and Nickel(II) in Phosphino Thioether Complexes: Molecular Structure and S-Dealkylation of (Ph2P(o-C6 H 4)SCH 3) 2Ni0," *J. Am. Chem. Soc.,* vol. 118, 1996.

[12] K. Tichmann, U. von Toussaint and W. Jacob, "Determination of the sticking coefficient of energetic hydrocarbon molecules by molecular dynamics," *J. Nucl. Mater.,* vol. 420, 2012.

[13] B. d. B. Darwent, Bond dissociation energies in simple molecules, Washington: U.S. National Bureau of Standards, 1970.

[14] R. Zaplotnik, G. Primc, D. Paul, M. Mozetič, J. Kovač and A. Vesel, "Atomic species generation by plasmas," in *Plasma applications for material modification: from microelectronics to biological materials*, Singapore, Jenny Stanford Publishing, 2021, pp. 107-177.

[15] P. Vašina, V. Kudrle, A. Talsky, P. Botoš, M. Mrazkova and M. Meško, "Simultaneous measurement of N and O densities in plasma afterglow by means of NO titration," *Plasma Sources Sci. Technol.,* vol. 13, 2004.

[16] F. Brencelj and et al., Vakuumska znanost in tehnika, Ljubljana: Društvo za vakuumsko tehniko Slovenije, 2003.

[17] B. J. Wood and H. Wise, "Kinetics of hydrogen atom recombination on surfaces," *JPC,* vol. 65, 1961.

[18] S. Markelj and I. Čadež, "Production of vibrationally excited hydrogen molecules by atom recombination on Cu and W materials," *J. Chem. Phys.,* vol. 134, 2011.

[19] G. Primc, D. Lojen, A. Vesel, M. Mozetič and R. Zaplotnik, "Oxygen atom density in a large reactor powered by four inductively coupled plasma sources," *Vacuum,* vol. 199, 2022.

[20] D. Paul, M. Mozetič, R. Zaplotnik, J. Ekar, A. Vesel, G. Primc and D. Đonlagič, "Recombination of oxygen atoms on the surface of oxidized polycrystalline nickel - temperature and pressure dependences," *Plasma Sources Sci. Technol.,* vol. 32, 2023.

[21] M. Cacciatore and M. Rutigliano, "Dynamics of plasma-surface processes: E-R and L-H atom recombination reactions," *Plasma Sources Sci. Technol.,* vol. 18, 2009.

[22] J. Wintterlin, S. Völkening, T. V. W. Janssens, T. Zambelli and G. Ertl, "Atomic and macroscopic reaction rates of a surface-catalyzed reaction," *Science,* vol. 278, 1997.

[23] M. Cacciatore, M. Rutigliano and G. D. Billing, "Eley-Rideal and Langmuir-Hinshelwood recombination coefficients for oxygen on silica surfaces," *J. Thermophys. Heat Trans.,* vol. 13, 1999.

[24] S. Ali, "Electron-ion recombination data for plasma applications," Thesis, Department of physics, Stockholm University, Stockholm, 2012.

[25] G. G. Dolgov-Saval'ev, B. A. Knyazev, Y. L. Koz'minykh and V. V. Kuznetsov, "An investigation of electron-ion recombination in inert gases," *Soviet Physics JETP,* vol. 30, 1970.

[26] M. A. Biondi and S. C. Brown, "Measurement of electron-ion recombination," *Physical Review,* vol. 76, 1949.

[27] H. Shirai and K. Tabei, "Measurement of electronic recombination coefficient in a helium plasma jet," *Phys. Rev. A,* vol. 7, 1973.

[28] J. C. Greaves and J. W. Linnett, "The recombination of oxygen atoms at surfaces," *Trans. Faraday Soc.,* vol. 54, 1958.

[29] S. Wickramanayaka, S. Meikle, T. Kobayashi, N. Hosokawa and Y. Hatanaka, "Measurements of catalytic efficiency of surfaces for the removal of atomic oxygen using NO2* continuum," *J. Vac. Sci. Technol. A,* vol. 9, 1991.

[30] M. Mozetič, "Application of extremely non-equilibrium plasmas in the processing of nano and biomedical materials," *Plasma Sources Sci. and Technol.,* vol. 24, 2015.

[31] G. Primc, R. Zaplotnik, A. Vesel and M. Mozetič, "Plasma characterization using catalytic probes," IJS, Ljubljana, 2019.

[32] A. Drenik, "The probability of heterogeneous recombination of hydrogen and oxygen atoms on the surfaces of fusion-relevant materials," Jožef Stefan International Postgraduate School, 2009.

[33] R. Zaplotnik, A. Vesel and M. Mozetič, "Atomic oxygen and hydrogen loss coefficient on functionalized polyethylene terephthalate, polystyrene, and polytetrafluoroethylene polymers," *Plasma Process Polym.,* vol. 15, 2018.

[34] B. Halpern and D. E. Rosner, "Chemical energy accomodation at catalyst surfaces," *J. Chem. Soc., Faraday Trans. 1,* vol. 74, 1978.

[35] F. Nasuti, M. Barbato and C. Bruno, "Material-dependent catalytic recombination modeling for hypersonic flows," *Journal of Thermophysics and Heat Transfer,* vol. 10, 1996.

[36] A. Drenik, A. Vesel, A. Kreter and M. Mozetič, "Recombination of hydrogen atoms on fine-grain graphite," *Applied Surface Science,* vol. 257, 2011.

[37] J. Tyczkowski, "Cold plasma produced catalytic materials," in *Plasma Science and Technology - Progress in physical states and chemical reactions*, London, InTech, 2016.

[38] M. Mozetič, U. Cvelbar, A. Vesel, A. Ricard and D. Babič, "A diagnostic method for real-time measurements of the density of nitrogen atoms in the post glow of an Ar-N2 discharge using a catalytic probe," *J. Appl. Phys.,* vol. 97, 2005.

[39] G. Primc, M. Mozetič, U. Cvelbar and A. Vesel, "Method and device for detection and measuring the density of neutral atoms of hydrogen, oxygen or nitrogen". Slovenia Patent WO 2015/176733, 26 11 2015.

[40] G. Primc, A. Vesel, G. Dolanc, D. Vrančić and M. Mozetič, "Recombination of oxygen atoms along a glass tube loaded with a copper sample," *Vacuum,* vol. 138, 2017.

[41] C. Xiong, Y. Wang, L. Lin, M. Gao, Y. Huang and P. K. Chu, "Deposition of nanocomposites coating on polyimide films by atmospheric pressure plasma for enhanced thermal conductivity," *Surfaces and Interfaces,* vol. 37, 2023.

[42] M. Mozetič, G. Primc, A. Vesel, R. Zaplotnik, M. Modic, I. Junkar, N. Recek, M. Klanjšek-Gunde, L. Guhy, M. K. Sunkara, M. C. Assensio, S. Milošević, M. Lehocky, V. Sedlarik, M. Gorjanc, K. Kutasi and K. Stana-Kleinschek, "Application of extremely non-equilibrium plasmas in the processing of nano and biomedical materials," *Plasma Sources Sci. Technol.,* vol. 24, 2015.

[43] A. Rajeshkannan, M. Ali, R. Prakash, R. Prasad, A. K. Jeevanantham and K. Jayaram, "Optimizing the process parameters in plasma arc cutting using taguchi approach for the case industry in Fiji," *Materials Today: Proceedings,* vol. 24, 2020.

[44] Z. Li, L. Li, G. Zhang, L. Song, Z. Tu and C. Han, "AZO work function enhanced by oxygen plasma immersion ion implantation," *Vacuum,* vol. 212, 2023.

[45] A. Brovko, O. Amzallag, A. Adelberg, L. Chernyak, P. V. Raja and A. Ruzin, "Effects of oxygen plasma treatment on Cd1-xZnxTe material and devices," *Nucl. Instrum. Methods Phys. Res. Sect. Accel. Spectrometers Detect. Assoc. Equip.,* vol. 1004, 2021.

[46] R. Donate, M. E. Aleman-Dominguez and M. Monzon, "On the Effectiveness of Oxygen Plasma and Alkali Surface Treatments to Modify the Properties of Polylactic Acid Scaffolds," *Polymers,* vol. 13, 2021.

[47] N. Recek, M. Mozetič, M. Jaganjac, L. Milkovič, N. Žarkovič and A. Vesel, "Improved proliferation of human osteosarcoma cells on oxygen plasma treated polystyrene," *Vacuum,* vol. 98, 2013.

[48] D. Lojen, R. Zaplotnik, G. Primc, M. Mozetič and A. Vesel, "Optimization of surface wettability of polytetrafluoroethylene (PTFE) by precise dosing of oxygen atoms," *Applied Surface Science,* vol. 598, 2022.

[49] M. Oliveira, P. Fernandez-Gomez, A. Alvarez-Ordonez, M. Prieto and M. Lopez, "Plasma-activated water: A cutting-edge technology driving innovation in the food industry," *Food Research International,* vol. 156, 2022.

[50] M. R. Boscariol, A. J. Moreira, R. D. Mansano, I. S. Kikuchi and T. J. Pinto, "Sterilization by pure oxygen plasma and by oxygen-hydrogen peroxide plasma: An efiicacy study," *Int. J. Pharm.,* vol. 353, 2008.

[51] R. R. Elfa, N. Nayan, M. K. Ahmad, K. M. Wibowo, C. F. Soon, M. Z. Sahdan, M. H. Mamat, M. Y. Ahmad and A. Aldalbahi, "Atmospheric pressure plasma needle jet treated on aluminium thin film for semiconductor industries," *Materials Today: Proceedings,* vol. 7, 2019.

[52] W. A. Saoud, A. A. Assadi, A. Kane, A.-V. Jung, P. Le Cann, A. Gerard, F. Bazantay, A. Bouzaza and D. Wolbert, "Integrated process for the removal of indoor VOCs from food industry manufacturing: Elimination of Butane-2,3-dione and Heptan-2-one by cold plasma-photocatalysis combination," *Journal of Photochemistry & Photobiology A. Chemistry,* vol. 386, 2020.

[53] F. C. Rufino, A. M. Pascon, L. C. J. Espindola, F. H. Cioldin, D. R. G. Larrude and J. A. Diniz, "Definition of CVD Graphene Micro Ribbons with Lithography and Oxygen Plasma Ashing," *Carbon Trends,* vol. 4, 2021.

[54] A. Belkind, S. Zarrabian and F. Engle, "Plasma cleaning of metals: Lubricant oil removal," *Metal Finishing,* vol. 94, 1996.

[55] K. Kutasi, R. Zaplotnik, G. Primc and M. Mozetič, "Controlling the oxygen species density distributions in the flowing afterglow of O2/Ar–O2 surface-wave microwave discharges," *J. Phys. D: Appl. Phys.,* vol. 47, 2014.

[56] D. Paul, M. Mozetič, R. Zaplotnik, G. Primc, D. Đonlagič and A. Vesel, "A Review of Recombination Coefficients of Neutral Oxygen Atoms for Various Materials," *Materials,* vol. 16, 2023.

[57] A. Vesel, "Heterogeneous surface recombination of neutral nitrogen atoms," *Materials and Technology,* vol. 46, 2012.

[58] I. Šorli and R. Ročak, "Determination of atomic oxygen density with a nickel catalytic probe," *Journal of Vacuum Science & Technology A,* vol. 18, 2000.

[59] G. Primc, R. Zaplotnik, A. Vesel and M. Mozetič, "Microwave discharge as a remote source of neutral oxygen atoms," *AIP Advances,* vol. 1, 2011.

[60] D. P. Lymberopoulos, V. I. Kolobov and D. J. Economou, "Fluid simulation of a pulsed-power inductively coupled argon plasma," *J. Vac. Sci. Technol. A,* vol. 16, 1998.

[61] K. Kutasi, B. Saoudi, C. D. Pintassilgo, J. Loureiro and M. Moisan, "Modelling the Low-Pressure N 2 – O 2 Plasma Afterglow to Determine the Kinetic Mechanisms Controlling the UV Emission Intensity and Its Spatial Distribution for Achieving an Efficient Sterilization Process," *Plasma Process. Polym.,* vol. 5, 2008.

[62] J. Marschall, "Laboratory determination of thermal protection system materials surface catalytic properties," RTO-EN-AVT-142, 2007.

[63] Y. C. Kim and M. Boudart, "Recombination of O, N and H atoms on Silica," *Langmuir,* vol. 7, 1991.

[64] G. Cartry, X. Duten and A. Rousseau, "Atomic oxygen surface loss probability on silica in microwave plasmas studied by a pulsed induced fluorescence technique," *Plasma Sources Sci. Technol.,* vol. 15, 2006.

[65] D. V. Lopaev, E. M. Malykhin and S. M. Zyryanow, "Surface recombination of oxygen atoms in O2 plasma at increased pressure: 1. The recombination probability and phenomenological model of surfae processes," *J. Phys. D: Appl. Phys.,* vol. 44, 2010.

[66] P. G. Dickens and M. B. Sutcliffe, "Recombination of oxygen atoms on oxide surfaces," *Trans. Faraday Soc.,* vol. 60, 1964.

[67] G. E. Melin and R. J. Madix, "Energy accommodation during oxygen atom recombination on metal surfaces," *Trans. Faraday Soc.,* vol. 67, 1971.

[68] A. L. Myerson, "Exposure-dependent surface recombination efficiencies of atomic oxygen," *J. Chem. Phys.,* vol. 50, 1969.

[69] M. Mozetič and U. Cvelbar, "Heterogeneous recombination of O atoms on metal surfaces," *Int. J. Nanosci.,* vol. 6, 2007.

[70] U. Cvelbar, M. Mozetič and A. Ricard, "Characterization of oxygen plasma with a fiber optic catalytic probe and determination of recombination coefficients," *IEEE Transactions on Plasma Science,* vol. 33, 2005.

[71] J. Ekar, P. Panjan, S. Drev and J. Kovač, "ToF-SIMS Depth Profiling of Metal, Metal Oxide, and Alloy Multilayers in Atmospheres of H2, C2H2, CO, and O2," *J. Am. Soc. Mass Spectrom.,* vol. 33, 2022.

[72] M. Mozetič, A. Vesel, J. Kovač, R. Zaplotnik, M. Modic and M. Balat-Pichelin, "Formation and reduction of thin oxide films on a stainless steel surface upon subsequent treatments with oxygen and hydrogen plasma," *Thin Solid Films,* vol. 591, 2015.

[73] J.-P. Booth, M. Mozetič, A. Nikiforov and C. Oehr, "Foundations of plasma surface functionalization of polymers for industrial and biological applications," *Plasma Sources Sci. Technol.,* vol. 31, 2022.

[74] I. Poberaj, M. Mozetič and D. Babič, "Comparison of fiber optics and standard nickel catalytic probes for determination of neutral oxygen atoms concentration," *J. Vac. Sci. Technol. A,* vol. 20, 2002.

[75] M. Balat-Pichelin, "Interactions of reactivegas flows and ceramics at high temperature - experimental methods for the measurements of species recombination during planetary entry," RTO-EN-AVT-142, 2007.

[76] M. Balat-Pichelin and E. Beche, "Atomic oxygen recombination on the ODS PM 1000 at high temperature under air plasma," *Applied Surface Science,* vol. 256, 2010.

[77] M. Balat-Pichelin, M. Pascarelli, L. Scatteia and D. Alfano, "Catalycity of zirconia nad of ZrBr2-based ultra-high temperature ceramics," in *Proceedings ot the 6th European Symposium on Aerothermodynamics for Space Vehicles*, Noordwijk, Netherlands, 2009.

[78] C. Guyon, S. Cavadias and J. Amouroux, "Heat and mass transfer phenomenon from an oxygen plasma to a semiconductor surface," *Surface and Coatings Technology,* Vols. 142-144, 2001.

[79] C. Guyon, S. Cavadias, I. Mabille, M. Moscosa-Santillan and J. Amouroux, "Recombination of oxygen atomic excited states produced by non-equilibrium RF plasma on different semiconductor materials: catalytic phenomena and modelling," *Catalysis Today,* vol. 89, 2004.

[80] P. Kolodziej and D. A. Stewart, "Nitrogen recombination on high-temperature reusable surface insulation and the analysis of its effect on surface catalysis," AIAA-87-1637, 1987.

[81] J. W. May and J. W. Linnett, "Recombination of atoms at surfaces," *Journal of Catalysis,* vol. 7, 1967.

[82] D. Pagnon, J. Amorim, J. Nahorny, M. Touzeau and M. Vialle, "On the use of actinometry to measure the dissociation in O2 DC glow discharges: determination of the wall recombination probability," *J. Phys. D: Appl. Phys.,* vol. 28, 1995.

[83] D. A. Stewart, "Determination of surface catalytic efficiency for thermal protection materials - room temperature to their upper use limit," in *31st Thermophysics Conference*, New Orelans, USA, 1996.

[84] D. A. Stewart, "Surface catalytic efficiency of advanced carbon carbon candidate thermal protection materials for SSTO vehicles," *NASA Technical Memorandum,* vol. 110383, 1996.

[85] D. A. Stewart, "Surface characterization of candidate metallic TPS for RLV," AIAA 99-3458, 1999.

[86] J.-P. Booth, O. Guaitella, A. Chatterjee, C. Drag, V. Guerra, D. Lopaev, S. Zyryanov, T. Rakhimova, D. Voloshin and Y. Mankelevich, "Oxygen (3P) atom recombination on a pyrex surface in an O2 plasma," *Plasma Sources Sci. Technol.,* vol. 28, 2019.

[87] J. T. Gudmundsson and E. G. Thorsteinsson, "Oxygen discharges diluted with argon: dissociation process," *Plasma Sources Sci. Technol.,* vol. 16, 2007.

[88] K. Arts, S. Deijkers, R. L. Puurunen, W. M. M. Kessels and H. C. M. Knoops, "Oxygen Recombination Probability Data for Plasma-Assisted Atomic Layer Deposition of SiO2 and TiO2," *J. Phys. Chem. C,* vol. 125, 2021.

[89] J. C. Greaves and J. W. Linnett, "Recombination of atoms at surfaces. Part 5. - Oxygen atoms at oxide surfaces," *Trans. Faraday. Soc.,* vol. 55, 1959.

[90] H. M. Bui, T. Kratky, I. Lee, R. Khare, M. Hiller, S. Wedig, S. Günther and O. Hinrichsen, "In situ impregnated Ni/Al2O3 catalysts prepared by binder jet 3D printing using nickel nitrate-containing ink," *Catalysis Communications,* vol. 182, 2023.

[91] M. M. Tohidi, B. Paymard, S. R. Vasquez-Garcia and D. Fernandez-Quiroz, "Recent progress in applications of cobalt catalysts in organic reactions," *Tetrahedron,* vol. 136, 2023.

[92] Y. Tang, Y. Cui, G. Ren, K. Ma, X. Ma, C. Dai and C. Song, "One-step synthesis of methanol and hydrogen from methane and water using non-thermal plasma and Cu-Modernite catalyst," *Fuel Processing Technology,* vol. 244, 2023.

[93] D. Wang, Y. Li, Y. Jiang, X. Cai and X. Yao, "Perspectives on surface chemistry of nanostructured catalysts for heterogeneous advanced oxidation processes," *Enviromental Functional Materials,* vol. 1, 2022.

[94] Y. Shi, W. Su, X. Wei, X. Song, Y. Bai, J. Wang, P. Lv and G. Yu, "Highly active MIL-68(In)-derived In2O3 hollow tubes catalysts to boost CO2 hydrogenation to methanol," *Fuel,* vol. 334, 2023.

[95] D. Paul, M. Mozetič, R. Zaplotnik, J. Ekar, A. Vesel, G. Primc and D. Đonlagič, "Loss of Oxygen Atoms on Well-Oxidized Cobalt by Heterogeneous Surface Recombination," *Materials,* vol. 16, 2023.

[96] S. Hassan, M. Suzuki, S. Mori and A. A. El-Moneim, "MnO2 /Carbon Nanowalls Composite Electrode for Supercapacitor application," *Journal of Power Sources,* vol. 249, 2013.

[97] Z. Gonzalez, S. Vizireanu, G. Dinescu, C. Blanco and R. Santamaria, "Carbon nanowalls thin films as nanostructured electrode materials in vanadium redox flow batteries," *Nano Energy,* vol. 1, 2012.

[98] N. Ozalp, H. Abedini, M. Abuseada, R. Davis, J. Rutten, J. Verschoren, C. Ophoff and D. Moens, "An overview of direct carbon fuel cells and their promising potential on coupling with solar thermochemical carbon production," *Renewable and Sustainable Energy Reviews,* vol. 162, 2022.

[99] S. Kwon, H. Choi, S. Lee, G. Lee, Y. Kim, W. Choi and H. Kang, "Room Temperature Gas Sensor Application of Carbon Nanowalls using Electrical

Resistance Change by Surface Adsorption of Toxic Gases," *Materials Research Bulletin,* vol. 141, 2021.

[100] P. Russo, M. Xiao and N. Y. Zhou, "Carbon nanowalls: A new material for resistive switching memory devices," *Carbon,* vol. 120, 2017.

[101] H.-X. Wang, N. Jiang, H. Zhang, A. Hiraki and R. Bu, "Fabrication of a three-dimensional complex carbon nanoneedle from carbon nanowalls," *Applied Surface Science,* vol. 257, 2010.

[102] C. Dai, Z. Feng, Q. Hu, J. Qiu, J. You, R. Guo, X. Iiu and H. Zhang, "Recent progress in modification and composite strategies of graphitic carbon nitride as catalysts for heterogeneous photo-Fenton reaction," *Materials Science in Semiconductor Processing,* vol. 167, 2023.

[103] W. Maiaugree, A. Tangtrakarn, S. Lowpa, N. Ratchapolthavisin and V. Amornkitbamrung, "Facile synthesis of bilayer carbon/Ni3S 2 nanowalls for a counter electrode of dye-sensitized solar cell," *Electrochimica Acta,* vol. 174, 2015.

[104] P. Slobodian, P. Riha, H. Kondo, U. Cvelbar, R. Olejnik, J. Matyas, M. Sekine and M. Hori, "Transparent elongation and compressive strain sensors based on aligned carbon nanowalls embedded in polyurethane," *Sensors and Actuators A,* vol. 306, 2020.

[105] O. Akhavan and E. Ghaderi, "Toxicity of Graphene and Graphene oxide nanowalls against bacteria," *ACS Nano,* vol. 4, no. 10, 2010.

[106] O. Akhavan, E. Ghaderi and R. Rahighi, "Toward Single-DNA Electrochemical biosensing by graphene nanowalls," *ACS Nano,* vol. 6, no. 4, 2010.

[107] E. C. Stancu, M. D. Ionita, S. Vizireanu, A. M. Stanciuc, L. Moldovan and G. Dinescu, "Wettability properties of carbon nanowalls layers deposited by a radiofrequency plasma beam discharge," *Materials Science and Engineering B,* vol. 169, 2010.

[108] Y. Wu, P. Qiao, T. Chong and Z. Shen, "Carbon nanowalls grown by microwave plasma enhanced chemical vapor deposition," *Advanced Materials,* vol. 14, no. 1, 2002.

[109] Y. Wu, B. Yang, B. Zong, H. Sun, Z. Shen and Y. Feng, "Carbon nanowalls and related materials," *J. Mater. Chem.,* vol. 14, 2004.

[110] M. Mozetič, A. Vesel, S. D. Stoica, S. Vizireanu, G. Dinescu and R. Zaplotnik, "Oxygen atom loss coefficient of carbon nanowalls," *Applied Surface Science,* vol. 333, 2015.

[111] A. Vesel, R. Zaplotnik, G. Primc, D. Paul and M. Mozetič, "Comparison of plasma deposition of carbon nanomaterials using various polymer materials as a carbon atom source," *Nanomaterials,* vol. 12, 2022.

Bibliography

Articles and Other Component Parts

4.1.1.1 1.01 Original scientific article

1. Domen Paul, Miran Mozetič, Rok Zaplotnik, Jernej Ekar, Alenka Vesel, Gregor Primc, Denis Đonlagić, "Loss of oxygen atoms on well-oxidized cobalt by heterogeneous surface recombination", *Materials*, 2023, vol. 16, iss. 17, 1-14 str., ilustr., ISSN 1996-1944, https://www.mdpi.com/1996-1944/16/17/5806, https://dirros.openscience.si/IzpisGradiva.php?id=16841, DOI: doi.org/10.3390/ma16175806. [COBISS.SI-ID 162250755], [JCR, SNIP]
2. Domen Paul, Miran Mozetič, Rok Zaplotnik, Jernej Ekar, Alenka Vesel, Gregor Primc, Denis Đonlagić, "Recombination of oxygen atoms on the surface of oxidized polycrystalline nickel—temperature and pressure dependences", *Plasma sources science & technology*, [Online ed.], 2023, vol. 32, [article no.] 075001, str. 1-13, ilustr., ISSN 1361-6595, https://iopscience.iop.org/article/10.1088/1361-6595/ace129#back-to-top-target, https://dirros.openscience.si/IzpisGradiva.php?id=16879, DOI: 10.1088/1361-6595/ace129. [COBISS.SI-ID 159683331], [JCR, SNIP, WoS up to 23. 9. 2023: no. of citations (TC): 1, without self-citations (CI): 1, without self-citations per author (CIAu): 0.14, Scopus]
3. Alenka Vesel, Rok Zaplotnik, Gregor Primc, Domen Paul, Miran Mozetič, "Comparison of plasma deposition of carbon nanomaterials using various polymer materials as a carbon atom source", *Nanomaterials*, [Online ed.], 2022, vol. 12, no. 2, str. 246-1-246-15, ISSN 2079-4991, DOI: 10.3390/nano12020246. [COBISS.SI-ID 93326595], [JCR, SNIP, WoS up to 18. 10. 2023: no. of citations (TC): 2, without self-citations (CI): 2, without self-citations per author (CIAu): 0.40, Scopus up to 1. 5. 2023: no. of citations (TC): 1, without self-citations (CI): 1, without self-citations per author (CIAu): 0.20]
4. Matej Holc, Alenka Vesel, Rok Zaplotnik, Domen Paul, Gregor Primc, Miran Mozetič, Peter Gselman, Nina Recek, "Surface modifications of wheat cultivar bologna upon treatment with non-equilibrium gaseous plasma", *Plants*, 2022, vol. 11, no. 12, str. 1552-1-1552-17, ISSN 2223-7747, DOI: 10.3390/plants11121552. [COBISS.SI-ID 111395843], [JCR, SNIP, WoS up to 15. 6. 2023: no. of citations (TC): 2, without self-citations (CI): 1, without self-citations per author (CIAu): 0.13, Scopus up to 15. 6. 2023: no. of citations (TC): 2, without self-citations (CI): 2, without self-citations per author (CIAu): 0.25]
5. Nina Recek, Alenka Vesel, Rok Zaplotnik, Domen Paul, Gregor Primc, Peter Gselman, Miran Mozetič, "Hydrophilization of corn seeds by non-equilibrium gaseous plasma", *Chemical and biological technologies in agriculture*, 2021, vol. 8, str. 32-1-32-11, ISSN 2196-5641, DOI: 10.1186/s40538-021-00231-w. [COBISS.SI-ID 68544771], [JCR,

SNIP, WoS up to 24. 3. 2023: no. of citations (TC): 3, without self-citations (CI): 1, without self-citations per author (CIAu): 0.14, Scopus up to 8. 4. 2023: no. of citations (TC): 3, without self-citations (CI): 1, without self-citations per author (CIAu): 0.14]

6. Robert Hauko, Damjan Andreevski, Domen Paul, Marko Šterk, Robert Repnik, "Teaching of the harmonic oscillator damped by a constant force: The use of analogy and experiments", *American journal of physics : a publication of American association of physics teachers*, [Print ed.], Sep. 2018, vol. 86, no. 9, str. 657-662, ilustr., ISSN 0002-9505, https://aapt.scitation.org/doi/pdf/10.1119/1.5044654, DOI: 10.1119/1.5044654. [COBISS.SI-ID 21676822], [JCR, SNIP, WoS up to 18. 5. 2023: no. of citations (TC): 13, without self-citations (CI): 11, without self-citations per author (CIAu): 2.20, Scopus up to 26. 10. 2023: no. of citations (TC): 16, without self-citations (CI): 14, without self-citations per author (CIAu): 2.80]

4.1.1.2 1.02 Review article

7. Domen Paul, Miran Mozetič, Rok Zaplotnik, Gregor Primc, Denis Đonlagić, Alenka Vesel, "A review of recombination coefficients of neutral oxygen atoms for various materials", *Materials*, Mar. 2023, vol. 16, iss. 5, [article no.] 1774, str. 1-50, ilustr., ISSN 1996-1944, https://www.mdpi.com/1996-1944/16/5/1774, https://dirros.openscience.si/IzpisGradiva.php?id=16288, DOI: 10.3390/ma16051774. [COBISS.SI-ID 142567939], [JCR, SNIP, WoS up to 24. 9. 2023: no. of citations (TC): 2, without self-citations (CI): 1, without self-citations per author (CIAu): 0.17, Scopus up to 3. 8. 2023: no. of citations (TC): 1, without self-citations per author (CIAu): 0.00]

4.1.1.3 1.12 Published scientific conference contribution abstract

8. Domen Paul, Miran Mozetič, Rok Zaplotnik, Alenka Vesel, Gregor Primc, "Neutral atom density and recombination coefficient determination in low-pressure MW plasma", In: *94th IUVSTA Workshop on reliable sensing and control of reactive plasmas : 29th May to 2nd June 2022, Kranjska Gora, Slovenia*, Gregor Primc (ed.), Ljubljana: Plasmadis, 2022, str. 30, ISBN 978-961-94716-1-6. [COBISS.SI-ID 119557891]

9. Domen Paul, Miran Mozetič, Rok Zaplotnik, Alenka Vesel, Gregor Primc, "Determining neutral atom density and recombination coefficients using catalytic tubes in low-pressure microwave-generated plasma", In: *Book of abstracts*, 28. Međunarodni znanstveni sastanak Vakumska znanost i tehnika, Njivice, Crikvenica, 18-20. Svibanj 2022 = 24. Mednarodno znanstveno srečanje Vakuumska Znanost in tehnika, Zadar, Crikvenica, 18.-20. maj 2022 = 26th International Scientific Meeting on Vacuum Science and Technology, Crikvenica, 18-20 May 2022, Maja Mičetić (ed.), Krešimir Salamon (ed.), Zagreb: Hrvatsko Vakuumsko Društvo = Croatian Vacuum Society, 2022, str. 33, ISBN 978-953-7941-42-0. [COBISS.SI-ID 108852483]

10. Blaž Burja, Domen Paul, R Gerber, Snežna Sodin-Šemrl, Matija Tomšič, Žiga Rotar, Katja Lakota, Mojca Frank Bertoncelj, et al., "Single-cell RNA sequencing reveals potent anti-inflammatory and antifibrotic activities of dimethyl-alpha-ketoglutarate on explanted skin from patients with systemic sclerosis", *eARD*, Elektronska izd., 2022, vol. 81, suppl. 1, str. 63, ISSN 1468-2060, https://ard.bmj.com/content/annrheumdis/81/Suppl_1/1689.1.full.pdf. [COBISS.SI-ID 110056451], [JCR, SNIP]

11. Alenka Vesel, Rok Zaplotnik, Gregor Primc, Domen Paul, Miran Mozetič, "Plasma deposition of carbon nanomaterials using waste polymer materials", In: *ECASIA 2022, 19th European Associated on Apllications of Surface abd Interface Analysis,*

29 May - 3 June, 2022, Limerick, Ireland, [1] str., https://az659834.vo.msecnd.net/eventsairwesteuprod/production-ulevents-public/12d702333be543cbaab0284652f331d1. [COBISS.SI-ID 117331715]

12. Nina Recek, Alenka Vesel, Rok Zaplotnik, Domen Paul, Gregor Primc, Peter Gselman, Miran Mozetič, "Hydrophilization of corn seeds by non%equilibrium gaseous plasma", In: *19th International Conference on Plasma Physics and Applications [and] 1st Workshop on Plasma Applications for Smart and Sustainable Agriculture, August 31 September 03 Magurele, Bucharest, Romani*, Silviu-Daniel Stoica (ed.), Bogdana Mitu (ed.), Gheorghe Dinescu (ed.), Bucharest: National Institute for Lasers, Plasma and Radiation Physics, 2021, str. 133, Book of abstracts, ISSN 2344-0481. [COBISS.SI-ID 76564483]

13. Domen Paul, Alenka Vesel, Rok Zaplotnik, Miran Mozetič, "Determination of the probability for recombination of neutral oxygen, nitrogen and hydrogen atoms on surfaces of carbon nanowalls", In: *27. mednarodno znanstveno srečanje Vakuumska znanost in tehnika : 9.-10. september 2021, Gozd Martuljek : program in knjiga povzetkov = 27th International Scientific Meeting on Vacuum Science and Techniques : 9-10 September 2021, Gozd Martuljek : program and book of abstracts*, Gregor Primc (ed.), Alenka Vesel (ed.), Ljubljana: Društvo za vakuumsko tehniko Slovenije: = Slovenian Society for Vacuum Technique, 2021, str. 51, ISBN 978-961-94431-2-5. [COBISS.SI-ID 76604931]

14. Domen Paul, Rok Zaplotnik, Gregor Primc, Alenka Vesel, Dane Lojen, Miran Mozetič, Aleš Hančič, "Comparison measument with different catalytic probes in RF and MV plasma", In: *8th Central European Symposium on Plasma Chemistry, 26th to 30th may 2019, Gozd Martuljek, Slovenia*, Gregor Primc (ed.), Ljubljana: Plasmadis, 2019, str. 68, ISBN 978-961-94716-0-9. [COBISS.SI-ID 32511527]

4.1.1.4 1.16 Independent scientific component part or a chapter in a monograph

15. Rok Zaplotnik, Gregor Primc, Domen Paul, Miran Mozetič, Janez Kovač, Alenka Vesel, "Atomic species generation by plasmas", In: *Plasma applications for material modification : from microelectronics to biological materials*, Francisco L. Tabarés (ed.), 1st ed., Singapore: Jenny Stanford Publishing, 2021, str. 107-177, ISBN 978-9-814-87735-0, ISBN 981-4-87735-2, DOI: 10.1201/9781003119203-4. [COBISS.SI-ID 73202947]

4.1.2 Monographs and Other Completed Works

4.1.2.1 2.09 Master's thesis

16. Domen Paul, *Resonančna rentgenska spektroskopija stolpičastih tekočekristalnih faz iz molekul z ukrivljeno sredico : magistrsko delo*, Maribor: [D. Paul], 2018, 33 f., ilustr., https://dk.um.si/IzpisGradiva.php?id=72279. [COBISS.SI-ID 24184328]

4.1.2.2 2.11 Undergraduate thesis

17. Domen Paul, *Razširjanje svetlobe po verigi nanodelcev : diplomski seminar*, Maribor: [D. Paul], 2016, 23 f., ilustr. [COBISS.SI-ID 22733320]

4.1.3 PERFORMED WORKS (EVENTS)

4.1.3.1 3.15 Unpublished conference contribution

18. Jernej Ekar, Domen Paul, *Delavnica Vakuum in plazma : Noč raziskovalk in raziskovalcev - 29. 9. 2023*, https://www.nocmoc.eu/#dogajanje. [COBISS.SI-ID 167007491]

Biography

Domen Paul was born in 1993 in Maribor where he also continued his education. In 2012, he graduated from II. Gimnazija Maribor. He got his bachelor's degree in physics in 2016 at the Faculty of Natural Sciences and Mathematics, University of Maribor. During his studies, Domen was active in various extracurricular activities, beginning with the project *Design of a Self-Sufficient Farm*, which was part of a Demola project during the 2014/2015 school year. His work encompassed the assessment and modeling of the use of electrical energy on a farm and the production of electricity with alternative, nature-friendly methods, such as wind farms and biomass. In the year 2015, Domen was also a researcher on the project called *Non-specific Back Pain – a Problem of the Workplace or Lifestyle?* The project aimed to analyze the effects of the workplace on the well-being of a human and design an ergonomic chair to alleviate back pain. In 2016, Domen was employed as a researcher at IOS (Institute for Environmental Protection and Sensors) in Maribor where he worked with optical fibers to design a sensor in a smart oven.

Following his undergraduate studies, Domen finished his master's in Physics in 2018. During this time, he was a researcher on a project called *A Study of Textile Systems with the Purpose of Heating in Cold Conditions* where he studied and tested different textiles with installed heaters in extreme environments. During his studies, Domen was also a tutor and instructor for physics and mathematics to younger students as part of the Student organization of the University of Maribor (ŠOUM) from 2015 to 2018. Due to this position, he also helped organize and run certain student events. For three years, he was also part of the student council and a member of the Committee for scientific endeavors at the University of Maribor for a year.

After finishing his master's thesis, Domen was employed as a researcher at the Slovenian Tool and Die Development Centre (TECOS) for a year where his work concerned various plasma systems.

In 2019, Domen began his doctoral studies in the Nanoscience and Nanotechnology program at the International Postgraduate School of Jožef Stefan along with the position of a young researcher at the Jožef Stefan Institute, performing his studies at the Department of Surface Engineering (F4). His duties encompassed experimental work with various plasma systems, as well as work with other devices, such as the mass spectrometer, optical spectrometer, atomic force microscope, secondary electron microscope, and so on. During this tenure, Domen also attended several scientific conferences.